THE OPTICAL AND NIR LUMINOUS ENERGY OUTPUT OF THE UNIVERSE
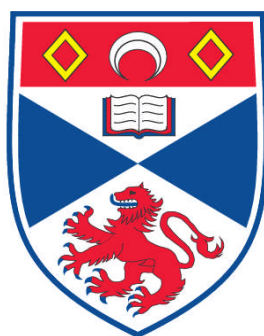## THE CREATION AND UTILISATION OF A 9 WAVEBAND CONSISTENT SAMPLE OF GALAXIES USING UKIDSS AND SDSS OBSERVATIONS WITH THE GAMA AND MGC SPECTROSCOPIC DATASETS

David Thomas Hill

**A Thesis Submitted for the Degree of PhD
at the
University of St. Andrews**

2011

**Full metadata for this item is available in
Research@StAndrews:FullText
at:
https://research-repository.st-andrews.ac.uk/**

**Please use this identifier to cite or link to this item:
http://hdl.handle.net/10023/1696**

The optical and NIR luminous energy output of the Universe

The creation and utilisation of a 9 waveband consistent sample of galaxies using UKIDSS and SDSS observations with the GAMA and MGC spectroscopic datasets

by

David Thomas Hill

Submitted for the degree of Doctor of Philosophy in Astrophysics

18th January 2011

University
of
St Andrews

Declaration

I, David Thomas Hill, hereby certify that this thesis, which is approximately 50,000 words in length, has been written by me, that it is the record of work carried out by me and that it has not been submitted in any previous application for a higher degree.

I was admitted as a research student in October 2007 and as a candidate for the degree of PhD in October 2007; the higher study for which this is a record was carried out in the University of St Andrews between 2007 and 2010.

Date   Signature of candidate

I hereby certify that the candidate has fulfilled the conditions of the Resolution and Regulations appropriate for the degree of PhD in the University of St Andrews and that the candidate is qualified to submit this thesis in application for that degree.

Date   Signature of supervisor

Permission for electronic publication

In submitting this thesis to the University of St Andrews I understand that I am giving permission for it to be made available for use in accordance with the regulations of the University Library for the time being in force, subject to any copyright vested in the work not being affected thereby. I also understand that the title and the abstract will be published, and that a copy of the work may be made and supplied to any bona fide library or research worker, that my thesis will be electronically accessible for personal or research use unless exempt by award of an embargo as requested below, and that the library has the right to migrate my thesis into new electronic forms as required to ensure continued access to the thesis. I have obtained any third-party copyright permissions that may be required in order to allow such access and migration, or have requested the appropriate embargo below.

The following is an agreed request by candidate and supervisor regarding the electronic publication of this thesis: Access to Printed copy and electronic publication of thesis through the University of St Andrews.

Date   Signature of candidate

Date   Signature of supervisor

Abstract

Theories of how galaxies form and evolve depend greatly on constraints provided by observations. However, when those observations come from different datasets, systematic offsets may occur. This causes difficulties measuring variations in parameters between filters. In this thesis I present the variation in total luminosity density with wavelength in the nearby Universe ($z < 0.1$), produced from a consistent reanalysis of NIR and optical observations, taken from the MGC, UKIDSS and SDSS surveys.

I derive luminosity distributions, best-fitting Schechter function parameterisations and total luminosity densities in $ugrizYJHK$, and compare the variation in luminosity density with cosmic star formation history (CSFH) and initial mass function (IMF) models. I examine the r band luminosity distribution produced using different aperture definitions, the joint luminosity- surface brightness (bivariate brightness) distribution in $ugrizYJHK$, comparing them to previously derived distributions, and how the total luminosity density varies with wavelength when surface brightness incompleteness is accounted for.

I find the following results. (1) The total luminosity density calculated using a non-Sérsic (e.g. Kron or Petrosian) aperture is underestimated by at least 15%, (2) Changing the detection threshold has a minor effect on the best-fitting Schecter parameters, but the choice of Kron or Petrosian apertures causes an offset between datasets, regardless of the filter used to define the source list, (3) The decision to use circular or elliptical apertures causes an offset in M^* of $0.20\,\text{mag}$, and best-fitting Schechter parameters from total magnitude photometric systems have a flatter faint-end slope than Kron or Petrosian photometry, (4) There is no surface brightness distribution evolution with luminosity for luminous galaxies, but at fainter magnitudes the distribution broadens and the peak surface brightness dims. A Choloniewski function that is modified to account for this surface brightness evolution fits the bivariate-brightness distribution better than an unmodified Choloniewski function, (5) The energy density per unit interval, $\nu f(\nu)$ derived using MGC and GAMA samples agrees within 90% confidence intervals, but does not agree with predictions using standard CSFH and IMF models. Possible improvements to the data and alterations to the theory are suggested.

Acknowledgements

I wish to acknowledge STFC for providing me with the means of support to undertake this project and my supervisor, Professor Simon Driver, whose knowledge and assistance has been invaluable. A number of other people deserve acknowledgement for helping in the preparation of this thesis: Nick Cross for patiently answering any UKIDSS queries I had, no matter how esoteric, Ian Taylor for keeping the computer network running despite my best efforts to sabotage it, Aaron Robotham and Ewan Cameron for acting as sounding boards, Lee Kelvin, for providing the Sérsic data used in the GAMA chapters, and Ivan Baldry, for determining the GAMA selection with such precision. Andrew Hopkins and Steve Wilkins have provided figures for this thesis, for which I am eternally grateful. Thanks must also go to all the other members of the astronomy department at the University of St Andrews, particularly Rowan Smith, Grant Miller and Marina Vika, for keeping me relatively sane during my time here, and to my mother and uncle for reminding me that there is a world outside of astronomy... despite my best efforts to ignore it.

This thesis is dedicated to the memory of my grandmother, Iris Jennings, who passed away on the 18th March 2010.

Contents

List of Figures

List of Tables

1

Introduction: The luminosity distribution and total luminosity density of galaxies

"There are more things in heaven and earth, Horatio, than are dreamt of in your philosophy." - Hamlet

In this chapter I introduce the scientific basis for the work I present in later chapters. I briefly describe the history of extragalactic astronomy, particularly focusing on the evolution of surveys. I outline the state of research into the initial mass function, the cosmic star formation history, and population synthesis models. I discuss the luminosity distribution of galaxies, its importance as a cosmological indicator, how it varies with wavelength, and how measurements of it have varied over time. Finally, I describe the bivariate brightness distribution, explaining why it is important, and how it is calculated.

1.1 A brief history of galaxy detection

In order to put the work within this thesis into context, within this section I summarise the history of extragalactic astronomy.

1.1.1 The existence of galaxies

Whilst astronomy is probably the oldest science studied by mankind, the examination of observations outside our Galaxy is a recent development. The first written account of the detection of Andromeda and the Large Magellanic Cloud was made in 964AD, by Abd al-Rahman al-Sufi, a Persian Astronomer, in his "Book of Fixed Stars" (Al Sufi, 964). He recorded the former as a "little cloud", and the latter as "the White Ox". The nature of these objects went unappreciated for almost a millennium. Time went by, empires rose and fell, and slowly but surely astronomical equipment improved. By the 18th century, thanks to the work of Brahe, Kepler, Copernicus and Galileo, the workings of the solar system ceased to be the unscientific astrological haze it had been since the dawn of man, and the scientific community began to look upon those "little clouds", and wonder what they were. It was from this question that the study of extragalactic astronomy began. First, however, the astronomical world had to realise that not every cloud had a silver (or more accurately, a hydrogen) lining.

In 1716, Edmund Halley listed 6 patches of sky as nebulae (Halley, 1716). These regions (the Orion Nebula, Andromeda, M22, NGC 5129, the Wild Duck Cluster and the Hercules Globular Cluster) became a source of conjecture. It was understood that telescopes were incapable of resolving sources at some distance - so the question arose, were these nebulae a form of luminous plasma, or were they a very distant, unresolved clustering of stars? In 1774, William Herschel (who 7 years later would discover Uranus), compared his observations of the Orion Nebula to a rough sketch made Christiaan Huygens a hundred years previously, and noticed that great changes had occurred. Over the course of his career (Herschel, 1786, 1789), he would start to systematically classify nebulous sources across the sky (and repeatedly change his mind about their makeup). His early work was advanced by a copy of the Messier catalogue (Herschel, 1784), the work of the French comet hunter Charles Messier, for whom these sources were a diversion from his true calling. In one of histories great ironies, it is for this work that he is remembered, as it is the earliest

astronomical catalogue of extended sources. However, despite the great advances made by the Herschel family (William's son John succeeded him and finished his father's catalogue of nebulae, Herschel 1864), other methods rather than direct imaging were necessary to solve the nebula conundrum. Strangely, and despite his work on nebulae, John Herschel never made the connection between the central-cluster with wavy arms shape of the Milky Way, and the spiral shape of some nebulae (particularly M51, whose shape was examined by Lord Rosse's reflecting telescope in 1845 - Figure 1.1; Nasim 2010). That came in 1852, when Stephen Alexander published a discussion titled "Milky Way - a Spiral" (Alexander, 1852). The work of the Herschel family forms the basis of the NGC catalogue (Dreyer, 1888), the earliest comprehensive extended-source catalogue, and one still used by amateur astronomers today.

The industrial revolution had led to great advances in chemistry, some of which were found to be useful to astronomers. Kirchhoff (1863) discovered that the spectra of the Sun could be used to calculate its chemical makeup. In 1869 Father Angelo Secchi proposed classifying stars into groups by their spectra, essentially the start of the study of stellar classification (Secchi, 1869). Simultaneously, William Huggins started examining the spectra of nebulae (Huggins & Miller, 1864). However, he worked under the misconception that they were planetary systems, as did many others at the end of the 19th century (Hoskin, 1999). His techniques found a number of gas clouds, and the idea of there being systems separate to the Milky Way (the so called island universe hypothesis) began to fade.

Photographic plates were used for the first time when the Great Comet of 1882 passed the Earth, allowing the systematic analysis of astronomical images for the first time (Gill, 1887). Two great advantages occurred when astronomy switched to photographic plates. Firstly, photographic plates allow much deeper studies (through longer exposures) than the human eye. Secondly, accurate studies of time variability became possible, as observations can be stored and analysed later. In 1908, Henrietta Leavitt found a population of stars in the Small Magellanic Cloud with a well defined pulsation period-luminosity relationship (Leavitt & Pickering, 1912). These sources, Cepheid variables, provide an accurate relative-distance indicator, as two Cepheids with the same period will have the same intrinsic luminosity. Using this data, Shapley (1918) estimated the distance to a number of globular clusters, and used this to estimate the size of the Galaxy. At 100 thousand

Figure 1.1: M51, as drawn by Lord Rosse

parsecs, this also seemed to be a counter argument to the island universe hypothesis (Shapley, 1919). Additionally, the number of spiral nebulae detected was constantly increasing. Hundreds of thousands of objects, each the size of the Milky Way? Such an idea seemed absurd. Particularly as van Maanen (1921) had recently observed four nebulae rotating. Not for the first time, and definitely not for the last, evidence that the Universe is far stranger than man would predict soon became apparent. Slipher (1913) measured the Doppler shift of a number of "spiral nebulae", including Andromeda, and found radial velocities of $\sim 1000\,\mathrm{km\,sec^{-1}}$. Curtis (1920) found evidence of edge-on nebulae with obvious dust-lanes, and reasoned that such a feature in the Milky Way would conceal any galaxies on the other side, causing the observed "zone of avoidance". The disagreement over the island-universe hypothesis came to a head when Curtis and Shapley engaged in what was known as "The Great Debate" (Hoskin, 1976). A muddled affair, it ended inconclusively, with both men claiming victory and astronomy none the wiser. In 1925, by detecting a Cepheid variable within Andromeda, and measuring its luminosity and pulsation period, Hubble (1925) deduced the distance to that galaxy, thus ending the debate. Extragalactic astronomy had begun, and astronomers began to examine the distribution of such sources.

1.1.2 The age of the sky survey

The advancement of science continued. Shapley & Ames (1932) created the first magnitude limited all-sky survey of extragalactic nebulae, defining their sample to be every source brighter than 13th magnitude; a population of just over 1000 sources. Hubble deduced the expansion of the Universe (Hubble, 1929). Einstein's general relativity formulation (Einstein 1948 gives a late review) was used to derive the theoretical basis for this observation (see also Friedmann 1924; Robertson 1935; Walker 1937). The second world war happened; a tragic occurrence for humanity, but the clear night skies induced by blackouts created a generation of budding astronomers and in the postwar period the military-surplus equipment and trained staff stimulated the nascent field of radio astronomy. The cold war began, and science and technology became a funding priority. In the 1960s and 70s, a series of major observatories were opened, including Kitt Peak in the US, Siding Spring Observatory in Australia (home of the Anglo Australian telescope, the AAT), and Mauna Kea Observatory in Hawaii (home of UKIRT). In 1949, the National Geographic Society - Palomar Observatory Sky Survey (NGS-POSS) began at the Palomar Observatory. This was an optical mapping of all sky North of $\delta = -30$ deg, with imaging taken using red and blue filters. Vorontsov-Vel'Yaminov & Arkhipova (1968) used this imaging to construct the "Morphological catalogue of galaxies", a survey of ~30 thousand galaxies. A similar mapping of the Southern sky was undertaken using the UK Schmidt Telescope at the AAT in the 1970s. These surveys were combined, and in 1994 their photographic plates were digitised, and distributed as the digitized sky survey (DSS, Morrison 1995). This was the first all-sky, computerised survey; the ancestor of the datasets used within this thesis.

Technological advancement meant that astronomy was no longer constrained to the visible parts of the electromagnetic spectra. In 1969, Neugebauer & Leighton presented the Two-micron sky survey (also known as IRc), a shallow NIR survey comprising less than 6000 sources with $K < 3$ mag, distributed across three quarters of the sky. Amongst these sources were a population of extremely red stars that were faint in the optical. The search for red stellar populations, such as brown dwarfs, has been a major attraction for infrared astronomy ever since (Price, 2009).

The APM survey (Maddox et al., 1990), was an optical survey of 4300 sq deg of the Southern galactic cap. Using an automated photographic plate scanning machine, 185 plates

from the Schmidt Telescope were scanned, and 20 million objects were detected. A magnitude limited ($m_{b_j} = 20.5$ mag) catalogue of 2 million galaxies was taken from this sample. Preparation for SDSS (Gunn & Knapp, 1993) and 2MASS (Kleinmann, 1992) began in the early nineties. SDSS was a successor survey to the DSS: a predominantly northern sky survey based at the same site, with the advantage of 50 years of technological advancement including, importantly, the switch from photographic plates to direct measurement using CCDs. SDSS imaging provides the majority of the optical data used within this thesis, and it is further described in Chapter 2. 2MASS had a similar relationship to IRc, with the great advances in NIR technology giving it the capacity to observe 11 magnitudes deeper and with $\sim 100\%$ sky coverage in three filters (JHK_s). This increase in scope allowed it to examine the L and T dwarf star populations for the first time (Kirkpatrick et al., 1999), and sources obscured by the dust in the Galactic plane (e.g. the overdensity of sources in Canis Major that may be a dwarf galaxy, Martin et al. 2004). 2MASS was followed up by UKIDSS (Lawrence et al., 2007), which began observing in 2005, is 3 magnitudes deeper than 2MASS, and observes using four filters ($YJHK$). UKIDSS imaging provides the NIR data for this thesis, and is described in Chapter 2.

1.1.3 The advancement in redshift surveys

However, progressively deeper photometry alone cannot answer most cosmological problems. Some form of distance indicator to the detected sources is necessary, such as using Cepheid variables (Leavitt & Pickering, 1912) or supernovae (Colgate, 1979) as standard candles. Cepheid variables are stars with a characteristic, periodic variation in brightness (due to an obscuring outer envelope of Helium that expands and contracts), with the period of the variation proportional to the luminosity of the star itself. Type Ia supernova have a similarly invariant property: the peak of their luminous output is constant, as is the rate at which the luminosity decays from that peak. From the observed apparent magnitude and the theoretical absolute magnitude, the distance to the galaxies containing these sources can be surmised. However, these techniques are not feasible indicators for large samples of sources. Firstly, they require source variability to be measured, thus requiring a large amount of telescope time. Secondly, the Cepheid variable method requires a specific stellar type to be resolvable within the source, and the supernova technique requires a
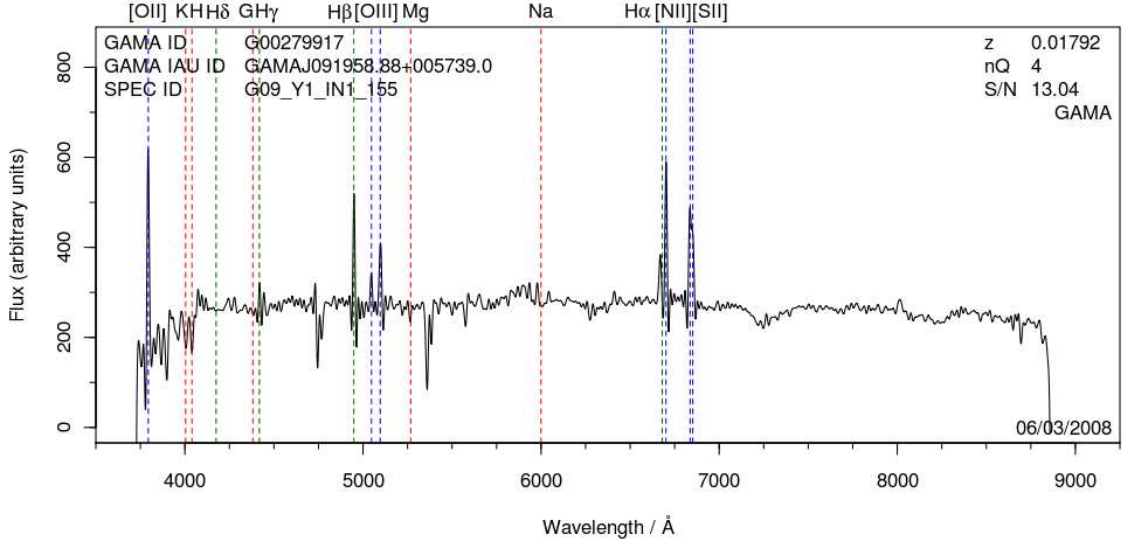
Figure 1.2: The spectra of GAMAJ091958.88+005739.0, an $r_{\mathrm{Kron}} = 15.37\,\mathrm{mag}$ galaxy within the GAMA sample. By matching the features of the galaxy spectrum (the vertical dashed lines) to a template, the source has been measured to have a redshift, $z = 0.01792$. This spectra was taken using the AAOmega instrument, on the AAT, and the image was produced by Lee Kelvin, on behalf of the GAMA survey team. Spectra in this form are available from the GAMA website, via the GAMA object inspection tools.

supernove to be detected within the source; unlikely, as supernovae occur infrequently - twice a century in a galaxy as large as ours (Diehl et al., 2006).

The standard method of measuring the distance to galaxies is the spectroscopic redshift. This involves examining the spectra of the galaxy, and using the offset in its features (e.g. emission and absorption lines) to measure its redshift (an example is shown in Figure 1.2). From the redshift, and assuming a cosmology, the distance to the source can be measured. This is an effect of the recessional velocity - distance relationship deduced by Hubble (1929), and in order to ascertain the true distance, the effects of the local velocity field (Sandage & Tammann, 1975) and the orbit of the Earth around the Sun on the apparent velocity must be accounted for.

To begin with, attempts at spectroscopic redshift surveys took a very long time. Spectral capture is a difficult process, requiring long exposures to obtain data of a reasonable quality. Humason et al. (1956) presented redshift data for 620 sources (taken from the Shapley-Ames catalogue), obtained over a 20 year period. Hubble himself had started that particular survey, but did not live long enough to see its conclusion. Further redshifts were obtained on a piecemeal basis by, amongst others, Mayall & de Vaucouleurs (1962),

Schmidt (1965) and Burbidge & Burbidge (1965).

Mayall (1960) noted that the traditional method used to capture spectra, via short-focus, long-duration photographic exposures, was becoming obsolete, as photoelectric scanning of the spectra by the telescope gave a series of efficiency gains, vastly increasing capture speed and eliminating the waste of time caused by interrupted exposures (due to atmospheric conditions or instrument problems). Kintner (1971) and Rood et al. (1972) used this new technology, in the form of an image-tube spectrograph on the 84 inch telescope at Kitt Peak, to undertake a redshift survey particularly focused on the Coma Cluster. Sandage (1978) obtained spectra for the fainter sources in the Shapley-Ames catalogue that were not sampled by Humason et al. (1956). Redshifts from Humason et al. (1956) and Sandage (1978) form the basis of the Revised Shapley-Ames catalog of bright galaxies (Sandage & Tammann, 1981); a compilation of all known morphological, photometric and spectroscopic information for the Shapley & Ames (1932) galaxies. At this time, the division between deep pencil-beam spectroscopic surveys, cluster surveys and shallow, all sky surveys began: as Sandage (1978) was completing his work, other groups (e.g. Tifft & Gregory 1976 and Kirshner et al. 1978) were undertaking specialised redshift surveys over smaller areas.

The CfA redshift survey (Tonry & Davis, 1979; Huchra et al., 1983) was a large (~ 2400 source) redshift survey, that sacrificed area of coverage (1.83 sr of coverage in the North galactic cap, 0.83 sr in the South galactic cap) for depth (complete to $m_B = 14.5\,\mathrm{mag}$), in order to examine structure beyond the Local Supercluster. This was cosmologically important, allowing the clustering (Davis & Peebles, 1983) and homogeneity (Davis & Huchra, 1982) of the Universe to be measured within a large volume of the Universe for the first time, and providing early evidence for the large scale filamentary structures observed today (Geller et al., 1987; Geller & Huchra, 1989). Redshift survey design became influenced by the need to test numerical simulations (e.g., Davis et al. 1985; White et al. 1987). da Costa et al. (1989) extended the southern coverage of the CfA survey, as part of the Southern Sky Redshift Survey (SSRS, da Costa et al. 1988), an attempt to map a diameter-limited sample of galaxies within the Southern sky. Both the CfA and SSRS projects were expanded, into CfA2 (Huchra et al. 1990, a Northern sky survey) and SSRS2 (da Costa et al. 1994, a Southern sky survey). Together, they contain approximately 10 thousand galaxies and cover over a third of sky to $\sim m_B = 15.5\,\mathrm{mag}$.

As survey astronomy extended its range beyond visible light, it was a small step to define spectroscopic surveys using other parts of the electromagnetic spectrum. The IRAS redshift survey sample (Fisher et al., 1995) was defined using $60\,\mu$m observations, producing a coherent sample across the entire sky, including the optical "zone of avoidance".

Further advances were made in optical astronomy. The Las Campanas Survey (Oemler et al., 1993), utilised a fibre-fed spectrograph that could simultaneously measure spectra for 100 objects. The 2dF galaxy redshift survey (2dFGRS, Colless et al. 2001) went further, utilising the AAT's 2dF multifibre spectrograph to simultaneously observe 400 sources. The 2dFGRS sample was taken from the APM galaxy catalogue (Maddox et al., 1990). Over 200 thousand galaxy spectra were observed, within $2000\,$sq deg of sky, to a limiting magnitude of $m_{b_j} = 19.45\,$mag. SDSS (York et al., 2000), as well as being a large area photometric survey, also produced spectra for over 1.6million sources, including 930 thousand galaxies (Strauss et al., 2002), with their main sample complete to $m_r = 17.77\,$mag. Within 20 years, the number of galaxy redshifts detected had increased by 2 orders of magnitude. The sky distribution of bright sources had become well measured. However, extragalactic astronomy, particular theories of groups and mergers, always needs observations that are deeper, in order to examine clusters of galaxies in greater detail.

The MGC (Liske et al., 2003) was a deeper survey, covering a $37.5\,$sq deg area within both 2dF and SDSS surveys. A highly complete ($> 99\%$) photometric survey covering all galaxies brighter than $m_B = 20\,$mag, the MGC combined redshifts from the literature (including 2dF and SDSS sources) with its own specific redshift survey (Driver et al., 2005). Its purpose was to examine a segment of the local Universe to a depth beyond the capabilities of 2dF and SDSS, and to deduce any inaccuracy within those datasets (Cross et al., 2004). MGC data is used within this thesis (in Chapter 3), and the survey is discussed in further detail in Section 2.1. The GAMA survey (Driver et al., 2010) is a larger, slightly deeper follow up to the MGC survey. Providing spectra for an highly complete ($\sim 98\%$), magnitude limited ($m_r < 19.4\,$mag) sample of over 100 thousand galaxies over $144\,$sq deg of sky, GAMA is an attempt to probe deeper than SDSS whilst still limiting the effects of cosmic variance. GAMA's region of coverage is also within the area probed by SDSS and 2dF (with partial coverage by MGC), with over 17 thousand sources within its sample having existing spectroscopy. GAMA data is used within this thesis, and the survey is discussed in further detail in Section 2.4.
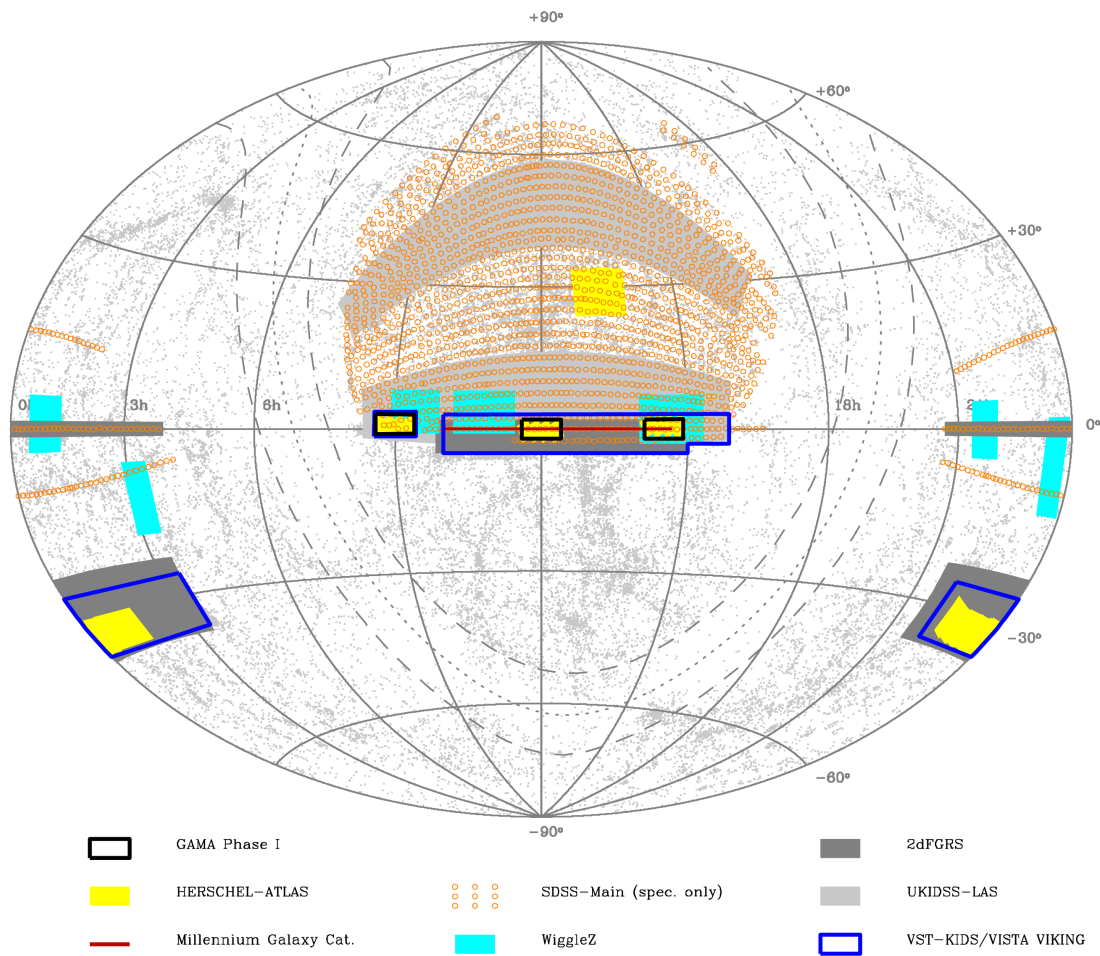
Figure 1.3: The sky position of the GAMA, SDSS main redshift survey, MGC and 2dFGRS datasets. Taken from Driver et al. (2010), with the author's permission.

1.1.4 Conclusion

The number of extended sources known no longer amounts to the thousands catalogued by Herschel, or the tens of thousands catalogued by Vorontsov-Vel'Yaminov & Arkhipova (Figure 1.4). SDSS alone has produced spectra for > 1 million galaxies and quasars, and has detected two orders of magnitude more. In order to understand the Universe, we must undertake rigorous statistical analysis of these sources, and account not only for the data, but any effect that would offset that data from the underlying distribution. The work in this thesis concentrates on two related quantities: the luminosity distribution of galaxies (how the density of galaxies in space varies with luminosity), and the total luminosity density (the density of luminous emission by galaxies). These quantities are described in sections 1.3 and 1.4. In order to measure these quantities accurately, the photometric techniques used must be consistent and reliable. The measurement of galaxy luminosity is not straightforward, and a number of methods exist. The methods used in this thesis are described in section 1.2. The bulk of this thesis, particularly chapters 3 and 4, concentrates on the processes undertaken, and the reliability tests performed, in order to show unequivocally that the photometry used to derive the results in chapter 5 are as accurate as current data quality allows. Data is taken from the MGC, SDSS and GAMA datasets, which are detailed in Chapter 2.

1.2 Measuring luminosity

Determining the true luminosity of a galaxy is not a simple task. The edges of galaxies are indeterminate, their shapes are amorphous and their light profiles are variable. Additionally, where galaxies are clustered, the light profiles from multiple objects may coalesce, and the ability to differentiate between the light coming from different sources may be compromised. In order to create a consistent photometric measurement, certain assumptions about the properties of each galaxy's light profile must be made. For instance, fixed size magnitudes assume that the total light emitted by a source can be detected within a certain radius, and model magnitudes assume that the source's light profile can be entirely fitted by a specified model, without any deviation. Different photometric methods work with different assumptions. This thesis uses measurements taken with three different photometric methods. The Kron and Petrosian photometric methods (sections 1.2.1 and

Messier (Messier)
General Catalogue of Nebulae and Clusters (Herschel)
NGC (Dreyer)
NGC+Index Catalogue Supplements (Dreyer)
Morphological catalogue of galaxies (Vorontsov–Velyaminov, based upon NGS–POSS)
APM (Maddox)
2MASS XSC (Jarrett)
SDSS DR7 PhotoPrimary 'Galaxy' sources (Abazajian)
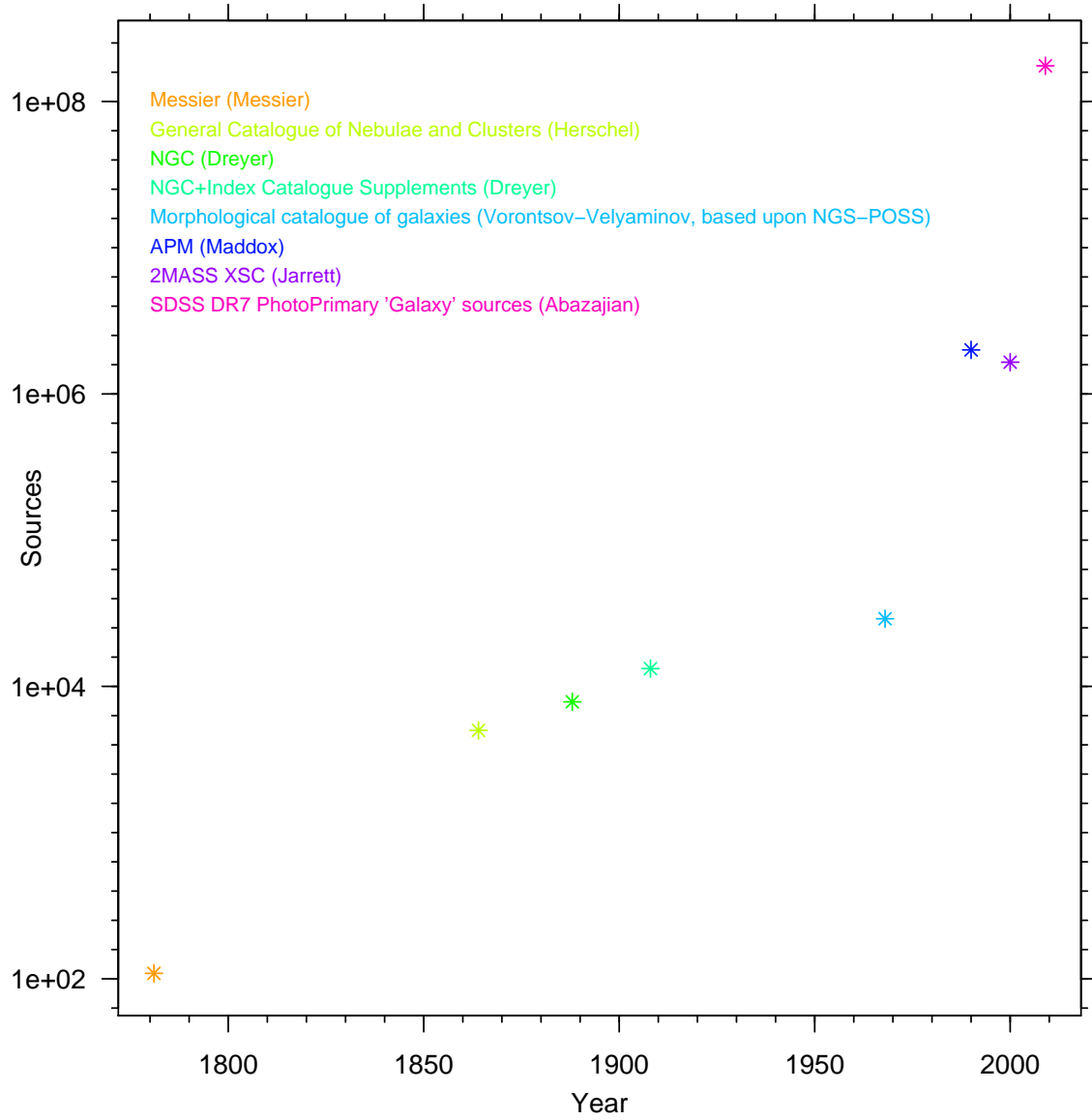
Figure 1.4: The increasing number of extended sources detected in sky survey datasets.

1.2.2) use the light profile of the galaxy to define the size of an aperture. The Sérsic photometric method (section 1.2.3) fits the light profile shape to the Sérsic law, and then calculates the total luminosity of the galaxy by integrating that model.

1.2.1 Kron magnitudes

The Kron magnitude system (Kron, 1980) uses the first moment of the surface brightness profile of a galaxy to calculate a characteristic radius for a source, i.e:

$$R_K = \frac{\int_0^\infty xI(x)dx}{\int_0^\infty I(x)dx} \tag{1.1}$$

where $I(x)$ is the light distribution function of the galaxy. In practice, the upper limit is truncated at an isophote equal to some fraction of the background.

The Kron magnitude system infers that within some multiple of this radius (Kron 1980 use a multiple of 2, this work uses $2.5R_{Kron}$), a significant fraction of the total light emitted by a galaxy will be detected ($> 90\%$), and the fraction is constant irrespective of the redshift of the source. Kron also states that the system works well in bad seeing conditions, regardless of the morphological type of the galaxy. This is a significant advantage over a simple isophotal magnitude system. `SExtractor` provides a Kron-style magnitude, with the name AUTO. In early releases of `SExtractor`, the AUTO magnitude was known to struggle in clustered environments. A further magnitude system (BEST) was defined that primarily used AUTO magnitudes, but switched to corrected isophotal magnitudes in high-density environments. In later versions, this issue was solved and use of the BEST system was deemed unnecessary.

1.2.2 Petrosian magnitudes

The Petrosian magnitude system (Petrosian, 1976) also uses the light profile of a galaxy to define a characteristic radius. In this case, the Petrosian radius is defined as the radius at which the surface brightness at that radius drops below a certain fraction of the average surface brightness within that radius, i.e. Define a ratio P:

$$P = \frac{\int_{r-\delta r}^{r+\delta r} 2\pi xI(x)dx/(\pi((r+\delta r)^2 - (r-\delta r)^2))}{\int_0^r 2\pi xI(x)dx/(\pi r^2)} \tag{1.2}$$

where $I(x)$ is the average surface brightness profile, and $\delta r \to 0$. The Petrosian radius is the radius at which P (this ratio is also referred to as $\frac{1}{\nu_{RPetro}}$ following Petrosian's original definition) drops below a certain value. The SDSS survey (Strauss et al., 2002) and `SExtractor` Petrosian magnitudes are both calculated using $\frac{1}{\nu_{RPetro}} = 0.2$. Using a multiple of the Petrosian radius to define an aperture will enclose a significant fraction of the total galactic emission ($2R_{Petro}$ theoretically encloses $> 80\%$ for a de Vaucouleurs profile, and $\sim 98\%$ of an exponential profile's light). As with the Kron magnitude system, an additional theoretical advantage of the Petrosian magnitude system is that it is redshift independent. In practice, as seeing quality diminishes and distance increases, the SDSS survey team (Blanton et al., 2001) have found that the fraction of light enclosed by $2R_{Petro}$ tends towards the return expected from a PSF profile source($\sim 95\%$).

A parameter called the Concentration Index can be defined that uses the Petrosian radius that contains a fraction of the galaxy's flux to calculate the Sérsic index of the source (Graham & Driver, 2005). The Concentration index is a ratio of two radii (often $\frac{R_{90}}{R_{50}}$; the radii that enclose 50% and 90% of the Petrosian flux of the galaxy), and varies with the underlying light profile. Using this parameter, it is possible to calculate the morphology of a galaxy, and to convert the Petrosian radius into an effective half light radius and the Petrosian luminosity into a Sérsic total luminosity.

1.2.3   Sérsic magnitudes and the 'missing light' problem

The two magnitude systems introduced so far have an important flaw. They fail to account for the light emitted by a galaxy outside of the radius of the aperture, and the fraction of light they miss varies with the surface brightness profile of the source. The 'missing light' problem is an important issue when calculating the true total luminosity density of the Universe, as it will force the apparent magnitude of every galaxy fainter by a potentially significant factor. Unfortunately, it is not an easy bias to correct. Aperture size can not be increased infinitely, as eventually it will cover other sources, leading to uncertainty in the distribution of the observed flux. Additionally, at some distance from the centre of each galaxy, the flux emission will drop so low that it will be contained within the noise properties of the image. An alternative method must be theorised. Once such method is to fit each galaxy to a theoretical surface brightness profile, and ascertain the total luminosity from the model. The Sérsic magnitude system is one way of achieving this
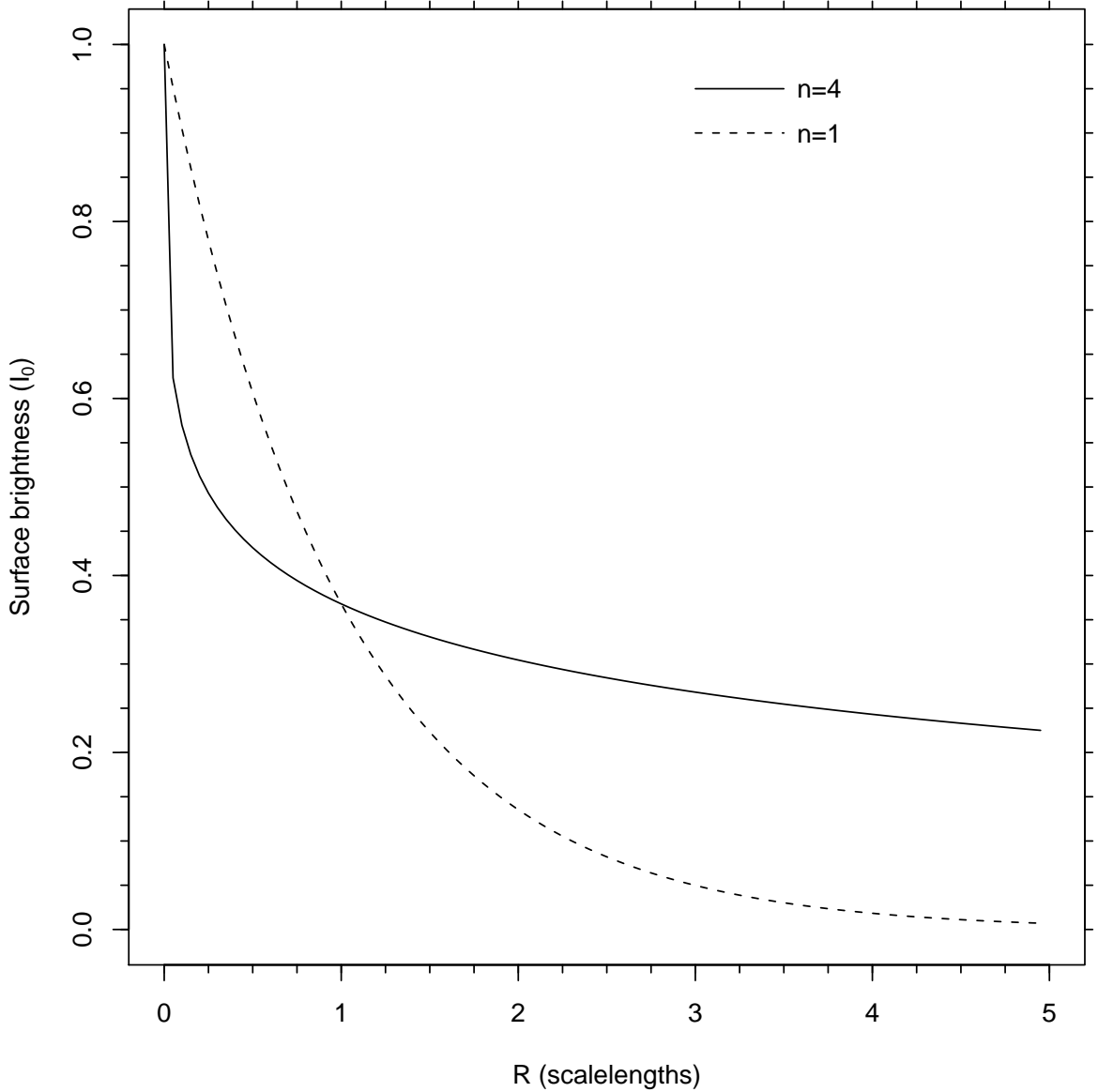
Figure 1.5: How the surface profile of a galaxy varies depending upon its Sérsic index.

result.

The Sérsic magnitude system (Sérsic, 1963) is a method of calculating the luminosity of a galaxy using the Sérsic law. This is a generalised surface brightness profile with the form:

$$I(R) = I_0 e^{-(\frac{R}{a})^{\frac{1}{n}}} \tag{1.3}$$

Where I_0 is the central surface brightness of the galaxy, a is a scale length, and n is the Sérsic index. When a galaxy has a de Vaucouleurs profile, $n = 4$. When a galaxy follows an exponential profile $n = 1$. Example surface brightness profiles are shown in Figure 1.5. The Sérsic photometric system infers that each galaxy smoothly follows a Sérsic surface

brightness profile. By measuring the parameters of the Sérsic profile (i.e., a, I_0 and n), the total luminosity of the galaxy can be calculated by integrating the profile to infinity (or to some truncation radius), i.e.:

$$L_{Total} = \int_0^\infty 2\pi R I(R) dR \qquad (1.4)$$

Sérsic magnitudes have one major advantage over the Kron and Petrosian systems. By integrating the Sérsic profile to infinity, Sérsic magnitudes recover all the light emitted by a galaxy, and not just the light emitted within the aperture. However, they have the major disadvantage that the galaxy's surface brightness profile must follow a Sérsic profile, without any deviation. If the galaxy's profile truncates at some radius, or otherwise ceases to follow the specified surface brightness profile, then the estimate of the total luminosity will be incorrect. This is particularly an issue with systems whose surface brightness profile seems to be composed of a series of distinct components, such as spiral galaxies. Calculating the parameters of the Sérsic function is also a difficult task. In order to guarantee the accurate recovery of the parameters, nearby objects (such as stars, galaxies and artefacts) must be masked or modelled. This thesis uses the `SIGMA` package (discussed later in Chapter 4) to undertake this analysis.

1.3   The galaxy luminosity distribution

The luminosity distribution of galaxies is a fundamental observable feature of the Universe. It is an account of how the space density of galaxies varies with flux, and provides an insight into how visible matter is fragmented. It was originally used to test Hubble's velocity-distance relation (Hubble, 1936a). However, it was also found to be important for other studies. For example, how luminosity is distributed is important in the calculation of the spatial covariance function (Peebles & Hauser, 1974), the determination of evolutionary and cosmological corrections (Brown & Tinsley, 1974), and the frequency of absorption lines in QSOs due to galaxies between the observer and the source (Bahcall, 1975). The luminosity distribution was also used to compare the distribution of radio and optical sources (Schmidt, 1968).

The luminosity distribution of galaxies is also a result that can be compared to simulation predictions. Computational simulations, such as semi-analytic modelling, attempt to

model the evolution of the Universe using a number of physical processes, e.g., tidal interactions and merging of galaxies and dark matter haloes, stellar formation and evolution, and the effects of shock heating and cooling on galaxies. Semi-analytical models that contain feedback mechanisms and suppress gas cooling can reproduce the flat faint-end slope of the luminosity distribution, though thermal conduction or gas expulsion from haloes is required to produce a sharp bright-end cutoff (see Benson et al. 2003). Simulations can also use the luminosity distribution parameters to set input parameters. For instance, Cole et al. (2000) constrain their brown dwarf fraction, Υ, stellar feedback parameters, $\alpha_{\text{hot}}, V_{\text{hot}}$, and yield, p, from luminosity distribution observations.

As well as allowing the comparison of observations to semi-analytical models, the luminosity distribution is also a step towards the derivation of the stellar mass function (Baldry et al., 2008). The galaxy stellar mass function shows how stellar matter is distributed between galaxies. In essence, it is to mass what the luminosity function is to light, and can be calculated from the luminosity function when it is combined with stellar Mass-to-Light ratio estimates in galaxies. The stellar mass function illustrates the distribution of baryonic matter within the Universe, an extremely important cosmological result, particularly when compared to the dark matter halo mass distribution found from examining velocity dispersion curves.

1.3.1 Methods of calculating the luminosity distribution

Here I examine the two most common methods used to generate the luminosity distribution of galaxies: the stepwise maximum likelihood method (SWML) that is used to generate the luminosity distributions in this thesis, and the $1/V_{\text{max}}$ method, that is used to normalise the SWML solutions to the universal luminosity density. In both cases, it is assumed that the population of galaxies that are input into the algorithm have been cut to a limiting apparent magnitude m_{lim} and redshift range $z_{min} < z < z_{max}$, and are complete within these limits.

$1/\mathrm{V_{max}}$ method

The Volume corrected distribution method ($1/\mathrm{V_{max}}$) is the simplest, and oldest (Schmidt, 1968)[1], method of calculating galaxy luminosity distributions. It works by weighting each galaxy by the volume that it could reside within and still be included within the sample. Galaxies are then allocated into bins based upon their luminosity. The value for each bin is the sum of the galaxy weights for all sources within it. For example, Equation 1.5 shows the formulae required to calculate the luminosity density within a bin that covers dM centred on M_s:

$$\phi(M_s)dM = \sum_{i=1}^{N_g} \frac{N(M_s - \frac{dM}{2} \le M_i \le M_s + \frac{dM}{2})}{V_{max}(M_i)} \tag{1.5}$$

where N_g is the number of galaxies within the sample, $N(x)$ is 1 if the statement x is true, and 0 otherwise, and $V_{max}(x)$ gives the volume a x magnitude galaxy would be visible within.

Unfortunately this method is dependent on the size of bins used; different sizes of bins can lead to different results for the same dataset. It has the advantage of making no assumptions about the shape of the LF, and has no dependence on the environment (Bell et al., 2003). A recent approach has been to calculate $1/\mathrm{V_{max}}$ for each source, and sum the parameters provided by the entire population to obtain the luminosity distribution.

SWML method

The SWML method, which is described in detail in Efstathiou et al. (1988), is a maximal-likelihood method of calculating binned luminosity distributions in a non-parametric manner.

Maximum-likelihood approaches attempt to find the distribution that has the highest probability of generating the observed sample. In the SWML case, this is computed by maximising $\mathcal{L}$ with respect to a discretised luminosity distribution, where $\mathcal{L}$ is the product of the probabilities of observing each galaxy within the sample's absolute magnitude limits (given the redshift of the galaxy). The resulting luminosity distribution can then be fit via χ^2-minimisation to determine the Schechter function parameters.

---

[1]This method was first proposed by Kafka (1967), in an unpublished preprint. Schmidt cites this, but has since been generally credited with its creation. (Felten, 1976)

As noted, the SWML method makes no apriori assumption of the form of the luminosity function, but does require an additional method for normalisation. The simplest method, and that adapted later in this thesis, is to (1) select an absolute magnitude range (M_1 to M_2), (2) find the number of galaxies inside this range ($N_{1 \to 2}$), (3) calculate the maximum and minimum redshifts over which galaxies of magnitude M_1 to M_2 can be seen and (4) integrate the standard expression for the volume interval ($V_{1 \to 2} = \frac{\delta V}{\delta z}$) over this redshift range for the specified cosmology. The SWML luminosity distributions are then scaled such that: $\phi(\mathrm{M}_1 \text{ to } M_2) = \frac{N_{1 \to 2}}{V_{1 \to 2}}$. The normalisation is in effect a $1/V_{\max}$-method with the SWML luminosity distribution rescaled to produce the required number of galaxies within the specified absolute magnitude range. Care must be taken to ensure that the calibration volume is complete for the range of absolute magnitudes selected. Willmer (1997) has found that, in samples where the faint end of the luminosity distribution is under-represented, the behaviour of the SWML method can be eccentric, with a larger α than expected being recovered. In Efstathiou et al. (1988) the method adopts a constant flux limit for all galaxies.

A minor modification was introduced by Norberg et al. (2002) when analysing 2dFGRS data in order to accommodate a refinement in the 2dFGRS input catalogue. The final method is shown in Equation 1.6, below:

$$\phi(M_k)dM = \frac{\sum_{i=1}^{N_g} W(M_i - M_k)}{\sum_{i=1}^{N_g} \frac{H(M_k - M_{\mathrm{faint}(z_i, m_{\lim,i})})}{\sum_{j=1}^{N_s} \phi(M_j)dM H(M_j - M_{\mathrm{faint}(z_i, m_{\lim,i})})}}$$

where:

$$W(x) = \begin{cases} 1 & \text{if } -\frac{dM}{2} \leq x \leq \frac{dM}{2} \\ 0 & \text{otherwise} \end{cases}$$

$$H(x) = \begin{cases} 1 & \text{if } x \leq -\frac{dM}{2} \\ \frac{1}{2} - \frac{x}{dM} & \text{if } -\frac{dM}{2} \leq x \leq \frac{dM}{2} \\ 0 & \text{otherwise} \end{cases}$$

(1.6)

where $\phi(M_k)$ is the luminosity density contained within a bin of width dM centred upon M_k. The sample contains N_g galaxies, and the method is set to use N_s bins. $M_{\mathrm{faint}(z,m)}$ gives the limiting absolute magnitude of an m mag object at redshift z. The W function serves the same purpose as the N function in the $1/\mathrm{V}_{\max}$ method described earlier; it

counts the number of galaxies with luminosity inside the range covered by the bin. The H function weights each galaxy depending upon which bins it could fall within, and the luminosity density present within those bins. It is therefore an iterative process, with each repetition using the luminosity density values calculated in the previous iteration.

The key modification between the Efstathiou et al. and Norberg et al. methods is the introduction of an individual magnitude limit ($m_{\mathrm{lim},i}$) for each object. The Norberg et al. method was also adopted by the 6dfGS and MGC (Jones et al., 2006; Driver et al., 2005) teams for dealing with non-uniform flux limits. It also allows for the construction of accurate luminosity distributions using bandpasses that did not define the limits of the sample.

1.3.2 The Schechter Function

The shape of the luminosity distribution in the UV-NIR follows a similar pattern. As luminosity decreases, the luminosity density increases exponentially, until a point is reached where the rate of increase flattens, and the distribution follows a power-law like relation. Attempts to parametrise the galaxy luminosity distribution began over half a century ago. The current standard, the Schechter function (Schechter, 1976), built upon work by Hubble (1936b) (who studied only the brightest galaxies and found a normally distributed sample), Zwicky (1957) (who extended the work to faint dwarf galaxies and found an exponential increase), Kiang (1961) and Abell (1958), amongst others. In terms of luminosity it contains both power law and exponential components; when converted into magnitudes it becomes a double exponential expression.

Schechter parametrised the galaxy luminosity density distribution as a three parameter function (Equation 1.7), with the M^* variable being the magnitude where the power law part of the function diminishes in strength, the α variable controls the power law slope and the ϕ^* variable normalises the function to the correct density. An example Schechter function is shown in Figure 1.6.

$$\frac{dn}{dM} = \phi(M) = 0.4\ln10\phi^* \frac{(10^{0.4(\mathrm{M_*-M})})^{\alpha+1}}{\mathrm{e}^{10^{0.4(\mathrm{M_*-M})}}} \tag{1.7}$$

The Schechter function represents the superposition of a series of bell-shaped, distinct galaxy populations. Many measurements of the Schechter parameters have been made

across the entire range of the electromagnetic spectrum. For example, Mauch & Sadler (2007) fit the Schechter function to 1.4GHz radio data, Budavári et al. (2005) fit it to UV GALEX data, and de Grandi et al. (1999) fit the Schechter parametrisation to the X-ray luminosity distribution of bright galaxy clusters. However, the Schechter function is only an approximate match to the galaxy luminosity distribution. Saunders et al. (1990) have found that the function isn't a good fit to FIR data, with the $60\,\mu$m luminosity distribution too broad to fit this parametrisation. Using 6dF NIR data, Jones et al. (2006) found that it does not turn down sharply enough at M^*, Blanton et al. (2003) found that there is a deviation from the function at the luminous end of the galaxy distribution and a strong positive correlation between the M^* and α parameters, and Bell et al. (2003) have attempted to modify it to fit their dataset more accurately. It is, however, the standard parametric fit adopted in the literature and therefore useful when comparing to earlier work.

1.4 The total galaxy luminosity density

The total galaxy luminosity density is the sum of the luminosity density of the entire galaxy population - the total light output (within the filter) by all galaxies, per unit volume. It is an important statistic, as it indicates the mean radiation field of the Universe. Observationally, however, it is technically impossible to compute to 100% accuracy, as below a certain luminosity threshold a galaxy cannot be detected and therefore the space density of such systems and their contribution to the luminosity density is unconstrained. In order to calculate it, it is therefore necessary to extrapolate from the luminosity distribution provided by the observable galaxy population to infinitesimally bright sources. This assumes that the luminosity distribution can be accurately parametrised across the entire luminosity range by a functional form, that this function is smooth and well-behaved, and has parameters that can be accurately derived from measurements at the bright end of the luminosity distribution. Section 1.4.1 details the calculation of the total luminosity density from Schechter function parameters.
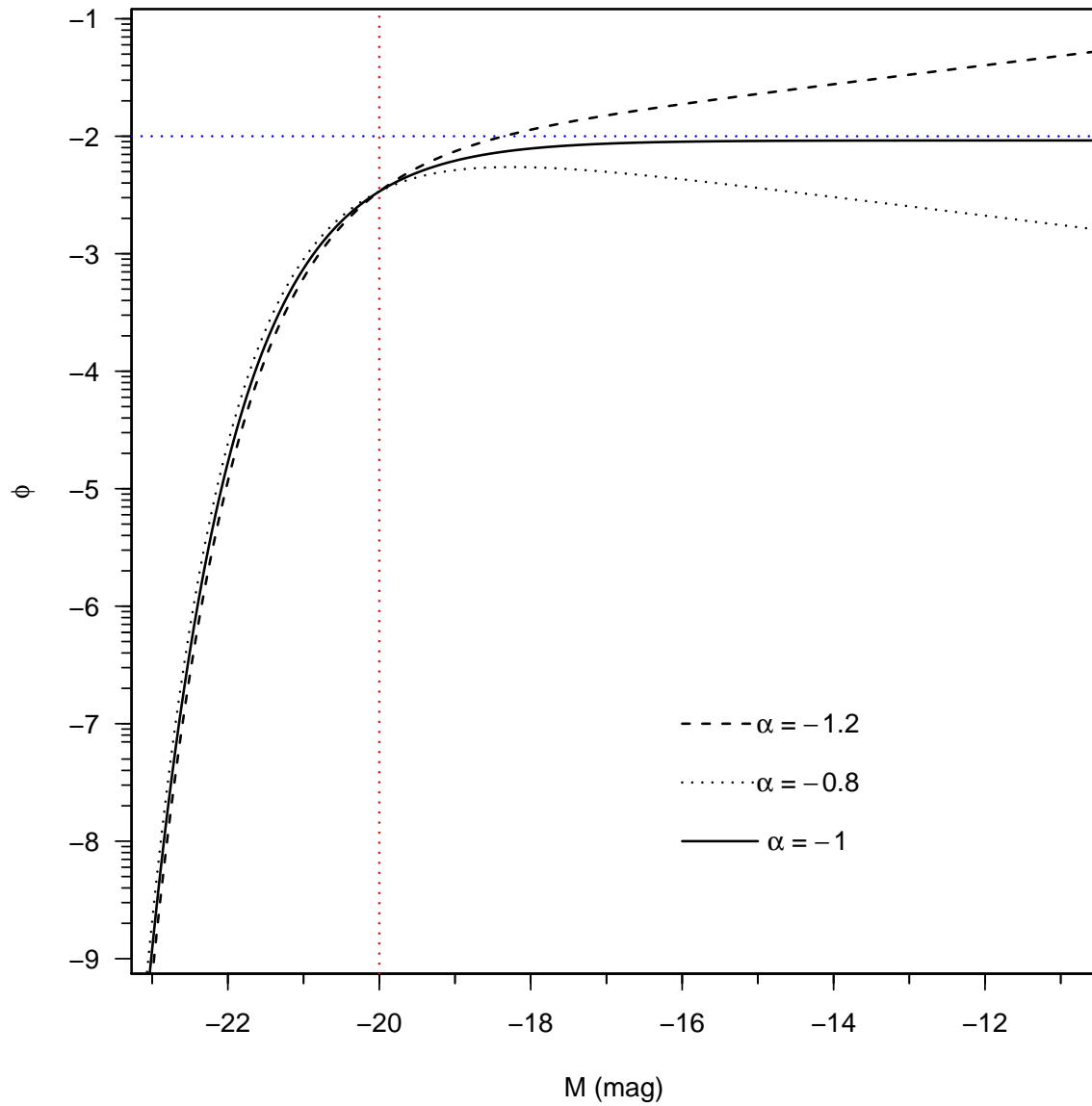
Figure 1.6: Three Schechter functions, ϕ, with varying α parameters, $M^* = -20$ and $\phi^* = 0.01$. The position of M^* is indicated by a dashed red line, ϕ^* by a dashed blue line. The $\alpha = -1$ Schechter function is shown as a black line, the $\alpha = -0.8$ Schechter function as a black dotted line, and the $\alpha = -1.2$ Schechter function as a black dashed line.

1.4.1 Calculation of the total luminosity density

The total luminosity density in a given waveband, j_λ, can be calculated using the Schechter function parameters (Equation 1.8):

$$j_\lambda = \phi_\lambda^* 10^{-0.4(M_{\lambda,*} - M_{\lambda,\odot})} \Gamma(\alpha_\lambda + 2) \tag{1.8}$$

It is found by integrating the luminosity function over all magnitude space. The total luminosity density measurements produced from the Schechter function integration (in units of $hL_{\odot,\lambda}\mathrm{Mpc}^{-3}$) can also be converted to energy density per frequency interval statistics ($hW\mathrm{Mpc}^{-3}\mathrm{Hz}^{-1}$), which are more useful when comparing data with significantly differing filter widths and for comparison to model SEDs. The conversion is made using:

$$\nu f(\nu) = \frac{c}{\lambda}.j_\lambda.10^{-0.4(M_{\odot,\lambda} - 34.10)} \tag{1.9}$$

where λ is the effective wavelength, j_λ is the total luminosity density and $M_{\odot,\lambda}$ is the absolute magnitude of the Sun in the specified filter. The constant value (34.10) derives from the definition of the AB magnitude scale (where 3631Jy equates to 0 mag; Oke & Gunn 1983). Note that the filter width technically should appear twice but cancels, i.e. to derive the total flux through the filter one should multiply by the filter width (in Hz), however to make a useful comparison it is more logical to show energy per δHz which requires dividing by the filter width (in Hz).

The principal aim of this thesis will be to produce robust luminosity density measurements from the u to K passbands (350 nm to 2.2 μm), allowing comparison to model predictions.

1.5 The Cosmic spectral energy distribution, and the importance of wavelength

Measuring the total luminosity density in different filters across the full UV/optical/NIR wavelength range (where starlight entirely dominates the energy output), allows us to build up the cosmic spectral energy distribution (CSED) for a representative volume of the local Universe. This illustrates how the radiation field varies with wavelength which, when combined with models of stellar light emission, provides constraints on the initial mass function of stars (IMF), the cosmic star formation history (CSFH) and population

synthesis models. For instance, observations in visible light, and in particular the wavelength range 350—550nm, are generally dominated by the most recently formed stellar population, whereas the light in the near infrared (herein referred to as the NIR) is typically dominated by the longer lived, lower mass stars that constitute the bulk of stellar mass (as well as some contamination from the AGB branch). Comparing the total luminosity density in the UV to the NIR would give us a guide to the ratio of emission from O and B stars against that produced by G and K stars. By combining the SEDs from a number of stellar spectral types, and attempting to fit them to total luminosity density points taken in a number of filters across the EM spectra (with the effects of dust obscuration removed), it would be possible to breakdown the total light emission by stellar type, and from there it is only a small step to calculate the relative number or mass density (by estimating the total light emitted per star of a given stellar type).

In this section, I outline the current state of research into the IMF, particularly focusing on galactic scales. I then discuss the cosmic star formation history; how it is measured, what it tells us, and how models explain this behaviour. Finally, I discuss the third and final piece of theory required to generate a CSED - population synthesis modelling.

1.5.1 The stellar IMF and the IGIMF

The stellar initial mass function (IMF) describes the distribution of the stellar mass in newly formed stars. It is integral to many other processes, such as modelling the properties of stellar systems and how they evolve with time, the speed of chemical enrichment, the number of SNII, and the calculation of mass to light ratios in galaxies.

The stellar IMF was first parametrised by Salpeter (1955), who noted that the local star counts could be fitted as a power law with slope $\alpha = -2.35$ between 0.4 and 10 $M_{\odot}$. Massey (2003) used young local clusters to reconfirm Salpeter's slope, Miller & Scalo (1979) examined the distribution below the bottom mass limit, and found that the IMF is actually fairly flat below $0.5 M_{\odot}$, and Weidner & Kroupa (2004) produced evidence that the IMF has a fundamental maximum limit at 150 $M_{\odot}$. From these alterations, a function form for the IMF was deduced. The canonical stellar IMF (Kroupa, 2007) is given by Equation 1.10.

$$\frac{dN}{dm} = \xi(m) = \begin{cases} m^{-1.3\pm0.3} & 0.08 \leq m/M_\odot \leq 0.5 \\ m^{-2.3\pm0.5} & 0.5 \leq m/M_\odot \leq 150 \end{cases} \qquad (1.10)$$

However, the mass where the Miller & Scalo (1979) flattening begins, and whether a similar change of slope happens at high masses has been the cause of much conjecture (e.g., Baldry & Glazebrook 2003). It has important consequences when modelling both the CSFH and the CSED. Miller & Scalo (1979) also found that the IMF could be modelled as a log-normal distribution, and Chabrier (2001) have tested an exponential form. Major discrepancies between the models would only be seen at substellar masses, and would particularly impact on the frequency of brown dwarf detections (Chabrier, 2001). Unfortunately, an IMF derived from an existing sample of stars is dependent upon a series of assumptions, particularly the mass-luminosity relation (Reid et al., 1999, 2002). The uncertainty produced by these dependencies is greater than the variation between the models. Counter-intuitively, the lack of certainty in the density and mass of the smallest stars is a major stumbling block on the way to modelling the total luminosity density from all galaxies.

In order to minimise such uncertainties, the mass functions of very young clusters (younger than a few Myr) are often examined. Such clusters are relatively pristine, as not enough time has elapsed for major evolution to occur. However, such clusters are often full of obscuring gas and dust, and early evolution is both rapid and violent (Kroupa, 2006). They are also often yet to reach virial equilibrium, making estimations of their masses dubious (Bastian & Goodwin, 2006). As older clusters have undergone dynamical evolution, and thus lost their brightest stars, the IMF unfortunately cannot be absolutely constrained by any one cluster, though relative constraints can be imposed based on a statistical analysis of the global population.

Weidner & Kroupa (2005) note that, above $1M_\odot$, IMF slopes for observed and model clusters are distributed normally around Salpeter's value, and assume the stellar IMF is a universal and invariant property. However, while they state that they see no reason for universality, the mass of evidence indicates that it is (Bastian et al., 2010). Larson (1998) question whether the IMF is actually invariant; a varying IMF may help describe the shape of the observed CSFH (Schaye et al., 2010).

For the work within this thesis, however, the IMF is required on a larger scale - the IMF

for an entire galaxy. Fortunately, the vast majority of stars form in clusters (Lada & Lada, 2003). The IMF for a galaxy can therefore be calculated by summing the IMF of every cluster within it. The integrated galaxial initial mass function (IGIMF), is found by combining the stellar initial mass function in clusters (which, as noted earlier, is believed to be invariant and universal) with the cluster mass function (also believed to be universal, Kroupa & Weidner 2003). The cluster mass function is observed to follow a power law, with slope $-\beta$. β is observed to be around 2 (Weidner & Kroupa, 2005). The β parameter is fundamentally important; a side effect of IGIMF theory is that the star formation rate for massive stars decreases as the IGIMF slope decreases, though the IMF of each cluster remains the same (Pflamm-Altenburg & Kroupa, 2009). β also controls the relative number of white dwarfs and SNII; for an IGIMF with $\beta = 2.2$, only 35% of the number of SNII and 89% the number of white dwarfs, are predicted relative to a Salpeter IMF (Kroupa & Weidner, 2005). A further property of the IGIMF theory is that the total SFR of the galaxy scales with the brightest youngest cluster within the galaxy, as that cluster indicates the point that the universal cluster mass function is populated to (Weidner et al., 2004).

The IGIMF theory is not without criticism. Elmegreen (2006) use Monte-Carlo simulations to show that when $\beta = 2$, there is little difference between the IGIMF and results assuming a simplistic, constant galaxy IMF. However, his methodology is disputed (Köppen et al., 2007); depending on the β parameter, the IGIMF can act like a constant galaxy IMF with a much steeper than Salpeter slope. However, this is also a cause for concern. Wilkins et al (in prep), have noted that the CSED produced by the IGIMF (with SFR calibrated using dust-correct UV luminosity functions at a number of redshifts), is a very bad fit to observations (see Figure 1.7), and that an IMF with a shallower than Salpeter slope is necessary to fit the data. Much research is still necessary in this field, and constraints from CSED observations are one way of selecting the correct properties of the galaxial IMF.

The IMF models used within this thesis are based around the canonical IMF, with variations in the high mass slope (a Salpeter slope, and a slope 0.2 shallower than Salpeter are used in Chapters 3 and 5). Both the IMF and the IGIMF are sensitive to the star formation history (Kroupa & Weidner, 2005; Hoversten & Glazebrook, 2008). In the next subsection I describe what is known about the cosmic star formation history, and how it
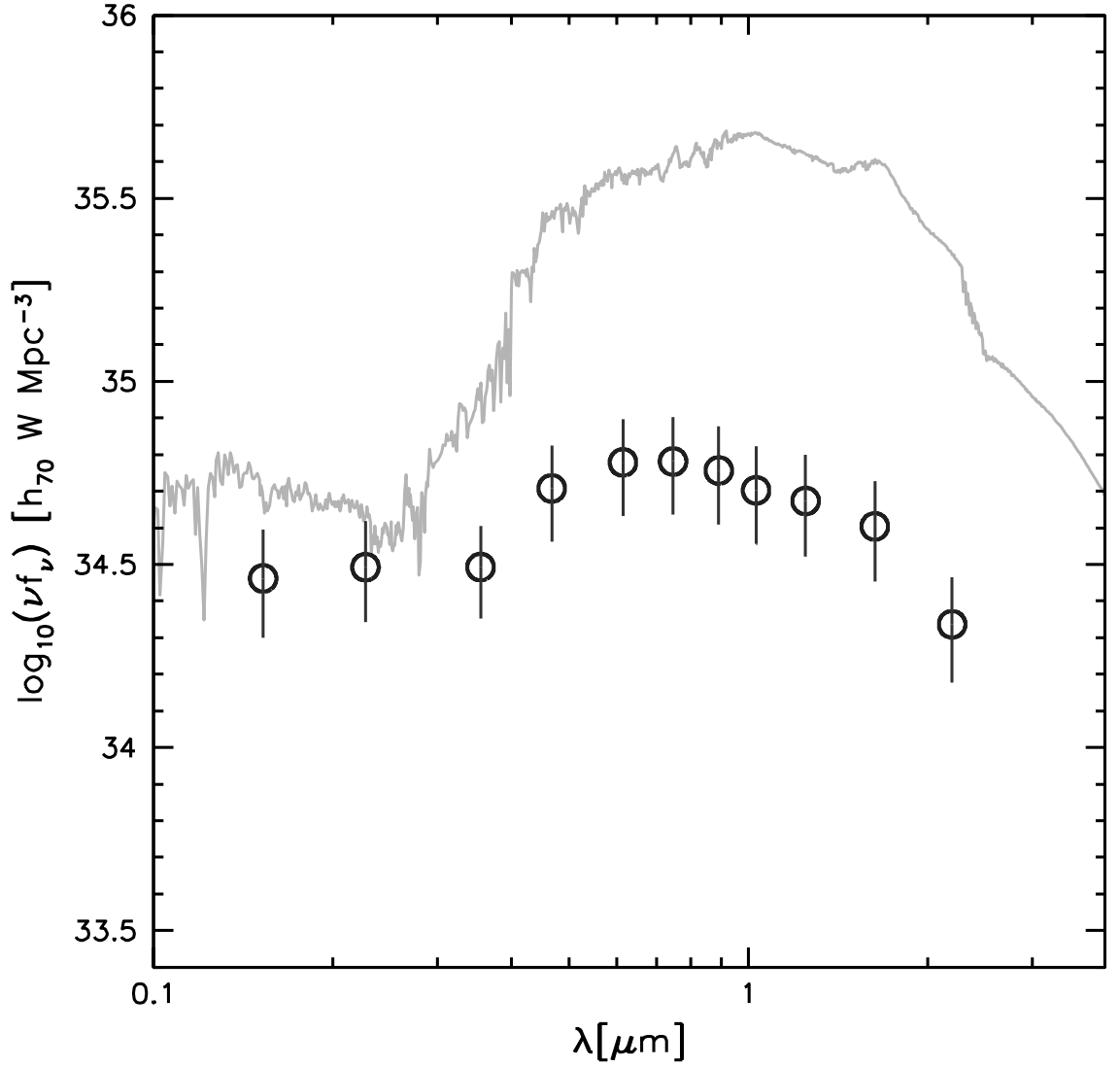
Figure 1.7: How an IGIMF model CSED compares to the observed datapoints, taken (with the author's permission) from Wilkins et al (in prep). UV indicators are used to calculate the SFH.

is measured.

1.5.2 The cosmic star formation history

The star formation history is a record of how the number of stars formed (i.e. the star formation rate) has varied over time, and is a key question in galaxy evolution studies. Combined with the stellar IMF, and integrated over all time, it gives the total stellar mass created. However, this does not account for mass loss processes, such as bright O and B stars that formed early, burnt through their fuel and moved off the main sequence. Population synthesis models must be used to calculate the amount of stellar mass lost in

this way, and the total stellar mass at any given time can then be calculated. Outside the Local Group, where stellar populations within galaxies are difficult to resolve, the SFH for a particular source is not easy to derive. Instead, we calculate the star formation history over all sources; the cosmic star formation history (CSFH).

The star formation history is measured by observing known SFR indicators at various redshifts (Madau, 1997; Hopkins & Beacom, 2006). These indicators include radio, FIR, UV continuum, Hα and OII emission. SFR indicators in some way correlate to the young stellar population - in the following sections I describe how. It should be noted that this isn't an exhaustive list; Georgakakis et al. (2003) calculate a SFR from X-Ray emission, distant ($z \geq 6$) galaxy star formation is calculated in Lyman break galaxies using the photometric dropout technique (see references in Hopkins 2007), and further constraints on the SFH can be imposed via SNII density rates (Hopkins & Beacom, 2006).

UV continuum emission

The great majority of UV continuum emission is produced by O and B stars on the main sequence (Madau, 1997). As these sources are short lived (less than 10 million years), their number (and thus the scale of the emission) is directly proportional to the star formation rate of that epoch, assuming a constant stellar IMF. Madau (1997) find that, when averaged over the entire galaxy population, UV continuum emission traces the conversion of cold gas to stellar mass well. For a single source, however, the tracer is not always reliable (Madau 1997 find under certain conditions, for instance, using a Scalo 1986 IMF with star formation bursts shorter than 1Gyr, intermediate stellar populations produce a significant fraction of 280 nm radiation). Also, UV emission is strongly attenuated by dust, and the effects of this must be accounted for.

Hα and OII

One of the best direct measurements of the current star formation rate is Hα emission (Kennicutt, 1998b). As with UV continuum emission, the strength of the Hα line indicates the number of young, massive stars emitting within the source; describing its recent star formation rate. However, optical CCDs can only detect this line to $z = 0.4$ (Gallego et al., 1995), and dust attenuates it. Other emission lines, with bluer wavelengths, become more useful for higher redshift sources. The OII doublet is often used as a replacement SFR

calibration for higher z sources (Gallego et al., 2002). OII is available in the optical until $z \sim 1.5$. While it is not directly linked to the same ionizing processes that produce the Hα emission, empirically it is strongly correlated with Hα, and conversions between the two indicators have been calculated (Hopkins, 2004). However, galaxies with AGN do not follow this standard Hα-OII correlation; Kennicutt (1992) states that Seyfert 2 galaxies produce too much OII emission, while Seyfert 1 type galaxies produce little. In order to correctly calibrate the SFR using OII, these sources must be found and dealt with accordingly.

FIR

The indicators described above both suffer greatly from dust attenuation. The FIR is where the dust re-emits the energy it absorbed. The level of FIR luminosity can be used as a tracer, particularly in sources where the young, massive stars are expected to dominate the emission. However, Kennicutt (1998a) describe a second form of emission in S0-Sab type galaxies, where the FIR luminosity is not correlated to the UV or Hα emission. Instead, the general radiation field (comprising all stellar types and not just the young, massive stars we wish to trace) or AGNs are heating the dust, and causing the FIR re-emission. This may provide up to half of the total FIR flux in edge-on spiral galaxies (Baes et al., 2010; Misiriotis et al., 2001; Kennicutt et al., 2009).

Radio continuum

Research has been shown that radio continuum emission from star forming galaxies is strongly correlated to their FIR luminosity (Condon, 1992; Yun et al., 2001); it is theorised that this correlation is caused by the relationship between cosmic ray production and star formation (Wunderlich & Klein, 1988; VERITAS Collaboration, 2009). As FIR emission can be used as a star formation rate calibration, this correlation allows 1.4GHz radio emission to also be used to track the SFH. However, there is a population of galaxies producing excessive radio emission (described in the literature as "monsters"), that do not follow this general trend. As with OII indicator, these sources must be accounted for in order to produce a correct SFR.
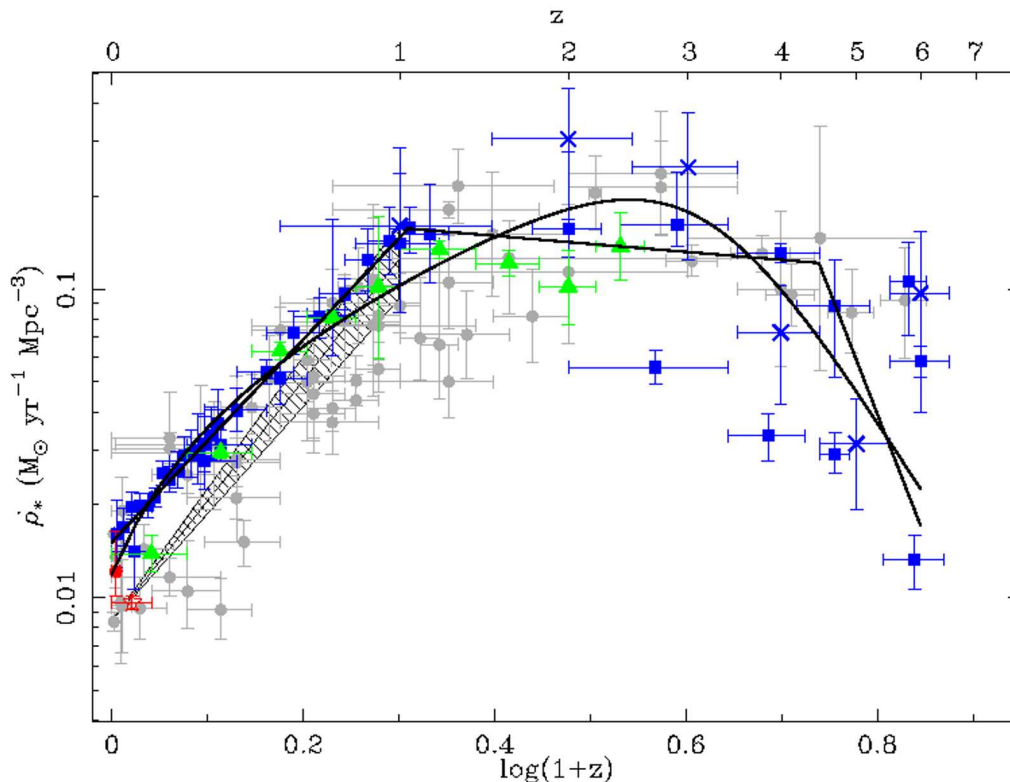
Figure 1.8: The evolution of SFR density with redshift, taken (with permission) from Hopkins (2007).

Shape of the CSFH and model fitting

Figure 1.8 (taken from Hopkins 2007) illustrates the variation in SFR density with time. This figure is a compilation of different SFR indicators, including UV (square points), Hα (filled circles), 1.4GHz (open stars) and 24μm (triangles, and hatched area). Two things are apparent - at $z < 1$, the SFH is well constrained by these indicators, and the SFR peaks between $z = 2$ to 3. The normalisation of the SFR density requires an IMF to be assumed. Figure 1.8 is normalised using a modified canonical IMF (the flattening is set to occur at $1 M_\odot$, rather than the $0.5 M_\odot$ in Equation 1.10 - see Baldry & Glazebrook 2003).

Using the data shown in Figure 1.8, hydrodynamical simulations have been run in order to find the processes that cause the shape of the CSFH. Schaye et al. (2010) have found that the shape can be roughly described as being limited by the size of the dark matter haloes at high z; as these haloes build up the SFR density increases towards intermediate redshifts, but is then quenched at low redshift by gas exhaustion, lower cooling

rates in hotter, lower density gas and self-regulated feedback processes from stars and accreting black holes. They also find that a top-heavy IMF would also help describe the observed form. Choi & Nagamine (2010) test two separate models, and simulate the effect that different cosmological parameters have on the CSFH. They also note that redshift evolution of the stellar IMF may be necessary to reproduce observations.

Calculation via the stellar mass history

Wilkins et al. (2008b) compiled a list of stellar mass density measurements, and observed how it varies with redshift. As stellar mass and star formation are intrinsically linked, this provided an alternative method of deriving the CSFH; one that is not dependent solely on the young, high mass stellar population. It is, however, still innately linked to the form of the IMF, and dependent on population synthesis models. At $z < 0.7$ they find a similar SFR to the indicators described above; at higher redshifts a discrepancy is apparent. The stellar mass history provides much lower SFR densities, with the scale of this discrepancy peaking at $z = 3$. In Wilkins et al. (2008a), they test the degeneracy of this result with a number of IMF models (using the PEGASE population synthesis code), and find no universal IMF that can account for the underdensity of stellar mass.

In this thesis, both the Hopkins (2007) and Wilkins et al. (2008b) star formation histories are tested. However, without accounting for the evolution in the stellar population, any CSED calculation will be grossly inaccurate. In the following section, I describe the third and final step required to calculate a coherent model of the CSED: population synthesis.

1.5.3 Population synthesis models

Earlier, it was noted that any attempt to calculate the CSFH or IMF from an observed population requires the use of a population synthesis model. In the UV to the NIR, where starlight produces the vast majority of galactic emission, galaxies can be considered simplistically as the sum of all stars within them. The earliest stellar population models (Tinsley, 1972) would take a sample population of stars (perhaps splitting them into stellar types based upon their metallicity and mass), model how they move on the

Hertzsprung-Russell diagram with time, and calculate the total amount of light emission at any age. More recent stellar population synthesis models are a bit more complicated. A recent review of the galaxy population synthesis field can be found in Walcher et al. (2010).

Stellar population synthesis models split into two groups. The first group (e.g. Bruzual & Charlot 2003) model each stellar population at a set of discrete ages (*isochrones*), and calculate the galactic light emission by summing the flux from all stars, using the flux for each star's particular stellar type and age. This is effective for stellar populations that do not rapidly evolve, but in stellar populations that undergo rapid evolution between isochrones (e.g. the TP-AGB branch, Marigo et al. 2010), there will be a discrepancy between the model's flux and the true flux. The second method (e.g. Maraston et al. 2006) models each stellar population via fuel usage rather than time steps; as the latter is directly linked to the evolutionary lifecycle, this should provide a more accurate method of modelling stellar evolution. Stellar population synthesis models therefore require accurate stellar tracks for all possible stellar populations; it is impossible to interpolate the correct total flux from incorrect tracks.

A number of different population synthesis models exist. Chen et al. (2010) and Longhetti & Saracco (2009) both compare 5 or more, calculating stellar mass estimates against real data. The models used within this thesis are produced using BC03 (Bruzual & Charlot 2003, the galaxy SEDs shown in Chapter 4), or PEGASE2 (Fioc & Rocca-Volmerange 1997, the CSED models produced by Steve Wilkins in Chapters 3 and 5). Both codes utilise the same stellar evolutionary tracks and spectral libraries (the Padova library, Alongi et al. 1993). They differ in the way they treat the hottest ($T > 50000$K) stars, and how they treat the TP-AGB phase (see Longhetti & Saracco 2009 for the specific libraries they use). PEGASE can model the effects of the infall, galactic wind and the fraction of close binary systems within a galaxy, as well as allowing the choice of IMF and SFR models. PEGASE2 (Fioc & Rocca-Volmerange, 1999) also provided dust extinction modelling, via a radiative transfer code, and expanded the evolutionary tracks to include variations in metallicity.

Within this section, I have briefly outlined current research in the IMF, the CSFH, and population synthesis models. Why does the cosmic star formation history have the shape observed? How accurate are the SFR indicators, and why do they differ? What is the shape of the IMF? Is the IMF universal, and does it evolve with time? These are all cur-

rently unanswered questions. By generating a CSED and comparing the results to IMF and CSFH combinations (via population synthesis models), the ability of different IMF functional forms and cosmic star formation histories to fit the data can be quantified, and a small step towards a solution can be made.

I have described the luminosity distribution and the total luminosity density as fundamental astronomical parameters with long histories. I have detailed the important research questions that they can help answer. An interested observer, at the point, must therefore be thinking - why hasn't this been done before, and if it has, why do you need to do it again? The conversion from the observed total luminosity density to a CSED datapoint is not straightforward, and previous measurements have produced an interesting offset between optical and NIR populations. In the next section I describe the difficulties in producing a coherent, accurate CSED; the correction required for dust attenuation and a discussion of the optical-NIR discrepancy.

1.5.4 Difficulties with the CSED

The $\nu f(\nu)$ parameters outlined in section 1.4.1 have no dependence on filter bandpass, and should provide an accurate measure of how the energy density varies with wavelength. However, without a correction, they will suffer from a wavelength dependent bias due to dust attenuation. In this section I first describe how this bias is removed. Secondly, I plot the distribution of previous CSED datapoints, and discuss the NIR-optical discrepancy.

The effects of dust attenuation

The radiation we detect is only some fraction of that produced, as a significant amount would be attenuated by dust within the host galaxies (Driver et al., 2007). This effect is apparent locally, and is the cause of the optical "zone of avoidance". Correcting for this dust attenuation (see Driver et al. 2008), it is possible to derive the pre-attenuated CSED. This should reconcile with the CSED predicted from our understanding of the cosmic star-formation history (e.g. Baldry & Glazebrook 2003, Wilkins et al. 2008b). It also should be noted that dust attenuation itself is wavelength dependent. The NIR is less susceptible to internal dust attenuation (Calzetti et al., 1994), with an estimated ~ 80 per cent, ~ 50 per cent and ~ 20 per cent of the integrated flux from galaxies being attenuated in the UV, Optical and NIR respectively (see Driver et al. 2008). These two benefits: the
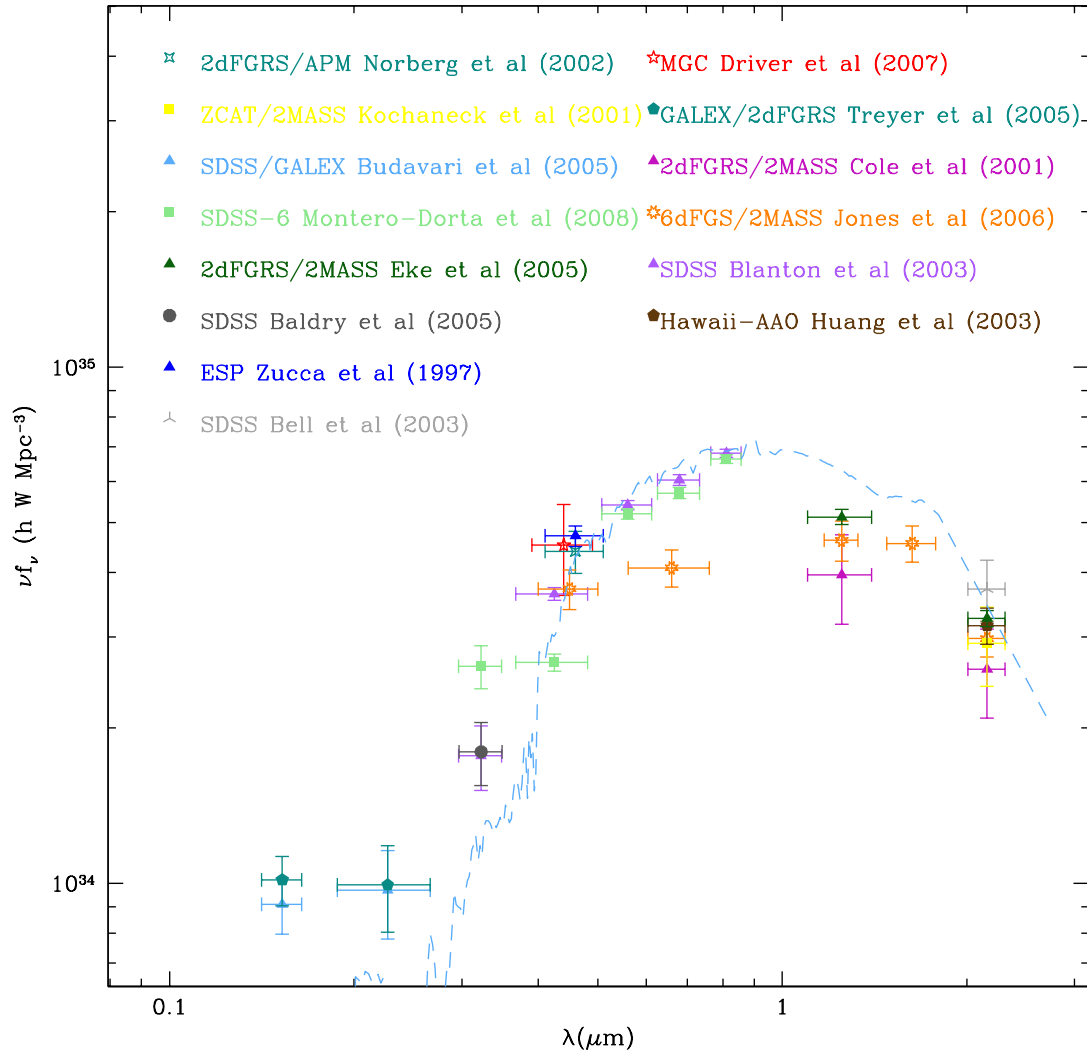
Figure 1.9: Cosmic energy output from 0.1 to $3\,\mu m$. The model line shows the SED of a 13.2Gyr Sa-type galaxy from the spectral template library of Poggianti (1997). Datapoints shown are taken from Baldry et al. (2005), Bell et al. (2003), Blanton et al. (2003), Budavári et al. (2005), Cole et al. (2001), Driver et al. (2007), Eke et al. (2005), Jones et al. (2006), Huang et al. (2003), Kochanek et al. (2001), Montero-Dorta et al. (2008), Norberg et al. (2002), Treyer et al. (2005) and Zucca et al. (1997).

focus on lower mass stars and lower attenuation, make NIR luminosity functions arguably more useful and accurate when attempting to characterise the underlying properties of the galaxy population.

The NIR/optical discrepancy

Previous results have shown an apparent discontinuity between the optical and near-IR data (see Figure 1.9). This was first seen in the cosmic SED shown in Figure. 2 of Baldry & Glazebrook (2003). In that case data from the SDSS (Blanton et al., 2003), GALEX (Wyder et al., 2005) and the NIR studies of Cole et al. (2001), Kochanek et al. (2001) and Huang et al. (2003) produced an apparently unphysical step-function between optical and NIR regimes. A similar result is seen when comparing the recent 6dfGS survey in JHK (Jones et al., 2006) with recent SDSS results in $ugriz$ (Blanton et al. 2003; Adelman-McCarthy et al. (2008)). Such a discrepancy in the CSED between optical and NIR wavelengths may be explained by: a very top heavy IMF (see Wilkins et al. 2008a), cosmic variance in the NIR data (e.g. Somerville et al. 2004), surface brightness selection bias in the NIR data (Smith et al., 2009), or spectroscopic incompleteness bias. Certainly, when one reviews the most recently published NIR luminosity densities one does find significant scatter. In particular, Kochanek et al. (2001) and Huang et al. (2003) examined insufficiently large volumes to overcome cosmic variance. Other attempts, such as Cole et al. (2001) and Jones et al. (2006), have probed greater volumes but are dependent on shallow 2MASS imaging data that has been shown to be susceptible to surface brightness (SB) bias, missing both galaxies and flux (e.g. Andreon 2002, Bell et al. 2003, Eke et al. 2005 and Kirby et al. 2008).

1.6 The bivariate brightness distribution, and the effects of surface brightness incompleteness

The surface brightness incompleteness of 2MASS and SDSS may have distorted previous CSED calculations greatly. Luminosity and surface brightness distributions are interdependent. Selection effects in either plane can affect the distribution in the other and the recovery of correct, complete luminosity distributions (and therefore accurate total luminosity densities) requires both properties to be properly accounted for. Previous work by Cross & Driver (2002) has shown that absolute surface brightness can cause uncertainty within the best-fitting Schechter parameters, as the M^* population of galaxies that determine the best fit will not be fully sampled. The SDSS survey suffers from apparent surface

brightness incompleteness fainter than $\mu_{r,50} = 23\,\mathrm{mag\,arcsec^{-2}}$ (the effective r band surface brightness within the half-light radii, see Baldry et al. 2010 and references therein). Any samples based upon that dataset, such as GAMA (Driver et al., 2009), must correct for this effect. Shallow 2MASS XSC data produces the same surface brightness bias in the NIR (Andreon, 2002). A joint luminosity - surface brightness analysis is an effective way of quantifying the impact of both luminosity and surface brightness incompleteness on a galaxy sample.

Furthermore, a much greater constraint is provided by simultaneously mapping a number of variables, rather than modelling them separately. As theoretical simulations can predict the size, surface brightness and luminosity distribution of galaxies in their model universes (see, for example, Cole et al. 1994, Bower et al. 2008 or Parry et al. 2009), the distribution of galaxies across luminosity - surface brightness space is also a useful result for cosmological theorists. If this distribution, known as the bivariate brightness distribution (BBD), is collapsed into a one dimensional distribution, it also produces either the luminosity distribution or the surface brightness distribution (depending on the direction of the collapse). The BBD is generally parametrised using the Choloniewski function (Choloniewski, 1985). This is discussed in Section 1.6.3. To summarise: the luminosity distribution is assumed to follow a Schechter parametrisation, with luminosity density distributed normally in the surface brightness plane. The peak of the surface brightness distribution is allowed to vary with magnitude.

1.6.1 Calculating the bivariate brightness distribution

In this section I describe the methods used to generate the bivariate brightness distribution (BBD) and the functional form that I will eventually attempt to model it with. I describe the Bivariate-SWML method used to calculate the distribution, and the Choloniewski function - a six parameter function fit that combines the Schechter function with a Gaussian surface brightness distribution. Finally, I modify that function to provide a form that fits the data more accurately. As with the monovariate luminosity distribution, it is important that the selection criteria utilised (in this case apparent magnitude, apparent surface brightness, redshift and size) produce a sample that is complete.

1.6.2 Bivariate SWML method

Sodre & Lahav (1993) extend the SWML method presented in Efstathiou et al. (1988) to simultaneously account for diameter and luminosity distributions. Following minor modification, this can be converted into a method to calculate SB and luminosity (see Section 3.6 of Driver et al. 2005). The luminosity density within each luminosity-surface brightness bin is calculated using:

$$\psi(M,\mu)dMd\mu = \psi_{jk}dMd\mu = \frac{\sum_{i=1}^{N_g} W(M_i - M_j, \mu_i^X - \mu_k^X)C(i)}{\sum_{i=1}^{N_g} \frac{H(M_j - M_{faint(z_i)}, \mu_k^X - \mu_{faint(z_i)}^X, i)}{\sum_{a=1}^{N_s}\sum_{b=1}^{N_t} \psi_{ab}dMd\mu \ H(M_a - M_{faint(z_i)}, \mu_b^X - \mu_{faint(z_i)}^X, i)}}$$

where:

$$W(x,y) = \begin{cases} 1 & \text{if } -\frac{\Delta M}{2} \le x \le \frac{\Delta M}{2} \text{ AND } -\frac{\Delta \mu}{2} \le y \le \frac{\Delta \mu}{2} \\ 0 & \text{otherwise} \end{cases}$$

$$H(x,y,w) = \begin{cases} 0 & \text{if } x \ge \frac{\Delta M}{2} \text{ OR } y \ge \frac{\Delta \mu}{2} \\ \frac{C(w)}{\Delta M \Delta \mu} \int_{-\frac{\Delta M}{2}}^{min(\frac{\Delta M}{2}, x - M_{bright(z_i)})} dM \int_{-\frac{\Delta \mu}{2}}^{min(\frac{\Delta \mu}{2}, y - \mu_{bright(z_i)}^X)} d\mu & \text{otherwise} \end{cases}$$

$$C(w) = \text{Completeness weighting for galaxy } w$$

(1.11)

Where $\psi(M,\mu)$ gives the luminosity density in the bin centred at M_j, μ_k (covering dM and $d\mu$), using photometry taken using the X filter. There are N_g galaxies in the sample, N_t steps of width $d\mu$ and N_s steps of width dM. The W function fulfils the same role as its equivalent in Equation 1.6 - it returns the number of galaxies within the sample that fall within the luminosity-surface brightness range covered by the bin. The H matrix generates a weight for each object using the limits of the sample and each source's redshift. Equation 1.11 also allows the definition of an individual surface brightness and luminosity limit for each galaxy, using a similar modification to that introduced in Equation 1.6. As the GAMA input catalogue is defined primarily by $r_{SDSS,Petrosian}$ apparent magnitude and apparent surface brightness criteria, this allows the BBD to be generated from any dataset that has observed the GAMA fields. There is one final advancement upon Equation 1.6. Equation 1.11 is further extended by the use of a $C(w)$ term, that adds an additional weight due to spectroscopic completeness. Spectroscopic completeness is accounted for by allocating each galaxy a weight based upon the incompleteness of galaxies with a similar apparent surface brightness and apparent magnitude.

Unfortunately, as with the monovariate SWML method described earlier, the Sodre & Lahav method can only derive the shape of the bivariate brightness distribution, and not the on-sky luminosity density. To return the true bivariate-brightness distribution, the generated ψ values must be scaled using a normalisation factor. As with section 1.3.1, the normalisation factor is calculated by deriving the luminosity density within a specified subsection of the sample. In this case, it is undertaken by calculating the number density of galaxies within a $1\,\mathrm{mag} \times 1\,\mathrm{mag\,arcsec^{-2}}$ region centred at M^*, μ^* (defined in section 1.6.3). This region is referred to as the normalisation region. It is very important that the normalisation region is both full sampled, and visible throughout the BBD's entire redshift selection range. If this condition is not met, the returned normalisation factor will be incorrect. The population of galaxies input into this algorithm must be cut using apparent magnitude, surface brightness and redshift selection criteria so that it is fully sampled.

1.6.3 The Choloniewski function

Using just the three parameter Schechter function, it is impossible to calculate where surface brightness bias is having an effect. Choloniewski (1985) enhanced the Schechter function, creating a 6 parameter function that fits the bivariate distribution of luminosity and diameter. This effectively extended the Schechter function into the surface brightness plane. This was further developed by Sodre & Lahav (1993), de Jong & Lacey (1999), Cross & Driver (2002), and Driver et al. (2005), creating the function that is now the standard fit to the bivariate brightness distribution. The Choloniewski function (Equation 1.12) assumes that the luminosity function is described by a Schechter function, with the population of the sources distributed normally in the surface brightness plane (Freeman, 1970):

$$\psi(M,\mu) = \frac{0.4\ln(10)}{\sqrt{2\pi}\sigma_{\mu^X}}\phi^* 10^{-0.4(M-M_X^*)(\alpha+1)} e^{-10^{-0.4(M-M_X^*)}} e^{-\frac{1}{2}(\frac{\mu^X-\mu^{X,*}-\beta\mu(M-M_X^*)}{\sigma_{\mu^X}})^2} \quad (1.12)$$

M^*, α and ϕ^* describe the distribution in the luminosity plane (see Section 1.3.2), with the surface brightness distribution modelled as a normal distribution with mean μ^* and standard deviation σ_μ. The β parameter allows μ^* to vary linearly with luminosity, and the $\frac{0.4ln(10)}{\sqrt{2\pi}\sigma_{\mu^X}}$ normalises the height of the normal distribution. Without this term, the

resultant ϕ^* parameter would not be comparable to its equivalent in Equation 1.7.

1.7 Overview

Until recently, any measurement that required NIR observations over a large area of sky was forced to rely on shallow 2MASS imaging. The UKIRT Infrared Deep Sky Survey (UKIDSS, Lawrence et al. 2007) is a programme of five NIR surveys, and greatly supersedes 2MASS. This thesis uses data from the shallowest (but most extensive) of these surveys: the Large Area Survey (UKIDSS-LAS). The survey is detailed in Section 2.3. The LAS is over 10x deeper than the 2MASS survey in K, and should therefore be much less susceptible to the SB effects discussed in the previous sections. Smith et al. (2009) produced a K-band SDSS-UKIDSS LAS luminosity function that appeared to agree closely with the results of Cole et al. (2001) and Jones et al. (2006). At first glance, this would suggest that 2MASS and UKIDSS photometry are consistent, the reported NIR LFs robust and the NIR/optical offset a physical phenomenon. However, due to an unresolved issue with the UKIDSS extraction software discussed in Chapter 3, Smith et al. question the validity of their own results. They also restricted their analysis to K-band only where, for the purpose of recovering the pre- and post attenuated CSED, it is more desirable to recover measurements in all available filters (i.e. $YJHK$).

Cosmic variance may also produce significant uncertainty. NIR surveys typically are based on lower redshift samples, e.g., 6dfGS (Jones et al., 2006) with $\langle z \rangle \approx 0.05$, with the optical data accessing deeper populations; e.g., SDSS Blanton et al. (2003) with $\langle z \rangle \approx 0.1$). In an ideal situation a derivation of the CSED would be produced from within a single survey, where the impact of cosmic variance would affect all filter measurements consistently. The purpose of this thesis is to generate such a dataset. In Chapter 3, by combining data from the Millennium Galaxy Catalogue (MGC), SDSS and UKIDSS LAS surveys I derive $ugrizYJHK$ luminosity distributions and pre- and post attenuated cosmic SEDs from within a single well understood volume of $\sim 71,000 h^3 \mathrm{Mpc}^3$, using a sample of ~ 10 thousand galaxies, selected using a deep $B_{MGC} = 20\,\mathrm{mag}$ apparent magnitude cut. In later chapters, I create a larger sample of ~ 250 thousand galaxies using the UKIDSS, SDSS and GAMA datasets, produce a second $ugrizYJHK$ CSED, and compare the results. The creation of the GAMA sample is detailed in Chapter 4, and the results derived are

discussed in Chapter 5.

2

Surveys

In order to generate the total luminosity density parameters required to model the CSED, data from a number of instruments must be combined with a spectroscopic survey. In this chapter I describe the surveys that provided these datasets. I detail their area coverage, limiting depth and the photometric and astrometric accuracy of the data they produce.

2.1 The Millennium Galaxy Catalogue (MGC)

The Millennium Galaxy Catalogue (Liske et al., 2003) is a deep ($B_{\mathrm{lim}} = 24\,\mathrm{mag}$, $\mu_{\mathrm{lim}} = 26\,\mathrm{mag\,arcsec}^{-2}$), B band galaxy survey created using the Wide Field Camera on the 2.5m Isaac Newton Telescope (INT), with observations taken between 1999 and 2001. Surveying a long (75°), thin (0.5°), equatorial strip amounting to 37 deg^2 of sky (30.88 deg^2 after cleaning and cropping), the MGC contains data on over a million objects, with 10,095 galaxies brighter than $B = 20\,\mathrm{mag}$ (this resolved sub-catalogue is referred to as MGC-Bright, and the integrity of every object within it has been verified by eye and fixed where

necessary). Photometry was performed during a single night, where 20 fields across the survey strip were observed, interspersed with observations of Landolt standard stars from standard areas SA98, SA101, SA104 and SA107.

Using the extensive overlap regions, for objects in the range $17 \leq B_{\mathrm{MGC}} \leq 21$ mag, the astrometric rms uncertainty has been shown to be ± 0.08 arcsec, and the photometric uncertainty ± 0.023 mag. The seeing ranged from 0.9 to 2 arcsec, with a median of 1.3 arcsec. Following observation, the data was sent to the Cambridge Astronomy Survey unit for primary data analysis. The zero point for each field was calculated by comparing it with the aforementioned Landolt standard star fields.

Object extraction was achieved using the `SExtractor` program (Bertin & Arnouts, 1996), with a constant surface brightness threshold, μ_{lim}, of 26 mag arcsec^{-2}. Photometry was extinction corrected using dust maps created by Schlegel et al. (1998).

Background subtraction in `SExtractor` is carried out by estimating the local background inside a number of meshes within a grid that covers the entire image. The background values are calculated using 3σ clipped median values within each mesh. A background map is then calculated by interpolating between the values from each mesh. The survey team selected the largest possible mesh size available in `SExtractor`, in order to carry out the background subtraction. This criteria limits the smoothing of low surface brightness extended objects. An artificial neural network was used to give every object in the survey a stellaricity parameter (1=star, 0=galaxy). Driver et al. (2005), have obtained redshifts for 96 per cent of MGC-Bright galaxies using the SDSS spectroscopic survey and 2dFGRS data releases, combined with a dedicated MGCz 2dF survey. All data is publicly available from http://www.eso.org/~jliske/mgc/.

2.2 The Sloan Digital Sky Survey (SDSS)

The Sloan Digital Sky Survey (SDSS, York et al. 2000) is the largest photometric and spectroscopic survey ever undertaken, and contains spectra of ~930k galaxies spread over 9000 deg^2 of sky, using five filters with average wavelengths between 300 and 1000 nm. These filters are denoted u, g, r, i and z. SDSS data has been publicly released in a series of 7 data releases. SDSS provide access to their data through two separate channels. The SDSS survey catalogue can be accessed from the catalogue archive server (CAS), which provides an SQL interface and documentation. Other data products, such as fits images

and the list of objects within each image, can be downloaded from the data archive server (DAS). This provides both an SQL interface and a structured file system that is accessible via ftp.

SDSS imaging is taken using a wide-field imaging array of 30 2048x2048 Tektronix CCDs with a pixel size of 0.396 arcsec, but only on nights where the seeing is < 1.5 arcsec and there is less than 1% uncertainty in the zeropoint. When conditions are worse, the SDSS team undertake spectroscopy. SDSS imaging is 95% complete to $u = 22.0\,\mathrm{mag}$, $g = 22.2\,\mathrm{mag}$, $r = 22.2\,\mathrm{mag}$, $i = 21.3\,\mathrm{mag}$ and $z = 20.5\,\mathrm{mag}$ (all depths measured for point sources in typical seeing using the SDSS photometric system, Abazajian et al. 2004). The SDSS magnitude system approximates the AB magnitude system, with slight offsets in u and z; $u_{AB} = u_{SDSS} - 0.04\,\mathrm{mag}$ and $z_{AB} = z_{SDSS} + 0.02\,\mathrm{mag}$. AB conversions to the Vega magnitude system (as used by UKIDSS) are shown in Table.2.1. SDSS imaging is optimised to provide the highest quality data in the *gri* passbands. In order to provide accurate colours, the r filter provides the definition of the aperture for extended sources (where r band data is unavailable, apertures are defined in a different band, indicated within a flag in the data - this is incidental for the data presented in this thesis, as r band data is always required). The g filter bandpass is very similar to the MGC B band filter. Cross et al. (2004) use this correspondence to quantify catalogue incompleteness, misclassification and photometric inaccuracy in the earliest SDSS data releases. The u and z filters lie at the edge of the UV and NIR regimes, respectively. Unfortunately, the quality of the u band data is low relative to the *gri* bands, making accurate estimations of extended source photometry difficult within this filter. This is analysed in Chapter 4.

The SDSS observations are structured as a series of *stripes*. Each *stripe* is produced by the drift-scan mode of the telescope. *Stripes* can be split into component *strips*. Two *strips* make up each *stripe*, as the CCD layout requires two offset pointings to entirely observe an area of sky. *Strips* are composed of *runs*, which denote a single scan. Finally, *runs* are composed of *camcols*. The 30 CCDs used to take the SDSS imaging are grouped into 6 columns. A *camcol* is the output from one of these columns. Over time, the coverage provided by the *stripes* has produced overlap that allows the main NGP region of the SDSS to be treated as a coherent, contiguous block. Instead of expecting users to download an entire *stripe*, each *stripe* has been cut into a series of *tiles*. Each *tile* has a small area of overlap with its neighbours. SDSS provide a standard *tile* name convention. It contains

Band	$\lambda\,(\mu\text{m})$	$M_\odot(AB)\,(\text{mag})$	$M_\odot(Vega)\,(\text{mag})$	$M_\odot(AB) - M_\odot(Vega)\,(\text{mag})$
u	0.3546	6.38	5.47	0.91
g	0.4670	5.15	5.23	-0.08
r	0.6156	4.71	4.55	0.16
i	0.7471	4.56	4.19	0.37
z	0.8918	4.54	4.00	0.54
Y	1.0305	4.52	3.89	0.63
J	1.2483	4.57	3.63	0.94
H	1.6313	4.71	3.33	1.38
K	2.2010	5.19	3.29	1.90

Table 2.1: The Absolute magnitude of the Sun in various filters for the AB and Vega systems along with the approximate filter central wavelength. These values were derived for us by Paul Hewett (priv. comm). $M_\odot$ differ from those in Table 1 of Blanton & Roweis (2007) by 0 mag, 0.03 mag, 0.07 mag, 0.03 mag and 0.03 mag in the u, g, r, i and z bands.

the number of the *run*, the passband, the *camcol* and the number of the *tile* within the *strip*. A list of all the *tiles* that constitute an area of sky can be generated by finding which section of a *stripe* observed that region.

In order to generate the MGC-SDSS-UKIDSS sample (Chapter 3), the SDSS dataset is matched to the MGC. The SDSS data in this case is taken from the fifth data release. SDSS-DR5 (Adelman-McCarthy et al., 2007), contains spectroscopy for 675 thousand galaxies over approximately 5740 deg^2. The GAMA input catalogue (Chapter 4, Baldry et al. 2010), is defined using data from the sixth data release catalogue. SDSS-DR6 (Adelman-McCarthy et al., 2008) contains spectroscopy for 790 thousand sources over approximately 7425 square degrees. The GAMA regions fall within the SDSS DR6 area of coverage, particularly stripes 9 to 16.

Astrometry for SDSS-DR6 (Pier et al., 2003) is undertaken by comparing r band observations to the USNO CCD Astrograph Catalog (UCAC, Zacharias et al. 2000), where it had coverage at time of release, or Tycho-2 (Høg et al., 2000), in regions that UCAC did not cover. For sources brighter than $r = 20$ mag, the astrometric accuracy when comparing to UCAC is 45mas, and when comparing to Tycho-2 is 75 mas. In both cases, there is a further 30 mas systematic error, and a relative error between filters (i.e., in $ugiz$) of 25-35 mas.

2.3 UKIRT Infrared Deep Sky Survey (UKIDSS)

UKIDSS (Lawrence et al., 2007) is a seven year near-infrared survey programme that will cover several thousand deg^2 of sky. As a set, the UKIDSS programme covers a

much larger volume of sky than any previous near-IR survey, due to the great increase in depth over previous surveys such as 2MASS (which, though covering a large area, is much shallower than UKIDSS). At the time this thesis was submitted, it is on its 7th data release (DR7PLUS), and is five years into its seven year run. The full UKIDSS program consists of five separate surveys, each probing to a different depth and for a different scientific purpose. The shallowest of these surveys, the UKIDSS Large Area Survey (LAS), contains the three GAMA fields and the MGC region.

The UKIDSS programme utilises the Wide Field Camera (WFCAM) on the 3.8m United Kingdom Infra-Red Telescope (UKIRT). WFCAM has the largest field of view of any IR camera used on a 4m telescope ($0.21\,\mathrm{deg}^2$). WFCAM has four 2048x2048 Rockewell detectors, which simultaneously observe different regions of the sky, and has a pixel size of 0.4 arcsec. In order to observe an entire square 'tile' of sky, the detectors are spaced with a gap of 94% of their active area between them. This allows a square $0.75\,\mathrm{deg}^2$ observation to be generated from four pointings, with only $0.0225\,\mathrm{deg}^2$ repeated coverage per pointing. WFCAM is designed to make a number of short (5-10s) exposures on the sky, slowly filling up 'tiles' and accumulating sets of 'tiles' to fill in sky area, or increase depth. To increase the quality of its data, a 'jitter' sequence is included that offsets frames by an integer number of pixels, reducing the effect of bad pixels and other flat field effects. The instrument is designed to use four parallel channels; treating each detector separately. UKIDSS imaging is provided with each detector's observation stored in a separate image header, producing a *multiframe* fits file that contains four images and a header containing general details about the observation (e.g., the exposure time or airmass).

All UKIRT observations are preset into blocks of 20-60 minutes, which are stored in a master database and can be sorted by the required climactic conditions (i.e. the standard of seeing, the brightness of the sky) and their priority. The selection of which observation will be made is left to the discretion of the observer at the telescope.

When complete, the LAS will cover $4000\,\mathrm{deg}^2$ of sky to target depths (5σ point source detections in Vega) of $K = 18.2\,\mathrm{mag}$, $H = 18.6\,\mathrm{mag}$, $J = 19.9\,\mathrm{mag}$ (after two passes; this thesis uses only the first J pass which is complete to $19.5\,\mathrm{mag}$) and $Y = 20.3\,\mathrm{mag}$ (for conversion to the AB system please see the offsets shown in Table. 2.1). LAS observations are required to have a seeing FWHM of $< 1.2\,\mathrm{arcsec}$, photometric rms uncertainty of $< 0.02\,\mathrm{mag}$ and astrometric rms of $< 0.1\,\mathrm{arcsec}$. Fields are calibrated using the large

number of unsaturated 2MASS stars that are present in every frame, transforming into the WFCAM colour system using empirically derived colour equations (Hewett et al., 2006). Each position on the sky is targeted for 40s per pass. Survey data for the MGC-SDSS-UKIDSS dataset (Chapter 3) is taken from the third data release (DR3PLUS), and the GAMA NIR dataset (Chapter 4) is produced from imaging within the fourth data release (DR4PLUS).

During this analysis a number of problems were encountered with the online catalogues generated by the Cambridge Astronomical Survey Unit (CASU), particularly affecting the calculation of Petrosian fluxes for deblended systems (as first noted in Smith et al. 2009). These issues are detailed in Chapter 3 and were considered sufficiently insurmountable to warrant re-deriving the source photometry from the reduced data. The derivation of the final MGC-SDSS-UKIDSS Y,J,H and K catalogues using SExtractor (Bertin & Arnouts, 1996) is also described in Chapter 3. Following the revision of the UKIDSS photometry, the level of uncertainty in individual fluxes in the Y, J, H, and K bands is estimated to be ± 0.05 mag. This value derives from a comparison between the original UKIDSS LAS data that is unaffected by the problems that force the reanalysis, and the revised photometry.

2.4 Galaxy and Mass Assembly (GAMA)

The GAMA project (Driver et al., 2009) aims to study galaxy formation and evolution using a range of cutting-edge instruments (AAT, VST, VISTA, ASKAP, HERSCHEL WISE, GALEX and GMRT), creating a database of ~350 thousand galaxies observed from UV to radio wavelengths. The first stage of the GAMA project, GAMA I, covers $144\,\mathrm{deg}^2$ of equatorial sky. In order to limit the effects of cosmic variance, the area of sky was split into three separate $4\,\mathrm{deg} \times 12\,\mathrm{deg}$ regions centred at 9h +1d (GAMA9), 12h +0d (GAMA12) and 14h30m +0d (GAMA15). These areas have complete SDSS coverage, and will be completely observed by UKIDSS-LAS when that survey is complete. Current coverage is shown in Figure 2.1. Between 2008 and 2010, the GAMA project was allocated 66 nights on the AAT to use the AAOmega spectrograph in order to carry out the GAMA I spectroscopic campaign.

A complete description of the input catalogue for the spectroscopic campaign can be found in Baldry et al. (2010). To summarise: the aim is to provide spectroscopy of all galaxies in the GAMA I regions brighter than $r_{\mathrm{petro,SDSS}} = 19.4\,\mathrm{mag}$, $z_{\mathrm{model,SDSS}} = 18.2\,\mathrm{mag}$
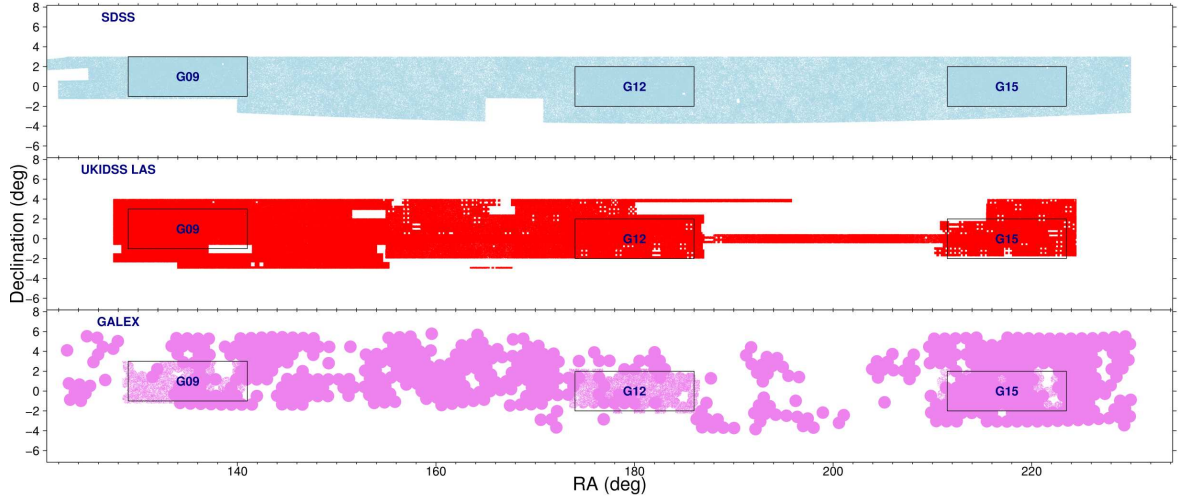
Figure 2.1: Coverage of the equatorial region of sky that contains the GAMA regions, by SDSS DR6 (blue), UKIDSS LAS (red) and GALEX (violet) imaging. The three rectangular boxes contain the regions of sky surveyed by the first GAMA proposal. G09 denotes the GAMA region centred around 9h, G12 denotes the GAMA region centred around 12h, and G15 denotes the GAMA region centred around 14.5h.

and $K_{\mathrm{kron,AB}} = 17.5\,\mathrm{mag}$, with the sample extended to $r_{\mathrm{petro,SDSS}} < 19.8\,\mathrm{mag}$ in the GAMA12 region. Source photometry was defined using the SDSS DR6 catalogue. Where a galaxy would not be selected by its r magnitude, but would be selected using the K or z magnitude cut, the galaxy must also have $r_{\mathrm{petro,SDSS}} < 20.5\,\mathrm{mag}$. This ensures that the galaxy is credible and the likelihood of obtaining a redshift within the 1 hour AAOmega observation period is reasonable. In order to guarantee a complete sample of galaxies, including compact objects, the GAMA input catalogue utilises a star-galaxy selection algorithm that includes optical (r_{psf}-r_{model}, g-i) and infrared colour selections (J-K). The latter uses colours taken from sources extracted using the pipeline described in Chapter 4.

GAMA I is 98% spectroscopically complete to the survey limits, making it one of the highest completeness galaxy surveys ever performed. The tiling strategy used to allocate objects to AAOmega fibres is detailed in Robotham et al. (2010). A breakdown of redshift completeness by luminosity and colour selection of the year 2 observations is shown in Table 5 of Baldry et al., and in Table 3 of the same paper the number of spectra taken from other surveys is quantified.

In the following chapters, I use data from each of these surveys to generate a sample of galaxies with photometry in $ugrizYJHK$. I use this sample to generate luminosity

distributions and total luminosity density parameters in 9 filters in the optical and the NIR. In the next chapter I detail the methods used to calculate these quantities.

3

The MGC-SDSS-UKIDSS common dataset

In this chapter I present a $ugrizYJHK$ catalogue of galaxy observations taken from the combination of the B band selected MGC-Bright catalogue of 10095 galaxies with UKIDSS-LAS and SDSS survey data. I generate new photometry from the SDSS and UKIDSS surveys and combine it with the MGC's B band selected source list. This catalogue is used to construct luminosity distributions in each of the nine filters, calculate the best-fitting parameters when these distributions are fit to the Schechter luminosity function, and calculate the total cosmic energy output within each passband. These datapoints are then compared to previous surveys, removing the apparent NIR/optical discrepancy that had previously been observed, and to theory, where they disagree with the parameters deduced from the Cosmic star formation history (CSFH) calculated by Wilkins et al. (2008b).

The work within this chapter has been published in Hill et al. (2010a).

3.1 Catalogue matching

In order to construct luminosity distributions for the same population of galaxies in different filters, it is necessary to match observations between surveys. Survey data is often presented in two forms - imaging (raw observations from the telescope, or reduced, post-processed data), and source catalogues. In a perfect world, the source catalogues produced by each survey would be consistent and flawless, making inter-survey matching a simple task. In practice, source catalogues are not always coherent. In the worst case, one of the catalogues may contain errors, making its output unusable. In other (more frequent) cases, a slight change in a parameter definition (for instance, the number of Petrosian radii the Petrosian aperture is set to contain, or the number of σ above the background a source must be to be detected) can modify the output source list, or the luminosity of each source within the catalogue. Such effects can produce systematic offsets, which may look like significant results to the unwary. Where discrepancies between source catalogues cannot be fixed, it becomes necessary to regenerate a source catalogue from the reduced images.

Within this section, I outline the matching undertaken between the MGC and the SDSS and UKIDSS-LAS surveys. The match between SDSS and the MGC was undertaken using a centroid proximity search between the survey catalogues. The same procedure was attempted between the MGC and UKIDSS-LAS survey catalogues. However, a critical error with the UKIDSS-LAS source catalogue made the results unreliable. It was necessary to repeat the source detection process on reduced UKIDSS imaging.

The MGC is taken as the master catalogue in all that follows as it is the deepest (in terms of flux sensitivity), contains the highest signal-to-noise detections and has been fully masked and eyeballed. Where necessary, objects within it have been reconstructed or deblended. It provides an accurate catalogue of objects, without the unfortunate side effects that are inherent in automated catalogue manufacture.

3.1.1 Data repository

In order to generate the MGC-SDSS-UKIDSS common dataset, a number of tools provided by the WFCAM Science Archive were utilised. The WFCAM Science Archive (WSA, Hambly et al. 2008) is the primary repository of raw and post-pipeline, calibrated UKIDSS

imaging. It also provides users with access to CASU-generated object catalogues for all five UKIDSS surveys, along with copies of catalogues from a number of other sources, including the SDSS and the MGC. These catalogues are accessible via an SQL interface, with full documentation provided by a Schema Browser system. The WFCAM team have also generated cross-matched data tables. These tables contain the IDs of sources in different catalogues that have a centroid separation less than a certain distance (10 arcsec).

3.1.2 SDSS-MGC matching

Using the SDSS DR5 database stored in the WFCAM Science Archive, a complete list of SDSS PhotoPrimary sources within the MGC region is output. The SDSS PhotoPrimary objects were matched to MGC-Bright objects using the STILTS catalogue matching tool (Taylor, 2006), with a maximum centroid separation tolerance of 2.5 arcsec. Where there were multiple matches within 2.5 arcsec to one MGC object, STILTS takes the closest matching object. Extinction corrected SDSS Petrosian apparent magnitudes (PETROMAG_X-EXTINCTION_X, where X is u, g, r, i or z) are adopted as the SDSS photometric solution. The final DR5-MGC-Bright matched catalogue contains 10050 SDSS-MGC matching galaxies (99.6 per cent of the 10095 sources that make up the MGC-Bright catalogue), the majority of failed matches coming from extreme low surface brightness systems and differences in deblending decisions.

3.1.3 UKIDSS-MGC matching

Existing CASU object catalogues

The LAS-MGC cross match table within the WSA (*lasSourceXmgcDetection*) contains ID numbers for all MGC objects within 10 arcsec of a LAS source, and the ID of that LAS source. Using this tool, catalogues matching MGC-Bright B band luminosities to their counterpart LAS Y, J, H and K band luminosities were downloaded. Sources were only selected when both the MGC and LAS objects were definitely galaxies (MGC CLASS= 1 and LAS $pGalaxy$> 0.9; this criteria is only used here to guarantee a galaxy-only sample, and is not used where completeness is important), not in an MGC exclusion region (*IN-EXR*= 0), with good photometry (*QUALITY* ≤ 2) and without major errors in the LAS observation (*ppErrBits*< 256; following Smith et al. 2009, this criteria removes all objects that lie within dither offsets, all possible crosstalk artifacts, objects with bad pixels and
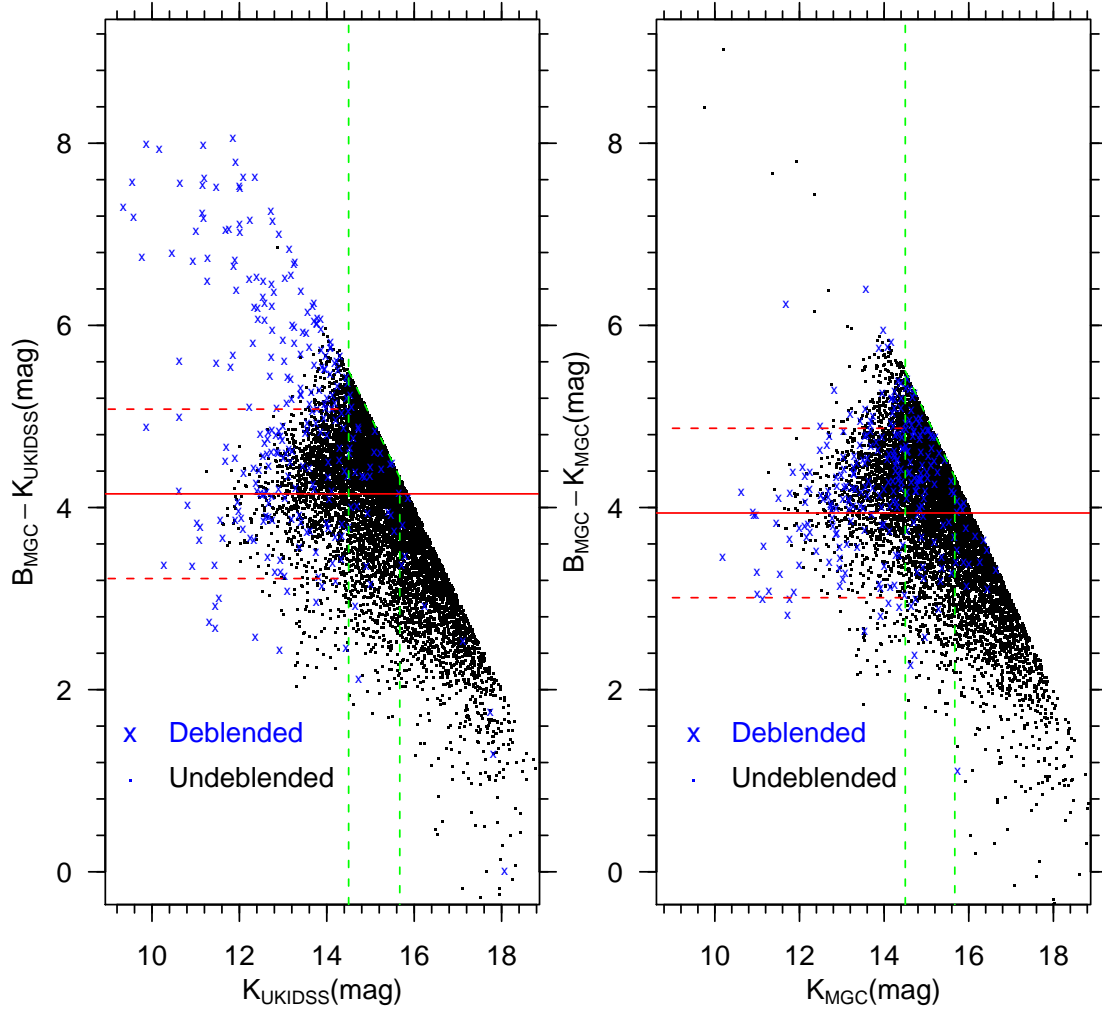
Figure 3.1: Comparisons between the MGC *B-K* values for *K* values taken from the UKIDSS Survey data (K_{UKIDSS}), and from Sextracted UKIDSS images (K_{MGC}). The dotted green lines are the apparent magnitude cuts used for the *K* band sample, and the red lines are the colour median and colour outlier lines for each sample.

objects close to saturation). The distance between the galaxy's centroid in the two surveys

had to be no more than 2.5 arcsec apart (*lasSourceXmgcDetection.distanceMins* $\leq 2.5/60$).

K_{UKIDSS} is defined as the *K* band Petrosian magnitude (*lasSource.kPetroMag*) taken from

the WSA dataset.

The deblending error

Unfortunately, a problem arises when the colour distribution of the sample is plotted (see the left image of Figure 3.1). There are a significant number of very bright objects that are extremely red. Smith et al. (2009) noted this issue and have traced this problem to a catastrophic fault in the CASU deblending algorithm, that causes deblended galaxies to become significantly brighter than their parent object, in some cases by several mag[1]. This is highlighted in the left hand image of Figure 3.1. While the undeblended bright galaxies (black points) are predominantly situated within $1\,\mathrm{mag}$ of the $B_{\mathrm{MGC}} - K_{\mathrm{UKIDSS}} = 4\,\mathrm{mag}$ line, the deblended bright galaxies (blue crosses) are spread across a much wider colour range.

Unfortunately the pre-deblended data is not output by the pipeline (when the CASU source extractor breaks up brighter galaxies, it does not generate any parameters for the parent object; Irwin et al, in preparation), so this fault is not trivial to correct or quantify. It is possible to remove the deblended galaxies from the sample by filtering upon an error bit designated as the deblender flag ($lasSource.kppErrBits\, \&\, \mathrm{0x00000010} = 0$), though this would leave a biased dataset. This option was adopted by Smith et al. (2009). Figure 3.2 illustrates the problem: although only 3.5 per cent of galaxies in the unlimited K band sample, 3.2 per cent in H, 3.1 per cent in J and 10.8 per cent in Y were deblended, the deblended population is not uniformly distributed across the apparent magnitude range.

Initially, an attempt was made to overcome the problem by using the SDSS optical colours to predict the Y, J, H and K band fluxes for the deblended galaxies. Unfortunately, the correlation was too noisy ($\Delta m \sim \pm 1\mathrm{mag}$), so the CASU standard catalogue products were abandoned. All Y, J, H and K photometry was re-derived from the reduced fits images.

Reanalysis of UKIDSS data using SExtractor

The WSA contains a tool (`MultiGetImage`) for extracting 1 arcminute $\times$ 1 arcminute fits images of 500 objects when given a list of their coordinates. The RA and Dec of every

---

[1]The WFCAM website describes the problem thus: "A pipeline processing bug has resulted in all CASU processed catalogue deblend components having erroneous values of Petrosian, Kron and Hall fluxes, radii and magnitudes. The problem does not affect those attributes for isolated (un-deblended) catalogue detections... Users interested in extended source fluxes for deblended components should use the isophotal values for the time being; at the time of writing (November 2008) we are planning to fix this problem in DR6 et seq."
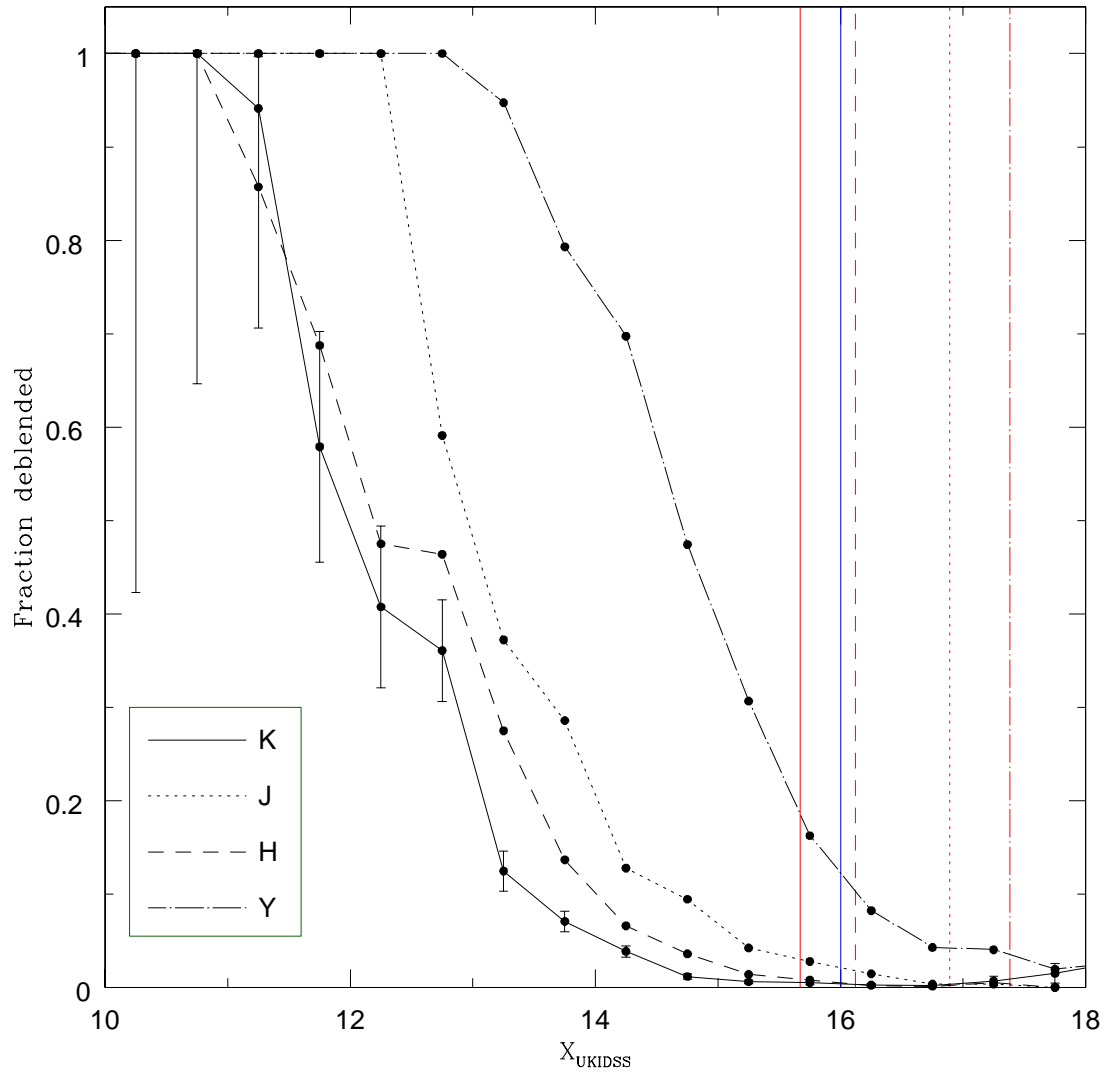
Figure 3.2: The fraction of galaxies deblended as a function of X_{UKIDSS}, where X is Y, J, H or K. The red vertical lines are the MGC-SDSS-UKIDSS band dependent apparent magnitude limits, the blue vertical line is the K band apparent magnitude limit of Smith et al. (2009).

MGC-Bright galaxy was input into this program, and images were extracted. A list of the galaxies where no image was available because of incomplete UKIDSS-LAS sky coverage was also produced.

The `SExtractor` object extraction program (Bertin & Arnouts, 1996) was used to extract sources from these images. In order to set up `SExtractor`, zeropoint, pixel size, gain, seeing and background level parameters were extracted from the UKIDSS image header. Fluxes and centroids for all sources in each image were catalogued. Both elliptical Petrosian aperture and BEST fluxes were calculated for each object. The `SExtractor` BEST flux generally uses the Kron flux, except in crowded regions where it uses a corrected isophotal flux. As B_{MGC} magnitudes were also calculated using BEST apertures, BEST magnitudes were adopted as the NIR photometry. K_{MGC} is defined as the `SExtractor` BEST magnitude and $K_{\mathrm{MGC,Petrosian}}$ as the `SExtractor` Petrosian magnitude.

The distance between each newly SExtracted object and the centre of the image were calculated, via the catalogued centroid positions and the axis sizes within each image header. As all extracted images were centred on the position of an MGC-Bright galaxy, the object that was extracted closest to the centre of each frame was assumed to be the match to that MGC galaxy. The apparent magnitude of the matching source was derived from its flux (F), exposure time (t), extinction (Ext), zeropoint (Z_{pt}) and airmass ($\sec\chi_{\mathrm{mean}}$). The former was taken from the `SExtractor` created catalogue, the rest were taken from UKIDSS fits file headers. The apparent magnitude was calculated using:

$$m = Z_{\mathrm{pt}} - 2.5\log_{10}(\frac{F}{t}) - \mathrm{Ext.}(\sec\chi_{\mathrm{mean}} - 1) \tag{3.1}$$

All nearest matches that were $> 2.5\,\mathrm{arcsec}$ from the MGC galaxy's centre were excluded. The right hand graph in Figure 3.1 show how the B_{MGC}-K_{MGC} distribution compares with that from WSA dataset. The online archive dataset contains 58 deblended galaxies with $B_{\mathrm{MGC}}-K_{\mathrm{UKIDSS}} > 6\,\mathrm{mag}$. When re-extracted, only 2 of those galaxies have $B_{\mathrm{MGC}}-K_{\mathrm{MGC}}$ in that range. One is a distant galaxy that is removed from the luminosity distribution when redshift limits were imposed; the other is just a very red galaxy. Figure 3.3 contains K band images of two of the deblended MGC galaxies, the position of their K_{MGC} and K_{UKIDSS} apertures and the luminosity returned using each method. Figure 3.4 shows how K_{UKIDSS}, K_{MGC} and $K_{\mathrm{MGC,Petrosian}}$ photometry compares. The dominant error in galaxy photometry is typically due to the flux measurement method. For an ordinary galaxy,

there is typically a difference of $\sim \pm 0.04\,\text{mag}$ between the apparent magnitude derived using elliptical aperture BEST and Petrosian methods. This is adopted as representative of the standard luminosity uncertainty.

Near-IR galaxies with no MGC match

It is possible that there are galaxies in the UKIDSS survey that have no match to the MGC, despite being inside its area of coverage. While some of these objects may be misclassified by the automated classification system, a number of these objects could potentially be extremely red galaxies (e.g. heavily dust attenuated or exceptionally high redshift galaxies) that have slipped below the $B_{\text{MGC}} = 20\,\text{mag}$ threshold and must be recovered for the calculation of the appropriate NIR luminosity function. Fits files for all UKIDSS galaxies ($pGal > 0.9$) with $X < B_{\text{MGC,threshold}} - (B_{\text{MGC,threshold}} - X_{\text{Survey}})_{\text{median}}$ were extracted. `SExtractor` was used to detect objects from these images (using the same parameters as in subsection 3.1.3), and to calculate their luminosity using the BEST aperture. All objects that were not covered by MGC CCDs were excluded. Following Liske et al. (2003), all objects with *stellaricity* > 0.98 were also excluded. The remaining objects that lie above the apparent magnitude limits (see subsection 3.2.1) were checked by eye, to remove any that looked like they were noise (or were otherwise suspect) that had been misclassified. A total of 100 NIR galaxies without a MGC match were found that were brighter than the K band apparent magnitude limit, 76 in H, 73 in J and 42 galaxies brighter than the Y band sample limit. However, as these galaxies were below the B band magnitude limit, they were not used in the calculation of the luminosity distribution.

Colour outliers

Whilst the new MGC-SDSS-UKIDSS catalogues produced by `SExtractor` contain a smaller number of colour outliers, some still remain and can be seen at the extremes in Figure 3.5). The median and standard deviation of $B - X$ was calculated, and colour outliers are defined to have a colour $> \text{Median} + 3\sigma$ or $< \text{Median} - 3\sigma$. These objects were re-examined. For 11 galaxies in the K band, 19 in H, 1 in J and 1 in Y, the program is incorrectly deblending an object. In these cases the `SExtractor` deblending parameters were modified to achieve a consistent deblending outcome.
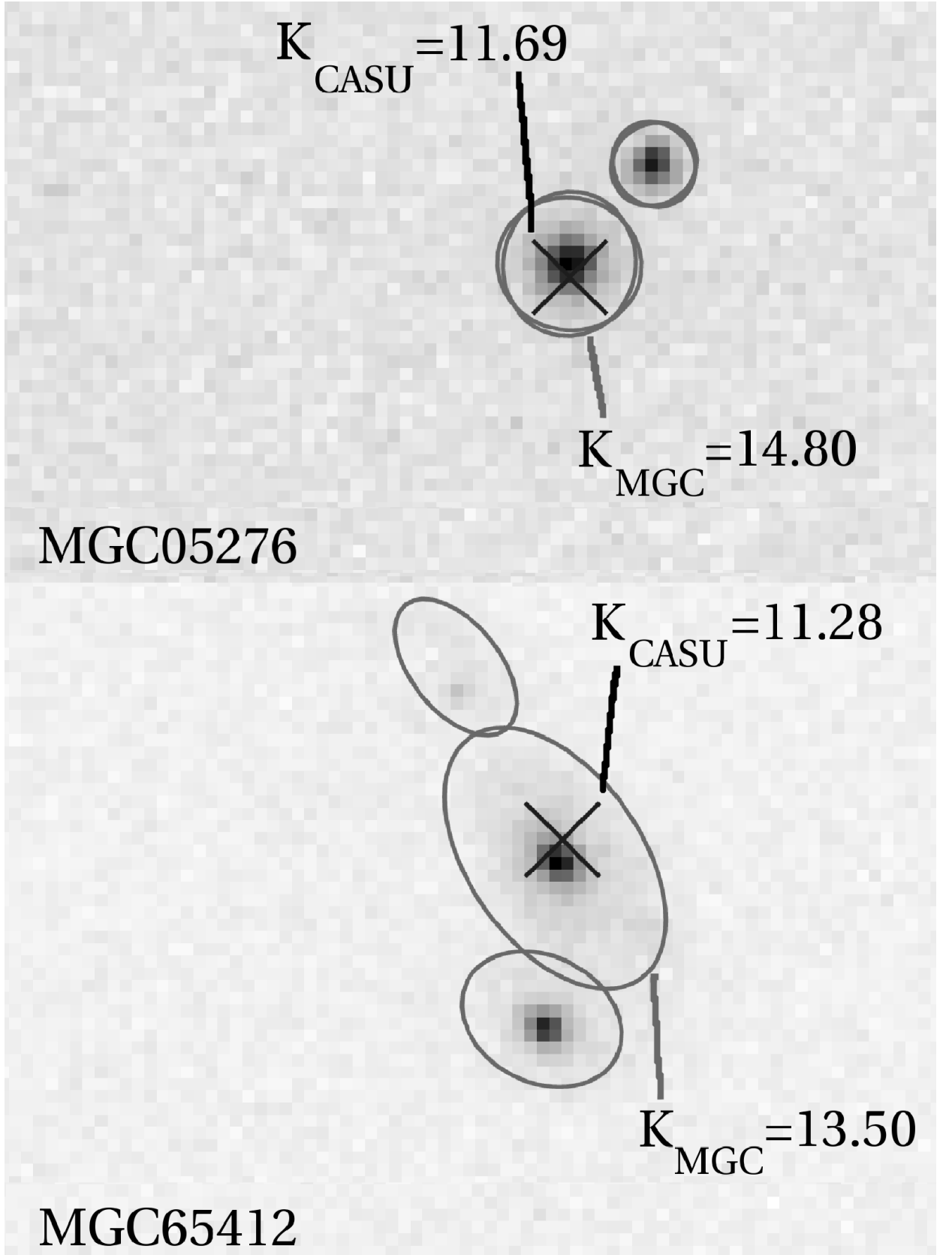
Figure 3.3: The position of the K_{MGC} Kron aperture (grey ellipse) and the central position of the K_{UKIDSS} galaxy (black cross) for the deblended galaxies MGC65412 and MGC05276
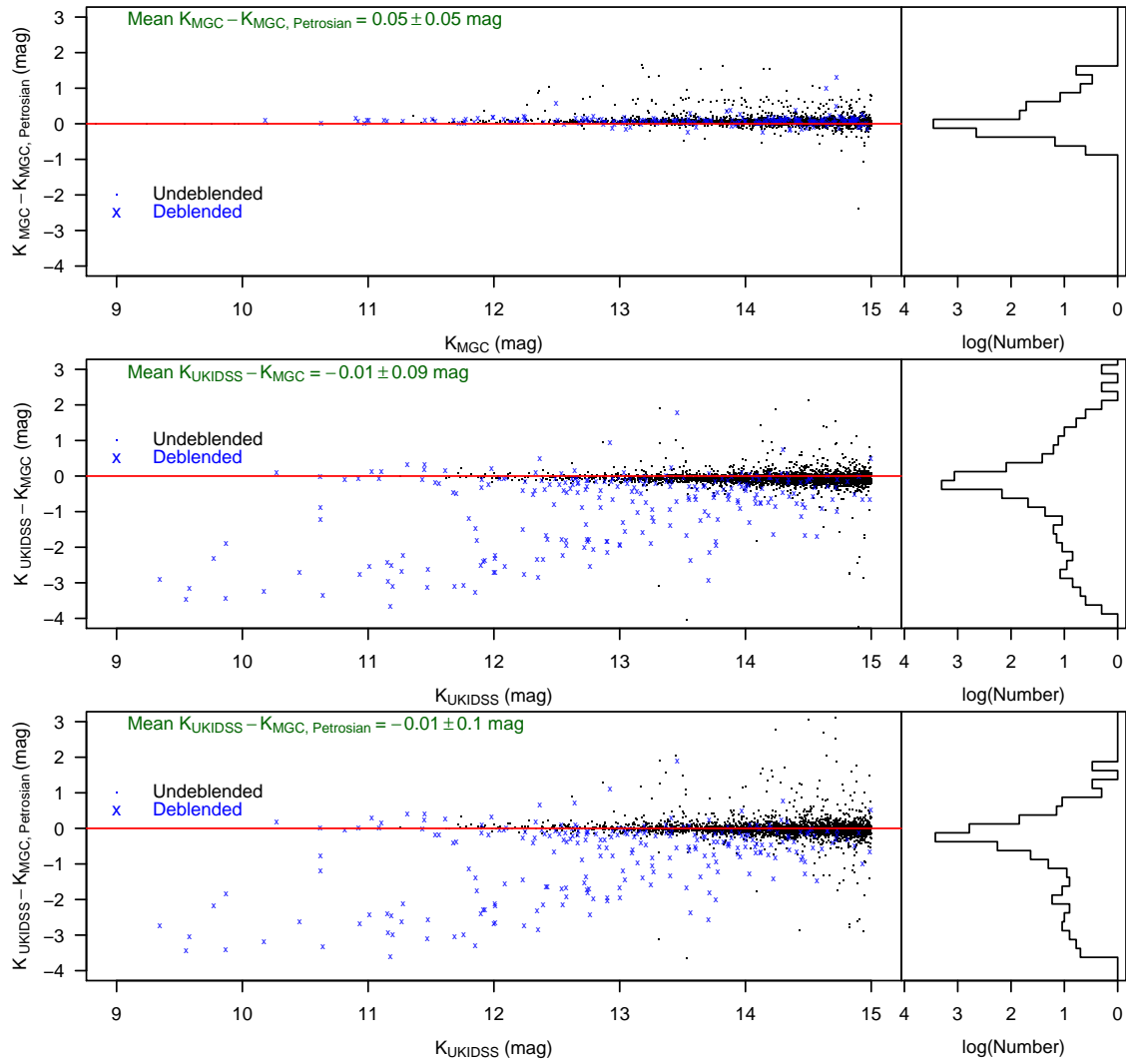
Figure 3.4: Comparisons between the K band galaxy luminosities using magnitudes taken from the UKIDSS Survey data (K_{UKIDSS}), and from SExtracted UKIDSS images using circular Petrosian ($K_{\text{MGC,Petrosian}}$) and BEST (K_{MGC}) methods. As in Figure 3.1, blue crosses are galaxies that have been flagged as deblended in the UKIDSS survey data, and black dots are those that have not.
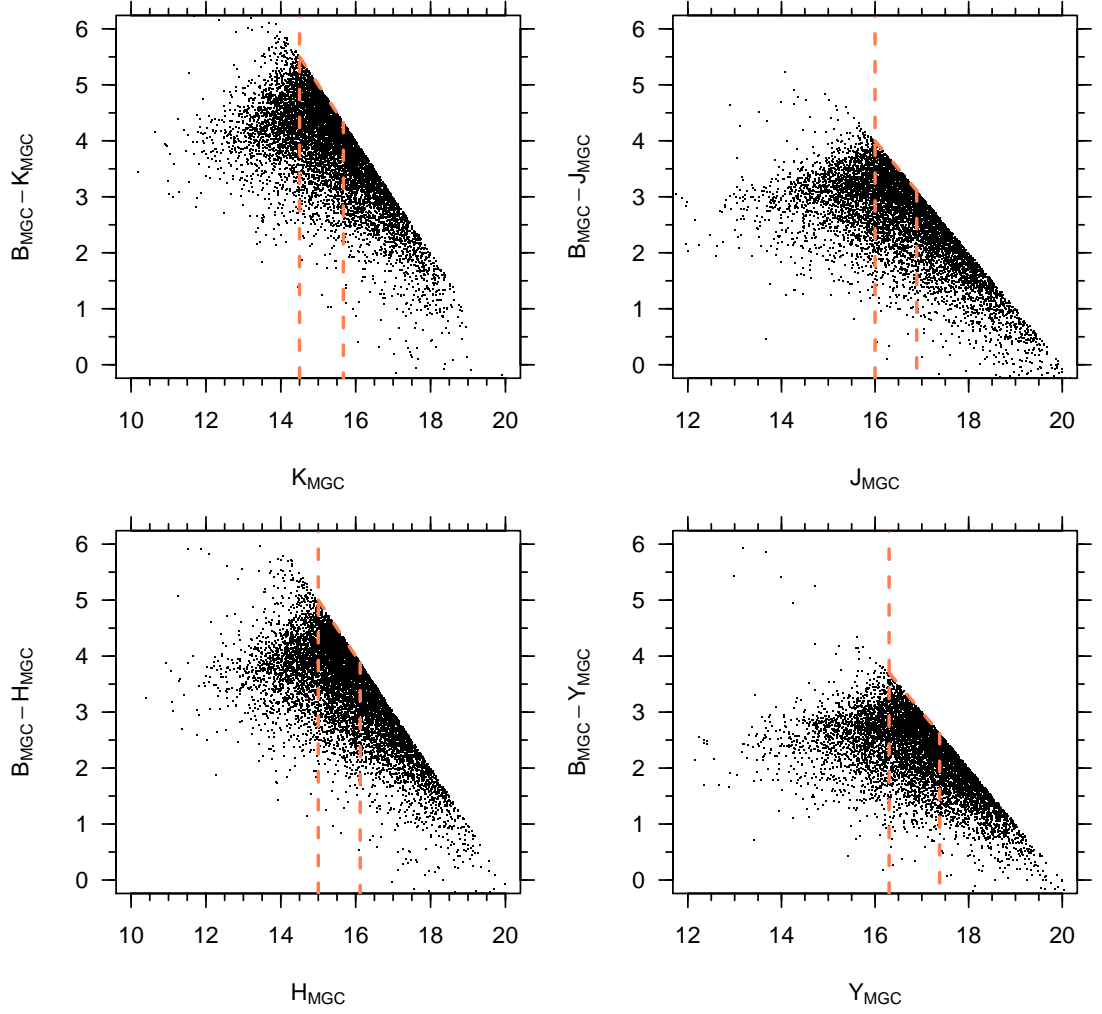
Figure 3.5: $B_{\mathrm{MGC}}, B_{\mathrm{MGC}} - X_{\mathrm{MGC}}$ and $X_{\mathrm{MGC}}, B_{\mathrm{MGC}} - X_{\mathrm{MGC}}$ graphs for $X{=}Y$, J, H and K band data. The vertical lines in the left hand graphs are the apparent magnitude cuts. All galaxies outside these limits are excluded from the MGC-SDSS-UKIDSS samples.
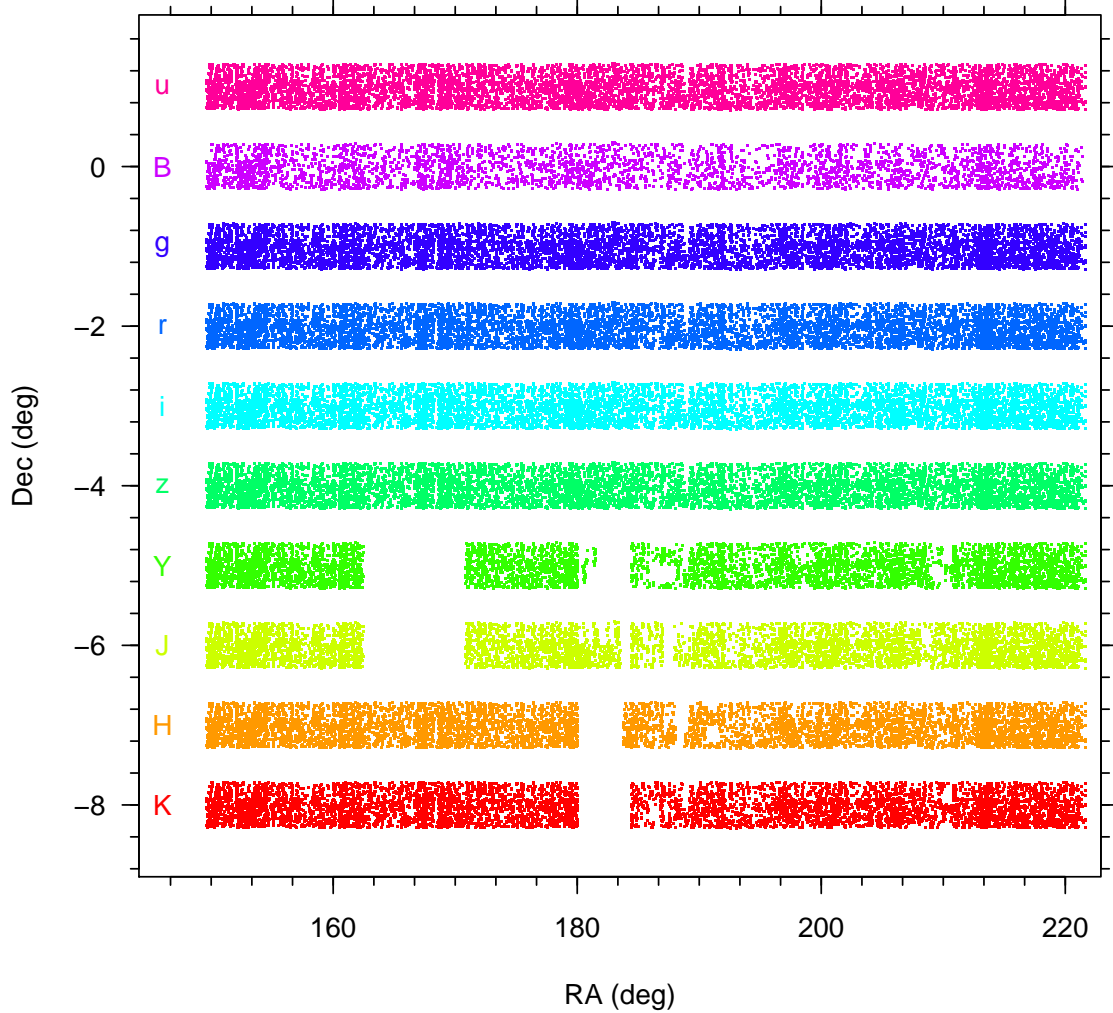
Figure 3.6: The distribution of galaxies along the common MGC-SDSS-UKIDSS region for (from top to bottom) the *ugrizYJHK* bands (as indicated). Note that the MGC data does not provide contiguous coverage within the designated area due to gaps between CCDs and masked regions around bright stars and satellite trails. The SDSS DR5 coverage of the MGC is complete while the UKIDSS LAS shows some clear gaps. The coverage is summarised in Columns 2 and 3 of Table 3.1.

3.1.4   Coverage

Figure 3.6 shows the coverage of the MGC region by the SDSS DR5 and UKIDSS LAS datasets. Note that the MGC footprint itself does not provide continuous coverage within a rectangle but rather a square-tooth profile (the INT WFC has a thick "L"-shaped footprint). The MGC region has also been carefully masked to remove objects close to bright stars, where the flux might be compromised, satellite trails, CCD defects, and edge effects

within the MGC region. This reduces the effective area on sky from $\sim38\,\mathrm{deg}^2$ to $30.88\,\mathrm{deg}^2$. However, this process also negates any issue of the blocking factor of distant galaxies by bright foreground stars as well as false detections due to spurious light scattering (e.g. diffraction spikes and ghosting). Full details of the MGC footprint and its masking are given in Liske et al. (2003).

SDSS DR5 provides complete coverage of the cleaned MGC region in all bands (see the *ugriz* coverage in Fig. 3.6). A detailed comparison of the photometry, astrometry, and deblending between the MGC and DR1 was described in detail in Cross et al. (2004) and Driver et al. (2006). In total MGC-Bright contains 10,095 galaxies to $B_{MGC} = 20.0\,\mathrm{mag}$. Matching detections were identified in the SDSS survey for 99.6 per cent of these sources. The majority of failed matches come from extreme low surface brightness systems and differences in deblending decisions.

The UKIDSS LAS DR3PLUS does not have complete coverage of the combined MGC-SDSS region ($YJHK$ coverage in Fig. 3.6) and the level of completeness varies between passbands. The gaps are due to data failing the UKIDSS data control process (typically seeing and sensitivity criterion). From the common regions the distribution of galaxies that have been flagged as containing major errors or requiring deblending (see Section 3.1.3), show no obvious bias along the strip (as one would expect given the quality control process). The area of overlap can therefore be derived based on the fraction of MGC galaxies with UKIDSS data available. The coverage of the SDSS and UKIDSS-LAS datasets is summarised in Columns 2 and 3 of Table.3.1

3.2 Generation of the luminosity distributions

In the previous section, $ugrizYJHK$ colours were derived for MGC-Bright galaxies from UKIDSS-LAS and SDSS observations. The MGC-SDSS-UKIDSS common sample is solely magnitude limited by the MGC's $B_{MGC} = 20.0$ magnitude cutoff. In order to generate an unbiased luminosity function in other passbands, it is necessary to implement a magnitude limit in the filter being used. In this section I generate complete, apparent magnitude-limited samples from this dataset, and calculate the absolute magnitude of all galaxies within each sample. From these datasets, the luminosity distribution in each passband is calculated using a modified SWML methodology, and the luminosity density is normalised

Band	Coverage	Area (deg^2)	Limit 1 (mag)	Limit 2 (mag)	Sample size (0.0033 <z<0.1)	$K(z)$	$E(z)$ range	β	$\Delta m_{z=0.1}$
u	100%	30.88	20.0	20.84	3267	$(2.16^{+0.95}_{-0.87})z$	-1.36—0		-0.01—0.31
g	100%	30.88	19.2	19.61	3328	$(2.71^{+0.74}_{-1.09})z$	-0.68—0		0.09—0.35
r	100%	30.88	17.9	18.76	2781	$(0.95^{+0.34}_{-0.52})z$	-0.45—0		0.00—0.13
i	100%	30.88	17.3	18.34	2623	$(0.48^{+0.38}_{-0.28})z$	-0.34—0		-0.01—0.09
z	100%	30.88	17.0	18.07	2437	$(0.03^{+0.33}_{-0.18})z$	-0.27—0		-0.01—0.04
Y	77%	23.69	16.3	17.38	1798	$(0.00^{+0.24}_{-0.12})z$	-0.23—0		-0.04—0.02
J	81%	25.07	16.0	16.89	1589	$(-0.61^{+0.27}_{-0.10})z$	-0.19—0		-0.08— -0.03
H	91%	27.89	15.0	16.12	1890	$(-0.28^{+0.24}_{-0.12})z$	-0.17—0		-0.06—0.00
K	91%	27.99	14.5	15.67	1785	$(-1.44^{+0.10}_{-0.02})z$	-0.15—0		-0.16— -0.13

Table 3.1: Parameters defining the coverage and depth(s) of the joint MGC-SDSS-UKIDSS common region along with the adopted $K(z)$ corrections and $E(z)$ ranges. Though no evolution ($E(z) = 0$) is specified, the β ranges in column 8 were used to calculate the scale of the uncertainty that evolution may produce. The range of $K(z)$-corrections in column 7 is used to calculate the uncertainty due to the K-correction. The sample size column gives the number of galaxies brighter than Limit 2 within the defined redshift limits. The $\Delta m_{z=0.1}$ column gives the range of effect the combined K+E correction can have on a $z = 0.1$ galaxy.

to the universal mean, accounting for overdensity of the MGC region.

3.2.1 $ugrizYJHK$ apparent magnitude limits for an unbiased sample

In order to derive luminosity distributions for multi-wavelength data from a B band spectroscopic sample it is important to consider the colour bias. Figure 3.7 shows the $B_{MGC} - X$ v X colour plots where X denotes $ugrizYJH$ or K. The most conservative approach to deriving an unbiased luminosity distribution is to simply define a complete sample within each band, i.e. cut the sample at a sufficiently bright flux where the full colour distribution is fully sampled (long dashed line) and where the number-counts have yet to show any indication of a turn-down (Fig. 3.8). Fig. 3.8 also shows that these samples extend deeper than those used in Montero-Dorta et al. (2008). The turn-over occurs roughly one magnitude deeper in each SDSS passband. The Montero-Dorta et al. limits are shown on Fig. 3.7 as long dash-short dash lines. In all SDSS passbands they cut more conservatively than the harshest limit required to define the MGC-SDSS-UKIDSS sample, particularly in the u band. The most liberal approach is to use all the data and define a unique flux limit for each individual object based upon the spectroscopic limit of $B_{\mathrm{MGC}} = 20.0\,\mathrm{mag}$ combined with the objects colour, i.e. $X_{\mathrm{limit}} = 20.0 - (B - X)$,

Table 3.2: Median colours and 3σ clipped standard deviations above the completeness limits defined by Flux limit 1 in Table. 3.1.

Colour	Median	Std (3σ clipped)
$u - B$	0.81	0.40
$B - g$	0.38	0.13
$B - r$	1.21	0.44
$B - i$	1.62	0.57
$B - z$	1.94	0.59
$B - Y$	2.56	0.62
$B - J$	3.06	0.51
$B - H$	3.82	0.59
$B - K$	4.25	0.59

using these B and X limits to appropriately weight each object (Fig. 3.7, dotted line). While the former will reduce the sample size significantly the latter will incorporate a large quantity of data in the regime where flux measurements may not be credible. A hybrid approach was adopted (Fig. 3.7, short dashed line) where mean colour was determined for each sample (solid line) and combined with the spectroscopic limit of $B_{\mathrm{MGC}} = 20.0\,\mathrm{mag}$ to determine a nominal limit, i.e. the limit where 50 per cent of the colour distribution was spectroscopically sampled. Each galaxy was then allocated a flux limit: the brighter of the nominal limit or that defined by the locus $X_{\mathrm{limit}} = 20.0 - (B_{\mathrm{MGC}} - X)$ (short dashed lines on Fig. 3.7). The conservative limits (Limit 1), nominal limits (Limit 2), and effective sample sizes are shown in Table 3.1. Table 3.2 shows the median colour and 3σ-clipped standard deviation derived from the data above the conservative limit (Limit 1). After the imposition of magnitude limits, every galaxy within each sample has a redshift. Figure 3.9 shows the distribution of the apparent magnitude cut samples by redshift.

3.2.2 SWML luminosity distributions

The $ugrizYJHK$ luminosity distributions were generated using a modified SWML method. This method is detailed in Section 1.3.1. To summarise: the SWML method is a maximal likelihood method that makes no prior assumption of the form of the luminosity distribution, calculating the visibility of each object separately, given a specified magnitude limit. The modification to the method utilised here allows the magnitude limit of each source to vary, providing a means of accounting for both the apparent magnitude limit of the filter and the fixed B band MGC apparent magnitude limit.

As the luminosity distribution employs absolute magnitudes, it is necessary to convert
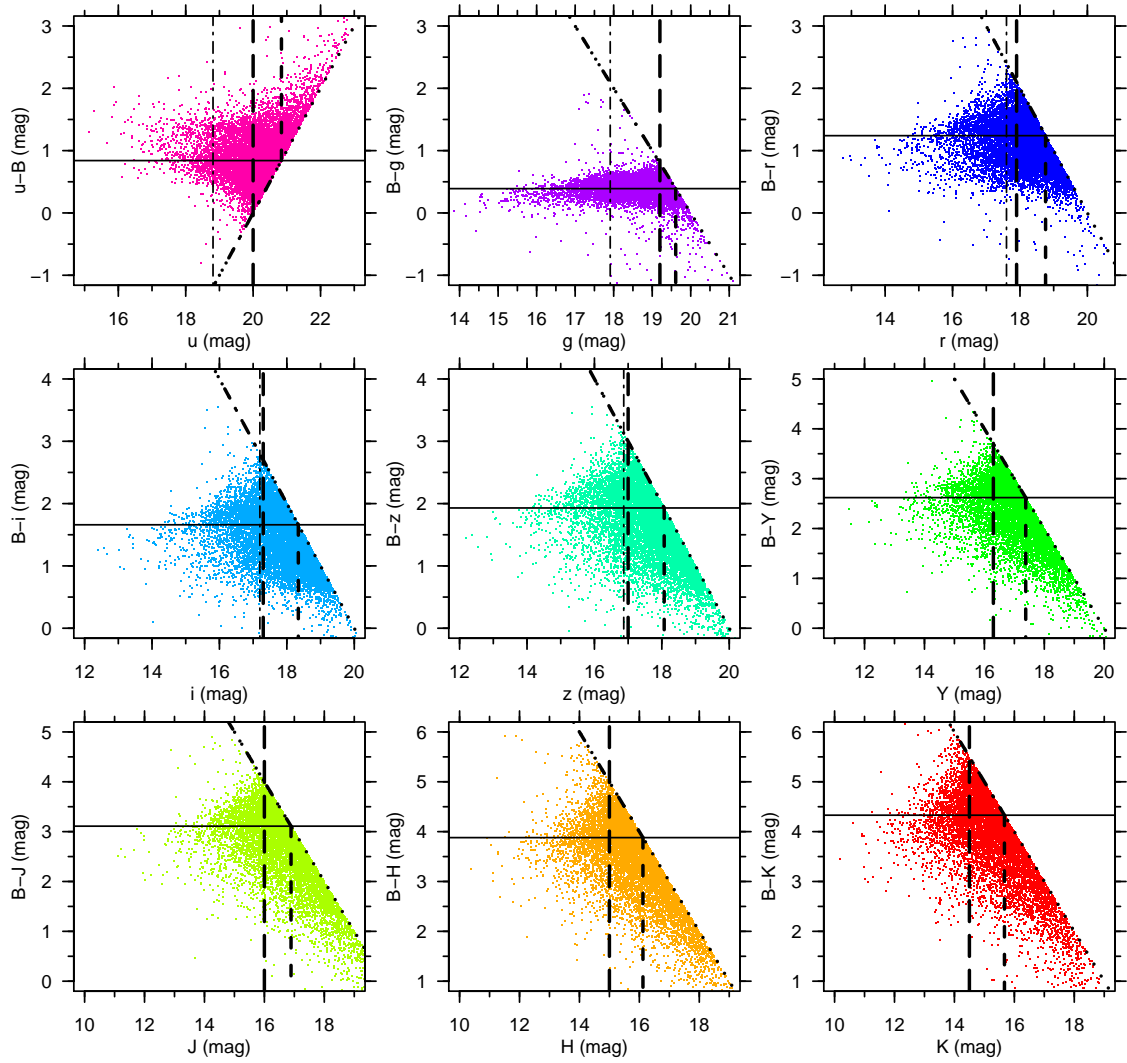
Figure 3.7: The colour-magnitude diagrams for the *ugrizYJHK* wavebands versus *B*. The vertical lines are the MGC-SDSS-UKIDSS apparent magnitude limits in *ugrizYJH* or *K*, the diagonal lines are the MGC *B* band magnitude limits.
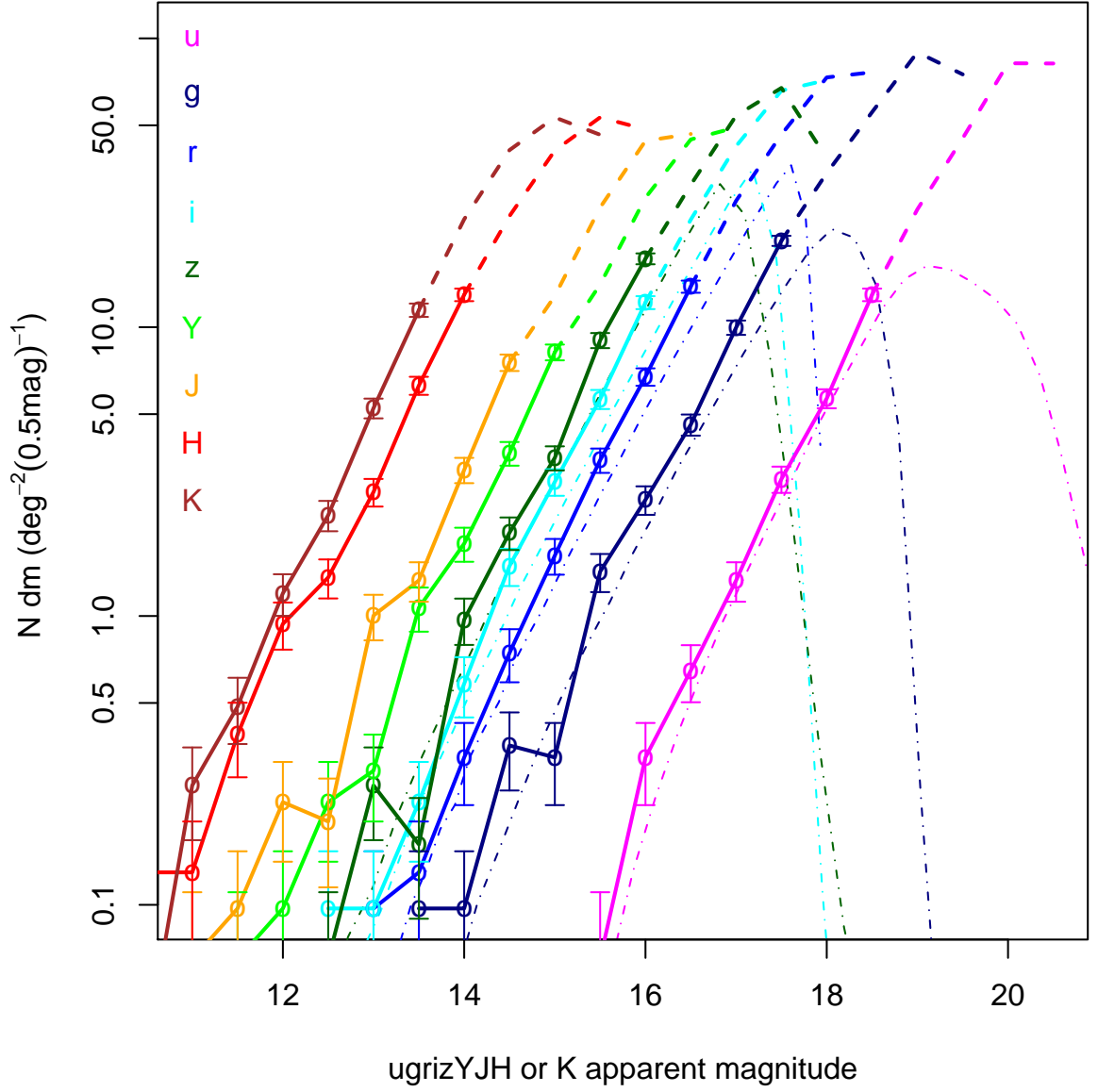
Figure 3.8: The number of galaxies, by apparent-magnitude in the *ugrizYJHK* filters. The dash-dot-dash lines are galaxy counts from Montero-Dorta et al. (2008). Montero-Dorta et al. justify their early downturn as an issue of redshift incompleteness, and introduce conservative magnitude cuts accordingly.

from apparent magnitudes. This requires the implementation of a cosmological model and $K(z)$ and $E(z)$-corrections. The prescription used is described below.

Cosmology

The adopted cosmological parameters were Ω_M=0.3, Ω_Λ=0.7, H_o=100 km s^{-1} Mpc^{-1}, compatible with both Jones et al. (2006) and Blanton et al. (2003). Galaxies were rejected if their redshift is outside the interval $0.0033 \leq z \leq 0.10$. The lower limit is defined as that required to overcome the local velocity field. The measured velocity of a galaxy has two components - a velocity due to the expansion of the Universe (which we wish to measure), and a velocity due to the motion of the source relative to the Milky Way (which is a cause of uncertainty). At lower redshifts, the velocity of the galaxy relative to the Milky Way becomes an sizeable component of the total velocity. The lower limit corresponds to a velocity of ~ 990 km s^{-1}, roughly one and a half times the speed of the motion of the Local Group relative to the Hubble Flow (see Driver et al. 2005). The upper redshift limit is chosen to minimise the uncertainty inherent in the adopted $K(z)$ and $E(z)$ corrections and ensure a uniform survey volume across all wavelengths.

$K + E$ corrections

For both $K(z)$ and $E(z)$ corrections global values were adopted. Monte-Carlo simulations were run over a suitably broad range of uncertainty to ensure that the final uncertainties on the Schechter function parameters were realistic. Unlike the Blanton et al. (2003) and Montero-Dorta et al. (2008) papers, absolute magnitudes were calculated with the SDSS passbands at z=0, rather than at z=0.1.

$K(z)$-corrections were derived (column 7 of Table 3.1) via the 13.2 Gyr Sa-type galaxy spectra from the synthetic library of Poggianti (1997), and the range of possible $K(z)$-corrections from the 7.2 Gyr Sa-type (the lower limit of column 7) and 15.0 Gyr El-type galaxy spectra (the upper limit).

The first four black points in Figure 11 of Prescott et al. 2009 (which shows the evolution of the u band luminosity density for different galaxy populations) indicate no evolution is occurring within $0.0033 < z < 0.1$. The quoted results do not employ an $E(z)$-correction; however the effect that including one would produce was estimated. This uncertainty was derived from the best-fitting Schechter parameters for five equally spaced β values

within the range shown in column 8 of Table 3.1. The standard deviation in these results was taken to be the evolutionary uncertainty. Any effects would predominantly impact the M^* parameter, with only a small change in the α and ϕ^* parameters. For instance, using the evolution in the u band luminosity density presented in Prescott et al. (2009) ($\beta = -1.36$, using the sign convention in Equation 3.2) and the prescription of Phillipps & Driver (1995) given by Equation 3.2[2]:

$$E(z) = 2.5\beta \log_{10}(1 + z) \tag{3.2}$$

where z is the redshift of the corrected galaxy. The inclusion of an evolutionary correction modifies the best-fitting M^* parameter by $0.09\,\mathrm{mag}$, the best-fitting α parameter by 0.02 and the best-fitting ϕ^* parameter by $0.0003\,\mathrm{h}^3\,\mathrm{Mpc}^{-3}$.

The effects of the $K(z) + E(z)$ corrections are, unsurprisingly, strongest in UV ($\pm 0.05\,\mathrm{mag}$ in M^* in the u band), and limited in the NIR ($\pm 0.01\,\mathrm{mag}$ in M^* in the K band). Blanton et al. (2003) have used the evolution correction as an explanation for an observed flattening of the faint-end of the luminosity function. Within this small redshift range there is no evidence to confirm that interpretation.

Malmquist Bias

Finally, uncertainty within its luminosity can move a galaxy into the wrong absolute-magnitude bin, and this effect increases the luminosity density within the brighter bins by a greater fraction than the fainter bins; i.e. a classical Malmquist bias. Where there is a large uncertainty in luminosity this must be compensated for. However, the typical luminosity uncertainty in the data, $\sim 0.03\,\mathrm{mag}$ rms uncertainty in $ugriz$ (Adelman-McCarthy et al., 2007), $0.04\,\mathrm{mag}$ in K (see section 3.1.3), $0.05\,\mathrm{mag}$ in H, $0.05\,\mathrm{mag}$ in J and $0.04\,\mathrm{mag}$ in Y, is small enough to make this unnecessary.
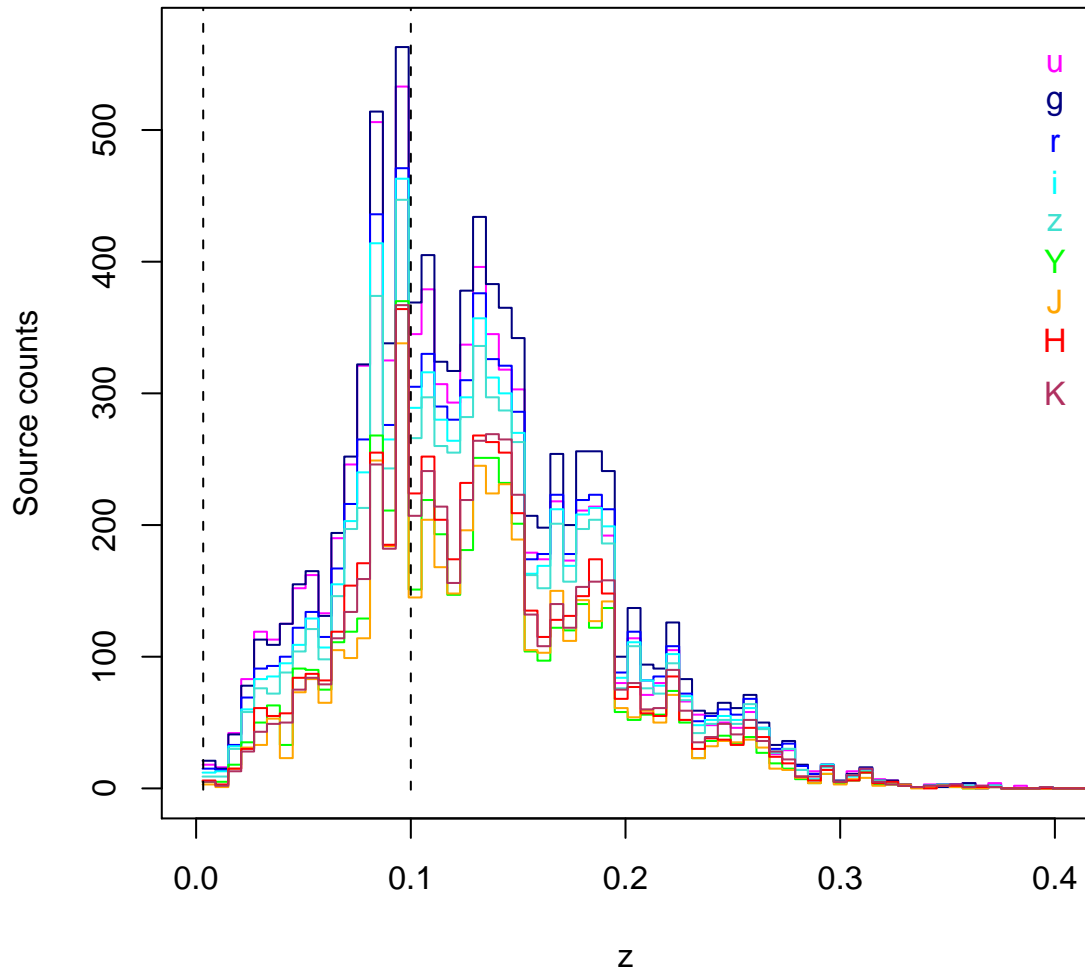
Figure 3.9: The redshift distribution of galaxies within the MGC-SDSS-UKIDSS apparent-magnitude limited matched samples, in bins of z=0.006. The dashed lines signify the sample redshift limits.

3.2.3   Normalisation

As the SWML calculates the relative density of the bins, and not their space density, it is necessary to normalise the luminosity density to the correct values. This requires the volume the sample is contained within to be derived. Within $30.88 \deg^2$ of sky, and using the cosmological parameters in section 3.2.2, the normalisation volume over the redshift range $(0.023 < z < 0.097)$ is calculated to be $71069 h^{-3} \mathrm{Mpc}^3$. The same redshift range is adopted for all nine filters to insure against cosmic variance. The redshift range is selected to be complete for a $1\,\mathrm{mag}$ range around the M^* point for each of the nine filters. The scale of the global overdensity is ascertained from SDSS-DR7 spectroscopic catalogue data for a $5150 \deg^2$ rectangular region of sky (130 to 236 deg RA, 0 to 58 deg Dec). An average source density of 13.00 de-reddened, $M_r^* \pm 0.5\,\mathrm{mag}$ galaxies per $\deg^2$ were found within the volume bound by this area and the MGC sample's redshift range. The MGC area contains a source density of 15.90 de-reddened, $M_r^* \pm 0.5\,\mathrm{mag}$ galaxies per $\deg^2$. Assuming that the area lost due to bright star holes within the SDSS region is the same fraction as that lost in the MGC region ($\sim 3\%$), the MGC is 19.3% overdense. This overdensity is visible in Figure 3.8. In each filter the volume was modified to account for the variation in the area of coverage, spectroscopic incompleteness (in all samples, $f_{C,X} = 1$), and the global over-density of the MGC region, i.e.:

$$V_X = V_B.f_{A,X}.f_{C,X}/f_{\mathrm{MGC}} \tag{3.3}$$

Where X is the filter, $f_{A,X}$ is the fraction of the MGC covered by filter X, $f_{C,X}$ is the sample completeness in filter X, and f_{MGC} is the global over-density of the MGC. Using these corrected volumes, and the number of galaxies within a one magnitude range that contains the M^* mag galaxies, the galaxy number-density was calculated and the unnormalised number-densities (ϕ-values) derived from the SWML method were scaled to reproduce the source density:

$$\phi(M) = N_X(M^* - 0.5 < M < M^* + 0.5)/V_X \tag{3.4}$$

---

[2]The β parameter in Equation 3.2 and the β variable in Prescott et al. (2009) will, by definition, have opposing signs.

Table 3.3: Derived Schechter function parameters in $ugrizYJHK$ for the magnitude limits indicated within the redshift range $0.0033 < z < 0.1$. The errors shown for the Schechter parameters are, in order, due to the sample size (i.e., Poisson statistical errors), K(z)-correction and E(z)-correction uncertainties. The errors shown for luminosity density and νf_ν statistics are due to sample size, and combined K+E correction uncertainties. These can be combined in quadrature to give the combined error. u and z results have been modified by $-0.04\,\mathrm{mag}$ and $0.02\,\mathrm{mag}$ to compensate for the discrepancy between SDSS and AB magnitude systems.

Sample	ϕ^* (h^3 Mpc^{-3})	M^* (mag)	α
$u <20.84$	$0.0279^{+0.0015+0.0004+0.0003}_{-0.0016-0.0004-0.0003}$	$-18.21^{+0.05+0.04+0.03}_{-0.05-0.04-0.03}$	$-0.93^{+0.03+0.01+0.01}_{-0.04-0.02-0.01}$
$g <19.81$	$0.0158^{+0.0011+0.0002+0.0001}_{-0.0008-0.0002-0.0001}$	$-20.08^{+0.05+0.06+0.02}_{-0.06-0.06-0.02}$	$-1.15^{+0.03+0.00+0.00}_{-0.02-0.00-0.00}$
$r <18.76$	$0.0124^{+0.0011+0.0001+0.0002}_{-0.0006-0.0001-0.0002}$	$-20.81^{+0.08+0.03+0.03}_{-0.05-0.03-0.03}$	$-1.18^{+0.04+0.01+0.01}_{-0.02-0.00-0.01}$
$i <18.34$	$0.0120^{+0.0010+0.0003+0.0002}_{-0.0008-0.0003-0.0002}$	$-21.16^{+0.07+0.01+0.01}_{-0.06-0.01-0.01}$	$-1.18^{+0.03+0.01+0.01}_{-0.03-0.00-0.01}$
$z <18.07$	$0.0109^{+0.0009+0.0002+0.0001}_{-0.0011-0.0002-0.0001}$	$-21.46^{+0.06+0.01+0.01}_{-0.09-0.01-0.01}$	$-1.18^{+0.03+0.01+0.00}_{-0.04-0.00-0.00}$
$Y <17.38$	$0.0146^{+0.0021+0.0002+0.0003}_{-0.0019-0.0002-0.0003}$	$-21.94^{+0.12+0.01+0.01}_{-0.11-0.01-0.01}$	$-1.06^{+0.08+0.01+0.01}_{-0.07-0.01-0.01}$
$J <16.89$	$0.0155^{+0.0017+0.0002+0.0002}_{-0.0016-0.0002-0.0002}$	$-22.20^{+0.11+0.01+0.01}_{-0.10-0.01-0.01}$	$-0.90^{+0.07+0.01+0.01}_{-0.07-0.01-0.01}$
$H <16.12$	$0.0149^{+0.0013+0.0001+0.0001}_{-0.0012-0.0001-0.0001}$	$-23.07^{+0.08+0.00+0.00}_{-0.08-0.00-0.00}$	$-0.99^{+0.05+0.00+0.00}_{-0.05-0.00-0.00}$
$K <15.67$	$0.0156^{+0.0015+0.0001+0.0000}_{-0.0014-0.0001-0.0000}$	$-23.36^{+0.09+0.01+0.00}_{-0.08-0.01-0.00}$	$-0.96^{+0.06+0.00+0.00}_{-0.05-0.00-0.00}$

3.3 $ugrizYJHK$ luminosity functions and densities

In the previous section I calculated the luminosity distributions produced from magnitude-limited samples of MGC-Bright galaxies that have been matched with UKIDSS and SDSS observations. In this section I fit the Schechter function to the luminosity distribution produced in each filter, discuss the quality of the fit and how it compares to previous measurements in the literature, and calculate the total luminosity density produced by integrating the best-fitting Schechter function across the entire magnitude range.

3.3.1 Luminosity function fits

The resulting luminosity distributions and fitted Schechter functions for all samples ($ugrizYJHK$) are shown in Figure 3.10 and the Schechter parameters tabulated in Table 3.3. In general the luminosity functions are reasonable fits to the luminosity distributions based on the reduced-χ^2 values. The most notable exceptions are in the z-band, which appears to show a tentative upturn at fainter magnitudes ($M_z \sim -17\,\mathrm{mag}$), and the i-band, which appears to shows the same effect fainter than $M_i \sim -16.5\,\mathrm{mag}$. The faint-end upturn is not dependent on the faint end magnitude limit; it remains if the samples are cut using the conservative limits (Limit 1 in Table 3.1), or the much brighter limits of the SDSS samples. However, it should be noted that the faint-end upturn is confined to these two passbands and is not a general characteristic of all nine luminosity distributions. There is
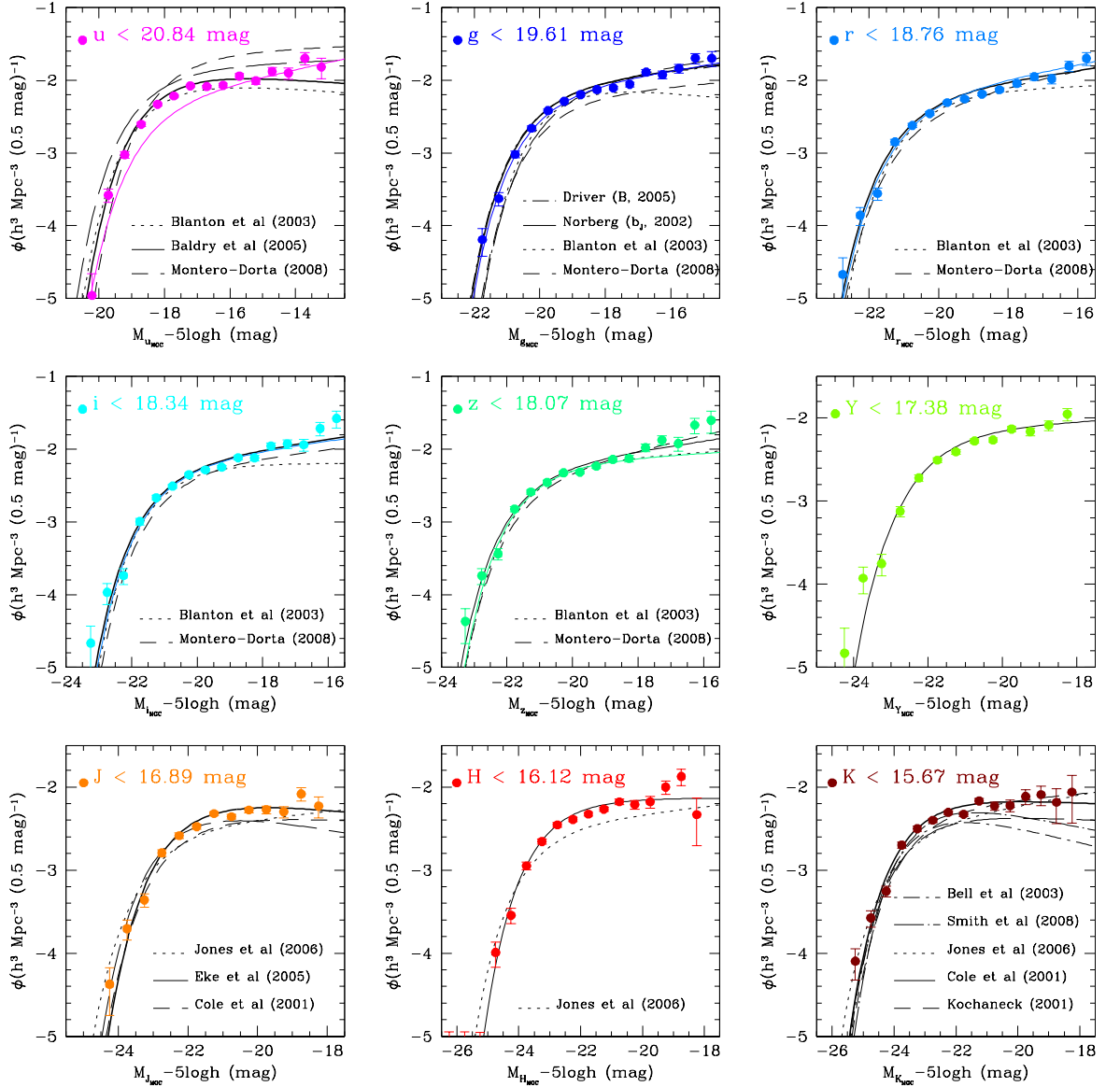
Figure 3.10: *ugrizYJHK* luminosity distributions and fitted Schechter functions, with comparison lines for Schechter parameters from equivalent surveys. The coloured lines show the best fit Schechter function for *ugriz* samples that have undergone the more conservative cuts introduced by Montero-Dorta et al.. Poissonian uncertainties are shown for each bin. It should also be noted that the absolute magnitudes in Baldry et al. (2005), Blanton et al. (2003) and Montero-Dorta et al. (2008) use SDSS passbands that have been redshifted to $z = 0.1$, and therefore have been k-corrected (and evolved, where applicable) back to $z = 0$. The Norberg et al. (2002) and Driver et al. (2005) comparison lines in the g band use the similar b_J and B filters, respectively, which have been transformed to the g band using the assumption that $B - V = 0.94$ mag from Liske et al. (2003), and filter conversions in Liske et al. (2003) and Blanton & Roweis (2007).

no sign of any obvious excess of very bright systems (possibly due to the defined redshift interval as Montero-Dorta et al. found an overdensity at $z > 0.1$), and in general the Schechter function provides good fits around the knee and brighter.

3.3.2   Comparison with prior measurements

Optical photometry

Overlaid on Figure 3.10 are selected recent measurements from other groups. In almost all cases the MGC-SDSS-UKIDSS results lie above those reported from the much larger SDSS survey results. As they are based upon SDSS photometry, this cannot be a photometric issue. Furthermore, as the MGC's over-density has been removed by calibrating the source density to a $5150 \deg^2$ region of the SDSS survey, it also cannot be due to cosmic variance. A further possibility is simply the difference in adopted $K(z)$ and $E(z)$ corrections. It is noticeable that the vertical offset does appear to show some wavelength dependence with the offset maximum in g ($\sim$30 per cent) and dropping to a minimum in z ($\sim$5 per cent). The MGC dataset extends approximately 1 mag deeper in all filters (the SDSS sample limits reported in Montero-Dorta et al. are 19.00, 17.91, 17.77, 17.24, 16.97 mag in $ugriz$ respectively, q.v. Table 2, column 5, and in Blanton et al. the $ugriz$ limits are 18.36, 17.69, 17.79, 16.91 and 16.50 mag, q.v. Table 1, column 2), has 100 per cent redshift completeness, and uses an identical redshift range for all filters ($0.023 < z < 0.097$). The recent study by Montero-Dorta et al. (2008), by comparison, had a median redshift completeness of 85 per cent (reported to be both wavelength and flux dependent) that may be partly due to the $\sim$55 arcsec minimum fibre proximity of the SDSS spectral survey and, although having significantly brighter flux limits, was used to probe to significantly higher redshifts ($z \leq 0.2$). Moreover, the normalisation adopted in Montero-Dorta et al. was the Davis & Huchra (1982) method. This uses the entire data set and tends to overly weight the normalisation towards the higher redshift range where incompleteness may be most severe. Without reanalysing the SDSS data using this methodology, it is not possible to ascertain the exact cause of the normalisation discrepancy. It is plausible that it is related to the use of this normalisation method and redshift incompleteness bias.

Fig. 3.11 examines the shape of the luminosity function in detail by showing the 1σ error contours from the best-fitting MGC-SDSS-UKIDSS Schechter function fits in the $M^* - \alpha$ plane. This illustrates the known degeneracy between M^* and α. Recent values from the literature, as indicated in Table 3.4, are shown as data points with error bars (colour coded on Fig. 3.11 according to filter). The dashed lines on Fig. 3.11 are the $ugriz$

contours produced when the MGC-SDSS-UKIDSS samples are conservatively cut at the brighter limits used by Montero-Dorta et al.. In general the optical data agree reasonably well with recent results from the two much larger SDSS studies of Blanton et al. (2003) and Montero-Dorta et al. (2008). The conservatively cut sample and the standard sample 1σ $M^* - \alpha$ contours overlap (except in the u band, which loses the largest fraction of galaxies following the brighter apparent magnitude cut). The volume of the common MGC-SDSS-UKIDSS region is much smaller, and the resulting uncertainty is significantly larger than the SDSS results. As an aside, while the SDSS results are generally consistent with the MGC-SDSS-UKIDSS data, they appear to be inconsistent with each other at a high level of significance. After estimating the $E(Z)$-uncertainty, it seems unlikely that this is the only cause of discrepancy between the two SDSS results (Montero-Dorta et al. do not use an evolution correction, Blanton et al. does). This suggests that significant unquantified systematics still remain and that the increase in statistical size from the MGC to the entire SDSS DR5 dataset does not necessarily increase the accuracy to which the measured LFs are known.

Near-IR photometry

In the NIR the discrepancies are more dramatic, perhaps as expected given the rapid development of NIR technologies. I am not aware of any published Y band luminosity functions for comparison. As with the optical photometry, the MGC-SDSS-UKIDSS results tend to produce a higher space-density of galaxies. This is perhaps expected given the significantly deeper imaging data. Comparing the MGC-SDSS-UKIDSS K-band result to Smith et al. (2009), whose data was also based on UKIDSS-LAS, there is excellent agreement at the bright-end but a discrepancy in the faint-end slope.

The near-IR best-fitting luminosity function shapes produced by the MGC-SDSS-UKIDSS sample are significantly offset from those derived by earlier studies. This presumably reflects the quality of the underlying imaging data. The near-IR data has improved greatly, with major increases in resolution (5x smaller pixel size) and depth ($\sim 2.7\,\mathrm{mag}$ deeper in the K band) provided by moving from very shallow 2MASS data to the less shallow UKIDSS LAS. The MGC-SDSS-UKIDSS sample of a few thousand galaxies is

Table 3.4: Schechter parameters for optical and NIR surveys in the literature

Reference	Band	Sample Size	λ (μm)	ϕ^* (Mpc^{-3})	M^* (mag)	α
Baldry et al. (2005)	u$^{0.1}$	43223	0.3224†	0.0086	-18.07‡	-1.05
Blanton et al. (2003)	u$^{0.1}$	113988	0.3224†	0.0305	-17.93	-0.92
Montero-Dorta et al. (2008)	u$^{0.1}$	159018	0.3224†	0.0495	-17.72	-1.05
This paper	u	3267	0.3546	0.0279	-18.21	-0.93
Blanton et al. (2003)	g$^{0.1}$	113988	0.4245†	0.0218	-19.39	-0.89
Montero-Dorta et al. (2008)	g$^{0.1}$	256952	0.4245†	0.0125	-19.53	-1.10
This paper	g	3328	0.4670	0.0158	-20.08	-1.15
Blanton et al. (2003)	r$^{0.1}$	113988	0.5596†	0.0149	-20.44	-1.05
Montero-Dorta et al. (2008)	r$^{0.1}$	466280	0.5596†	0.0093	-20.71	-1.26
This paper	r	2781	0.6156	0.0124	-20.81	-1.18
Blanton et al. (2003)	i$^{0.1}$	113988	0.6792†	0.0147	-20.82	-1.00
Montero-Dorta et al. (2008)	i$^{0.1}$	461928	0.6792†	0.0114	-20.93	-1.14
This paper	i	2623	0.7471	0.0120	-21.16	-1.18
Blanton et al. (2003)	z$^{0.1}$	113988	0.8107†	0.0135	-21.18	-1.08
Montero-Dorta et al. (2008)	z$^{0.1}$	422643	0.8107†	0.0092	-21.40	-1.26
This paper	z	2437	0.8918	0.0109	-21.46	-1.18
This paper	Y	1798	1.0305	0.0146	-21.94	-1.06
Jones et al. (2006)	J	93841	1.250	0.0071	-22.85	-1.10
Eke et al. (2005)	J	43553	1.250	0.0139	-22.39	-0.82
Cole et al. (2001)	J	17173	1.250	0.0104	-22.36	-0.96
This paper	J	1589	1.2483	0.0155	-22.20	-0.90
Jones et al. (2006)	H	90317	1.644	0.0072	-23.54	-1.11
This paper	H	1890	1.6313	0.0149	-23.07	-0.99
Jones et al. (2006)	K	113988	2.198	0.0074	-23.83	-1.16
Cole et al. (2001)	K	17173	2.198	0.0108	-23.44	-0.96
Kochanek et al. (2001)	K	4192	2.198	0.0116	-23.39	-1.09
Bell et al. (2003)	K	6282	2.198	0.0143	-23.29	-0.77
Smith et al. (2009)	K	36663	2.198	0.0176	-23.17	-0.81
This paper	K	1785	2.2010	0.0156	-23.36	-0.96

† adjusted to effective filter rest wavelength for object at $z = 0.1$ (and then propagated through to the calculation of j and νf_ν).

‡ adjusted to $h = 1$.
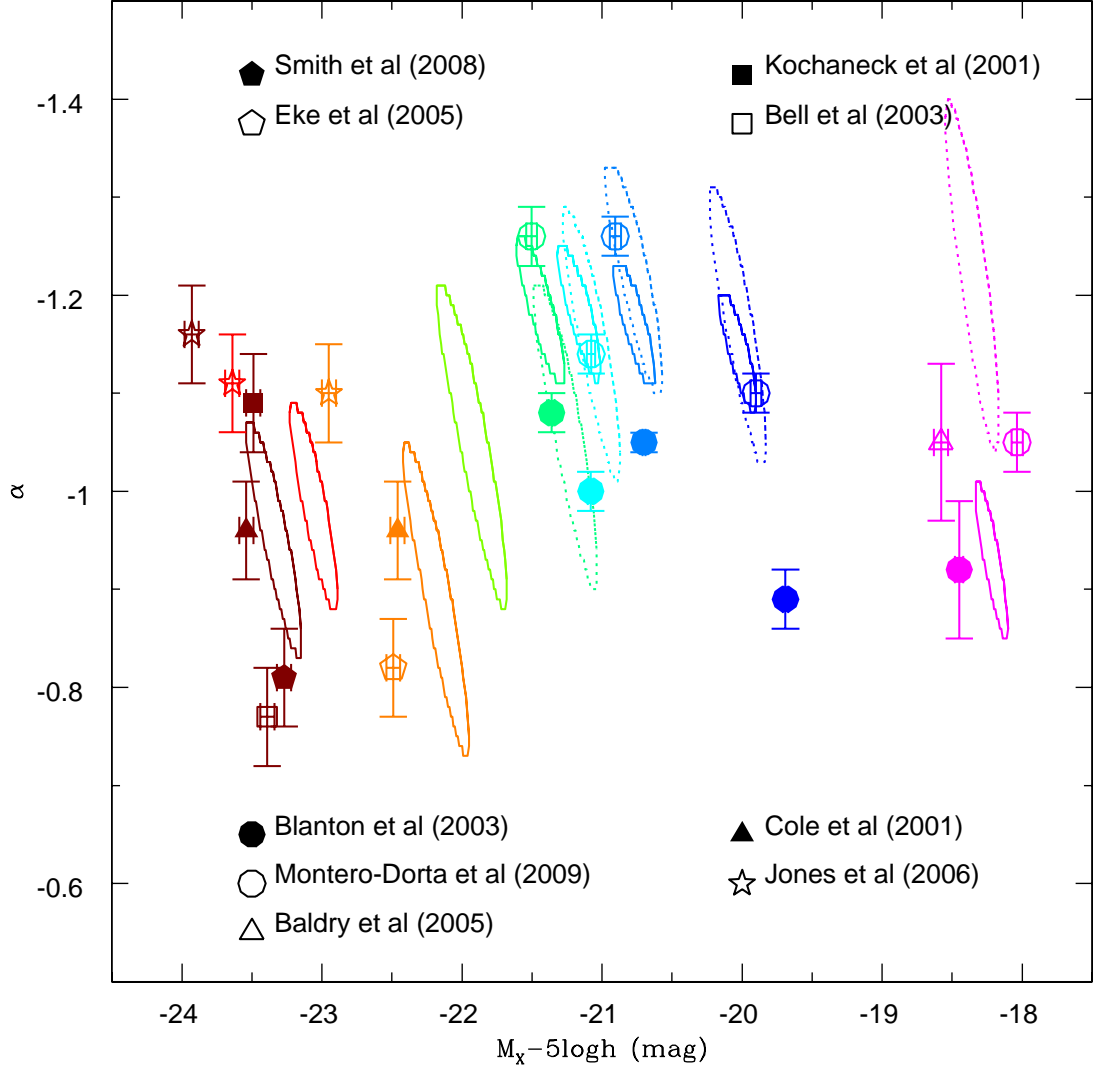
Figure 3.11: *ugrizYJHK* 1σ error contours for the LF fits from Fig. 3.10, with LF fits and α uncertainties from equivalent surveys. Dashed contours are from samples that have undergone the more conservative cuts introduced by Montero-Dorta et al.. SDSS equivalent survey points have been transformed from the filter system at $z = 0.1$ to the filter system at $z = 0$. Note that uncertainties due to K+E corrections are not included in the error contours, and they purely show the uncertainty in the chi-squared best fitting.

insufficient in size to enable a full bi-variate brightness analysis (e.g., Driver et al. 2005). However, Smith et al. (2009) have quantified the surface brightness limitations of the UKIDSS LAS data in the K-band. As the MGC-SDSS-UKIDSS dataset is based upon the same survey data as Smith et al., it is reasonable to adopt their K-band limit for completeness of $M_K - 5 \log_{10} h = -17.5 \, \text{mag}$. Using the mean colours indicated in Table. 3.2, the $YJHK$ luminosity distributions were re-derived within the revised magnitude range, with no significant alterations to the best-fitting Schechter parameters. Whilst surface brightness selection bias is a concern, the implication is that it is unlikely to be affecting the best-fitting function parametrisation. The best-fitting parameter selection is dominated by systems within the bright-end bins of the luminosity distribution.

3.4 The CSED points from the MGC-SDSS-UKIDSS sample

The total luminosity density (j) can be determined by integrating the Schechter function down to an infinitesimally faint luminosity (section 1.4.1). The MGC-SDSS-UKIDSS j and $\nu f(\nu)$ statistics are shown in Table 3.5, and values for previous surveys are in Table 3.6. Figure. 3.12 shows the position of the MGC-SDSS-UKIDSS total luminosity density values compared with previous measurements. The step-function seen between previous optical and NIR surveys is no longer markedly apparent (c.f. Figure 1.9, though there may be a slight deficit between z and Y, and the J point is noticeably diminished). This perhaps suggests that cosmic variance may indeed have played a part in this discrepancy. Generally, MGC-SDSS-UKIDSS data points are consistent with what has been published before but provide a relatively smooth distribution within a single survey. This suggests that constructing the CSED from within a single survey volume is critically important.

The MGC-SDSS-UKIDSS CSED values are subject to the effects of dust attenuation. Figure. 3.13 shows the pre- (lower) and post- (upper) attenuated values. In order to correct the cosmic SED for the effects of dust attenuation, the prescription laid out in Driver et al. (2008) is followed; this results in corrections of $\times 2.27$, $\times 1.69$, $\times 1.56$, $\times 1.47$, $\times 1.41$, $\times 1.35$, $\times 1.32$, $\times 1.22$, and $\times 1.15$ in u, g, r, i, z, Y, J, H, and K respectively (black, open symbols). Dust corrections calculated using the prescription laid out in Section 3.3 of Calzetti et al.
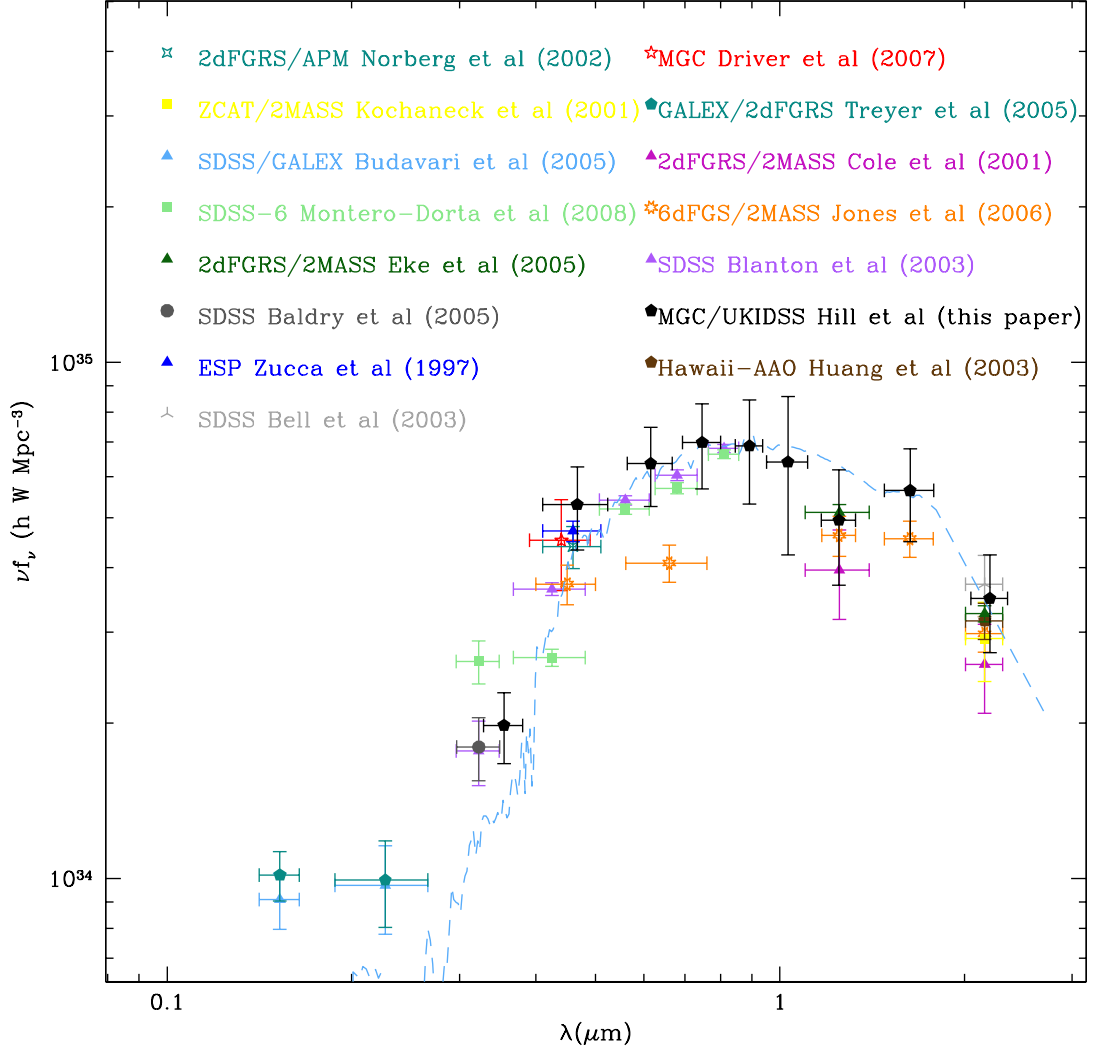
Figure 3.12: Cosmic energy output from 0.1 to 3 μm. The model line shows the SED of a 13.2Gyr Sa-type galaxy from the spectral template library of Poggianti (1997). Also shown are datapoints from Baldry et al. (2005), Bell et al. (2003), Blanton et al. (2003), Budavári et al. (2005), Cole et al. (2001), Driver et al. (2007), Eke et al. (2005), Jones et al. (2006), Huang et al. (2003), Kochanek et al. (2001), Montero-Dorta et al. (2008), Norberg et al. (2002), Treyer et al. (2005) and Zucca et al. (1997).

Table 3.5: Derived cosmic energy output parameters. Magnitude limits and magnitude system conversions are the same as Table 3.3.

Sample	$\mathbf{j}$ ($\times 10^8$ h $L_\odot$ Mpc^{-3})	νf_ν ($\times 10^{34}$ h W Mpc^{-3})	νf_ν (corrected, same units)
$u <20.84$	$1.91^{+0.24+0.15}_{-0.25-0.14}$	$1.98^{+0.25+0.15}_{-0.22-0.14}$	$4.50^{+0.57+0.35}_{-0.50-0.32}$
$g <19.81$	$2.17^{+0.33+0.17}_{-0.34-0.15}$	$5.31^{+0.80+0.41}_{-0.61-0.38}$	$8.97^{+1.35+0.68}_{-1.04-0.64}$
$r <18.76$	$2.29^{+0.37+0.14}_{-0.40-0.14}$	$6.35^{+1.03+0.40}_{-0.93-0.38}$	$9.91^{+1.60+0.62}_{-1.45-0.58}$
$i <18.34$	$2.66^{+0.47+0.13}_{-0.56-0.12}$	$6.99^{+1.25+0.33}_{-1.03-0.32}$	$10.3^{+1.83+0.49}_{-1.52-0.47}$
$z <18.07$	$3.07^{+0.68+0.12}_{-0.47-0.11}$	$6.89^{+1.53+0.26}_{-1.18-0.25}$	$9.71^{+2.16+0.37}_{-1.67-0.36}$
$Y <17.38$	$3.24^{+1.08+0.16}_{-0.93-0.15}$	$6.41^{+2.14+0.31}_{-1.66-0.30}$	$8.66^{+2.89+0.42}_{-2.24-0.40}$
$J <16.89$	$3.17^{+0.82+0.13}_{-0.72-0.12}$	$4.95^{+1.28+0.20}_{-1.04-0.19}$	$6.53^{+1.68+0.26}_{-1.38-0.25}$
$H <16.12$	$5.38^{+1.11+0.05}_{-0.99-0.05}$	$5.65^{+1.16+0.05}_{-0.95-0.05}$	$6.89^{+1.42+0.07}_{-1.16-0.07}$
$K <15.67$	$6.98^{+1.49+0.13}_{-1.44-0.13}$	$3.48^{+0.74+0.06}_{-0.65-0.06}$	$4.01^{+0.85+0.07}_{-0.74-0.07}$

(2000) are also shown; using $E_S(B - V) = 0.16$ (from the same paper), this results in corrections of $\times2.46$, $\times2.02$, $\times1.69$, $\times1.51$, $\times1.39$, $\times1.3$, $\times1.22$, $\times1.13$, and $\times1.06$ in u, g, r, i, z, Y, J, H, and K respectively (red, open symbols). Overlaid are three expectations derived by Stephen Wilkins (priv. comm) from various cosmic SFH+IMF combinations using the PEGASE code. The blue curve is based on the cosmic star-formation history (CSFH) assembled by Hopkins & Beacom (2006) from direct measurements reported in the literature but with a Salpeter IMF flattened below $0.5M_\odot$. The brown curve uses the same CSFH but adopts the best fitting IMF of Wilkins et al. (2008a), which has a high-mass slope slightly shallower than the typical Salpeter value (i.e., -2.15 rather than -2.35).

Both appear to be inconsistent with the MGC-SDSS-UKIDSS data, with the data fitting the blue curve in the optical and then tending towards the brown curve in the NIR. An intermediate solution could perhaps be found that would fit. The purple curve also adopts a Salpeter IMF, but with the cosmic star-formation history derived by Wilkins et al. (2008b). This is based on constraints from the evolution of the total stellar mass history and generally predicts a lower star-formation rate at higher redshift than reported in Hopkins & Beacom (2006). However, like the brown curve, the magenta curve fails to fit the data at shorter wavelengths.

In conclusion: the MGC-SDSS-UKIDSS CSED statistics are broadly consistent with the range of results reported in Wilkins et al. (2008a) and Wilkins et al. (2008b), and that refined measurements of the CSED should provide useful additional constraints on the CSFH and IMF. Such improvements should arise via the following measures:

1. A larger statistical sample

Table 3.6: Luminosity densities for optical and NIR surveys in the literature

Reference	Band	Sample Size	λ (μm)	j ($\times$ 10^8 h $L_\odot$ Mpc^{-3})	νf_ν (10^{34} h W Mpc^{-3})
Baldry et al. (2005)	$u^{0.1}$	43223	0.3224†	2.28	1.80
Blanton et al. (2003)	$u^{0.1}$	113988	0.3224†	2.24	1.77
Montero-Dorta et al. (2008)	$u^{0.1}$	159018	0.3224†	3.34	2.64
This paper	u	3267	0.3546	1.91	1.98
Blanton et al. (2003)	$g^{0.1}$	113988	0.4245†	1.75	3.63
Montero-Dorta et al. (2008)	$g^{0.1}$	256952	0.4245†	1.29	2.67
This paper	g	3328	0.4670	2.17	5.31
Blanton et al. (2003)	$r^{0.1}$	113988	0.5596†	1.85	5.39
Montero-Dorta et al. (2008)	$r^{0.1}$	466280	0.5596†	1.78	5.19
This paper	r	2781	0.6156	2.29	6.35
Blanton et al. (2003)	$i^{0.1}$	113988	0.6792†	2.11	6.03
Montero-Dorta et al. (2008)	$i^{0.1}$	461928	0.6792†	1.99	5.71
This paper	i	2623	0.7471	2.66	6.99
Blanton et al. (2003)	$z^{0.1}$	113988	0.8107†	2.71	6.81
Montero-Dorta et al. (2008)	$z^{0.1}$	422643	0.8107†	2.64	6.63
This paper	z	2437	0.8918	3.07	6.89
This paper	Y	1798	1.0305	3.24	6.41
Jones et al. (2006)	J	93841	1.250	2.97	4.62
Eke et al. (2005)	J	43553	1.250	3.29	5.11
Cole et al. (2001)	J	17173	1.250	2.53	3.94
This paper	J	1589	1.2483	3.17	4.95
Jones et al. (2006)	H	90317	1.644	4.34	4.52
This paper	H	1890	1.6313	5.38	5.65
Jones et al. (2006)	K	113988	2.198	5.86	2.93
Cole et al. (2001)	K	17173	2.198	5.20	2.60
Kochanek et al. (2001)	K	4192	2.198	5.46	2.89
Bell et al. (2003)	K	6282	2.198	5.58	2.79
Smith et al. (2009)	K	36663	2.198	6.22	3.11
This paper	K	1785	2.2010	6.98	3.48

† adjusted to effective filter rest wavelength for object at $z = 0.1$ (and then propagated through to the calculation of j and νf_ν).

2. Deeper NIR photometry

3. Matched photometry/deblended solutions across all filters

4. A full bi-variate brightness distribution to model the selection bias

5. More sophisticated modelling of the $K(z)$ and $E(z)$ corrections

The Galaxy And Mass Assembly Survey (GAMA) provides these improvements. In the following chapters, I will generate SDSS and UKIDSS photometry for the GAMA sample, and undertake a full bi-variate brightness distribution using this larger, deeper sample.
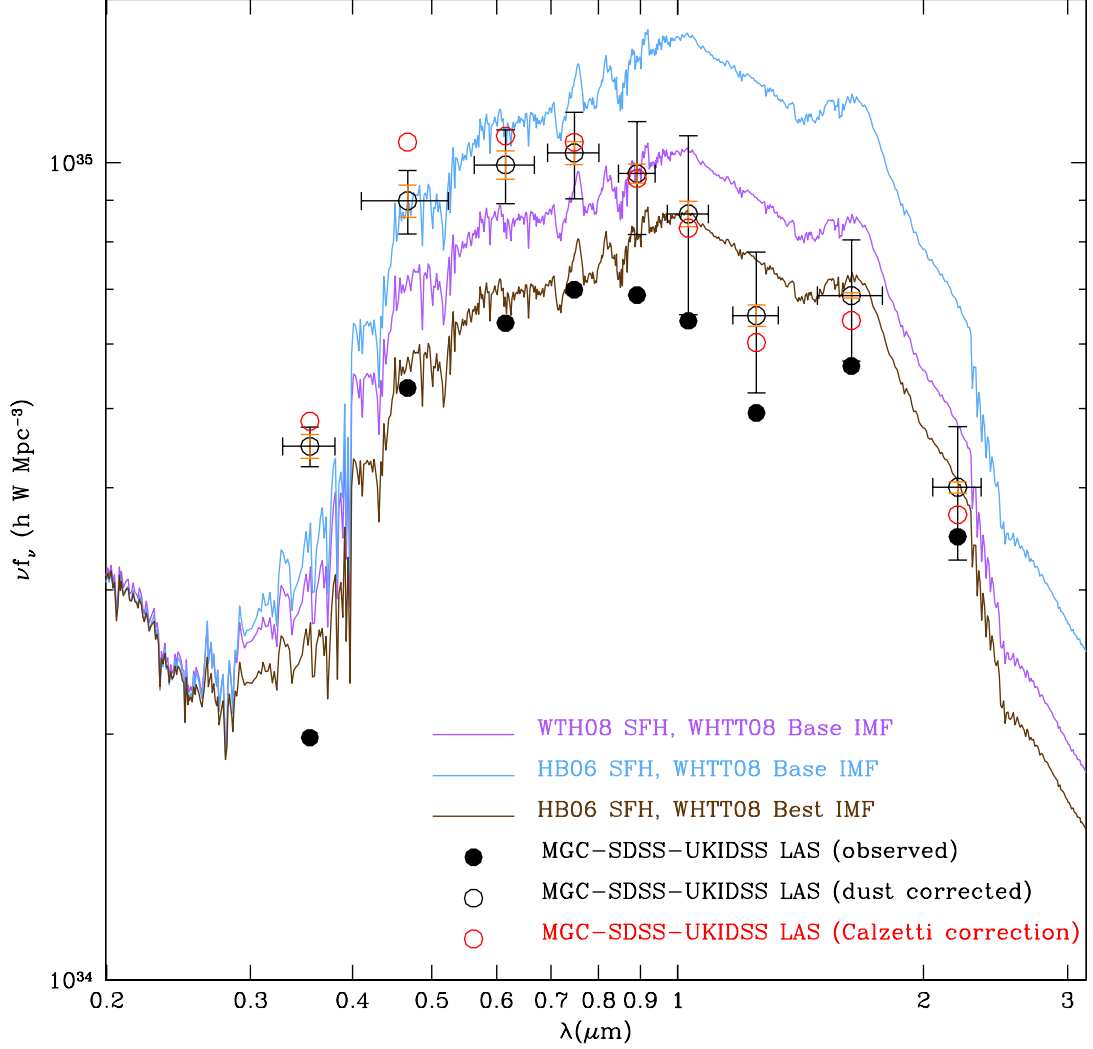
Figure 3.13: The cosmic spectral energy distribution as derived from the combined MGC-SDSS-UKIDSS LAS surveys compared to that expected from various cosmic star-formation history/initial mass function combinations as indicated (Wilkins priv. comm.). The blue model uses the canonical IMF shown in Equation 1.10 and a CSFH taken from FIR indicators in Hopkins & Beacom (2006). The brown model uses the canonical IMF shown in Equation 1.10, but with a flatter than Salpeter high mass slope ($\alpha = -2.15$), and a CSFH taken from FIR indicators in Hopkins & Beacom (2006). The purple curve using the canonical IMF shown in Equation 1.10, with a CSFH taken from the stellar mass indicators in Wilkins et al. (2008b). Solid symbols are the raw empirical data uncorrected for dust attenuation and open symbols are corrected for dust attenuation following Driver et al. 2008 (black), or Calzetti et al. 2000 (red). Errors are only shown for the Driver et al. data for clarity, and are split into two components; the black errorbars show the uncertainty due to chi-squared fitting, the orange errorbars show the uncertainty due to K and E corrections.

4

The GAMA $ugrizYJHK$ sample: Creation of the sample

In the previous chapter, I described the process undertaken to produce CSED datapoints from a combined MGC-SDSS-UKIDSS sample. I noted the refinements necessary to produce tighter constraints upon the CSFH and IMF. The GAMA survey provides some of these improvements. In this chapter, I detail the production of the GAMA photometric sample. The GAMA photometric sample provides self-consistent extended source photometry from SDSS and UKIDSS observations. I describe the construction of the large (Gigapixel scale) GAMA mosaics. I compare and contrast the photometric methods that are used to generate source catalogues from the GAMA imaging using the `SExtractor` object extraction utility and the `SIGMA` Galfit wrapper. I undertake analysis of the discrepancies between the `SExtractor` generated catalogues and those produced by the SDSS object extraction pipeline. I test the quality of the Sérsic magnitudes generated by the `SIGMA` package. Finally, I calculate the uncertainty within the photometry and the appar-

ent magnitude limits of the *ugrizYJHK* GAMA dataset.

The work within this chapter has been accepted by MNRAS, but has currently not been published. It is available on the arXiv (Hill et al., 2010b). The Sérsic photometric catalogue, and the entire software infrastructure behind `SIGMA` is the work of Lee Kelvin. I generated the mosaics, and the Kron and Petrosian catalogues, and undertook the comparison of the Sérsic catalogue to the other photometric samples. The matching of GAMA to Galex is the work of Aaron Robotham.

4.1 Consistent NIR and optical photometry

Consistently comparing observations between different surveys is a difficult task. Surveys make observations at different times of the year and with different atmospheric conditions, which causes zeropoint and seeing parameters to vary across the sky, and store their data as a series of smaller frames. When matching between surveys one may find an object in the centre of the frame in one survey is split across two frames in another survey. There may also be variation in the angular scale of a pixel between different instruments, and even when two instruments have the same pixel size, a shift of half of a pixel between two frames can cause significant difficulties in calculating colours for small, low surface brightness objects. The GAMA survey aims to circumvent these difficulties by creating Gigapixel scale mosaics with a common zeropoint and consistent WCS calibration. The construction process is outlined within this section.

To generate the image mosaics, the Terapix `SWARP` (Bertin et al., 2002) utility is used. This is a mosaic generation tool, and how it is utilised is described in subsection 4.1.4. First, the data must be transformed to take into account differences in sky conditions and exposure times between observations. For every image, the current zeropoint must be ascertained (see the distribution in Figure 4.1), and the image transformed to a defined standard. This process is described in subsections 4.1.1 and 4.1.2.

4.1.1 UKIDSS: Acquisition of data and renormalisation to a common zeropoint

UKIDSS imaging is stored within the WFCAM Science Archive (WSA). 862 Y, 883 J, 931H and 928 K band compressed UKIDSS-LAS fits files were downloaded, each containing observations of the GAMA regions. These files were decompressed using the `imcopy`
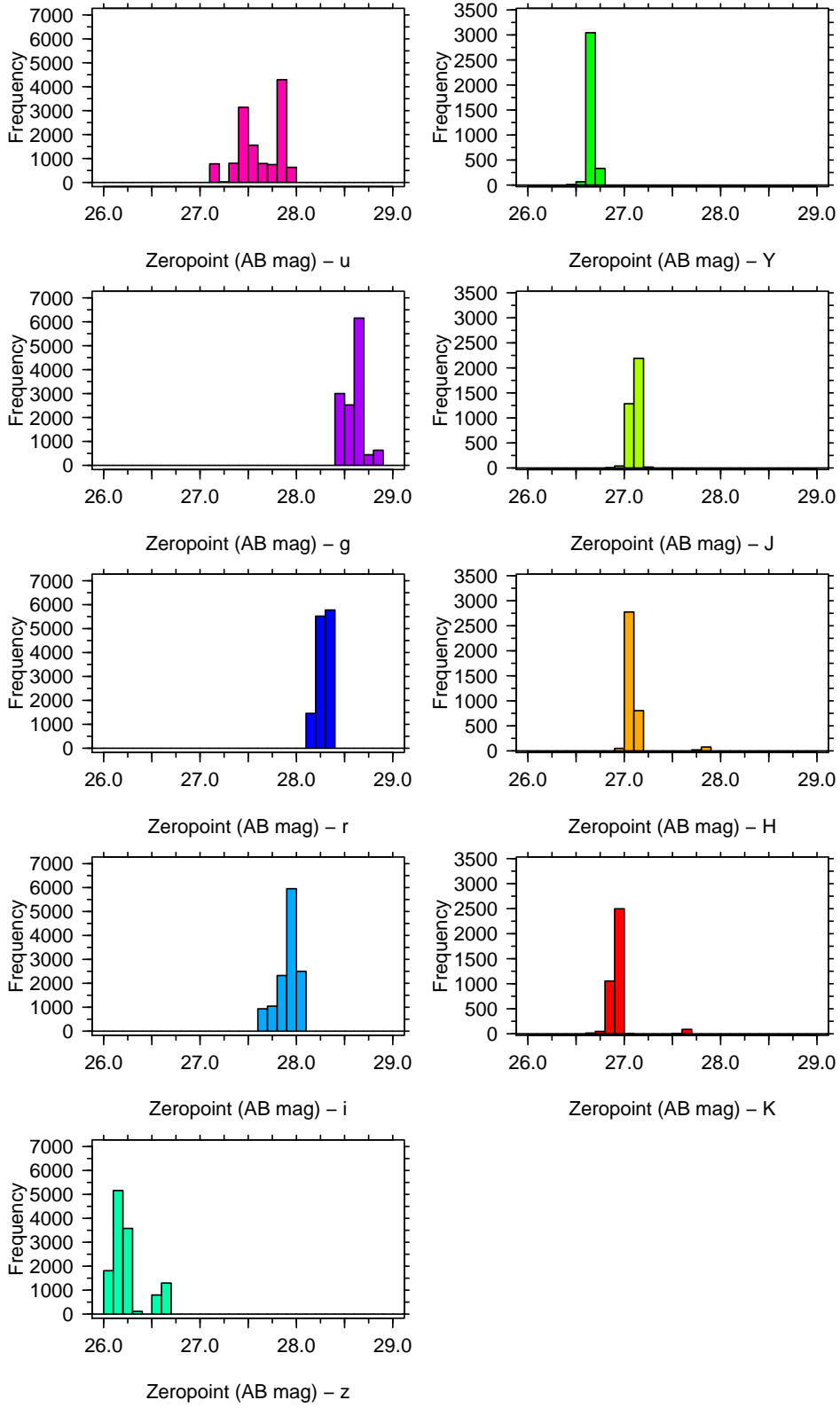
Figure 4.1: A histogram of the calculated total zeropoints for the fields used to create the master region mosaics.

Band	AB offset (mag)
u	-0.04
g	0
r	0
i	0
z	+0.02
Y	0.634
J	0.938
H	1.379
K	1.900

Table 4.1: Conversion to AB magnitudes. The SDSS photometric system is roughly equivalent to the AB magnitude system, with only small offsets in the u and z passbands. UKIDSS photometry is calculated on the Vega magnitude system, and conversions are from Hewett et al. (2006). Whilst UKIDSS data is converted using a high precision parameter, it should be noted that the conversion uncertainty is only known to $\sim \pm 0.02$ mag (Cohen et al., 2003).

utility. The files for each band are stored and treated separately.

A specially designed pipeline accesses each file, reads the *MAGZPT* (ZP_{mag}), *EXP_TIME* (t), airmass ($0.5 * (AMSTART + AMEND) = \sec\chi_{\mathrm{mean}}$) and *EXTINCT* (Ext) keywords from the fits header and creates a total AB magnitude zeropoint for the file using Equation 4.1.

$$ZP_{\mathrm{total}} = ZP_{\mathrm{mag}} - 2.5\log(\frac{1}{t}) - \mathrm{Ext} \times (\sec\chi_{\mathrm{mean}} - 1) + \mathrm{ABV_X} \tag{4.1}$$

where ABV_X is the AB magnitude of Vega in the X band (Table 4.1).

To correct each frame to a standard zeropoint (30), the value of each pixel is multiplied by a factor, calculated using Equation 4.2. Whilst the distribution of frame zeropoints is shown in Figure 4.1 in bins of 0.1 mag, the actual zeropoint of each frame is used to calculate the total AB magnitude zeropoint. This has a far smaller variation (e.g., ± 0.02 mag in photometric conditions in the JHK filters; Warren et al. 2007).

$$\mathrm{pixelmodifier} = 10^{-0.4(\mathrm{ZP_{total}} - 30)} \tag{4.2}$$

A new file is created to store the corrected pixel table, and the *MAGZPT* fits header parameter is updated. The *SKYLEVEL* and *SKYNOISE* parameters are then scaled using the same multiplying factor.

4.1.2 SDSS: Acquisition of data and renormalisation to a common zeropoint

The tsField and fpC files for the 12757 SDSS fields that cover the GAMA regions were downloaded from the SDSS data archive server (*das.sdss.org*) for all five passbands. Again, the files for each passband are stored and treated separately.

A specially designed pipeline brings in the *aa* (zeropoint), *kk* (extinction coefficient) and *airmass* keywords from a field's tsField file, and the *EXPTIME* (*t*) keyword from the same field's fpC file. Combining these using Equation 4.3, the current total AB magnitude zeropoint of the field (ZP_{total}) is calculated:

$$ZP_{\text{total}} = -aa - 2.5\log(1/\text{t}) - \text{kk} \times \text{airmass} + \text{sAo} \tag{4.3}$$

where *sAo* is the offset between the SDSS magnitude system and the actual AB magnitude system ($-0.04\,$mag for *u*, $0.02\,$mag for *z*, otherwise 0). The SDSS photometric zeropoint uncertainty is estimated to be no larger than $0.03\,$mag in any band (Ivezić et al., 2004). The multiplier required to transform every pixel in the field is calculated (using Equation 4.2) to a standard zeropoint (30). As every pixel must be modified by the same factor, the `fcarith` program (part of the `Ftools` package) is utilised, to multiply the entire image by pixelmodifier. In a small number of fields (249/12757), the WCS calibration has been set up so that the Right Ascension and Declination axes are mapped to nonstandard axes (whilst the Right Ascension/Declination to row/column mapping is not orthogonal, Right Ascension is usually mapped to the image row and Declination to the image column). The `SWARP` utility does not deal with this alteration correctly. To rectify this problem the axes of the affected images are flipped back to the conventional mapping and the image header parameters modified to correct for this alteration. Each transformed field is stored in a new file, and this new set of files is used to create the GAMA mosaics.

4.1.3 Correction of seeing bias

As observations were taken in different conditions there is an intrinsic seeing bias between different input images, and between different filters (Figure 4.2). This could cause inaccuracies in photometric colour measurements that use apertures defined in one filter to
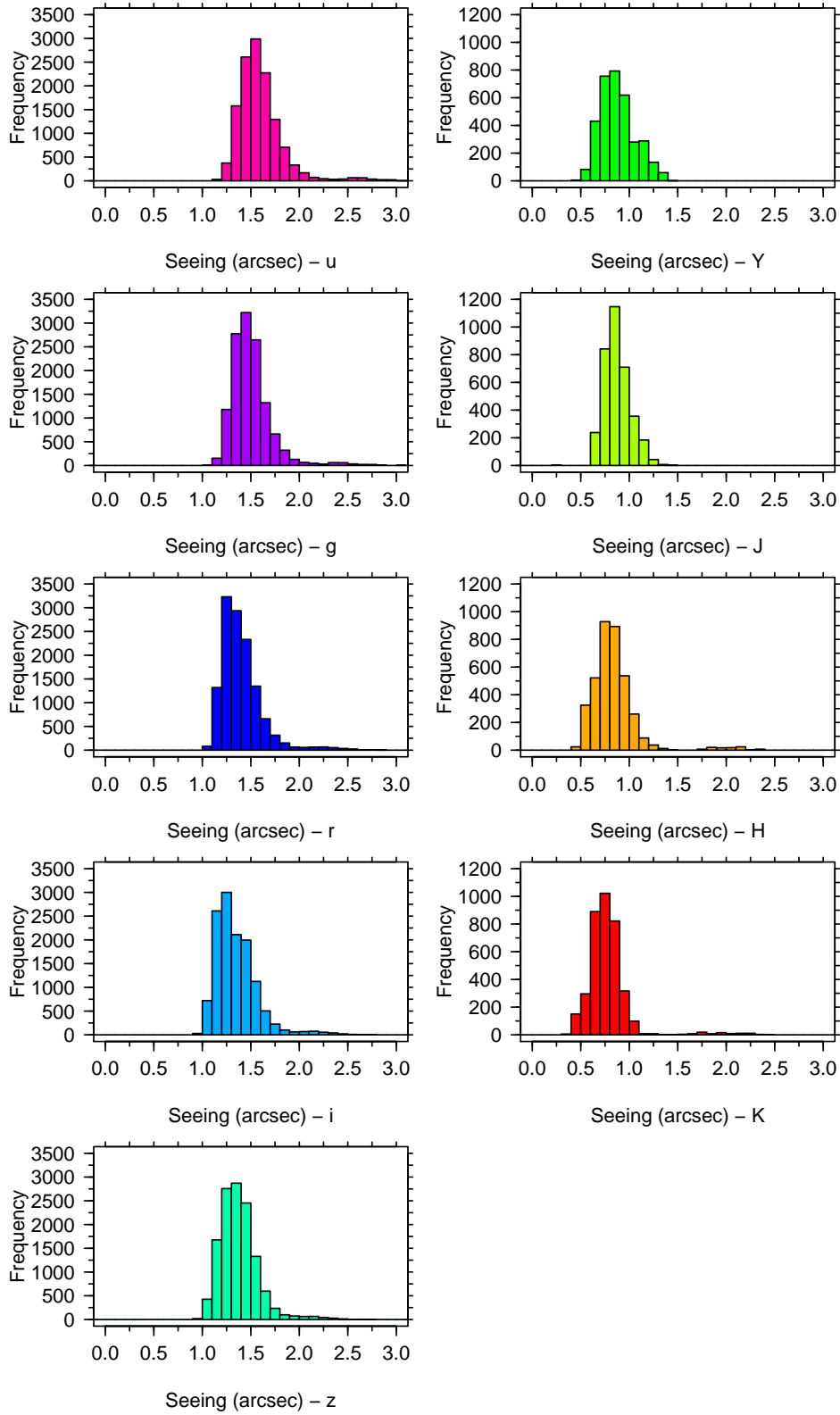
Figure 4.2: A histogram of the calculated seeing of the fields used to create the master region mosaics.

derive magnitudes in a second filter. To rectify this problem, it is necessary to degrade the better quality images to a lower seeing. However, if images were degraded to the lowest quality seeing (3.12 arcsec), the ability to resolve the smallest galaxies in the sample would be lost. The normalised images are therefore degraded to 2 arcsec seeing. The fraction of images with seeing worse than 2 arcsec is 4.4%, 2.7%, 2.5%, 2.1%, 1.7%, 0%, 0%, 1.3% and 0.9% in u, g, r, i, z, Y, J, H and K, respectively. Images with worse seeing than 2 arcsec are included in the degraded seeing mosaics. No attempt is made to modify their seeing. Although each survey uses a different method of calculating the seeing within their data (SDSS use a double Gaussian to model their PSF, UKIDSS use the average FWHM of the stellar sources within the image), it is assumed that the seeing provided for every frame is correct.

To achieve a final PSF FWHM of 2 arcsec (σ_{final}) it is assumed that the seeing within an image follows a perfect Gaussian distribution, $\sigma_{initial}$. Theoretically, a Gaussian distribution can be generated from the convolution of two Gaussian distributions. The `fgauss` utility (also part of the `ftools` package) can be used to convolve an input image with a circular Gaussian with a definable standard deviation (σ_{req}), calculated using Equation 4.4 (the full derivation of this relation is shown in Appendix A).

$$\sigma_{req} = \sqrt{(\frac{\text{FWHM}_\text{d}}{2\sqrt{2\ln 2}})^2 - (\frac{\text{FWHM}_\text{image}}{2\sqrt{2\ln 2}})^2} \tag{4.4}$$

As each UKIDSS frame has a different seeing value, it is necessary to break each fits file into its four constituent images. This is not necessary for SDSS images (which are stored in separate files). However, it is necessary to retrieve the SDSS image seeing from the image's tsField file. The SDSS image seeing is stored in the *psf_width* column of the tsField file. Where an image has a seeing better than the specified value, the `fgauss` utility is used to convolve the image to the specified value. Where an image has a seeing worse than the specified value, the image is copied without modification using the `imcopy` utility. Both utilities produce a set of UKIDSS files containing two HDUs: the original instrument header HDU and a single image HDU with seeing greater than or equal to the specified seeing. The output SDSS files contain just a single image HDU.

4.1.4 Creation of master region images

The `SWARP` utility is a multi-thread capable co-addition and image-warping tool that is part of the Terapix pipeline (Bertin et al., 2002). `SWARP` is used to generate complete images of the GAMA regions from the normalised LAS/SDSS fits files. It is vital that the pixel size and area of coverage is the same for each filter, as `SExtractor`'s dual-image mode requires perfectly matched frames. A pixel scale of 0.4×0.4 arcsec is defined, and 117000×45000 pixel files centred around 09h00m00.0s, $+01\text{d}00'00.0''$ (GAMA 9), 12h00m00.0s, $+00\text{d}00'00.0''$ (GAMA 12), and 14h30m00.0s, $+00\text{d}00'00.0''$ (GAMA 15) are generated. `SWARP` is set to resample input frames using the default LANCZOS3 algorithm, which the Terapix team found was the optimal option when working with images from the Megacam instrument (Bertin et al., 2002).

`SWARP` produces mosaics that use the TAN WCS projection system. As UKIDSS images are stored in the ZPN projection system, `SWARP` internally converts the frames to the TAN projection system. There is also an astrometric distortion present in the UKIDSS images that `SWARP` corrects using the *pv2_3*, *pv2_1*, *crpix1*, *crpix2*, *cd1_1*, *cd1_2*, *cd2_1* and *cd2_2* fits header parameters[1].

`SWARP` is set to subtract the background from the image, using a background mesh of 256×256 pixels (102×102 arcsec) and a back filter size of 3×3 to calculate the background map. The background calculation follows the same algorithm as `SExtractor` (Bertin & Arnouts, 1996). To summarise: it is a bicubic-spline interpolation between the meshes, with a median filter applied to remove bright stars and artefacts.

Every mosaic contains pixels that are covered by multiple input frames. `SWARP` is set to use the median pixel value when a number of images overlap. The effects of outlying pixel values, due to cosmic rays, bad pixels or CCD edges, should therefore be reduced. `SWARP` generates a weight map (Figure 4.3) that contains the flux variance in every pixel, calibrated using the background map described above. As the flux variance is affected by overlapping coverage, it is possible to see the survey footprint in the weight map. The weight map can be used within `SExtractor` to compensate for variations in noise. It is not used when calculating the GAMA photometry, for two reasons. Firstly, there is overlap between SDSS fpC frames. This overlap is not from observations, but from the method

---

[1]An analysis of the astrometric distortion can be found in CASU document VDF-TRE-IOA-00009-0002 , currently available from http://www.ast.cam.ac.uk/vdfs/docs/reports/astrom/index.html

used to cut the long SDSS stripes into sections (see Chapter 2). `SWARP` would not account for this, and the weighting of the overlap regions on the optical mosaics would be calculated incorrectly. Secondly, using the weight maps would alter the effect of mosaic surface brightness limit variations upon the output catalogues. As surface brightness effects will be modelled later, an unweighted photometric catalogue is preferable.

A small number of objects will be split between input frames. `SWARP` can reconstruct them, with only small defects due to CCD edges. One such example is shown in Figure 4.4. Both seeing-corrected and uncorrected mosaics are created for each passband and region combination. Each file is 20Gb in size. In total, the mosaics require just over 1 Terabyte of storage space.

4.2 Photometry

A major problem with constructing multi-wavelength catalogues is that the definition of what constitutes an object can change across the wavelength range (see Appendix B, particularly Figure B.1). This can be due to internal structure such as dust lanes or star forming regions becoming brighter or fainter in different passbands, causing the extraction software to deblend an object into a number of smaller parts in one filter but not in another. This can lead to large errors in the resulting colours. It is not certain that the SDSS object extraction process will produce the same results as the extraction process used to create the UKIDSS object catalogues. Seeing, deblending and aperture sizes will differ, compromising colours. To create a consistent multi-wavelength sample, the photometry needs to be recalculated consistently across all 9 filters. At the same time, it is possible to move from the circular apertures of SDSS and UKIDSS to full elliptical apertures, as well as investigate a variety of photometric methods. The source catalogues are generated using the `SExtractor` software (Bertin & Arnouts, 1996). This is an object extraction utility, and its use is described in subsection 4.2.5.

Four different methods are used to define object positions and apertures. Three `SExtractor` catalogues (Bertin & Arnouts, 1996) are produced, and one Sérsic catalogue (based upon `GALFIT 3`, Peng et al. 2007), in addition to the original SDSS dataset. The generation of the three new `SExtractor` catalogues is detailed in section 4.2.5. Each of the new `SExtractor` catalogues contain magnitudes calculated using two different elliptical, ex-
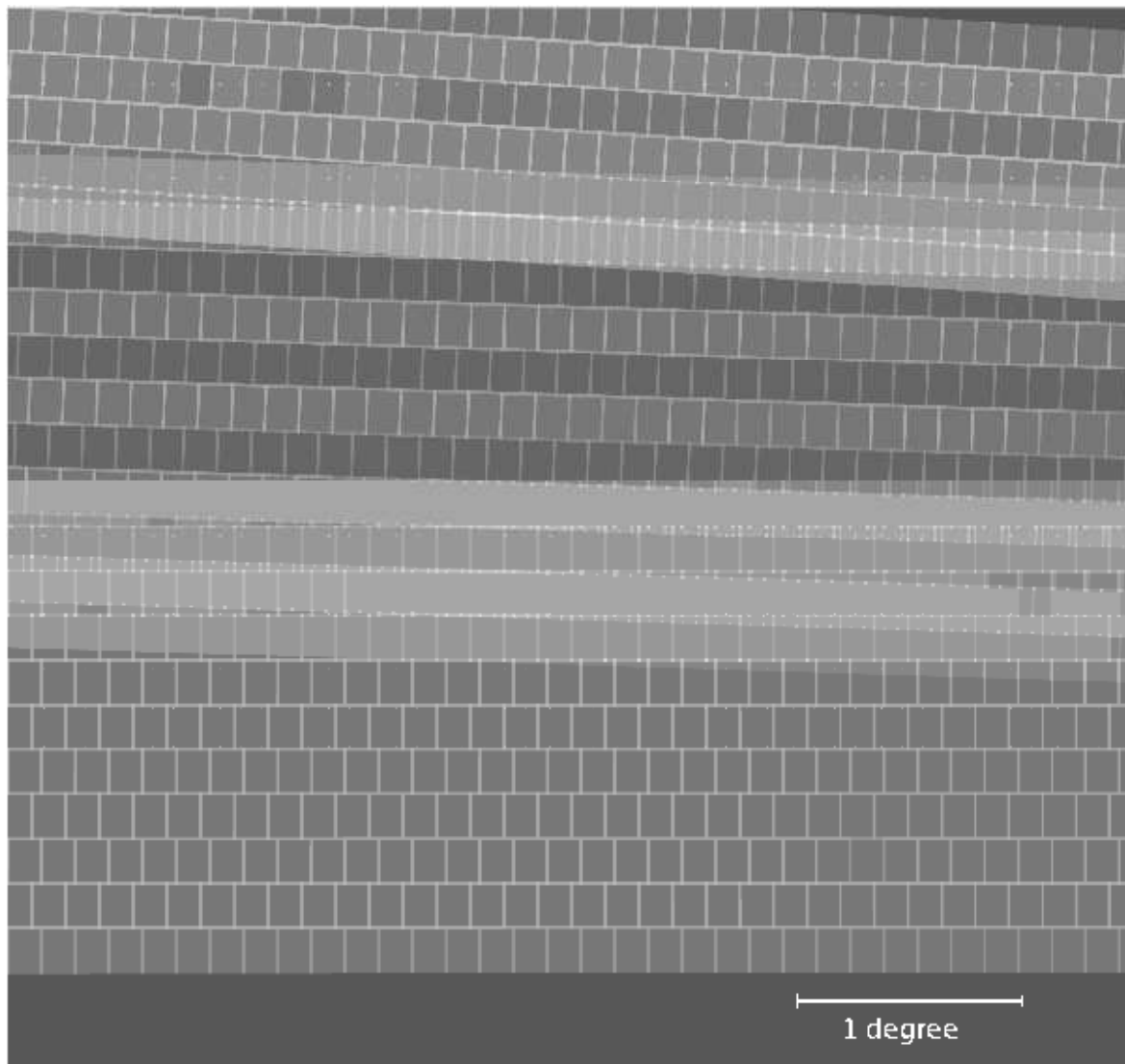
Figure 4.3: The *r* band weightmap of the 45000x45000 pixel subset region (5x5 deg; defined in Section 4.3). Joins and overlap between frames are apparent (light grey). The mosaic does not have imaging of the top right corner or the bottom section (dark grey). These areas lie outside the region of interest as the mosaics are slightly larger in Declination than the GAMA regions themselves.
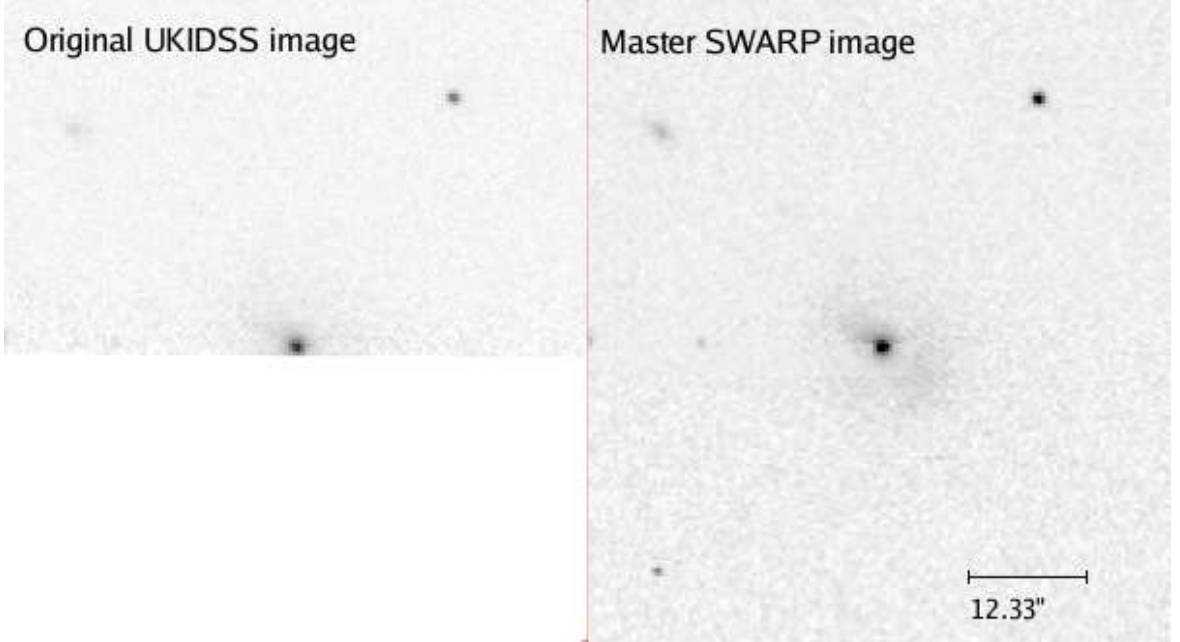
Figure 4.4: A comparison between the original normalised image and the K band mosaic image of a galaxy on the bottom edge of an input UKIDSS frame. The bottom section of the galaxy is not part of this image and it has been stitched together on the mosaic using `SWARP`.

tended source apertures: the Kron and the Petrosian magnitude systems. They are briefly described in sections 4.2.1, 4.2.2 and 4.2.3. A specially designed pipeline (`SIGMA GAMA`, Kelvin et al. 2010, based upon `GALFIT 3`) is used to calculate a total magnitude for each galaxy via its best fitting Sérsic profile. This aperture system, and the process used to generate it, is described in Sections 4.2.4 and 4.2.6.

It is not obvious which photometric method will produce the optimal solution. Whilst the Sérsic photometric method solves the missing light problem (the Petrosian and Kron magnitude systems do not account for the light emitted by a galaxy outside of the aperture, producing a systematic underestimation of the actual luminosity of a galaxy), it requires high quality data to calculate the set of parameters that best model the galactic light profile. The Kron and Petrosian magnitude systems will work with lower quality data, but may underestimate the flux produced by a galaxy. In this section I describe the photometric systems that are used. Later, in sections 4.4 and 5.1, I will examine the different results produced by the choice of the photometric system.

4.2.1   Self defined Kron and Petrosian apertures

An *independent* catalogue was constructed for each filter, containing elliptical Kron and Petrosian apertures. These independent catalogues were then matched across all 9 wave-

bands using `STILTS` (see section 4.2.7 and Taylor 2006). The apertures will therefore vary in size, potentially giving inconsistent colours, and as deblending decisions will also change, inconsistent matching between catalogues may occur. However, as the apertures are defined from the image they are used on, there can be no problem with magnitudes being calculated for objects that do not exist, or with missing objects that are not visible in the r band.

The self-defined catalogues are generated from the basic mosaics, where no attempt to define a common seeing for the mosaic has been made. This method should generate the optimal list of sources in each band; however, as the precise definition of the source will vary with wavelength, the colours generated using this method will be inaccurate and subject to aperture bias. As the mosaic has variations in seeing, the PSF will also vary across the image.

4.2.2   r band defined Kron and Petrosian apertures

`SExtractor` is used to define a sample of sources in the r band image, and then use the r band position and aperture information to calculate their luminosity within each filter (using the `SExtractor` dual image mode). As the aperture definitions do not vary between wavebands this method gives internally consistent colours, and as the list itself does not change source matching between filters is unnecessary. However, where an object has changed in size (see Appendix B), does not exist (e.g. an artefact in the r band sample) or when the r band aperture definition incorrectly includes multiple objects the output colours may be compromised. Any object that is too faint to be visible within the r band mosaic will also not be detected using this method. However, such objects will be fainter than the GAMA sample's selection criteria, and would not be included within the GAMA sample. The r band-defined catalogues are generated from the seeing-degraded mosaics. They provide an optically-defined source sample.

This method is analogous to the SDSS source catalogues, which define their apertures using the r passband data (unless the object is not detected in r, in which case a different filter is chosen). However, the GAMA photometric pipeline has a broader wavelength range as it now includes NIR measurements from the same aperture definition. Furthermore, the SDSS Petrosian magnitudes have not been seeing-standardised. While all data is taken at the same time, the diffraction limit is wavelength dependent and different fractions of light

will be missed despite the use of a fixed aperture. SDSS model magnitudes do account for the effects of the PSF.

4.2.3   K band defined Kron and Petrosian apertures

This method works in the same way as the previous method, but uses the K band image as the detection frame rather than the r band image. The total area is limited, as the K band coverage is incomplete. However, for samples that require complete colour coverage in all 9 filters, this is not a problem. As with r band-defined catalogues, the K band-defined catalogues are generated from the seeing-corrected mosaics. They provide a NIR-defined source sample. The K-band defined Kron magnitudes were used in the GAMA input catalogue (Baldry et al., 2010) to calculate the star-galaxy separation $J - K$ colour and the K band target selection.

4.2.4   Sérsic apertures

The `SIGMA` modelling wrapper (see section 4.2.6 and Kelvin et al. 2010 for more details), which is based upon the galaxy fitting software `GALFIT` 3.0 (Peng et al., 2007), was used to fit a single-Sérsic component to each object independently in 9 filters ($ugrizYJHK$), and recover their Sérsic magnitudes, indices, effective radii, position angles and ellipticities. Source positions are initially taken from the GAMA input catalogue, as defined in Baldry et al. (2010). All Sérsic magnitudes are self-defined; as each band is modelled independently of the others, the aperture definition will vary and colour may therefore be compromised.

Single-Sérsic fitting is comparable to the SDSS model magnitudes. `SIGMA` therefore should recover total fluxes for objects that have a Sérsic index in the range $0.3 < n < 20$, where model magnitudes force a fit to either an exponential (n=1) or deVaucouleurs (n=4) profile. The systematic magnitude errors that arise when model magnitudes are fit to galaxies that do not follow an exponential or deVaucouleurs profile (Graham, 2001; Brown et al., 2003) do not occur in `SIGMA`. The SDSS team developed a composite magnitude system, CMODEL, that calculates a magnitude from the combination of the n=1 and n=4 systems, in order to circumvent this issue (Abazajian et al., 2004). CMODEL magnitudes are compared to the Sérsic magnitudes later. Sérsic magnitudes do not suffer from the missing-flux issue that affects Kron and Petrosian apertures. Petrosian magnitudes may

underestimate a galaxy's luminosity by 0.2 mag (Strauss et al., 2002), while under certain conditions a Kron aperture may only recover half of a galaxy's total luminosity (Andreon, 2002). The Sérsic catalogues are generated from the seeing-uncorrected mosaics, as the seeing parameters are modelled within `SIGMA` using the `PSFEx` software utility (E. Bertin, priv. comm).

4.2.5 Object Extraction of Kron and Petrosian apertures

The `SExtractor` utility (Bertin & Arnouts, 1996) is a program that generates catalogues of source positions and aperture fluxes from an input image. It has the capacity to define the sources and apertures in one frame and calculate the corresponding fluxes in a second frame. This dual image mode is computationally more intensive than the standard `SExtractor` single image mode. Using the u, g, r, i, z, Y, J, H and K images created by the `SWARP` utility, a catalogue of sources is defined independently (for the self-defined catalogues), using the r band mosaics (for the r band-defined catalogue) or the K band mosaics (for the K band-defined catalogue) and their flux is calculated in all nine bands. The normalisation and `SWARP` processes removed the image background and standardised the zeropoint; therefore a constant *MAG_ZEROPOINT=30*, and *BACK_VALUE=0* is used. `SExtractor` generates both elliptical Petrosian (2.0 R_{Petro}) and Kron-like apertures (2.5 R_{Kron}, called *AUTO* magnitudes). `SExtractor` Petrosian magnitudes are computed using $\frac{1}{\nu_{RPetro}} = 0.2$, the same parameter as SDSS. As the mosaics have been transformed onto the AB magnitude system, all magnitudes generated by the GAMA photometric pipeline are AB magnitudes. The `SExtractor` default detection filter was used.

The seeing convolution routine smooths out the background and correlates the read noise of the images (this is apparent in Figure. B.1). As `SExtractor` detects objects of $> x\sigma$ above the background (where x is a definable parameter, set to 1 in the default file and for the seeing unconvolved catalogues), this assists the detection process, allowing `SExtractor` to find objects to a much greater depth, thus increasing the number of sources extracted using the standard setup. However, these new objects are generally much fainter than the photometric limits of the GAMA spectroscopic campaign, many are false detections, and the time required to generate the source catalogues (particularly using `SExtractor` in dual image mode) is prohibitively large. Using a 10000x10000 pixel subset of the GAMA9 r band mosaic, the *DETECT_THRESH* parameter that would output a cata-
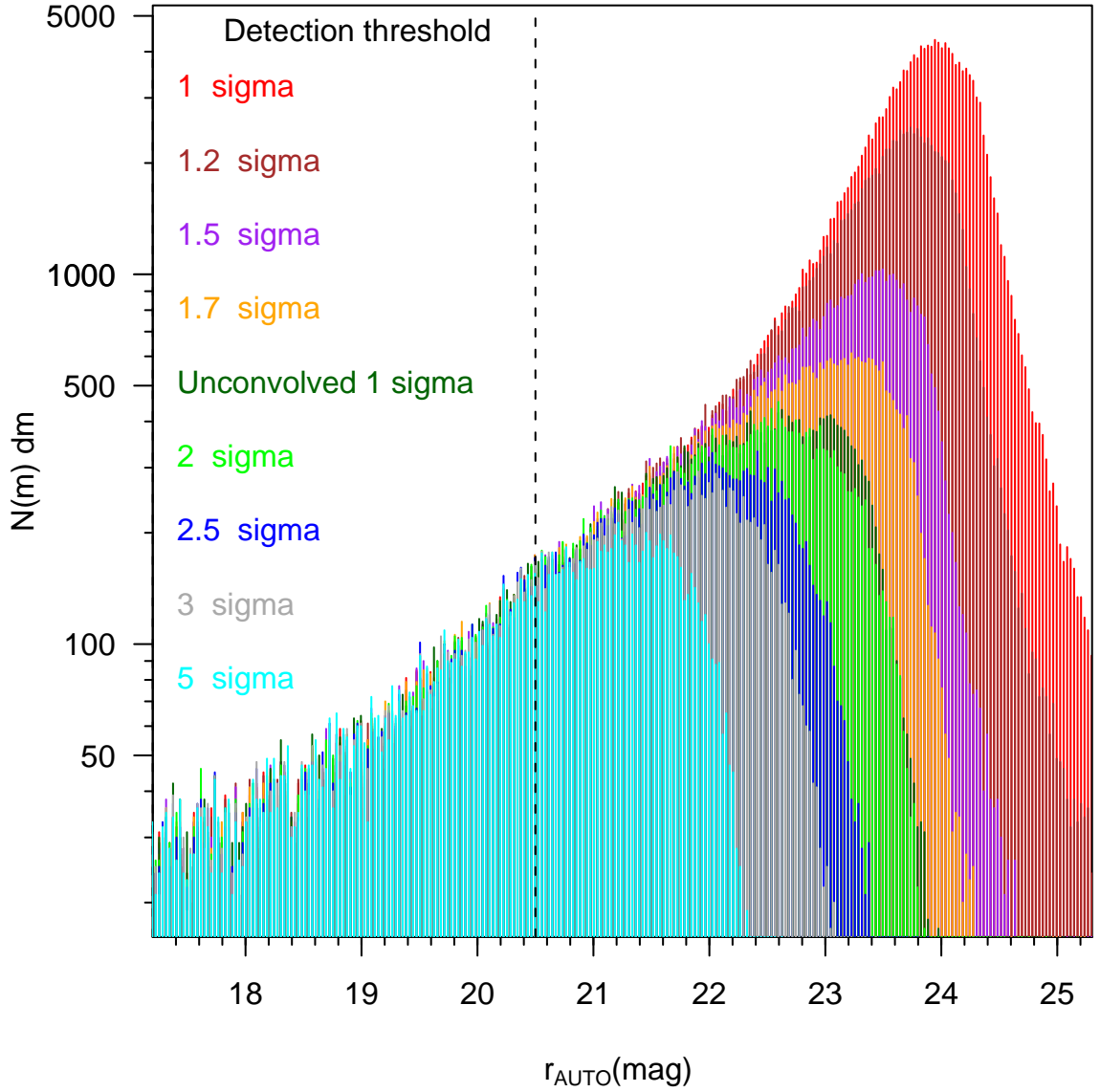
Figure 4.5: The effects of changing the SExtractor *DETECT_THRESH* parameter on a subset of a *r* band mosaic. The dotted black line is the *r* band sample limit of the GAMA survey.

logue of approximately the same depth and size as the unconvolved catalogue within the spectroscopic limits (see section 2.4) was calculated. The distribution of objects with different *DETECT_THRESH* sigma parameters, compared to the unconvolved catalogue, is shown in Figure 4.5. A *DETECT_MINAREA* of 9 pixels is used. As the unconvolved catalogue is slightly deeper than the 2σ, but not as deep as the 1.7σ convolved catalogue, a *DETECT_THRESH* parameter of 1.7σ is used to generate the convolved catalogues. The 1.7σ and 1σ catalogues have consistent number counts to $r_{\text{auto}} = 21$ mag; half a magnitude beyond the r_{SDSS} band magnitude limit of the GAMA input catalogue.

4.2.6 Object extraction for Sérsic magnitudes

Sérsic magnitudes are obtained as an output from the galaxy modelling package `SIGMA` (Structural Investigation of Galaxies via Model Analysis). `SIGMA` is an automating-wrapper to the `GALFIT` 3.0 galaxy decomposition package. For full details of the `SIGMA` modelling program, see Kelvin et al. (2010). The specific working of this package constitutes no part of this thesis, and the following work relies on the proviso that the results it outputs are as accurate an estimation of the Sérsic magnitude as it is possible to make, given the resolution and quality of the imaging.

4.2.7 Catalogue matching

The definition of the GAMA spectroscopic target selection (herein referred to as the tiling catalogue) is detailed in Baldry et al. (2010), and is based on original SDSS DR6 data. The revised photometry must be attached to this catalogue in order to connect it to the AAOmega spectra. The tiling catalogue utilises a mask around bright stars that should remove most objects with bad photometry and erroneously bright magnitudes, as well as implementing a revised star-galaxy separation quantified against the spectroscopic results. It has been extensively tested, with sources that are likely to be artefacts, bad deblends or sections of larger galaxies viewed a number of times by different people. By matching the matched-photometry catalogues to the tiling catalogue, the results of this rigorous filtering process are accessed, and a full, self-consistent set of colours for all of the objects that are within the GAMA sample are generated (if the object is within a region that has been observed in all nine passbands). As the tiling catalogue is also used when redshift targeting, the completeness in all the passbands of the GAMA survey is calculable. The GAMA tiling catalogue is a subset of the GAMA master catalogue (herein referred to as the master catalogue). The master catalogue is created using the SDSS DR6 catalogue stored on the CAS[2]. Unlike the master catalogue, the tiling catalogue undertakes star-galaxy separation, and applies surface brightness and magnitude selections.

`STILTS` (Taylor, 2006) is a catalogue combination tool, with a number of different modes. It is used to join the region catalogues together to create *r*-defined, *K*-defined and self-

---

[2]Using the query SELECT * FROM dr6.PhotoObj as p WHERE (p.modelmag_r - p.extinction_r < 20.5 or p.petromag_r - p.extinction_r < 19.8) and ((p.ra > 129.0 and p.ra < 141.0 and p.dec > -1.0 and p.dec < 3.0) or (p.ra > 174.0 and p.ra < 186.0 and p.dec > -2.0 and p.dec < 2.0) or (p.ra > 211.5 and p.ra < 223.5 and p.dec > -2.0 and p.dec < 2.0)) and ((p.mode = 1) or (p.mode = 2 and p.ra < 139.939 and p.dec < -0.5 and (p.status & dbo.fphotostatus('OK_SCANLINE')) > 0))

defined aperture photometry catalogues that cover the entire GAMA area. It is also used to match these catalogues to the GAMA tiling catalogue.

The matched-photometry catalogues are matched to the GAMA tiling catalogue with a centroid tolerance of 5 arcsec, using the STILTS *tskymatch2* mode. *tskymatch2* is run using the flags $join = 1 and 2$, $find = best$ and $error = 5$; this finds the best match within 5 arcsec and outputs only those objects that have a match in both datasets (5 arcsec is chosen following experience with the previous version of the extraction pipeline; it should be noted that any objects within 2 arcsec will be within the same fibre when spectra are retrieved using the AAO instrument).

In order to generate the self-defined catalogue, the *tcat* mode is used to generate a set of self-defined aperture samples for each filter that cover the entire GAMA region. The *tskymatch2* mode is then used (with the same parameters used to create the matched-aperture matched catalogues) to combine each filter to the GAMA tiling catalogue. These 9 files are then joined (using the *tjoin* mode), and all duplicated columns are removed.

4.2.8   Source catalogues

The catalogues that have been generated are listed in Table 4.2. The syntax of the *Key* column is as follows. $X[u]$ means a u band magnitude from an X band-defined aperture, $\{u\}$ means a self-defined u band magnitude and $+$ denotes a STILTS *tskymatch2* 5 arcsec, unique nearest-object match between two catalogues (see Section 4.2.7). Where two datasets are combined together without the $+$ notation (i.e., the final two lines), this denotes a STILTS *tmatch2*, *matcher="exact"* match using SDSS OBJID as the primary key. Note that in a set of self-defined samples ($\{ugrizYJHK\}$), each sample must be matched separately (as each contains a different set of sources), and then combined. This is not the case in the aperture defined samples (where each sample contains the same set of sources). Subscripts denote the photometric method used for each catalogue.

4.3   Testing the GAMA catalogues

In this section I examine the sources detected by the SExtractor implementation used to create the r and K defined matched-aperture catalogues. I define a subsection of the

Catalogue Name	Key	Abbreviation
r-defined catalogue	$r[ugriz]_{SDSS} + r[ugrizYJHK]_{GAMA:Petro,Kron}$	catrdef
self-defined catalogue	$r[ugriz]_{SDSS} + \{ugrizYJHK\}_{GAMA:Petro,Kron}$	catsd
K-defined catalogue	$r[ugriz]_{SDSS} + K[ugrizYJHK]_{GAMA:Petro,Kron}$	catKdef
Sérsic catalogue	$r[ugriz]_{SDSS}\{ugrizYJHK\}_{GAMA:Sersic}$	catsers
GAMA master catalogue	$(r[ugriz]_{SDSS}\{r\}_{GAMA:Sersic})$ $+$ $\{ugrizYJHK\}_{GAMA:Petro,Kron}$	catmast

Table 4.2: The names of the generated catalogues, the prescription used to create them and their abbreviated filename. The syntax in the Key column is summarised in section 4.2.8.

GAMA 9 region and undertake object extraction, following the prescription detailed in the previous section. I compare the results to those produced by the SDSS and UKIDSS survey catalogues, visually inspecting sources where there are differences. Using this analysis, I calculate the level of source incompleteness due to misdetection by the GAMA, SDSS and UKIDSS extraction pipelines.

4.3.1 Test region

In order to test the detection and deblending outcomes within the GAMA catalogues, a subsection of 25 sq deg has been chosen from near the centre of the GAMA 9 region (the pixels used are 20000–65000 in the x direction of the mosaic, and 0–45000 in the y direction). This region was chosen as it contains some of the issues facing the entire GAMA subset, such as area incompleteness. UKIDSS observations miss a large fraction of the subset area - approximately 3.02 sq deg of the region has incomplete NIR coverage. The subset region was also chosen because it partially contains area covered by the Herschel ATLAS science verification region (see Eales et al. 2009). Within this region, SExtractor was ran, and the results are compared to the source list produced by SDSS and UKIDSS extraction software. Unless otherwise specified, all magnitudes within this section were calculated using r-defined apertures.

4.3.2 Numerical breakdown

After generating source catalogues containing self-consistent colours for all objects in the subset region (using the process described in subsections 4.2.5 and 4.2.7), an r band aperture-defined subset region catalogue containing 1810134 sources and a K band aperture-defined subset region catalogue containing 2298224 sources are produced. These are here-after referred to as the r band and K band catalogues. These catalogues contain many

sources that are not useful, such as sources with incomplete colour information, sources that are artefacts within the mosaics (satellite trails, diffraction spikes, etc), sources that are stars and sources that are fainter than the GAMA survey limits.

4.3.3 Match to the GAMA tiling catalogue

The unfiltered r and K band catalogues were matched to the master catalogue with a centroid tolerance of 5 arcsec, using the STILTS *tskymatch2* mode (see Section 4.2.7). Table 4.3 contains a breakdown of the fraction of matched sources that have credible X_{AUTO} and X_{PETRO} for all nine passbands (sources with incorrect $AUTO$ or $PETRO$ magnitudes have the value 99 as a placeholder; a cut at $X = 50$ is imposed to remove such objects). Generally, the low quality of the u band SDSS images causes problems with calculating extended source magnitudes, and this shows itself in the relatively high fraction of incomplete sources. This problem does not affect the other SDSS filters to anywhere near the same extent. SDSS observations do not cover the complete subset area, but they have nearly complete coverage in both the r-defined (which is dependent on SDSS imaging) and K-defined (reliant on UKIDSS coverage) catalogues. The UKIDSS observations cover a smaller section of the subset region, with the Y and J observations (taken separately to the H and K) covering the least area of sky. This is apparent in the r band catalogue, where at least 16% of sources lack $PETRO$ or $AUTO$ magnitudes in one or more passband. By its definition the K band catalogue requires K band observations to be present; as such there is a high level of completeness in the $grizH$ and K passbands. However, the number of matched SDSS sources in the K band catalogue itself is 4.2% lower than in the r band catalogue.

There are 138233 master catalogue SDSS sources within the subset region. 119330 SDSS objects have matches (within a 5 arcsec tolerance) in both the r band and K band master-cat matched catalogues (this number is found by matching SDSS OBJID between the catalogues). Those SDSS objects that do not have matches in both master-cat matched catalogues are shown in Figure 4.6. The reasons for the missing objects are detailed in section 4.3.4.
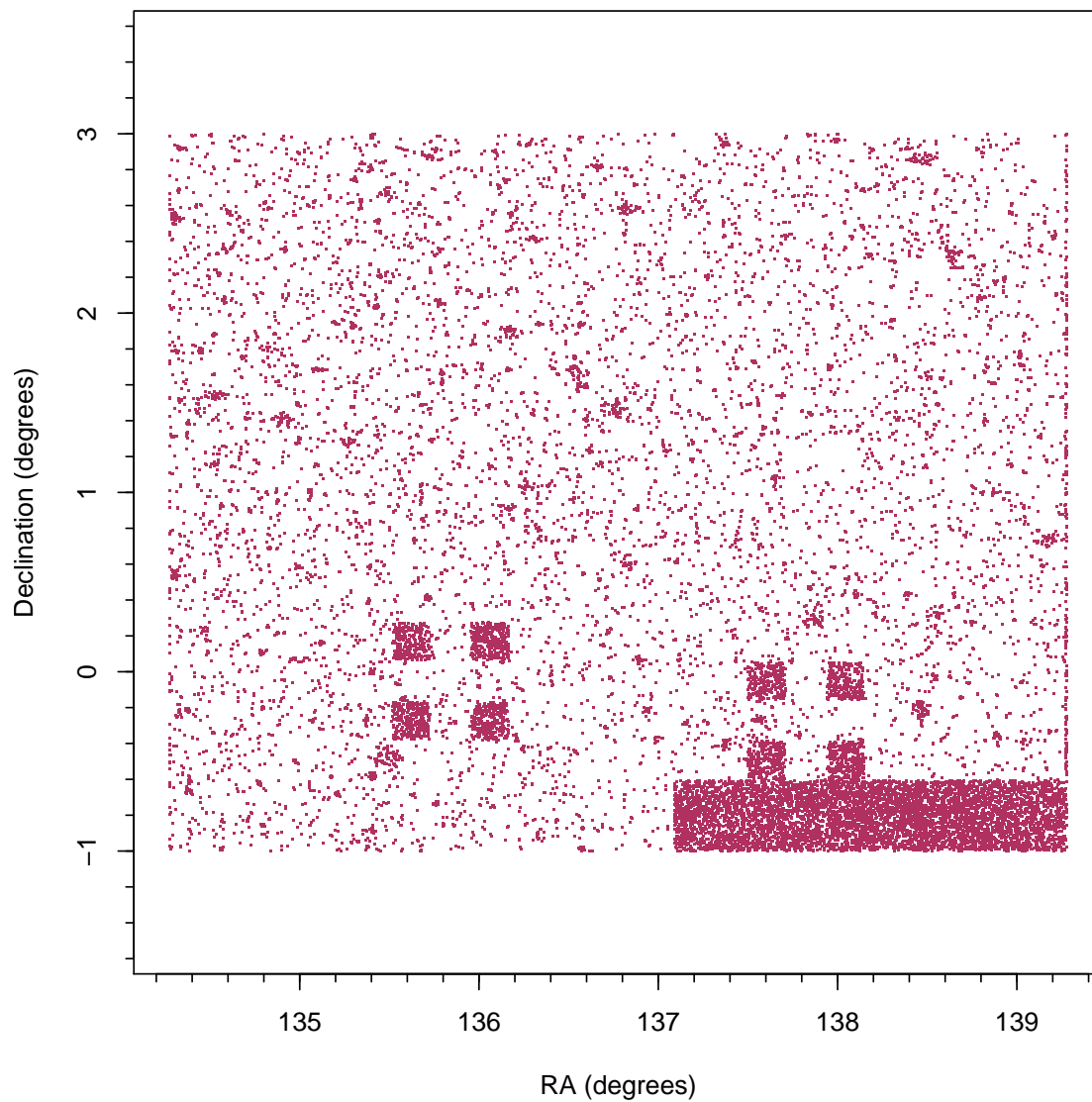
Figure 4.6: The Right Ascension and Declination of SDSS objects that are not in either the *r* or *K* band master-cat matched catalogue. The darker areas denotes a higher density of unmatched objects.

Band	% Cover	Sources (r)	% (r)	Sources (K)	% (K)
Total	-	129488	-	123740	-
u	100	111403	86	105801	86
g	100	129169	100	123317	100
r	100	129481	100	123610	100
i	100	129358	100	123533	100
z	100	128287	99	122479	99
Y	88	108167	84	109672	89
J	89	109364	84	109816	89
H	96	121212	94	121846	98
K	94	118224	91	122635	99

Table 4.3: Number of sources within the subset region with good `SExtractor` X_{Auto} and X_{Petro}, where X is $ugrizYJHK$, from the r or K band-defined aperture catalogues matched to the GAMA master catalogue. The total number of sources within the GAMA master catalogue for this region of sky is 138233. % Cover is defined relative to r band cover; where SDSS coverage does not exist there are no GAMA master catalogue sources.

4.3.4 SDSS sources missing in the matched aperture catalogues

There are 18903 SDSS sources that are not found when the master catalogue is matched to either the r or K-defined subset region catalogues; 13.7% of the total number of master catalogue sources within the subset region. Figure 4.6 shows their distribution on the sky. 8745 sources are not found within the r-defined catalogue (6.3% of the master catalogue sample) and 14493 are not found within the K-defined catalogue (10.5% of the sample), with 4335 of the sources unmatched to either the r or the K-defined sample (3.1% of the master catalogue sample). As the SDSS sample is defined by optical data, it is unsurprising that a far larger number of sources are not found within the K-defined catalogue. Of the 18903 unmatched master catalogue sources, only 2367 have passed star-galaxy separation and are brighter than the GAMA spectroscopic survey magnitude limits ($r < 19.8$ or zK selected).

All 8745 SDSS sources where the r-defined subset region catalogue does not contain a match within 5 arcsec were visually inspected (using r band imaging). Table 4.4 contains a summary of the reasons why there was no r band match. Using the `SExtractor` detection failure rate from the subset region as a guide to the detection failure rate for the entire GAMA region, `SExtractor` will miss approximately 2.8% of the objects recovered by SDSS. A second problem was flagged through the inspection process; a further 1.7% of the master catalogue sources within the subset region were not visible. Either these

Table 4.4: A breakdown of the reasons for faulty detections in the 8745 SDSS objects that are not matched to the r band subset region catalogue. The images of the SDSS objects were generated from the standard r band GAMA mosaics, and all 8745 objects were viewed by one observer (DTH). The criteria selection is as follows. The first category is chosen in those cases where an object has a nearby neighbour or may have been deblended into multiple sources by the SDSS algorithm. The second category is chosen where the position of the object is covered by a spike/trail. The third category is where a source is visible by eye. The fourth category is where a source is not visible above the noise. The fifth category is chosen when a source is obviously part of a larger structure. The sixth category is chosen when the SDSS data is too low quality for visual classification to be undertaken.

Reason for non-detection	Number of objects	GAMA master catalogue subset sample (%)
Possible deblending mismatch	601	0.4
Saturation spike / satellite or asteroid trail	404	0.3
`SExtractor` detection failure	3831	2.8
Either a low surface brightness source or no source	2391	1.7
Part of a large deblended source	1463	1.1
Low image quality making detection difficult	55	0.04

objects are low surface brightness extended objects, possibly detected in a different band, or the SDSS object extraction algorithm has made a mistake. A further 1.8% of sources within the GAMA master catalogue will be missed by `SExtractor` due to differences in deblending decisions (either failing to split two sources or splitting one large object into a number of smaller parts), low SDSS image quality making `SExtractor` fail to detect any objects, or an artefact in the image being accounted for by `SExtractor` (such as a saturation spike from a large star being detected as a separate object in SDSS).

4.3.5 Sources in the r band catalogue that are not in the GAMA master catalogue

To be certain that the SDSS extraction software is providing a complete sample, a check was made to see whether the r band subset region catalogue contains sources that should be within the GAMA master catalogue but are not. There are 61351 sources within the r-defined subset region catalogue that have a complete set of credible *AUTO* and *PETRO* magnitudes, and are brighter than the GAMA spectroscopic survey limits. 619 of these sources do not have SDSS counterparts. These sources were visually inspected; a breakdown is shown in Table 4.5. Similar issues cause missing detections using the SDSS or `SExtractor` algorithms. However, some of the unseen sources that `SExtractor` detected may be due to the image convolution process (Section 4.1.3) gathering up noisy-pixel

Type of source	Number of objects
Source	171
No visible source	274
Section of bright star	163
Possible deblend mismatch	10
Low image quality making detection difficult	1

Table 4.5: A breakdown of the 619 r defined catalogue objects brighter than the GAMA sample limits that are not matched to the GAMA master catalogue. The images of the subset region catalogue objects were generated from the standard r band GAMA mosaics, and all 619 objects were viewed by one observer (DTH).

flux from a region with high background noise and rearranging it so that it overcomes the detection threshold. Alternatively, these additional sources may be extremely faint galaxies that have been discovered due to the convolution process; without deeper data is impossible to tell. Figure 4.7 shows the distribution of $r_{Auto} \leq 20.5$ mag sources detected when `SExtractor` is run upon an original SDSS image file (covering $\sim 0.04\,\mathrm{deg}^2$), and the sources from the same file after it has undergone the image convolution process. 233 sources are found in the original SDSS frame, and 3 additional sources are included within the convolved frame sample. An examination of two sources that are in the convolved frame dataset and not in the original sample shows the effect: these sources have r_{Auto} luminosities of 20.64 mag and 20.77 mag pre-convolution, but r_{Auto} luminosities of 20.40 mag and 20.48 mag post-convolution. Taking the SDSS non-detection rate within the subset region to be the same as the non-detection rate over the entire GAMA region, it is expected that the SDSS algorithm will have failed to detect $\sim$0.1% of sources brighter than the GAMA spectroscopic survey limits. Approximately 1000 sources will not have been included within the master catalogue.

4.3.6 Sources in the K band catalogue that are not in the UKIDSS DR5PLUS database

The UKIDSS DR5 catalogue was also tested. A catalogue was generated from the WSA that selects all UKIDSS objects within the GAMA subset region[3]. This catalogue was matched to the K band-defined subset region catalogue. Of the 69537 K band-defined subset region catalogue sources, 4548 have no match to an UKIDSS object within a tolerance of 5 arcsec. K band images of those objects that are brighter than the GAMA

---

[3]The query "SELECT las.ra, las.dec, las.kPetroMag FROM lasSource as las WHERE $las.ra < 139.28$ AND $las.ra > 134.275$ AND $las.dec > -1$ AND $las.dec < 3$" was used
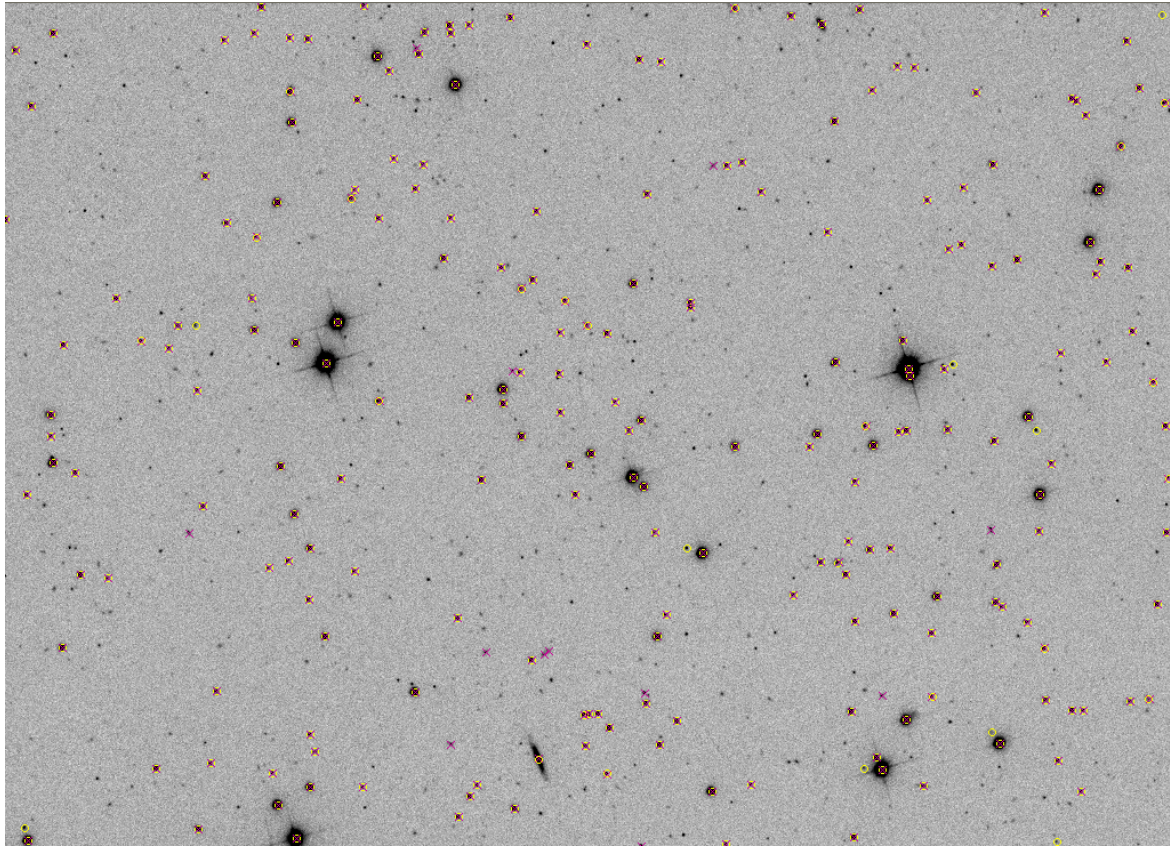
Figure 4.7: A comparison between the objects detected when `SExtractor` is run over an original SDSS image, and when it is run over the convolved, mosaic imaging. Yellow circles are sources with $r \leq 20.5$ mag detected from the GAMA mosaic, red crosses are sources that are detected from the original SDSS data.

spectroscopic survey K band limit ($K_{AUTO} \leq 17.6$ mag) were inspected. 29 of the 117 unmatched objects were found to be real sources that are missed by the UKIDSS extraction software; a negligible fraction of the entire dataset. A large (but unquantified) fraction of the other 88 sources are suffering from the convolution flux-redistribution problem discussed in Section 4.3.5. The background fluctuations in K band data are greater than in the r band, making this a much greater problem.

4.4   Properties of the catalogues

In this section I compare how the distribution of the galaxy population varies between photometric systems. I detail the construction of a clean unambiguous sample of sources. I examine the dispersion in luminosity produced the different photometric systems for sources within this clean sample. I attempt to infer the best photometric solution by examining the colour distribution of the sample, modelling the galaxy population with a double-Gaussian function in order to account for the inherent bimodality.

4.4.1   Constructing a clean sample

In order to investigate the photometric offsets between different photometric systems, a sample of galaxies is required that have a complete set of credible photometry, and are unaffected by deblending decisions. This has been created via the following prescription. The r-defined aperture catalogue is matched to the GAMA master catalogue with a tolerance of 5 arcsec. Any GAMA objects that have not been matched, or have been matched to multiple objects within that tolerance (when run in *All match* mode STILTS produces a *GroupSize* column, where a *NULL* value signifies no group) are removed. This catalogue is then matched to the 9 self-defined object catalogues, in each case removing all unmatched and multiply matched GAMA objects. As the convolution routine will cause problems with those galaxies that contain saturated pixels, those galaxies that are flagged as saturated by SDSS are also removed. The sample is then linked to the Sérsic pipeline catalogue (using the SDSS OBJID as the primary key). All Sérsic magnitudes where the pipeline has flagged that the model is badly fit or where the photometry has been compromised are removed, and the result is then matched to the K band aperture-defined catalogue. Again, all unmatched and multiple matched sources are removed. This gives a final population of

18065 galaxies that have clean r-defined, K-defined, self-defined and Sérsic magnitudes, are not saturated and cannot have been mismatched. Having constructed a clean, unambiguous sample of common objects, any photometric offset can only be due to differences between the photometric systems used. As objects that are badly fit by the Sérsic pipeline are removed, it should be noted that the resulting sample will, by its definition, only contain sources that have a light profile that can be fitted using the Sérsic function.

4.4.2 Photometric offset between systems

Figures 4.8, 4.9, 4.10, 4.11 and 4.12 illustrate the dispersion between different photometric systems produced by this sample. Each figure shows the mean, median and standard deviation in the colour offset for that photometry, and these parameters have also been tabulated in Table 4.6. Figure 4.8 compare Kron and Petrosian magnitudes; in all other figures the photometric system is compared to SDSS PETROMAG. In all photometry systems, the gri relationships are tightest, with the u and z relationships subject to a greater scatter, breaking down almost entirely in Figures 4.11 and 4.12. The correlation between the SDSS PETROMAG and the r-defined Petrosian magnitude (Figure 4.10) looks much tighter than that between the SDSS PETROMAG and the self-defined Petrosian magnitude (Figure 4.11); the r-defined Petrosian magnitudes are taken from the convolved imaging and the self-defined Petrosian magnitudes are taken from the unconvolved imaging. The standard deviation of the samples are similar, with marginally more scatter in the self-defined sample (0.129 mag against 0.148 mag). The median offset between SDSS Petrosian and the r-defined Petrosian magnitude, however, is 0.01 mag greater.

Figure 4.12, showing the relationship between the Sérsic magnitude and the SDSS PETRO-MAG, produces median $\Delta m_{SDSS} - m_{Sersic}$ values of 0.12, 0.06, 0.06, 0.07 and 0.09 mag in $ugriz$. These values can be compared to those presented in Figure 13 of Blanton et al. (2003) (-0.14, 0.00, 0.06, 0.09 and 0.14 mag at $z = 0.1$, using the $^{0.1}ugriz$ filters), given the variance in the relationship (the standard deviation in the GAMA samples are 0.77, 0.28, 0.21, 0.22 and 0.40 mag, respectively). A significant fraction ($\sim 28\%$) of the sample has $r_{SDSS} - r_{Sersic} > 0.5$ mag, and therefore lies beyond the boundaries of this image. These offsets are significant, and will be discussed further in Section 4.5. The r-defined aperture photometry is the closest match to SDSS PETROMAG photometry. Figure 4.13

Band	Photometry	Mean (mag)	Median (mag)	σ (mag)
u	r-defined AUTO - r-defined PETRO	-0.00	-0.04	0.43
u	SDSS PETROMAG - r-defined AUTO	0.04	-0.01	0.56
u	SDSS PETROMAG - r-defined PETRO	0.05	0.02	0.70
u	SDSS PETROMAG - self-defined PETRO	-0.10	-0.11	0.90
u	SDSS PETROMAG - Sérsic	0.19	0.12	0.77
u	SDSS CMODEL - Sérsic	-0.10	-0.07	0.77
g	r-defined AUTO - r-defined PETRO	-0.03	-0.03	0.10
g	SDSS PETROMAG - r-defined AUTO	0.03	0.01	0.14
g	SDSS PETROMAG - r-defined PETRO	0.06	0.04	0.18
g	SDSS PETROMAG - self-defined PETRO	0.03	0.02	0.23
g	SDSS PETROMAG - Sérsic	0.14	0.06	0.28
g	SDSS CMODEL - Sérsic	0.08	-0.00	0.28
r	r-defined AUTO - r-defined PETRO	-0.02	-0.02	0.05
r	SDSS PETROMAG - r-defined AUTO	0.02	0.01	0.11
r	SDSS PETROMAG - r-defined PETRO	0.04	0.03	0.13
r	SDSS PETROMAG - self-defined PETRO	0.02	0.02	0.15
r	SDSS PETROMAG - Sérsic	0.12	0.06	0.21
r	SDSS CMODEL - Sérsic	0.07	0.01	0.21
i	r-defined AUTO - r-defined PETRO	-0.03	-0.03	0.06
i	SDSS PETROMAG - r-defined AUTO	0.04	0.01	0.14
i	SDSS PETROMAG - r-defined PETRO	0.07	0.05	0.16
i	SDSS PETROMAG - self-defined PETRO	0.02	0.01	0.15
i	SDSS PETROMAG - Sérsic	0.13	0.07	0.22
i	SDSS CMODEL - Sérsic	0.07	0.01	0.22
z	r-defined AUTO - r-defined PETRO	-0.01	-0.02	0.21
z	SDSS PETROMAG - r-defined AUTO	0.02	-0.01	0.22
z	SDSS PETROMAG - r-defined PETRO	0.03	0.02	0.31
z	SDSS PETROMAG - self-defined PETRO	-0.04	-0.04	0.40
z	SDSS PETROMAG - Sérsic	0.17	0.09	0.40
z	SDSS CMODEL - Sérsic	0.07	-0.01	0.38

Table 4.6: Colour offsets from Figures 4.8, 4.9, 4.10, 4.11, 4.12 and 4.13.

shows the relationship between the GAMA Sérsic magnitude, and the optimal model magnitude provided by SDSS (CMODEL). The model magnitudes match closely, with negligible systematic offset between the photometric systems in gri.

4.4.3 Colour distributions

In order to identify the optimal photometric system, it is assumed the intrinsic colour distribution of a population of galaxies can be approximated by a double-Gaussian distribution (the superposition of a pair of Gaussian distributions with different mean and standard deviation parameters). This distribution can model the bimodality of the galaxy
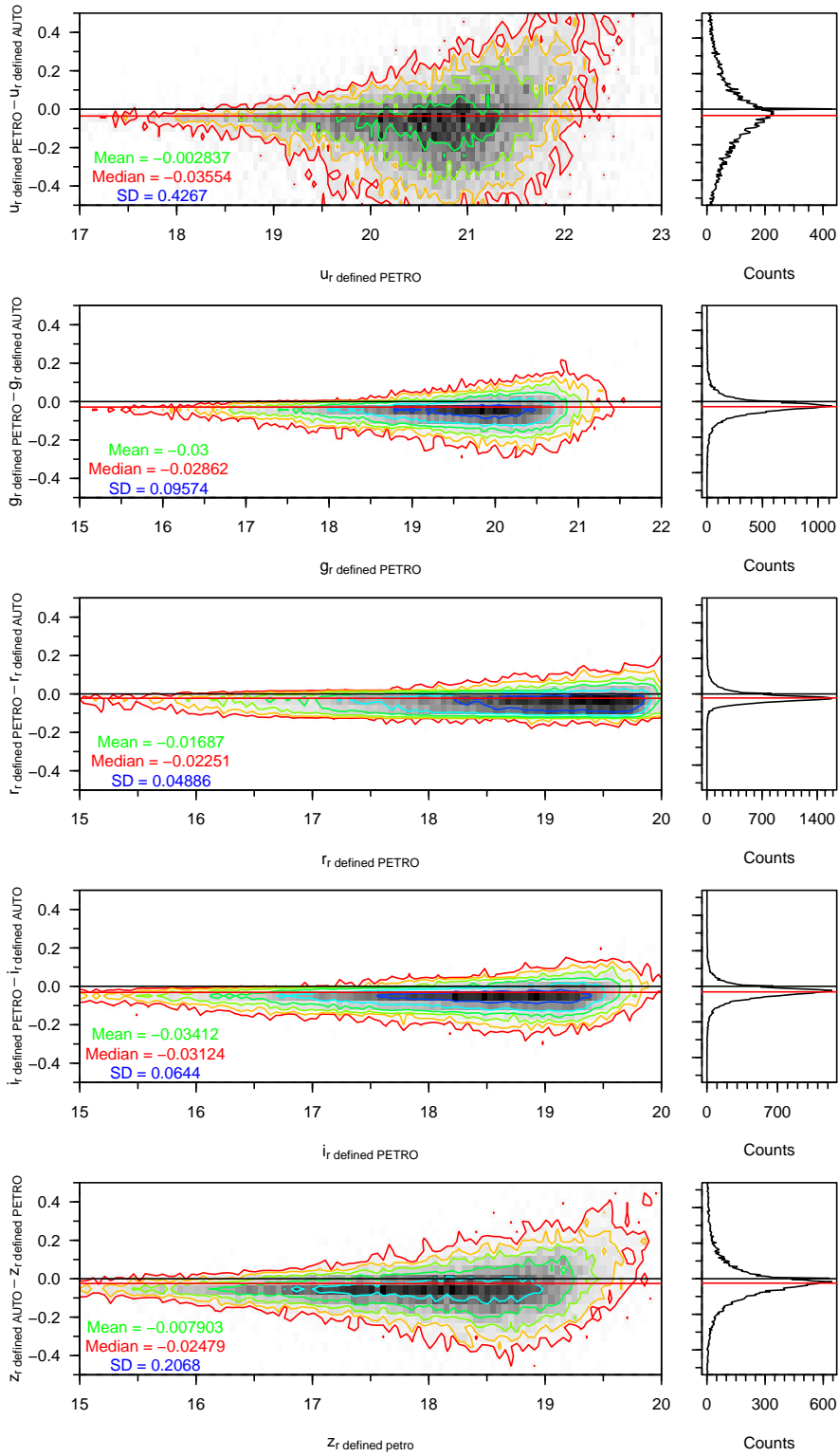
Figure 4.8: GAMA r-defined aperture Petrosian minus Auto magnitudes for a clean sample of galaxies in *ugriz*. Contours are for 4 to 512 galaxies per bin, rising geometrically in powers of 2. Bins are $0.05\,\mathrm{mag}{\times}0.05\,\mathrm{mag}$ in size.
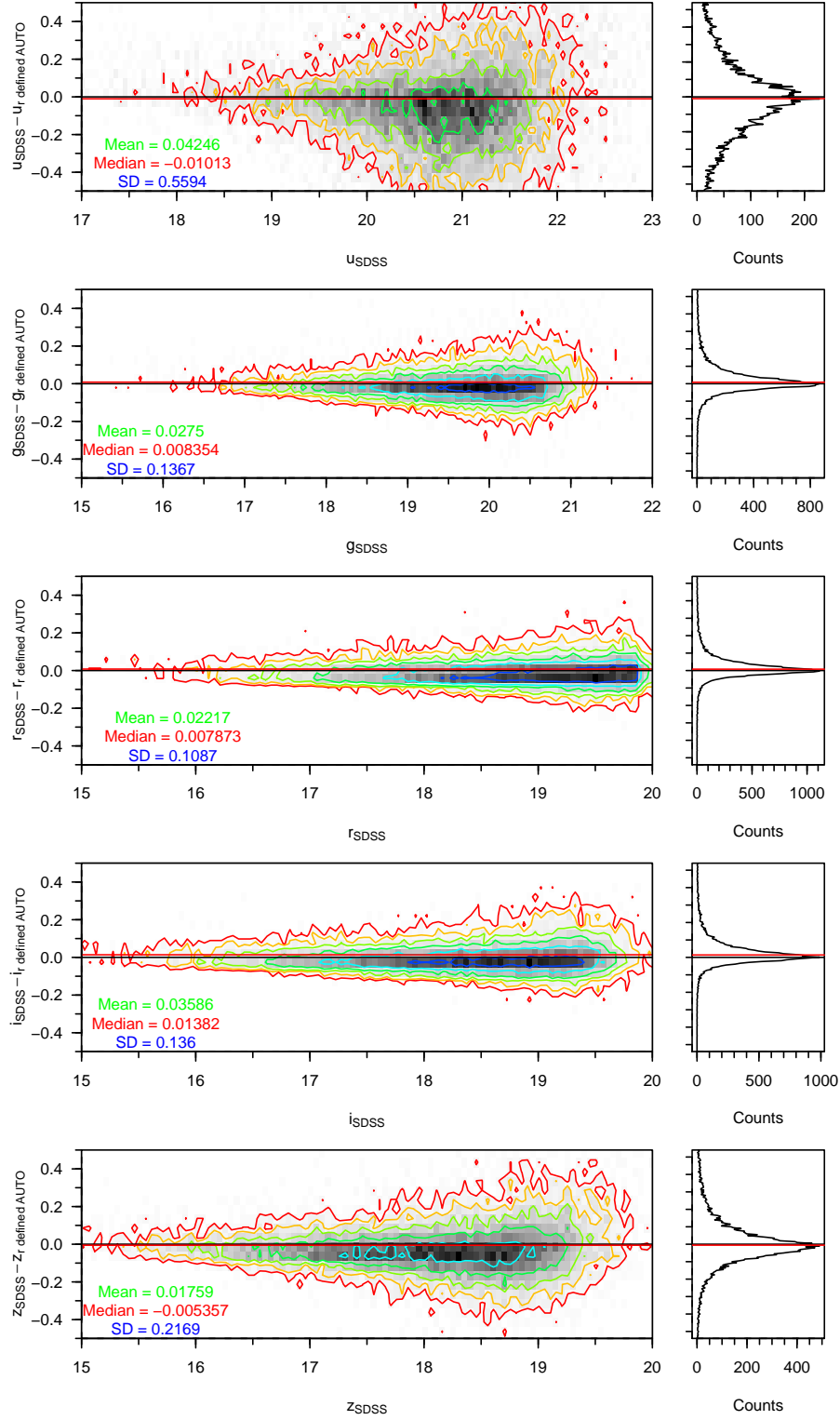
Figure 4.9: SDSS PETROMAG minus GAMA r-defined aperture Auto magnitudes for a clean sample of galaxies in *ugriz*. Contours are for 4 to 512 galaxies per bin, rising geometrically in powers of 2. Bins are $0.05\,\text{mag}\times0.05\,\text{mag}$ in size.
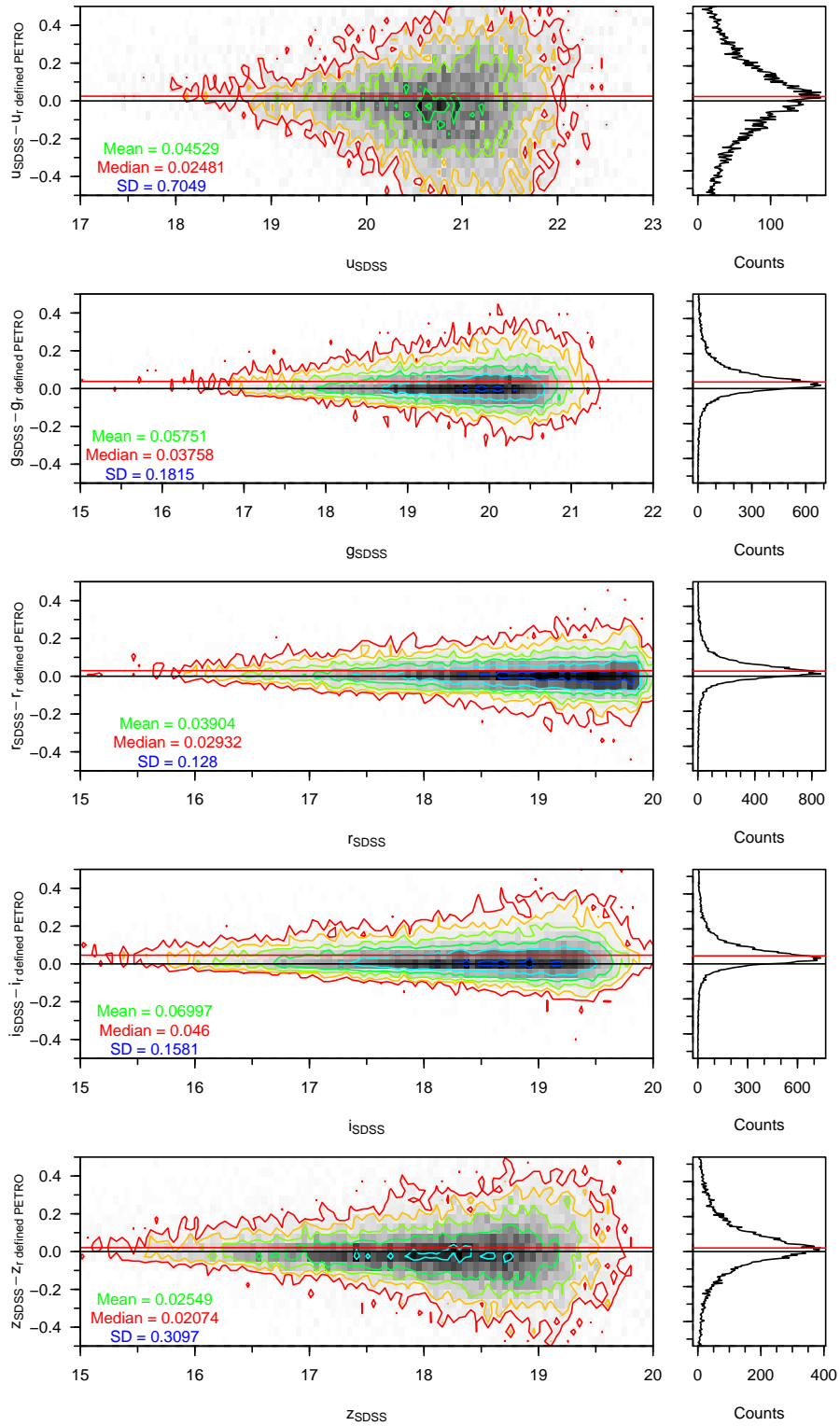
Figure 4.10: SDSS PETROMAG minus GAMA r-defined aperture Petrosian magnitudes for a clean sample of galaxies in *ugriz*. Contours are for 4 to 512 galaxies per bin, rising geometrically in powers of 2. Bins are 0.05 mag×0.05 mag in size.
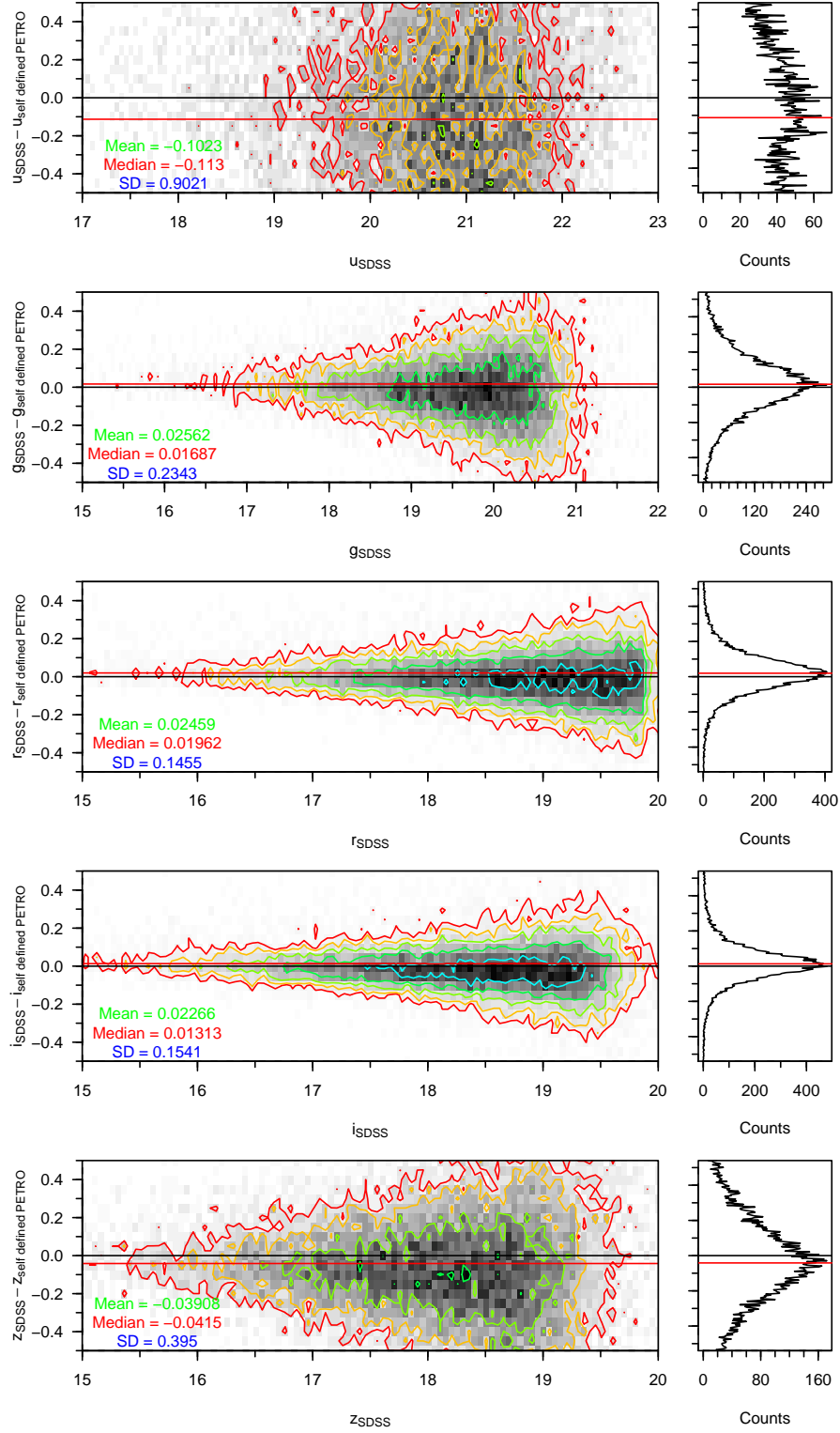
Figure 4.11: SDSS PETROMAG minus GAMA self-defined aperture Petrosian magnitudes for a clean sample of galaxies in *ugriz*. Contours are for 4 to 512 galaxies per bin, rising geometrically in powers of 2. Bins are $0.05\,\text{mag} \times 0.05\,\text{mag}$ in size.
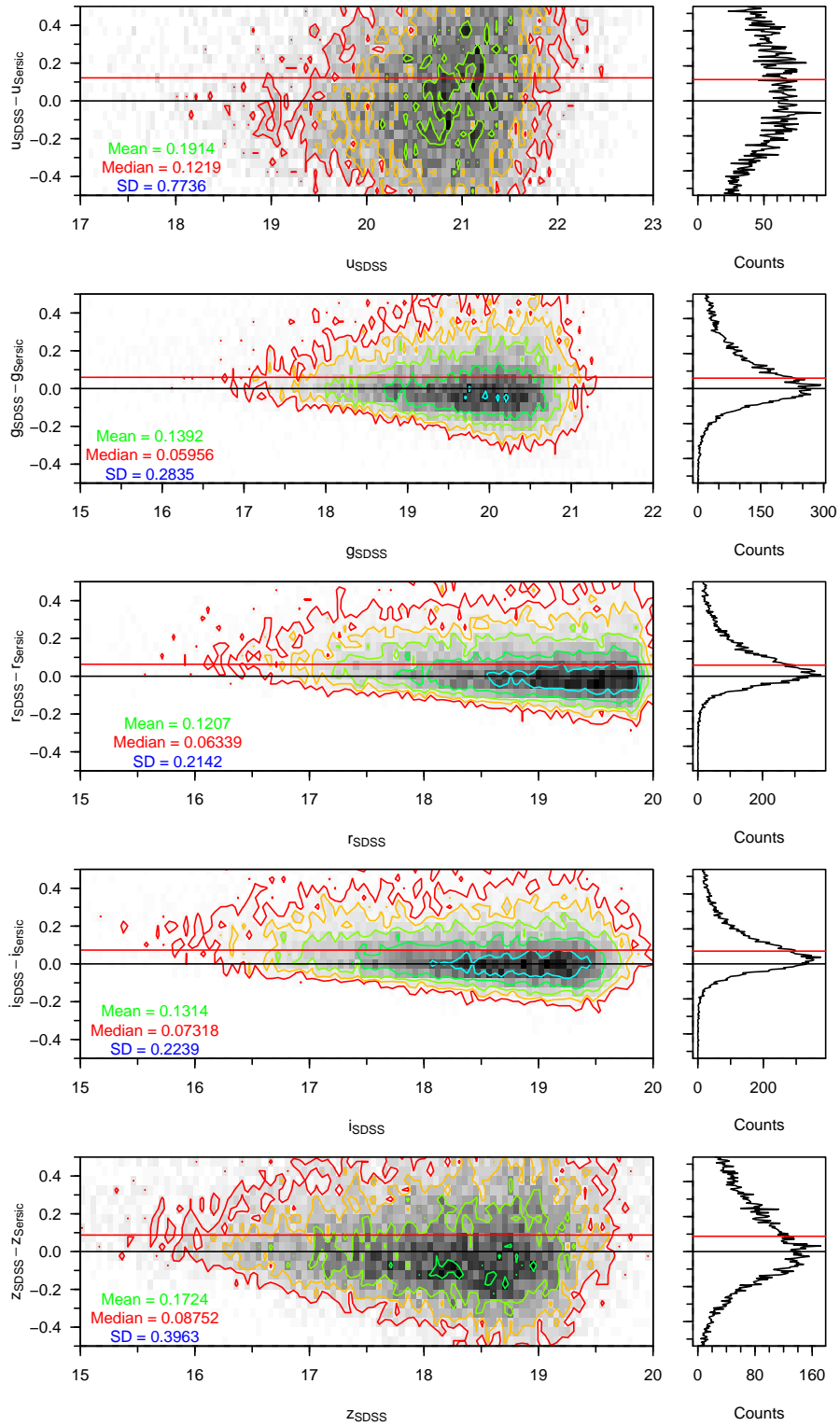
Figure 4.12: SDSS PETROMAG minus GAMA Sérsic magnitudes for a clean sample of galaxies in *ugriz*. Contours are for 4 to 512 galaxies per bin, rising geometrically in powers of 2. Bins are 0.05 mag×0.05 mag in size.
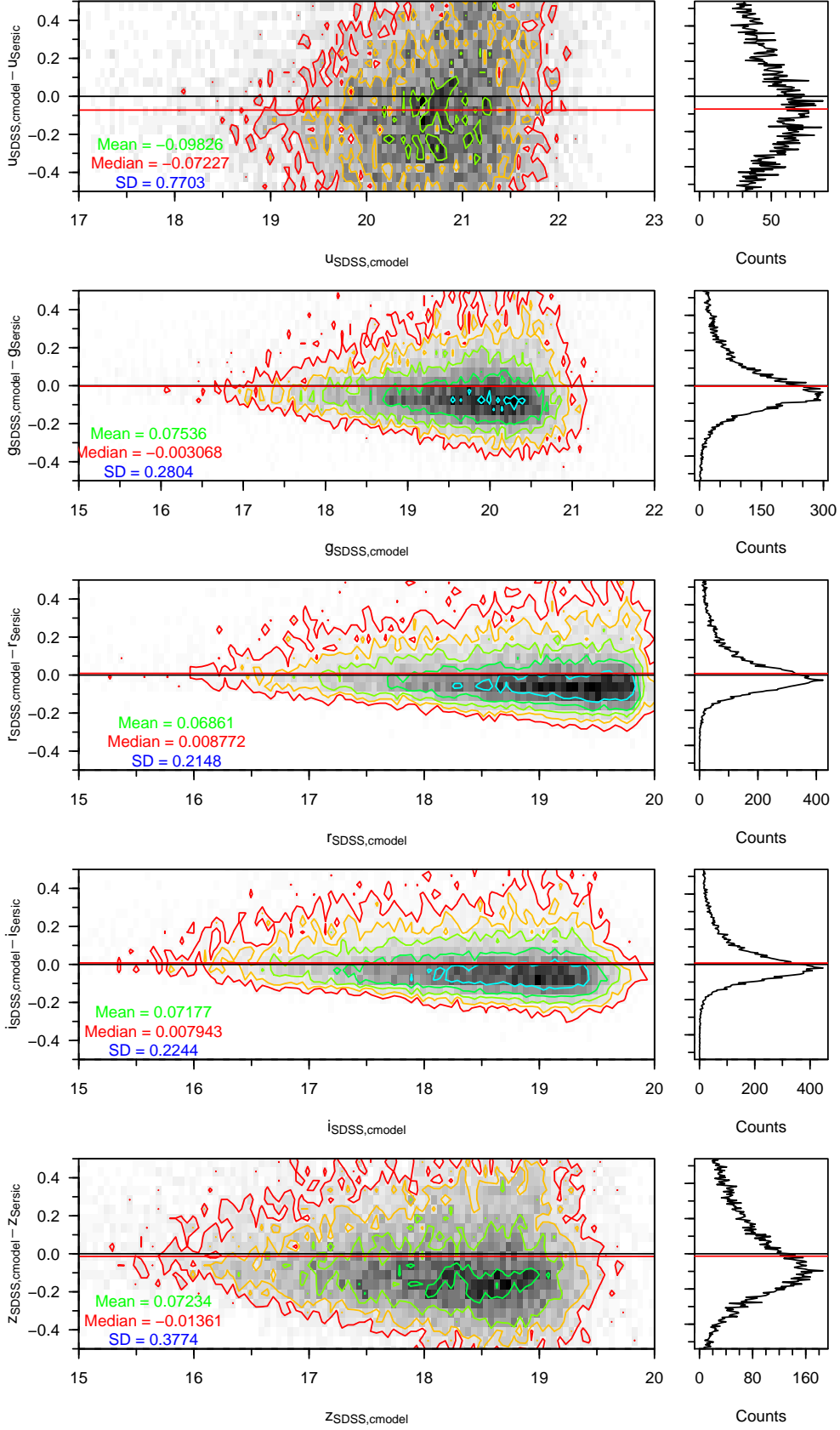
Figure 4.13: SDSS CMODEL minus GAMA Sérsic magnitudes for a clean sample of galaxies in *ugriz*. Contours are for 4 to 512 galaxies per bin, rising geometrically in powers of 2. Bins are 0.05 mag×0.05 mag in size.

115

population. The presence of noise will broaden the distribution; hence the narrowest colour distribution reveals the optimal photometric system for calculating the colours of galaxies, and therefore deriving accurate SEDs. Figure 4.14 shows the $(u-r)$ and $(r-K)$ colour distributions for each photometric system, for objects within the subset region. In order to calculate the dispersion in the colour distribution, colour-distribution histograms are generated (with bins of $0.1\,\mathrm{mag}$), and the double-Gaussian distribution parameters that best fit each photometric system are found. The best-fitting standard deviation parameters for each sample are shown at the bottom of each plot, and are denoted $\sigma_{X,1}$ and $\sigma_{X,2}$ (where X is the photometric system fitted). The σ parameters are also tabulated in Table 4.7. The sample with the smallest set of σ parameters should provide the optimal photometric system.

The SDSS, GAMA r-defined aperture and GAMA K-defined distributions (the first, third and fourth diagrams on the top two rows) show a very similar pattern; a tight distribution of objects with a small number of red outliers. As expected, when apertures are used that are defined separately in each filter (the second diagram on the top two rows), the colour distribution of the population is more scattered ($\sigma_{Petro,1} = 0.7576\,\mathrm{mag}$, $\sigma_{Petro,2} = 0.7919\,\mathrm{mag}$, $\sigma_{Auto,1} = 0.5886\,\mathrm{mag}$, $\sigma_{Auto,2} = 0.7086\,\mathrm{mag}$) and does not show the bimodality visible in the matched aperture photometry (at the bright end of the distribution there are two distinct sub-populations; one sub-population above $u - r = 2\,\mathrm{mag}$, the other below). For the same reason, and probably because of the low quality of the observations, the $(u-r)$ plot using the Sérsic magnitudes (the final diagram on the top row) has the broadest colour distribution ($\sigma_{Sersic,1} = 0.6242\,\mathrm{mag}$, $\sigma_{Sersic,2} = 1.098\,\mathrm{mag}$), although it is well behaved in $(r$-$K)$.

To generate a series of $(r-K)$ colours using the UKIDSS survey (leftmost plot on the bottom two rows), all galaxies within the UKIDSS catalogue[4] were matched (with a maximum tolerance of $5\,\mathrm{arcsec}$) to a copy of the tiling catalogue that had previously been matched with the K band aperture-defined catalogue. The distribution of $(r-K)$ colours taken from the SDSS and UKIDSS survey catalogues is the first diagram on the bottom two rows of the image. As the apertures used to define the UKIDSS and SDSS sources are not consistent, the tightest $(r-K)$ distribution comes from the GAMA K-defined aperture sample (fourth from the left on the bottom row, with $\sigma_{Auto,1} = 0.3137\,\mathrm{mag}$,

---

[4]A query is run at the WSA on UKIDSSDR5PLUS looking for all objects within the subset region with *lasSource.pGalaxy* > 0.9 & *lasSource.kPetroMag* < 20 - equivalent to $K_{AB} < 21.9\,\mathrm{mag}$

Colour	Photometry	σ_1 (mag)	σ_2 (mag)
u-r	SDSS Modelmag	0.3262	0.5222
u-r	Self-defined PETRO	0.7576	0.7919
u-r	r-defined PETRO	0.4316	0.6379
u-r	K-defined PETRO	0.4128	0.6018
u-r	GAMA Sérsic	0.6242	1.098
u-r	Self-defined AUTO	0.5886	0.7086
u-r	r-defined AUTO	0.3681	0.5630
u-r	K-defined AUTO	0.3484	0.5426
u-r	GAMA Total Mag	0.3681	0.5630
r-K	SDSS/UKIDSS Petromag	0.3342	0.5807
r-K	Self-defined PETRO	0.3359	0.6015
r-K	r-defined PETRO	0.3286	0.6150
r-K	K-defined PETRO	0.3188	0.5876
r-K	GAMA Sérsic	0.3640	0.6159
r-K	Self-defined AUTO	0.3285	0.5535
r-K	r-defined AUTO	0.3203	0.5238
r-K	K-defined AUTO	0.3137	0.4921
r-K	GAMA Total Mag	0.3203	0.5238

Table 4.7: σ parameters from Figure 4.14.

$\sigma_{Auto,2} = 0.4921\,\text{mag}$). The GAMA sample that relies on matching objects between self-defined object catalogues (the second diagram on the bottom two rows) has the broadest distribution ($\sigma_{Petro,1} = 0.3359\,\text{mag}$, $\sigma_{Petro,2} = 0.6015\,\text{mag}$). The distribution of sources in the Sérsic $(r - K)$ colour plot is much tighter than in the $(u - r)$, though still not as tight as the distribution in the fixed aperture photometric systems ($\sigma_{Sersic,1} = 0.364\,\text{mag}$, $\sigma_{Sersic,2} = 0.6159\,\text{mag}$). Figure 4.14 confirms the utility of the GAMA method: by redoing the object extraction, self-consistent colour distributions based on data taken by multiple instruments have been generated that have a far smaller scatter than a match between the survey source catalogues ($\sigma_{SDSS+UKIDSS,1} = 0.3342\,\text{mag}$, $\sigma_{SDSS+UKIDSS,2} = 0.5807\,\text{mag}$).

One final comparison between the GAMA photometry colour distribution and that provided by SDSS and UKIDSS survey data has been made. Figure 4.15 displays the $X - H$ distribution produced by the GAMA galaxies with complete $ugrizYJHK$ photometry and good quality redshifts within $0.033 < z < 0.6$. The effective wavelengths of the filter set for each galaxy are shifted using the redshift of the galaxy. The colour distribution provided by the GAMA photometry produces fewer outliers than the SDSS/UKIDSS survey data sample, and is well constrained by the BC03 (Bruzual & Charlot, 2003) models.
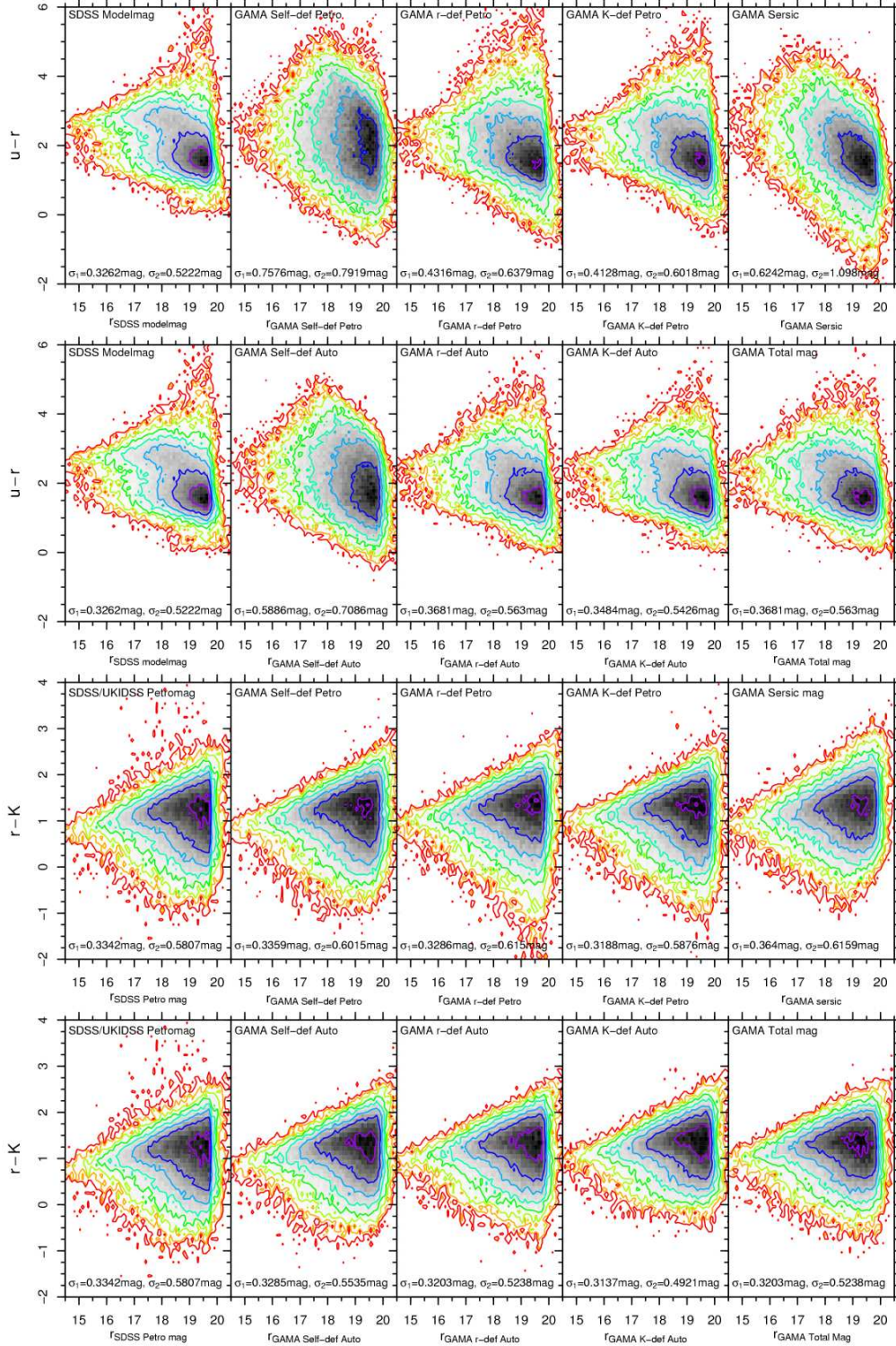
Figure 4.14: A comparison between the u minus r and r minus K colours produced using SDSS MODELMAG, GAMA self-defined Petrosian magnitudes, GAMA r/K-defined Petrosian magnitudes, Sérsic and GAMA Total magnitudes for objects in the subset region. Contours shown are 2 to 512 galaxies per bin, rising geometrically in powers of 2. Bins are 0.1 mag in width in each axis. The σ parameters come from the best-fitting bivariate-Gaussian distribution, when it is fit to the colour-distribution histogram in each plot.
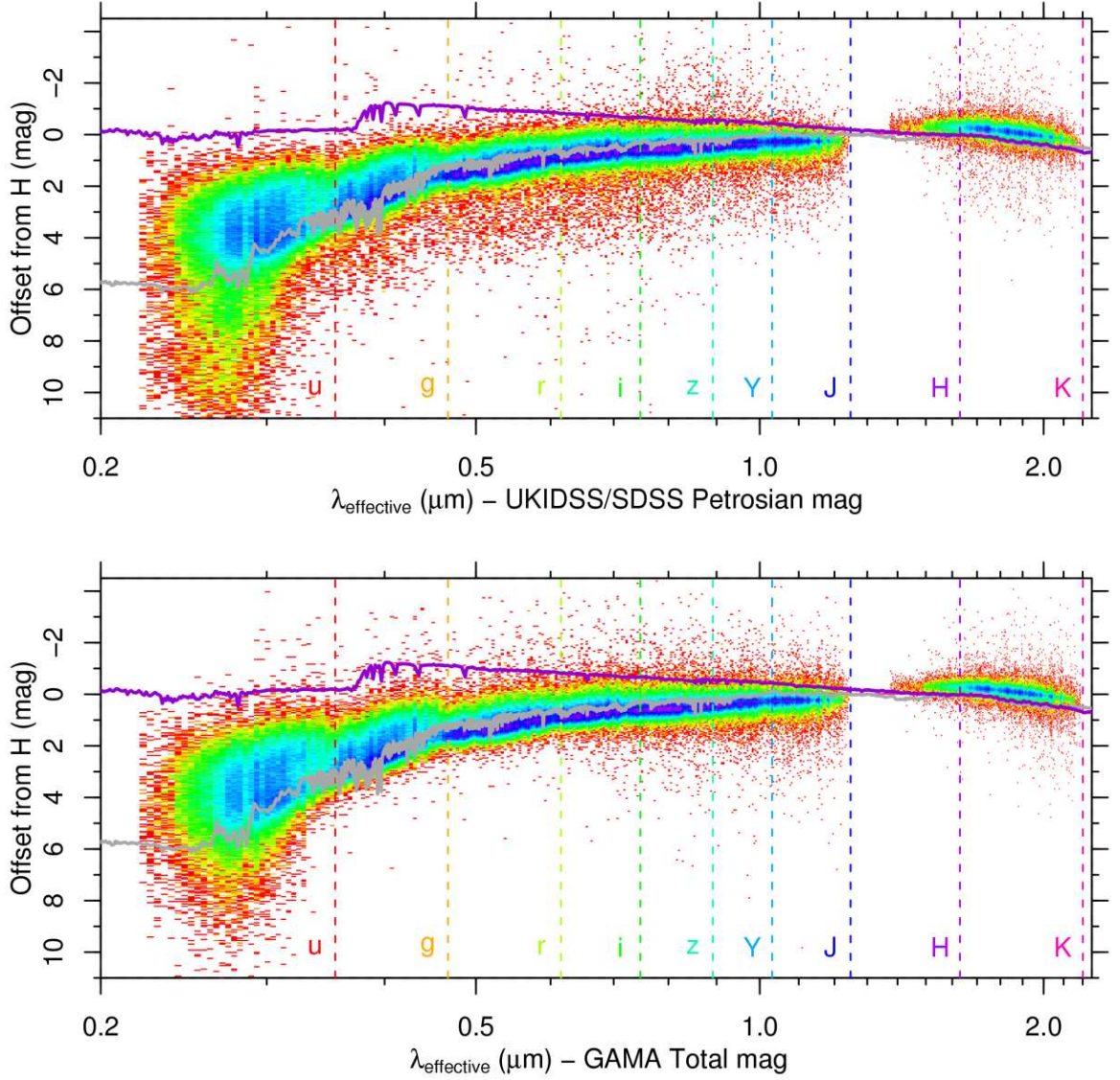
Figure 4.15: A comparison between the $X - H$ colours produced using SDSS magnitudes and GAMA Total magnitudes. Data comes from all GAMA galaxies with good quality redshifts $(0.033 < z < 0.6)$ and complete $ugrizYJHK$ photometry. Effective wavelengths are calculated from the redshift of the galaxy and the filter effective wavelength, and the dataset is binned into a 50×50 bin matrix. Two Bruzual-Charlot 03 SSP instantaneous-burst models are also plotted. Both models use the Chabrier (2003) IMF, with mass cutoffs at 0.1 and $100\,M_{\odot}$. Stellar evolution is undertaken using the Padova 1994 prescription. The dark grey line is a model evolved to 11 Gyr, with Z=0.05 and Y=0.352. The purple line is a model evolved to 0.25 Gyr, using Z=0.02 (Z$_{\odot}$) and Y=0.28.

4.5 Final GAMA photometry

Previously, in sections 4.3 and 4.4, I have shown that the optimal deblending outcome is produced by the original SDSS data, but the best colours come from the r-defined aperture photometry (Section 4.4.3). I have shown that the r-defined aperture photometry agrees with the SDSS PETROMAG photometry. However, it has also been demonstrated that SDSS PETROMAG misses flux when compared to the Sérsic total magnitude. In this section I describe the GAMA photometric catalogue that is released to the public. I test the Sérsic photometry against reliable photometric data, and compare the resulting distribution against predictions from theory. I outline a method to produce 'Fixed aperture' magnitudes with consistent colours, combining the Sérsic r magnitude with colours from Kron photometry. This combined dataset provides the final GAMA photometry: the best photometric solution possible for data of this quality. I then ascertain the level of uncertainty within the photometry because of variations in the aperture definition and Gain within the mosaic. I derive the apparent magnitude limits of the GAMA photometry, via the number counts. I summarise how the data has been combined with Galex UV observations, and provide SEDs for 10 galaxies, comparing the results with the equivalent datapoints taken from the UKIDSS/SDSS survey catalogues and Bruzual & Charlot (2003) model SEDs.

4.5.1 Sérsic magnitudes

In order to check the reliability of the Sérsic photometry pipeline, its distribution against a reliable photometric system must be examined. The distribution of the Sérsic photometry is tested against the r-defined AUTO photometry. Figure 4.16 shows the distribution of Sérsic - GAMA r-defined AUTO magnitude against r-defined AUTO magnitude for all objects in the GAMA sample that have passed the GAMA star-galaxy separation criteria and have credible AUTO magnitudes. Whilst there is generally a tight distribution, the scatter in the u band, in particular, is a cause for concern.

Graham et al. (2005) analytically calculate how the ratio of Sérsic flux to Petrosian flux changes with the Sérsic index of the object. The fraction of light missed by a Petrosian aperture is dependent upon the light profile of source. Figure 4.17 shows the distribution of Sérsic - GAMA r-defined Petrosian magnitude against Sérsic index, redshift, absolute and

apparent magnitude for all r-band objects in the GAMA sample that have passed the star-galaxy separation criteria, and have credible r, u and K r-defined PETRO magnitudes. Graham et al. report a $0.20\,$mag offset for an $n = 4$ profile, and a $0.50\,$mag offset for an $n = 8$ profile. The median $r_{Sersic} - r_{Petrosian}$ offset for objects with $3.9 < n < 4.1$ in this sample is $-0.115\,$mag, with rms scatter of $0.212\,$mag, and $-0.408\,$mag, for objects with $7.9 < n < 8.1$, with rms scatter of $0.292\,$mag. Both results agree with the reported values, within uncertainties. The magnitude offset with Sérsic index function from Figure. 2 (their Panel a) of Graham et al. (2005) is shown in the uppermost plot of Figure 4.17. The function is an extremely good match to the GAMA photometry. Figure 4.18 shows the distribution of Sérsic - SDSS CMODEL magnitude against Sérsic index, redshift, absolute and apparent magnitude for all r-band objects in the GAMA sample that have passed the star-galaxy separation criteria, and have credible r, u and K r-defined PETRO magnitudes. The distributions are very similar to those produced by the Sérsic-Petrosian colours in Figure 4.17. An exception is the distribution with Sérsic index, where the Sérsic - CMODEL offset is distributed closer to $0\,$mag, until n=4, at which point the Sérsic magnitude detects more flux. As the CMODEL magnitude is defined as a combination of n=1 and n=4 profiles, it is unsurprising that it cannot model high n profile sources as well as the GAMA Sérsic magnitude, which allows the n parameter greater freedom.

The r band Sérsic magnitude shows no unexpected behaviour[5]. Sérsic profiling is reliable when undertaken using the higher quality SDSS imaging (particularly gri), but not when using the noisier u band data. It is clear that the u band Sérsic magnitude is not robust enough to support detailed scientific investigations. In order to access a Sérsic-style total magnitude in the u band, it is therefore necessary to create one from existing, reliable data. An approach is devised in Section 4.5.2.

Finally, there is an important caveat to all Sérsic photometry. This photometric system assumes that every object in the sample follows a Sérsic profile. In cases where this is not the case (for instance, tidally interacting objects), the results from the Sérsic photometry are unlikely to be accurate.

---

[5]I have visually inspected the 139 galaxies that are distributed in the $-22 \leq M_{r,Sersic} - 5log_{10}h \leq -21.5$ magnitude bin (i.e., the bright objects where Sérsic profiling would be over-estimating the source luminosity) and only 2 have suffered catastrophic failures. These profiles are viewable at http://star-www.st-and.ac.uk/~dth4/139eye/
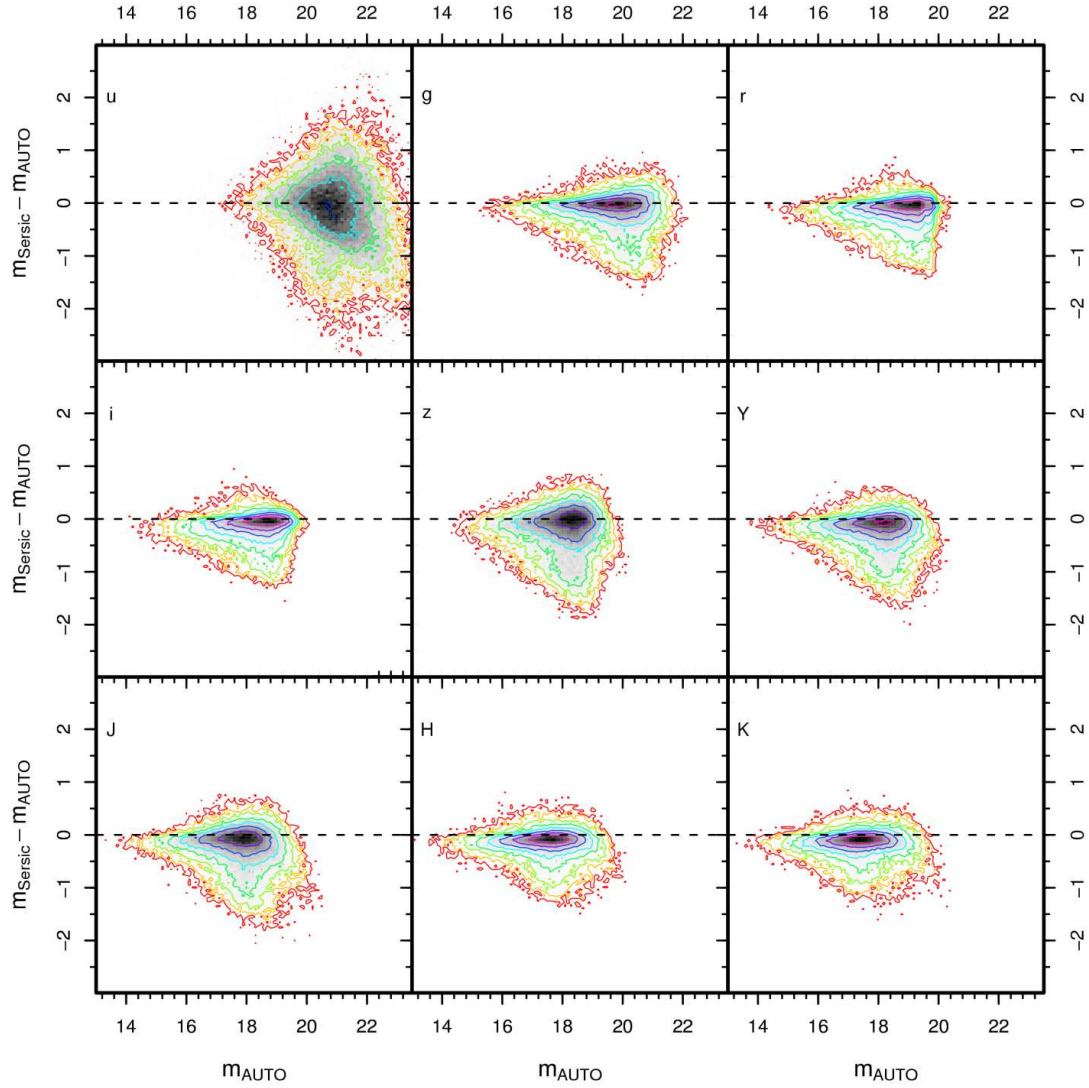
Figure 4.16: Sérsic minus GAMA *r*-defined Auto magnitude against *r*-defined Auto magnitude, in all nine bands, for all objects in the GAMA sample that pass the star-galaxy separation criteria, and have credible *ugrizYJHK r*-defined Auto magnitudes. Contours increase geometrically in powers of 2, from 4 to 512. Bins are $0.1\,\mathrm{mag}$ (x axis) $\times$ $0.05\,\mathrm{mag}$ (y axis) in size.
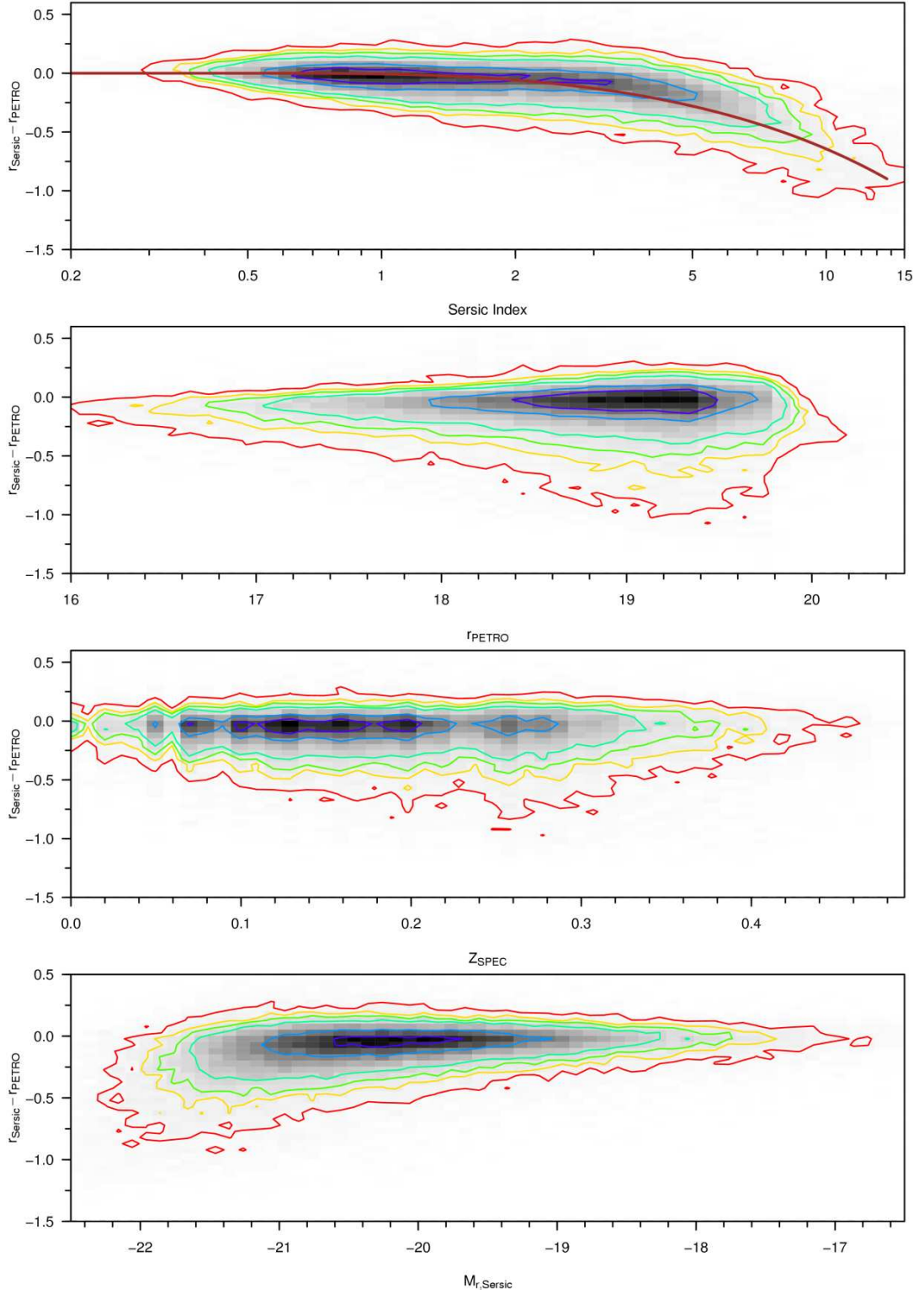
Figure 4.17: Sérsic r - GAMA r-defined Petrosian r against Sérsic index, r-defined r band Petrosian magnitude, z, $M_{r,Sersic}$ for all objects in the GAMA sample that have passed the star-galaxy separation criteria, and have credible $ugrizYJHK$ r-defined Petrosian magnitudes. Contours increase geometrically in powers of 2, from 4 to 512. The brown function plotted in the Sérsic r - GAMA r-defined Petrosian r against Sérsic index plot is taken from Figure. 2 (upper panel) of Graham et al. (2005).
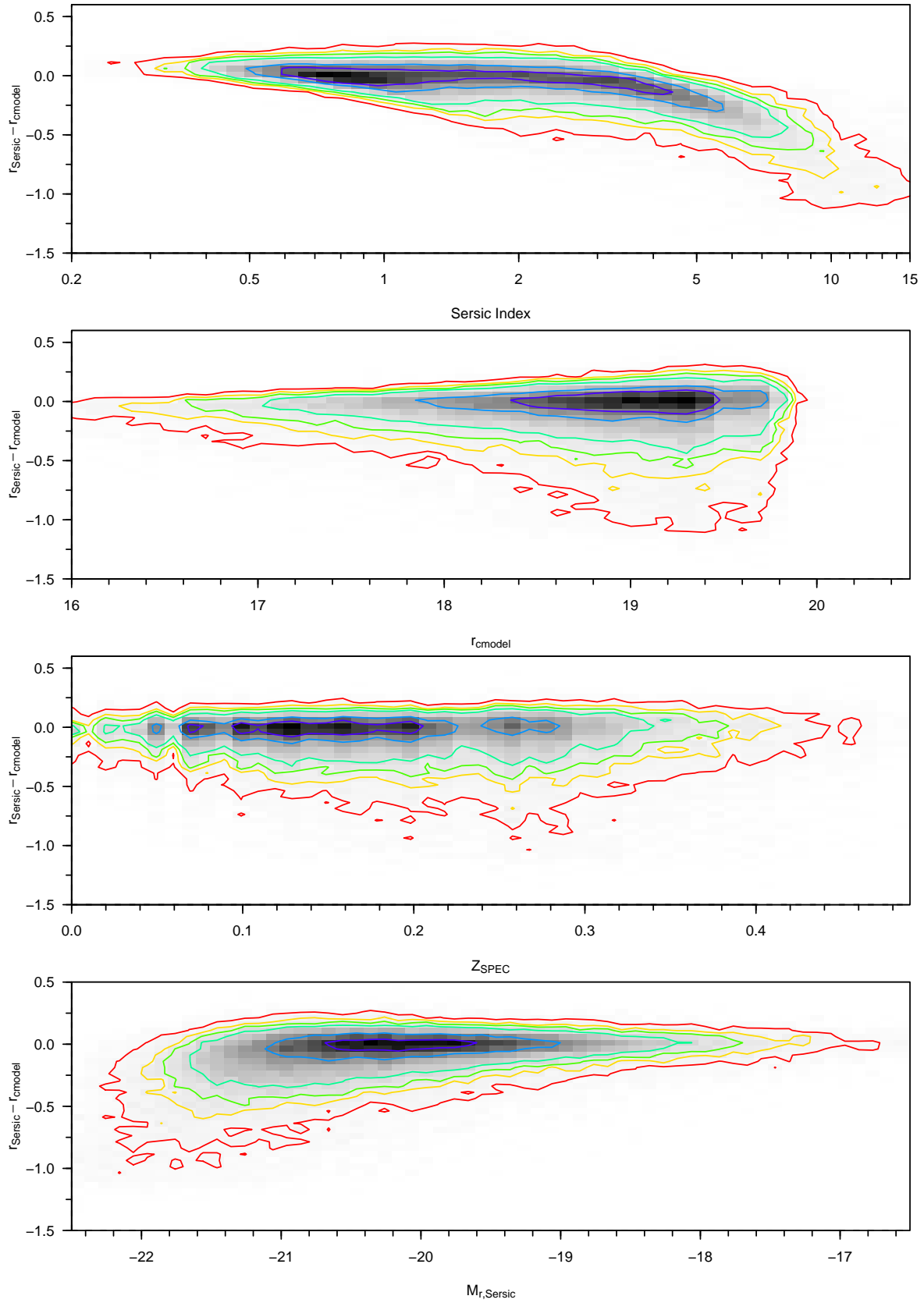
Figure 4.18: Sérsic r - SDSS CMODEL r magnitude against Sérsic index, SDSS r CMODEL magnitude, z, $M_{r,Sersic}$ for all objects in the GAMA sample that have passed the star-galaxy separation criteria, and have credible urK r-defined Petrosian magnitudes. Contours increase geometrically in powers of 2, from 4 to 512.

4.5.2 'Fixed aperture' Sérsic magnitudes

As mentioned in Section 4.2.4, the Sérsic magnitude is taken from a different aperture in each band. Sérsic magnitudes can therefore not be used to generate accurate colours (compare the scatter in the Sérsic colours and the AUTO colours in Figure 4.19). The u band Sérsic magnitudes are not considered to be credible (see Section 4.5.1). However, the r band Sérsic luminosity function may be more desirable than the light-distribution defined aperture r band luminosity functions. The calculation of the total luminosity density using a non-Sérsic aperture system may underestimate the parameter. A system is required that accounts for the additional light found by the Sérsic magnitude, but also provides a credible set of colours.

A further magnitude system is derived. X_{total} is defined using the equation $X_{total} = (X_{auto} - r_{auto}) + r_{Sersic}$, where $auto$ is the r-defined $AUTO$ magnitude. In effect, this creates a measure that combines the total r band flux with optimal colours, using SDSS deblending to give the most accurate catalogue of sources (by matching to the GAMA master catalogue); the best of all possibilities. This system assumes that the colour from the r-defined AUTO aperture would be the same as the colour from a r-defined Sérsic aperture. However, this is the closest estimation to a fixed Sérsic aperture that can be made at this time.

4.5.3 Uncertainties within the GAMA photometry

The gain value in SDSS data is constant within each stripe but varies between stripes. The SDSS mosaic creation process that is detailed in sections 4.1.2 and 4.1.4 combines images from a number of different stripes to generate the master mosaic. As the mosaics are transformed from different zeropoints, the relationship between electrons and pixel counts will be different for each image. Each mosaic must suffer from variations in gain. The `SExtractor` utility can be set up to deal with this anomaly, by using the weightmaps generated by `SWARP`. However, this may introduce a level of surface brightness bias into the resulting catalogue that would be difficult to quantify. The `SExtractor` magnitude error is calculated via the first quartile value, taken from the distribution of gain parameters used to create the mosaic. The Gain used in the SDSS calculation is the average for the
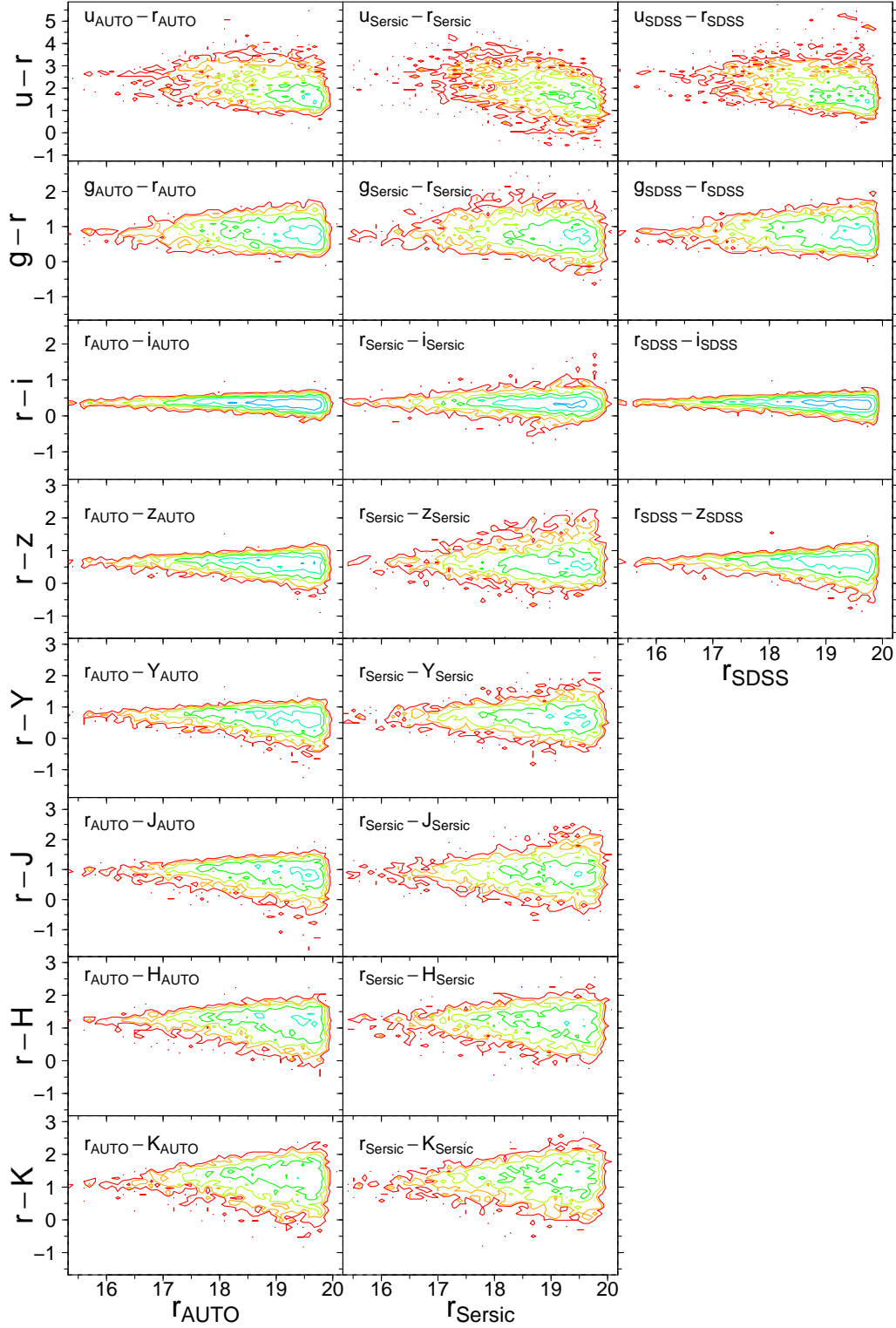
Figure 4.19: *X-r* distributions from GAMA Auto magnitudes, GAMA Sérsic magnitude and SDSS PETROMAGS (left to right), against *r*, for all $X = u,g,i,z,Y,J,H$ and K. Sources used are those within the subset region with credible Auto and Sérsic magnitudes, and without the SDSS saturated object bit set. Contours increase geometrically in powers of 2, from 2 to 512 galaxies bin^{-1}. Bins are $0.1\,\text{mag} \times 0.1\,\text{mag}$ in size

strip. The `SExtractor` error is calculated using Equation 4.5:

$$\Delta m = \frac{1.0857\sqrt{A\sigma^2 + \frac{F}{\text{gain}}}}{F} \tag{4.5}$$

Where A is the area of the aperture, σ is the standard deviation in noise and F is the total flux within the aperture. By using the first quartile gain value, the $\frac{F}{\text{gain}}$ component of the magnitude uncertainty calculation may be overestimated. However, given the amount of background noise in the mosaic, this component will constitute only a small fraction towards the error in the fainter galaxies, and in the brighter galaxies the uncertainty in magnitude due to the aperture definition will be much greater than the `SExtractor` magnitude error itself. The `SExtractor` magnitude error is calculated separately for each aperture type, and is available within the GAMA photometric catalogues.

As attempt was made to quantify the uncertainty due to the aperture definition, in order to calculate its extent relative to the `SExtractor` magnitude error. The cleaned sample defined in section 4.4.1 were used. The dispersion in calculated magnitude between the different photometric methods for this sample are shown in Figures 4.8, 4.9, 4.10, 4.11 and 4.12. Figure 4.20 shows the relative scales of the uncertainty due to a galaxy's aperture definition (calculated from the standard deviation in AUTO/PETRO luminosities from the SDSS survey and the r/K/self-defined catalogues) and the error generated by `SExtractor` in the r band. The aperture definition uncertainty is generally much greater than that due to background variation and $\frac{S}{N}$ that `SExtractor` derives (i.e., the majority of the distribution is to the right of the black line). Figure 4.21 shows how the standard deviation in a galaxy's r band magnitude changes with apparent magnitude. Whilst this uncertainty is larger than the `SExtractor` magnitude error, it is fundamentally a more consistent judgement of the uncertainty in a given galaxy's brightness as it does not assume that any particular extended-source aperture definition is correct. Whilst the dispersion of the relationship increases with apparent magnitude (along with the number of galaxies), the modal standard deviation is approximately constant. Taking this to be a good estimate of the average uncertainty in the apparent magnitude of a galaxy within the sample, the level of confidence in the published apparent magnitudes is ± 0.03 mag in gri, ± 0.06 mag in z, and ± 0.20 mag in u. The same statistics are calculated in the NIR passbands (though
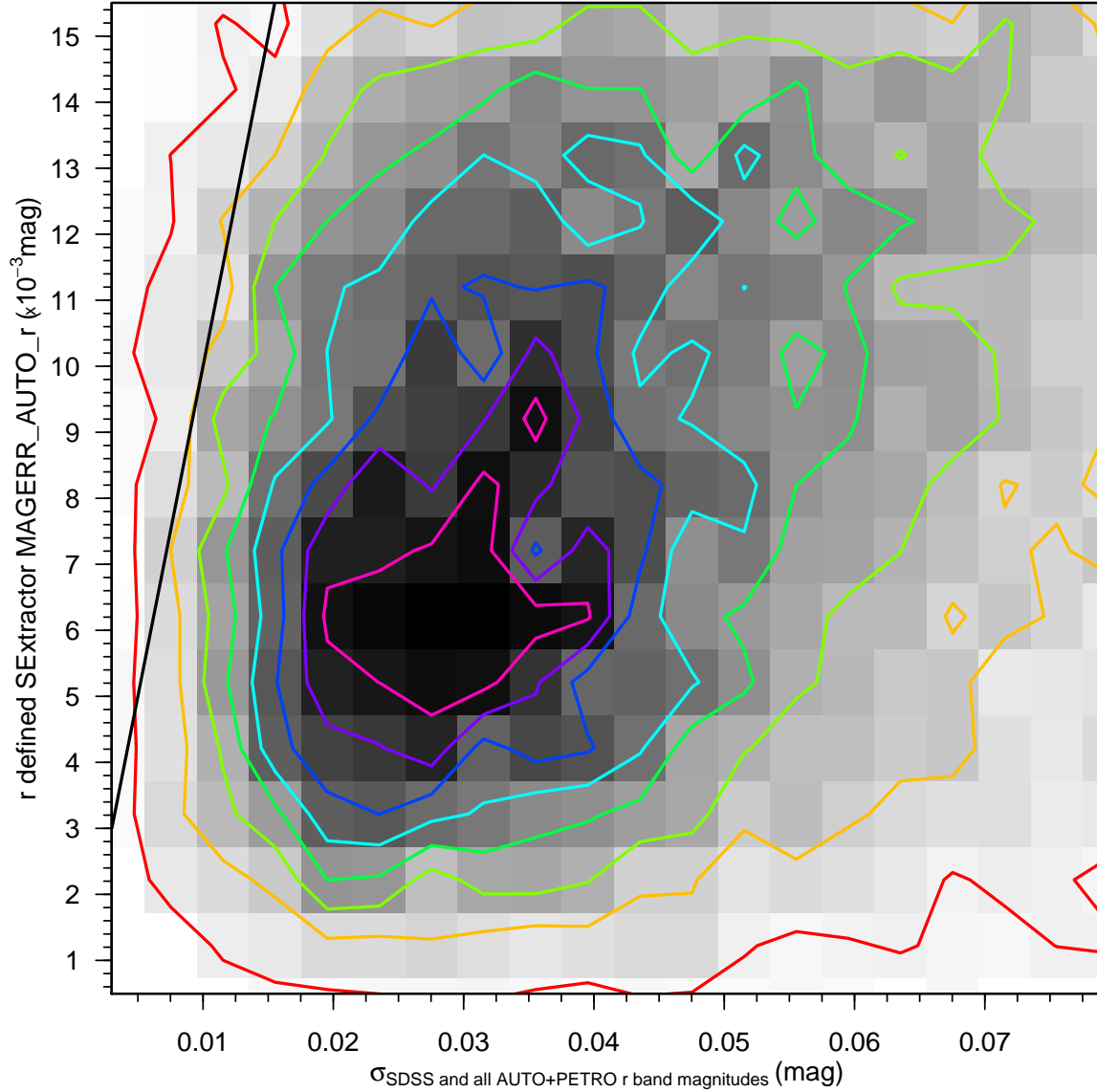
Figure 4.20: The distribution of standard deviation in r band apparent magnitude against SExtractor's calculated magnitude error (using the first quartile gain from the gain distribution of the mosaic's input images) for the clean sample of galaxies, using SDSS, r-defined, K-defined and self-defined AUTO and PETRO magnitudes to calculate the standard deviation. Contours rise linearly by 16 galaxies bin^{-1}, ranging from 8 to 120 galaxies bin^{-1}. Bins are 0.004 mag (x axis) $\times$ 0.001 mag (y axis) in size.

without SDSS PETROMAG). The confidence levels in the published apparent magnitudes are within ± 0.05 mag in $YJHK$; approximately two and a half times the size of the photometric rms error UKIDSS was designed to have (± 0.02 mag, Lawrence et al. 2007).
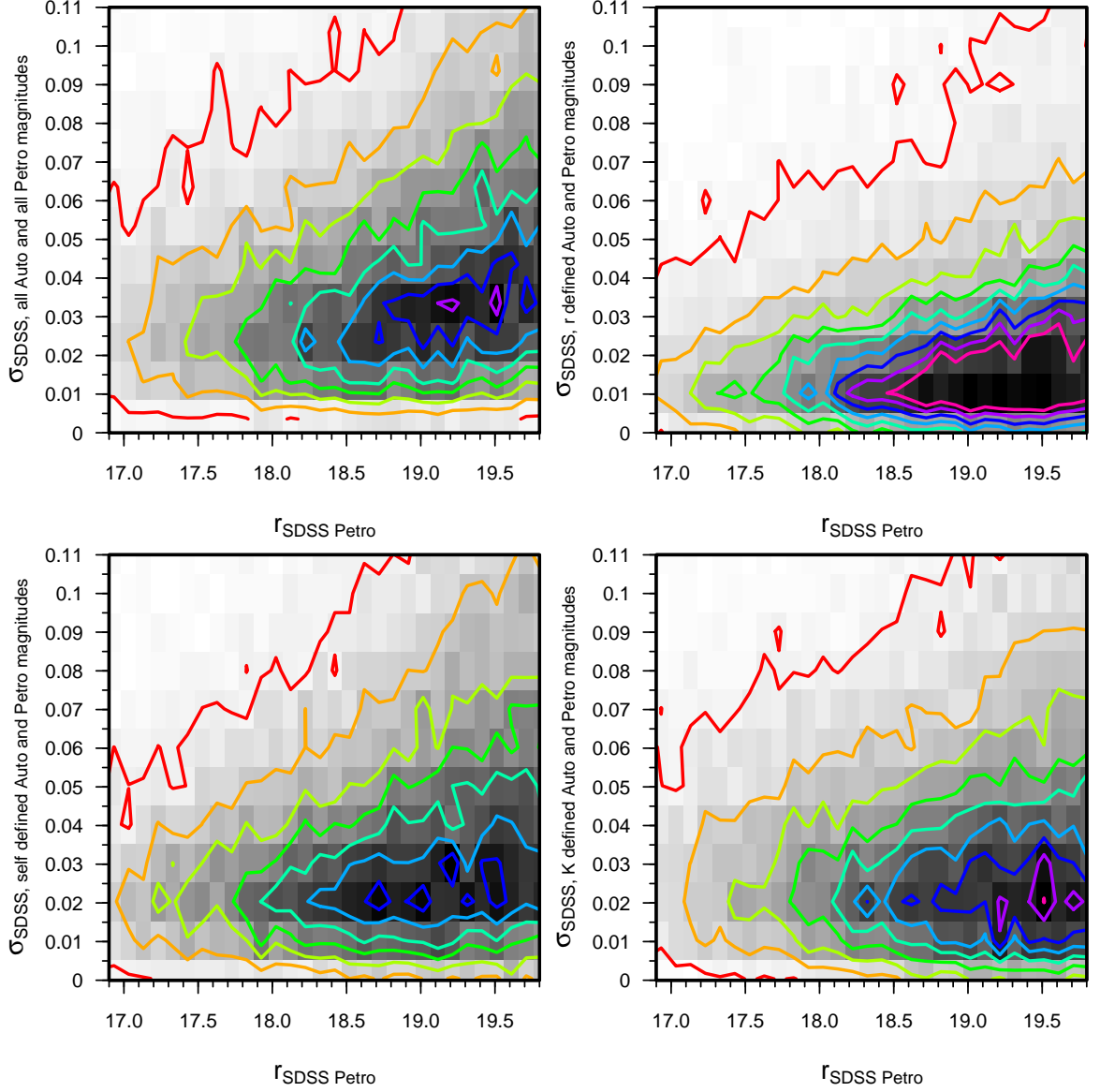
Figure 4.21: The distribution of standard deviation in r band apparent magnitude against apparent magnitude for the clean sample of galaxies, using four different sets of magnitudes to calculate the standard deviation in each case. Contours rise linearly by 20 galaxies bin^{-1}, ranging from 10 to 170 galaxies bin^{-1}. Bins are 0.1 mag (x axis) $\times$ 0.01 mag (y axis) in size.

4.5.4 Number counts

In order to construct a unbiased dataset, it is necessary to calculate the apparent magnitude where the GAMA sample ceases to be complete. GAMA falls within the apparent magnitude range where galaxy number counts increase linearly with increasing magnitude. The apparent magnitude limit of the GAMA sample can be ascertained by finding the magnitude where this relation no longer holds.

Definition of GAMA galaxy sample used in this section

The GAMA sample used in this section is defined as those SDSS objects that are within the area that has complete $ugrizY JHK$ colour coverage, and have passed the star-galaxy separation criteria. Of the 908022 objects in the GAMA master catalogue, only 124622 fulfil this criteria. The area of sky that has complete GAMA $ugrizY JHK$ coverage is 129.1232 ± 0.0008 sq deg; 89.7% of the entire GAMA region. All magnitudes in this section are r-defined $AUTO$ magnitudes, unless otherwise defined.

Determination of apparent magnitude limits

Figure 4.22 shows how the sky density of GAMA galaxies in the nine passbands varies with apparent magnitude. The distributions peak in the 0.1 magnitude bins centred at $u = 21.25$, $g = 20.55$, $r = 19.75$, $i = 19.25$, $z = 18.75$, $Y = 18.65$, $J = 18.45$, $H = 18.05$ and $K = 17.75$ mag. Tables 4.8, 4.9 and 4.10 contain the number counts of GAMA galaxies in $ugrizY JHK$, this time using 0.25 magnitude bins. Poissonian uncertainties are also included. Both sets of data have been converted to $\mathrm{deg}^{-2}\ \mathrm{mag}^{-1}$ units.

The r band number count drop off, despite hitting the PETROMAG_R= 19.8 mag GAMA main sample magnitude limit, is not absolute because the SDSS limit was extended to PETROMAG_R= 20.5 mag in the GAMA 12 region so that useful filler objects could be selected, and because radio/K/z band selected objects in G9 and G15 will also be included within the catalogue. Objects that are fainter than $r_{model} = 20.5$ mag (722 sources; 0.5% of the sample) will be due to differences in object extraction between SDSS and `SExtractor`, as mentioned in previous sections.

The turnovers in Figure 4.22 will occur where the $r = 19.8$ mag limit is reached for galaxies with the median $passband - r$ colour. GAMA is within the domain where the number of galaxies within a magnitude bin increases linearly with increasing apparent magnitude.

A deviation from this relationship is visible in the figure approximately 3 magnitude bins before the turnover occurs in all bands except r. This effect is due to colour incompleteness becoming a factor. Unfortunately, despite the radio/K/z selection, there will be a population of objects that are bright in other passbands, but too faint in r to be included within the GAMA sample. Assuming the $passband - r$ colour distribution is approximately Gaussian, this population will feature predominantly in the apparent magnitude bins near the turnover, causing the characteristic flattening that is seen. Accounting for this effect, the apparent magnitude sample limits of the GAMA sample is defined to be a few bins brighter than this turnover, where the linear relationship still holds. The apparent magnitude limits are set to $u = 21.0$, $g = 20.3$, $r = 19.8$, $i = 19.0$, $z = 18.5$, $Y = 18.4$, $J = 18.2$, $H = 17.8$ and $K = 17.6$ mag.

GAMA apparent-magnitude limited catalogues

Table 4.11 contains the sizes of the apparent magnitude limited samples, and their current redshift completeness. The magnitude limited optical samples contain approximately forty thousand less galaxies than the equivalent samples in Blanton et al. (2003), which covers the SDSS DR2 region, but extend two magnitudes deeper. When number counts are compared to 6dFGS (Jones et al., 2006); the GAMA samples are also smaller in area coverage, but similar in size and much deeper in magnitude completeness. The MGC-SDSS-UKIDSS sample (Chapter 3), the previous attempt at defining a sample across the optical and NIR, was just one tenth of the size and was $0.2 - 1.8$ mag shallower. A small fraction of the GAMA dataset has not been spectroscopically sampled. After the completion of the 2008-2009 allocations of AAOmega spectroscopy, the apparent magnitude limited samples have $\geq 75\%$ completeness. After the completion of the 2010 allocation, the mean overall redshift completeness of the GAMA survey was 94.4% (Driver et al., 2010).

4.5.5 Incorporating GALEX data

The GAMA sample has also been combined with UV data. The GAMA master catalogue has been matched to GALEX photometry (Wyder et al., 2005). As GALEX observations are low resolution (typical imaging FWHM ~ 10 arcsec), the matching is complex compared to the simple UKIDSS/SDSS matching described within this chapter, as a number of
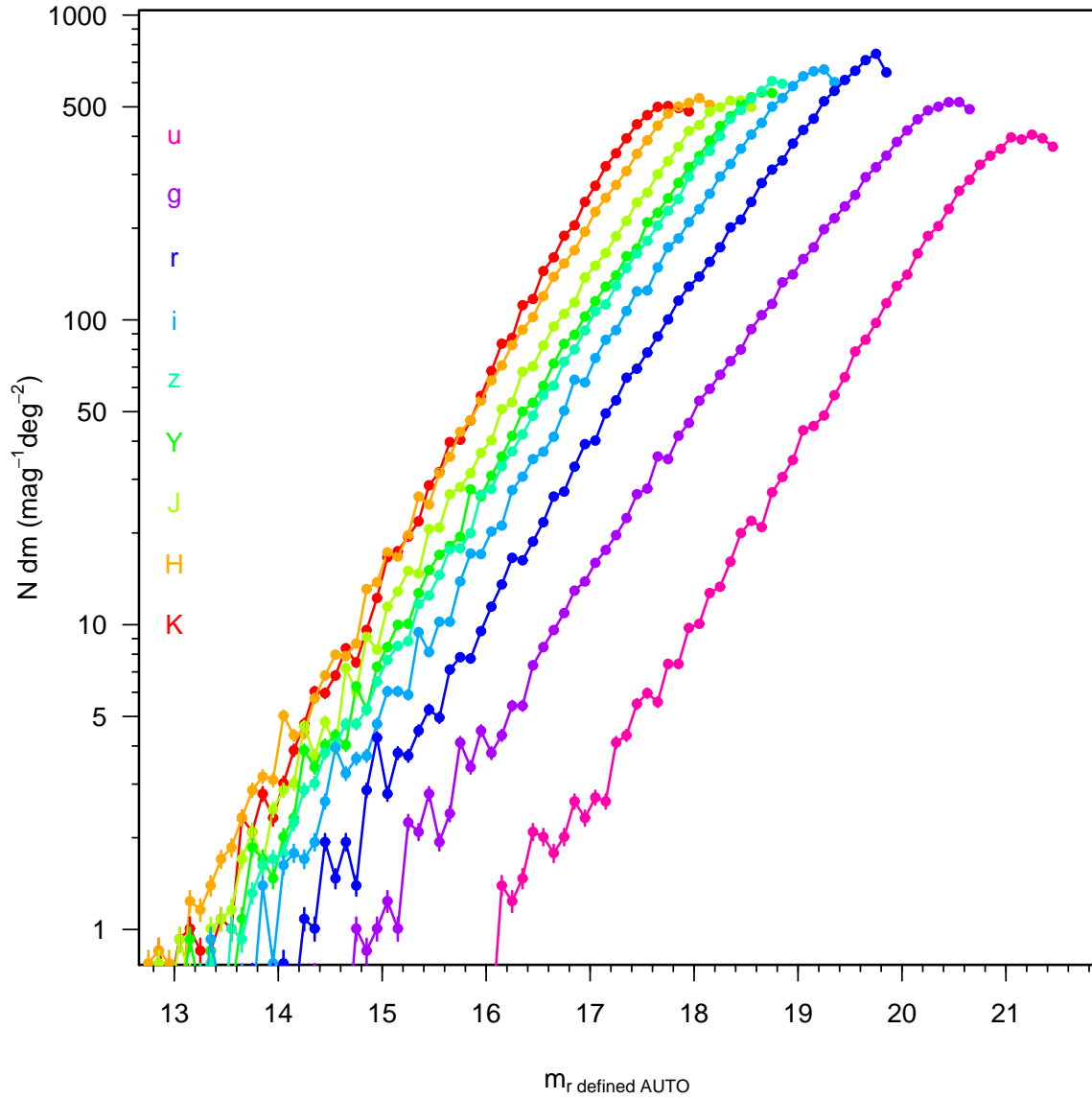
Figure 4.22: Number counts of GAMA galaxies (sources that have passed the star-galaxy separation criteria) with good *ugrizY JHK* colours, split into 0.1 magnitude bins and divided by the total area they cover. Error bars shown are for Poissonian number counts.

u (mag)	$N_u(m) \pm \sigma_{N_u(m)}$ $(deg^{-2}\ (mag)^{-1})$	g (mag)	$N_g(m) \pm \sigma_{N_g(m)}$ $(deg^{-2}\ (mag)^{-1})$	r (mag)	$N_r(m) \pm \sigma_{N_r(m)}$ $(deg^{-2}\ (mag)^{-1})$
12.125	0.031 ± 0.015	10.125	0 ± 0	10.125	0.031 ± 0.015
12.375	0 ± 0	10.375	0 ± 0	10.375	0 ± 0
12.625	0 ± 0	10.625	0 ± 0	10.625	0 ± 0
12.875	0 ± 0	10.875	0.031 ± 0.015	10.875	0.031 ± 0.015
13.125	0 ± 0	11.125	0 ± 0	11.125	0 ± 0
13.375	0.031 ± 0.015	11.375	0 ± 0	11.375	0.124 ± 0.031
13.625	0.093 ± 0.027	11.625	0.031 ± 0.015	11.625	0.062 ± 0.022
13.875	0.062 ± 0.022	11.875	0 ± 0	11.875	0 ± 0
14.125	0.093 ± 0.027	12.125	0.062 ± 0.022	12.125	0.031 ± 0.015
14.375	0.062 ± 0.022	12.375	0.124 ± 0.031	12.375	0.031 ± 0.015
14.625	0.062 ± 0.022	12.625	0.031 ± 0.015	12.625	0.062 ± 0.022
14.875	0.062 ± 0.022	12.875	0.031 ± 0.015	12.875	0.155 ± 0.035
15.125	0.124 ± 0.031	13.125	0.031 ± 0.015	13.125	0.217 ± 0.041
15.375	0.248 ± 0.044	13.375	0.062 ± 0.022	13.375	0.186 ± 0.038
15.625	0.279 ± 0.046	13.625	0.062 ± 0.022	13.625	0.558 ± 0.066
15.875	0.527 ± 0.064	13.875	0.248 ± 0.044	13.875	0.589 ± 0.068
16.125	0.929 ± 0.085	14.125	0.248 ± 0.044	14.125	0.712 ± 0.074
16.375	1.735 ± 0.116	14.375	0.712 ± 0.074	14.375	1.425 ± 0.105
16.625	1.828 ± 0.119	14.625	0.62 ± 0.069	14.625	1.611 ± 0.112
16.875	2.478 ± 0.139	14.875	0.836 ± 0.08	14.875	3.16 ± 0.156
17.125	3.098 ± 0.155	15.125	1.27 ± 0.099	15.125	3.253 ± 0.159
17.375	4.616 ± 0.189	15.375	2.478 ± 0.139	15.375	4.771 ± 0.192
17.625	6.01 ± 0.216	15.625	2.447 ± 0.138	15.625	6.536 ± 0.225
17.875	8.457 ± 0.256	15.875	4.089 ± 0.178	15.875	8.333 ± 0.254
18.125	11.772 ± 0.302	16.125	4.213 ± 0.181	16.125	13.352 ± 0.322
18.375	17.1 ± 0.364	16.375	6.32 ± 0.221	16.375	17.286 ± 0.366
18.625	22.273 ± 0.415	16.625	9.139 ± 0.266	16.625	24.783 ± 0.438
18.875	31.815 ± 0.496	16.875	13.166 ± 0.319	16.875	34.2 ± 0.515
19.125	44.763 ± 0.589	17.125	16.728 ± 0.36	17.125	46.808 ± 0.602
19.375	58.58 ± 0.674	17.375	24.225 ± 0.433	17.375	64.28 ± 0.706
19.625	84.973 ± 0.811	17.625	31.722 ± 0.496	17.625	85.933 ± 0.816
19.875	117.159 ± 0.953	17.875	42.719 ± 0.575	17.875	118.491 ± 0.958
20.125	159.754 ± 1.112	18.125	58.673 ± 0.674	18.125	151.452 ± 1.083
20.375	211.736 ± 1.281	18.375	74.502 ± 0.76	18.375	200.955 ± 1.248
20.625	282.831 ± 1.48	18.625	101.299 ± 0.886	18.625	271.524 ± 1.45
20.875	351.602 ± 1.65	18.875	132.122 ± 1.012	18.875	347.885 ± 1.641
21.125	396.304 ± 1.752	19.125	170.256 ± 1.148	19.125	454.357 ± 1.876
21.375	386.731 ± 1.731	19.375	222.175 ± 1.312	19.375	575.729 ± 2.112
		19.625	282.428 ± 1.479	19.625	695.832 ± 2.321
		19.875	356.559 ± 1.662	19.875	540.445 ± 2.046
		20.125	446.148 ± 1.859		
		20.375	505.471 ± 1.979		
		20.625	492.894 ± 1.954		

Table 4.8: Number counts for the *ugr* filters, using r-defined AUTO photometry, with Poissonian uncertainties.

i (mag)	$N_i(m)\pm\sigma_{N_i(m)}$ $(deg^{-2}\ (mag)^{-1})$	z (mag)	$N_z(m)\pm\sigma_{N_z(m)}$ $(deg^{-2}\ (mag)^{-1})$	Y (mag)	$N_Y(m)\qquad\pm\sigma_{N_Y(m)}$ $(deg^{-2}\ (mag)^{-1})$
9.375	0 ± 0	9.375	0 ± 0	9.375	0.031 ± 0.015
9.625	0 ± 0	9.625	0.031 ± 0.015	9.625	0 ± 0
9.875	0.031 ± 0.015	9.875	0 ± 0	9.875	0.031 ± 0.015
10.125	0 ± 0	10.125	0.031 ± 0.015	10.125	0 ± 0
10.375	0.031 ± 0.015	10.375	0 ± 0	10.375	0 ± 0
10.625	0 ± 0	10.625	0.124 ± 0.031	10.625	0.124 ± 0.031
10.875	0.124 ± 0.031	10.875	0.031 ± 0.015	10.875	0.031 ± 0.015
11.125	0.031 ± 0.015	11.125	0.031 ± 0.015	11.125	0.031 ± 0.015
11.375	0.031 ± 0.015	11.375	0 ± 0	11.375	0 ± 0
11.625	0 ± 0	11.625	0.031 ± 0.015	11.625	0.062 ± 0.022
11.875	0.031 ± 0.015	11.875	0.031 ± 0.015	11.875	0.062 ± 0.022
12.125	0.031 ± 0.015	12.125	0.093 ± 0.027	12.125	0.093 ± 0.027
12.375	0.186 ± 0.038	12.375	0.217 ± 0.041	12.375	0.186 ± 0.038
12.625	0.186 ± 0.038	12.625	0.248 ± 0.044	12.625	0.217 ± 0.041
12.875	0.124 ± 0.031	12.875	0.31 ± 0.049	12.875	0.403 ± 0.056
13.125	0.372 ± 0.054	13.125	0.558 ± 0.066	13.125	0.651 ± 0.071
13.375	0.682 ± 0.073	13.375	0.62 ± 0.069	13.375	0.743 ± 0.076
13.625	0.62 ± 0.069	13.625	1.022 ± 0.089	13.625	1.022 ± 0.089
13.875	0.96 ± 0.086	13.875	1.611 ± 0.112	13.875	1.673 ± 0.114
14.125	1.704 ± 0.115	14.125	1.983 ± 0.124	14.125	2.478 ± 0.139
14.375	2.168 ± 0.13	14.375	3.501 ± 0.165	14.375	3.779 ± 0.171
14.625	3.748 ± 0.17	14.625	4.554 ± 0.188	14.625	4.585 ± 0.188
14.875	3.965 ± 0.175	14.875	5.545 ± 0.207	14.875	6.289 ± 0.221
15.125	5.917 ± 0.214	15.125	8.116 ± 0.251	15.125	9.015 ± 0.264
15.375	8.302 ± 0.254	15.375	11.555 ± 0.299	15.375	13.506 ± 0.323
15.625	10.749 ± 0.289	15.625	16.697 ± 0.36	15.625	17.689 ± 0.37
15.875	16.635 ± 0.359	15.875	21.994 ± 0.413	15.875	25.774 ± 0.447
16.125	22.211 ± 0.415	16.125	32.031 ± 0.498	16.125	34.727 ± 0.519
16.375	31.598 ± 0.495	16.375	43.4 ± 0.58	16.375	49.937 ± 0.622
16.625	40.984 ± 0.563	16.625	61.43 ± 0.69	16.625	69.484 ± 0.734
16.875	60.872 ± 0.687	16.875	83.703 ± 0.805	16.875	93.802 ± 0.852
17.125	82.464 ± 0.799	17.125	113.318 ± 0.937	17.125	124.873 ± 0.983
17.375	111.367 ± 0.929	17.375	151.266 ± 1.082	17.375	161.83 ± 1.12
17.625	142.995 ± 1.052	17.625	198.849 ± 1.241	17.625	221.277 ± 1.309
17.875	193.397 ± 1.224	17.875	264.213 ± 1.43	17.875	292.124 ± 1.504
18.125	253.432 ± 1.401	18.125	356.156 ± 1.661	18.125	375.424 ± 1.705
18.375	336.423 ± 1.614	18.375	458.973 ± 1.885	18.375	480.285 ± 1.929
18.625	438.093 ± 1.842	18.625	561.2 ± 2.085	18.625	549.831 ± 2.064
18.875	549.336 ± 2.063	18.875	582.39 ± 2.124		
19.125	649.457 ± 2.243				
19.375	564.205 ± 2.09				

Table 4.9: Number counts for the izY filters, using r-defined AUTO photometry, with Poissonian uncertainties.

J (mag)	$N_J(m) \pm \sigma_{N_J(m)}$ $(deg^{-2}\ (mag)^{-1})$	H (mag)	$N_H(m) \pm \sigma_{N_H(m)}$ $(deg^{-2}\ (mag)^{-1})$	K (mag)	$N_K(m) \pm \sigma_{N_K(m)}$ $(deg^{-2}\ (mag)^{-1})$
9.125	0 ± 0	9.125	0.031 ± 0.015	9.125	0 ± 0
9.375	0 ± 0	9.375	0 ± 0	9.375	0.031 ± 0.015
9.625	0.031 ± 0.015	9.625	0.031 ± 0.015	9.625	0 ± 0
9.875	0.031 ± 0.015	9.875	0 ± 0	9.875	0.031 ± 0.015
10.125	0 ± 0	10.125	0.093 ± 0.027	10.125	0.031 ± 0.015
10.375	0.062 ± 0.022	10.375	0.062 ± 0.022	10.375	0.062 ± 0.022
10.625	0.062 ± 0.022	10.625	0.031 ± 0.015	10.625	0.031 ± 0.015
10.875	0.062 ± 0.022	10.875	0 ± 0	10.875	0.062 ± 0.022
11.125	0 ± 0	11.125	0 ± 0	11.125	0 ± 0
11.375	0 ± 0	11.375	0.031 ± 0.015	11.375	0 ± 0
11.625	0.031 ± 0.015	11.625	0.124 ± 0.031	11.625	0.062 ± 0.022
11.875	0.124 ± 0.031	11.875	0.155 ± 0.035	11.875	0.062 ± 0.022
12.125	0.155 ± 0.035	12.125	0.248 ± 0.044	12.125	0.186 ± 0.038
12.375	0.217 ± 0.041	12.375	0.372 ± 0.054	12.375	0.217 ± 0.041
12.625	0.31 ± 0.049	12.625	0.527 ± 0.064	12.625	0.31 ± 0.049
12.875	0.527 ± 0.064	12.875	0.774 ± 0.077	12.875	0.682 ± 0.073
13.125	0.712 ± 0.074	13.125	0.867 ± 0.082	13.125	0.867 ± 0.082
13.375	0.898 ± 0.083	13.375	1.518 ± 0.108	13.375	1.022 ± 0.089
13.625	1.549 ± 0.11	13.625	2.23 ± 0.131	13.625	1.735 ± 0.116
13.875	2.076 ± 0.127	13.875	3.098 ± 0.155	13.875	2.478 ± 0.139
14.125	3.191 ± 0.157	14.125	4.492 ± 0.187	14.125	3.903 ± 0.174
14.375	4.43 ± 0.185	14.375	6.041 ± 0.216	14.375	5.545 ± 0.207
14.625	5.7 ± 0.21	14.625	7.806 ± 0.246	14.625	7.621 ± 0.243
14.875	8.147 ± 0.251	14.875	12.763 ± 0.314	14.875	10.192 ± 0.281
15.125	12.639 ± 0.313	15.125	17.72 ± 0.37	15.125	17.689 ± 0.37
15.375	17.224 ± 0.365	15.375	24.194 ± 0.433	15.375	23.915 ± 0.43
15.625	24.163 ± 0.433	15.625	35.036 ± 0.521	15.625	35.966 ± 0.528
15.875	33.425 ± 0.509	15.875	49.379 ± 0.618	15.875	49.999 ± 0.622
16.125	46.715 ± 0.601	16.125	70.413 ± 0.738	16.125	77.879 ± 0.777
16.375	66.448 ± 0.717	16.375	94.298 ± 0.855	16.375	109.198 ± 0.92
16.625	92.222 ± 0.845	16.625	133.237 ± 1.016	16.625	158.422 ± 1.108
16.875	121.434 ± 0.97	16.875	176.792 ± 1.17	16.875	218.272 ± 1.3
17.125	162.976 ± 1.123	17.125	245.781 ± 1.38	17.125	305.631 ± 1.538
17.375	220.348 ± 1.306	17.375	319.602 ± 1.573	17.375	406.031 ± 1.773
17.625	288.159 ± 1.494	17.625	420.931 ± 1.806	17.625	488.99 ± 1.946
17.875	384.191 ± 1.725	17.875	504.448 ± 1.977	17.875	491.716 ± 1.951
18.125	464.796 ± 1.897	18.125	515.229 ± 1.998		
18.375	521.394 ± 2.009				

Table 4.10: Number counts for the *JHK* filters, using r-defined AUTO photometry, with Poissonian uncertainties.

Band	Sources	Redshifts	% Redshifts
Star-galaxy separation criteria only	124622	82926	66.5
u≤21.0	46006	39767	86.4
g≤20.3	67913	58956	86.8
r≤19.8	106032	79672	75.1
i≤19.0	74885	66981	89.4
z≤18.5	59470	55202	92.8
Y≤18.4	57739	53339	92.4
J≤18.2	60213	54264	90.1
H≤17.8	55734	51033	91.6
K≤17.5	46424	43252	93.2

Table 4.11: The number of sources within the star-galaxy separation and apparent magnitude limited GAMA samples that have a complete set of good *ugrizYJHK* r-defined magnitudes, the number of those sources that have redshifts from first and second year data and the percentage redshift completeness. Apparent magnitudes are r-defined magnitudes, using the AB magnitude system.

separate SDSS objects may be matched to one larger GALEX object. The precise method of generating the GALEX matches is described in Robotham et al (in prep). In summary, all SDSS objects within the 90% Petrosian radius of a GALEX source are considered to be contributing flux to that source. The flux of the GALEX object is then apportioned to the SDSS objects, with the allotted fraction calculated via the distance between the SDSS and GALEX object. If no other nearby source is within 2.5 mag (in g) of the closest match, all flux is assigned to the closest match. GALEX has two distinct filters NUV and FUV. The generated magnitudes are stored within columns labelled *MAG_AUTO_FUV* and *MAG_AUTO_NUV*.

4.5.6 SED fits using GAMA data

The SEDs of 10 galaxies selected at random from the GAMA sample are shown in Figure 4.23. The GAMA-Galex UV luminosities, GAMA Total luminosities and Petrosian luminosities taken from the UKIDSS and SDSS surveys are shown, and 2 Bruzual-Charlot (Bruzual & Charlot, 2003) galaxy models with different ages and metallicities are overplotted as a guide. The models are normalised via least squares best-fitting to the 9 GAMA datapoints. For image clarity, the uncertainties on SDSS and UKIDSS datapoints are not shown. GAMA UV uncertainties are taken from `SExtractor` magnitude errors. GAMA optical and NIR uncertainties are calculated using the standard deviation in the luminosity when different photometric methods are used (following the method described in Section 4.5.3). In some cases, the photometry provided by survey catalogues and the
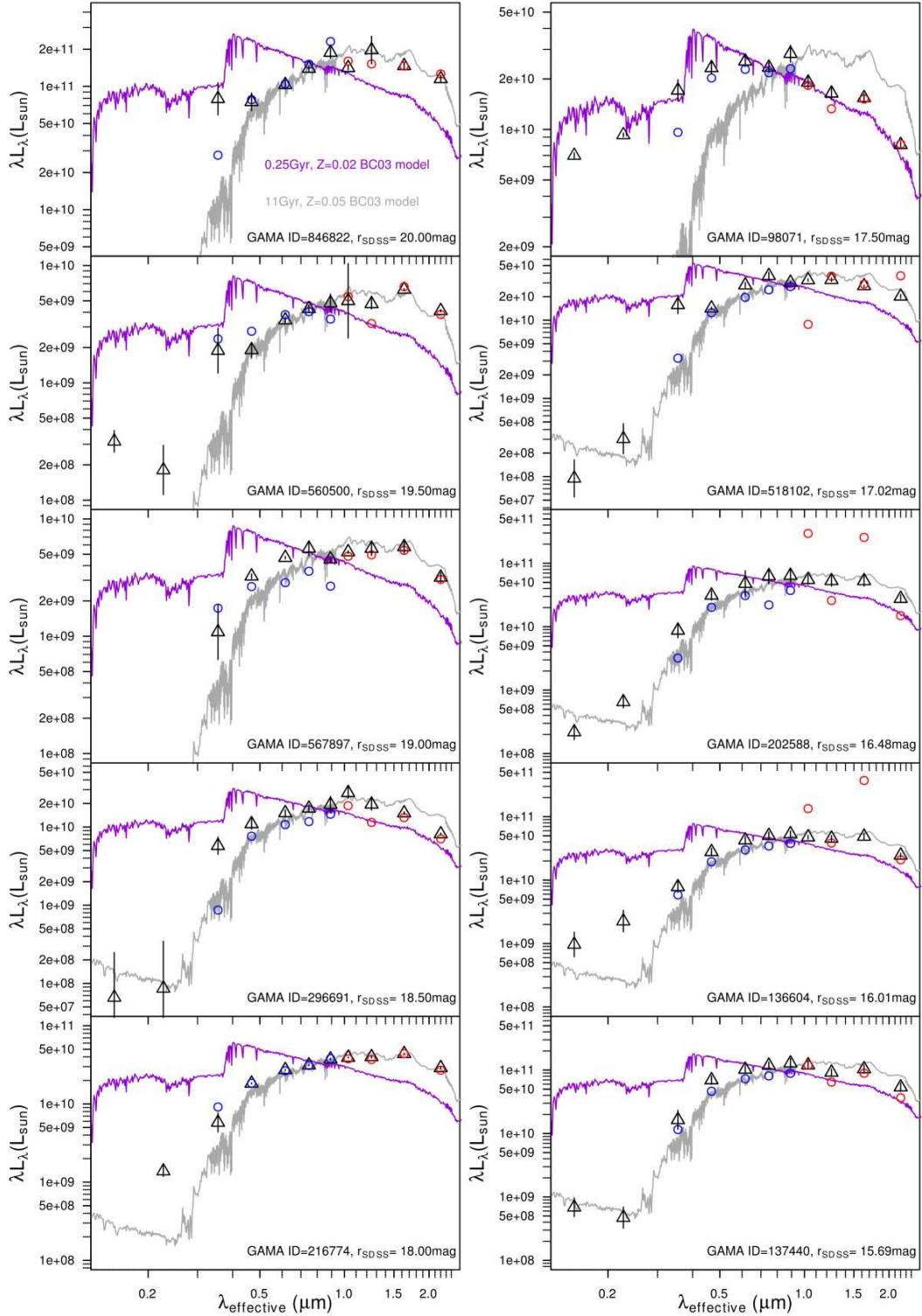
Figure 4.23: SEDs of 10 GAMA galaxies using GAMA matched GALEX photometry and r defined AUTO $ugrizYJHK$ photometry (black triangles), and the comparable SDSS (blue circles) and UKIDSS (red circles) PETROMAG photometry. Uncertainties shown for GAMA $ugrizYJHK$ points are calculated from the standard deviation in the photometry (as in Section 4.5.3). GAMA-GALEX uncertainties are `SExtractor` errors from the GALEX pipeline catalogues. Two Bruzual-Charlot 03 models are also plotted: the grey line is a 11 Gyr model using Z=0.05 and the purple line is a 0.25Gyr model using Z=0.02 (Z⊙). The models shown are the same as those in Figure 4.15.

137

GAMA photometry are near identical, and match the galaxy models well (see 216774 and 137440 on Figure 4.23). In other cases, where there is a discrepancy between the derived luminosities and the Survey-catalogue parameters, the GAMA photometry is a better fit to the models (e.g., 202588, 518102 on Figure 4.23). The r-defined AUTO colours are judged to be a significant improvement.

4.5.7   Released GAMA photometry

The GAMA photometry described in this chapter provides the *GamaPhotom* catalogue. This catalogue is filtered and combined with the other GAMA catalogues to produce the first GAMA data release, defined in Driver et al, 2010. (in prep).

In the following chapter, I use the dataset defined here to quantify biases within the original input catalogue, and to produce CSED parameters from the GAMA catalogue. This provides a larger, deeper sample than the MGC-SDSS-UKIDSS dataset in Chapter 3, with matched-aperture photometry available throughout all optical and NIR passbands. The larger sample size also allows joint luminosity-surface brightness modelling without Poissonian uncertainty becoming a serious inconvenience. This dataset therefore provides four of the five improvements I outlined in Chapter 3.

5

The GAMA $ugrizYJHK$ sample: Statistical analysis

In Chapter 4, I produced the GAMA photometric sample from reduced SDSS and UKIDSS imaging. I also outlined the work undertaken to ascertain that the source detection algorithm works effectively, the photometric distribution of the sample is well understood, the level of uncertainty within the photometry is known, and that the apparent magnitude limits of the sample are quantified. I have shown that the colours produced by the photometry have a higher consistency than those produced by combining the UKIDSS and SDSS survey catalogues.

In this chapter, I undertake a series of empirical tests to calculate the effects of different biases within the dataset. I calculate the effects upon the best fitting Schechter parameters when different photometric systems are used to derive the luminosity distribution. This is undertaken using r band photometry. I generate bivariate brightness distributions, in order to judge the effects that surface brightness incompleteness have upon the sam-

ple, and where such effects occur. I compare the best-fitting Choloniewski models to the GAMA samples with those found in the literature, and I also compare the quality of the fit between the Choloniewski models and the data to the quality of the fit between the modified-functional form described in Chapter 1 and the data.

Finally, I present the main result of this thesis. In Chapter 3 I presented a set of *ugrizY JHK* CSED datapoints from a MGC-SDSS-UKIDSS selected population of galaxies. In this chapter, I present a set of *ugrizY JHK* datapoints from a GAMA defined sample of galaxies, accounting for the effects of surface brightness incompleteness, inconsistency between survey catalogues, the choice of photometric method and cosmic variance. I compare this dataset to the earlier MGC-SDSS-UKIDSS result, and theoretical models that combine a universal IMF with a recent estimate of the cosmic star formation history and the PEGASE stellar population synthesis code.

5.1   The impact of the photometric method on the observed luminosity distribution

The work within this section has been accepted by MNRAS, but has currently not been published. It is available on the arXiv (Hill et al., 2010b).

5.1.1   Comparison between r band luminosity functions

In order to illustrate the effect that the photometric method has on statistical measurements of the galaxy population, the r band luminosity function is derived using 9 different photometric methods applied to the same population of galaxies. This allows the comparison of all the photometric systems discussed in Chapter 4, and the original SDSS photometry. This should provide a consistent analysis for each method, removing all systematic effects except for that produced by the photometric method.

5.1.2   Luminosity distribution and function measurement

A number of techniques exist for measuring the galaxy luminosity distribution (see Willmer 1997), and functions to parametrise it. This section follows the methodology described in Chapter 1. The stepwise maximum-likelihood method (SWML), originally described in detail in Efstathiou et al. (1988), is used, and the standard functional form, the Schechter luminosity function (Schechter, 1976) is assumed. In Chapter 1, a unique flux

limit for each object was described, based upon the spectroscopic limit and an individual magnitude limit. This magnitude limit is used to calculate the photometric offset between the studied photometric method and the SDSS PETROMAG photometry used for spectroscopic selection. The apparent magnitude threshold is set for each object using $r_{\mathrm{aperture,limit}} = 19.4\,\mathrm{mag}$. A known weakness of the SWML method is that it requires normalisation to calculate the luminosity density. The method of luminosity density scaling described in Chapter 1 is utilised. This involves calculating the number density of galaxies within a 1 magnitude range containing the M^* galaxies, and using this to work out the required scaling multiplier.

Cosmic variance within the GAMA regions is also accounted for. The source density of galaxies within a 5150 sq deg section of the SDSS survey (large enough for cosmic variance to be negligible) with de-reddened $-21.09 < M_r - 5\log_{10}\mathrm{h} < -20.09$ (i.e. $M^* - 5\log_{10}\mathrm{h} \pm 0.5\,\mathrm{mag}$, taking $M^* - 5\log_{10}\mathrm{h}$ from the r-defined r_{AUTO} photometry) and $0.033 < z < 0.1$ is calculated, and compared with the source density calculated (using the same catalogue) from the GAMA regions of sky. Figure 20 of Driver et al. (2010) states that the GAMA regions are 85% as dense as the SDSS superpopulation[1]. The universal ϕ^* parameter can therefore be calculated by scaling the GAMA ϕ^* parameter by a further factor of $\frac{1}{0.85}$.

The area incompleteness of the K band-defined sample is accounted for by calculating the normalisation volume with Area=133.5 sq deg (the total coverage of the GAMA regions by K band UKIDSS data), rather than the Area=143.9 sq deg used for the other samples.

5.1.3   Sample selection

The sample is limited by the star-galaxy separation criteria from Baldry et al. (2010) and an apparent magnitude limit of $r \leq 19.4\,\mathrm{mag}$ (imposed on the de-reddened magnitude system used to calculate the luminosity function). A brighter apparent magnitude cut than that defined in Section 4.5.4 is used, because 19.4 mag is the GAMA sample's target completeness limit over all three regions. Brighter than this limit the samples are 91.3% spectroscopically complete (using r_{AUTO}). The samples suffer greatly from spectroscopic incompleteness fainter than this magnitude limit. Limits based on the spectroscopic limit

---

[1] In essence, the GAMA survey is a post-stratified sampling of the SDSS, with the GAMA regions a stratum of the entire SDSS area. The SDSS source density is a universal parameter of the superpopulation, and can be used to improve the accuracy of the total luminosity density estimation made from the GAMA dataset.

and a photometric offset (i.e. $19.4 - (r_{SDSS} - r_{aperture})$) are derived for each individual galaxy. To remove the necessity of modelling the K or E corrections for each galaxy, a redshift limit of $0.0033 < z \leq 0.1$ is also introduced. An evolution $\beta = 0$ is used (where $E(z) = 2.5\beta \log_{10}(1 + z)$, setting $\beta = 0$ denotes no evolution in this redshift range), and $K(z) = 0.95z$ (following the r band in Table 4.3). The SDSS EXTINCTION_R parameter is used to de-redden all photometric methods in the same manner. The data from the three GAMA regions is combined, and treated as one sample. Column 2 of Table 5.1 contains the sample sizes.

5.1.4 The effects of the aperture definition system on output Schechter parameters

Figure 5.1 shows the luminosity distributions generated from different aperture systems, and illustrates how dependent the best-fitting luminosity function parameters are on the choice of aperture definition. The best fitting Schechter function parameters (calculated via χ^2 minimisation) are shown in Table 5.1. The systematic uncertainty between photometric methods is clearly larger than the random uncertainty in each result.

The proximity of the r-defined and self-defined luminosity distributions signify that changing the `SExtractor` detection threshold (these catalogues utilise a detection threshold of 1.7 σ and 1 σ respectively) has a limited effect on the properties to $r < 19.4 \, \text{mag}$ ($M^* - 5\log_{10}h \pm 0.055 \, \text{mag}$, $\alpha \pm 0.014$, $\phi^* \pm 0.0005 \, \text{h}^3 \text{Mpc}^{-3}$). There is an offset between the K-defined and r-defined best fitting luminosity functions. This is not caused by the cosmic variance in the missing area of the K band sample as the best fitting Schechter function parameters vary only slightly when this is accounted for. By using the *COVER_BITWISE* flag, a population of galaxies can be defined that are covered by K band imaging. The best fitting Schechter parameters for an r_{Auto} sample within the exact area covered by K band imaging (and normalised to the smaller volume) are $M^* - 5\log_{10}h = -20.791 \, \text{mag}$, $\alpha = -1.115$, and $\phi^* = 0.0132 \, \text{h}^3 \text{Mpc}^{-3}$ - consistent with the area-complete LF within the uncertainty. The offset must therefore be caused by a systematic alteration in the definition of the apertures used to calculate the flux of the galaxy population. The most likely cause of this is that the UKIDSS data is shallower, leading to slightly smaller aperture sizes. Alternatively, galaxies may be intrinsically smaller in K.

The best-fitting elliptical Kron and Petrosian aperture luminosity functions are similarly

Magnitude system	Sources	$M^* - 5\log_{10}h$	α	ϕ^* (h^{3}Mpc^{-3})	j ($\times\, 10^8\ h\ L_\odot\ Mpc^{-3}$)
Montero-Dorta et al. (2008)	-	-20.71	-1.26	0.0093	1.78
Blanton et al. (2003)	-	-20.44	-1.05	0.0149	1.85
MGC-SDSS-UKIDSS (Chapter 3)	-	-20.81	-1.18	0.0124	2.29
SDSS PETROMAG	12599	$-20.612^{+0.031}_{-0.021}$	$-1.076^{+0.013}_{-0.010}$	$0.0146^{+0.0006}_{-0.0003}$	$2.06^{+0.13}_{-0.12}$
SDSS MODELMAG	12740	$-20.812^{+0.029}_{-0.023}$	$-1.146^{+0.011}_{-0.009}$	$0.0124^{+0.0004}_{-0.0003}$	$2.23^{+0.15}_{-0.13}$
r-defined AUTO	12292	$-20.789^{+0.035}_{-0.024}$	$-1.111^{+0.015}_{-0.009}$	$0.0128^{+0.0006}_{-0.0003}$	$2.18^{+0.17}_{-0.15}$
r-defined PETRO	12268	$-20.818^{+0.026}_{-0.034}$	$-1.112^{+0.010}_{-0.012}$	$0.0127^{+0.0003}_{-0.0004}$	$2.22^{+0.16}_{-0.15}$
K-defined AUTO	10855	$-20.596^{+0.029}_{-0.031}$	$-1.063^{+0.012}_{-0.013}$	$0.0141^{+0.0004}_{-0.0004}$	$1.95^{+0.13}_{-0.12}$
K-defined PETRO	11265	$-20.699^{+0.034}_{-0.029}$	$-1.087^{+0.013}_{-0.011}$	$0.0138^{+0.0006}_{-0.0004}$	$2.13^{+0.17}_{-0.16}$
self-defined AUTO	12284	$-20.734^{+0.033}_{-0.028}$	$-1.097^{+0.013}_{-0.011}$	$0.0133^{+0.0006}_{-0.0004}$	$2.14^{+0.17}_{-0.16}$
self-defined PETRO	12247	$-20.781^{+0.031}_{-0.028}$	$-1.100^{+0.012}_{-0.011}$	$0.0131^{+0.0004}_{-0.0004}$	$2.21^{+0.16}_{-0.16}$
Sérsic (TOTAL)	12711	$-21.142^{+0.038}_{-0.030}$	$-1.203^{+0.011}_{-0.009}$	$0.0101^{+0.0004}_{-0.0003}$	$2.58^{+0.21}_{-0.20}$

Table 5.1: The number of sources that pass the star-galaxy separation criteria, redshift limit and $r \leq 19.4$ mag limit, depending on which magnitude system is used to define the r band magnitude, with comparison luminosity function parameters from SDSS (Montero-Dorta et al. 2008, Blanton et al. 2003) and SDSS+MGC defined samples (Chapter 3). All magnitudes use the AB magnitude system, and have been de-reddened using the EXTINCTION_R SDSS parameter. j statistics are calculated using $M_{\odot,r}$=4.71 from Table 2.1. Note that the comparison study samples have much brighter magnitude limits; 17.77 mag in Montero-Dorta et al., 17.79 mag in Blanton et al. and 18.76 mag in Chapter 3

distributed in the r, K and $self$-defined samples, indicating that the choice of light-distribution defined aperture does produce an offset that can be quantified. Whether the aperture is circular or elliptical is important. The SDSS PETROMAG luminosity distribution should be similar to the r and self-defined elliptical *PETRO* distributions, but there is a noticeable $M^* - 5\log_{10}h$ offset (0.20 mag; inset of Figure 5.1). There is also a marked discrepancy between luminosity distributions calculated using total magnitude apertures (Sérsic and SDSS MODELMAG), and light-distribution defined apertures. The luminosity distributions of the former are overdense for faint galaxies ($M_r - 5\log_{10}h \geq -16$), and their best fitting power-law slopes are thus flatter.

The Sérsic luminosity distribution also measures higher densities of the brightest galaxies. Although this result was anticipated, it is important to ensure that the Sérsic fits are good. The 139 galaxies that are distributed in the $-22 \leq M_r - 5\log_{10}h \leq -21.5$ magnitude bin have been visually inspected, and only 2 have suffered catastrophic fitting failures[2]. The remainder are generally well fit, though prominent spiral features do pose difficulties for the fitting algorithm. Of the 527 galaxies with $M_{r,\text{Sersic}} - 5\log_{10}h < -21$ mag within the redshift limited, apparent magnitude cut sample, only 8 have $m_{r,\text{SDSS}} - m_{r,\text{Sersic}} > 0$. The marked discrepancy between the Sérsic $M^* - 5\log_{10}h$ parameter and that generated with the other samples (0.33 mag brighter) is indicative of a scenario where galaxies are moved out of the magnitude bins near $M^* - 5\log_{10}h$, and into the brighter bins. M^* is not an independent parameter, it is correlated with the other Schechter parameters, and accordingly the ϕ^* parameter has declined. The total luminosity density (j in Table 5.1), whilst 15% higher, is consistent with that generated by the SDSS model magnitude within uncertainties. As GAMA Sérsic magnitudes are not truncated, but the SDSS model magnitudes are truncated at $7R_e$ for a de Vaucouleurs profile / $3R_e$ for an elliptical profile, an offset in M^* between these photometric systems is expected. No matter which aperture system is used, the luminosity distribution is overdense in the $M_r - 5\log_{10}h > -16$ magnitude bins when compared to the best fitting luminosity function. This indicates an upturn in the space density of galaxies at the dwarf-giant boundary, and the limitations of the single Schechter function fit.

As noted in Chapter 1, the Schechter parameters generated are taken from a sample that will suffer surface brightness incompleteness fainter than $\mu_{r,50} = 23 \, \text{mag arcsec}^{-2}$ (the SDSS effective r band surface brightness within the half-light radius, see Baldry et al.

---

[2]These profiles are viewable at http://star-www.st-and.ac.uk/~dth4/139eye/

2010 and references therein). Later in this chapter, the scale of this effect is tested by undertaking a complete bivariate brightness analysis of the sample. The total luminosity densities shown here may therefore be systematically underdense due to surface brightness limitations (c.f. Cross & Driver 2002). It is also apparent that the simple Schechter function parametrisation is no longer a good fit for the luminosity distribution of galaxies at fainter magnitudes; there is an obvious upturn in each sample that is not being modelled. As the Sérsic photometric system is the only system that accounts for missing light, it is the most effective way of calculating the total luminosity distribution. However, there are two caveats to this result. Firstly, Sérsic photometry inherently assumes that all galaxies can be fit by Sérsic profiles. Secondly, the Sérsic magnitudes I present here are for non-truncated profiles. Whilst there is some evidence that this assumption is valid (Hu et al., 1989; Bland-Hawthorn et al., 2005; Pohlen et al., 2004), it is uncertain whether it is true in all cases (van der Kruit, 2001). For galaxies that are truncated, the Sérsic magnitude will overestimate their total luminosity, and the total luminosity density I state here may be too great.

5.1.5 The effects of surface brightness bias on the presented luminosity distributions

Aperture selection can systematically bias the calculation of the luminosity distribution, particularly where a sample has a high surface brightness threshold (see Cross & Driver 2002, particularly their Figure 5). The SDSS photometric pipeline unfortunately is incomplete for $\mu_{r,50} > 23\,\mathrm{mag\,arcsec^{-2}}$ (the effective surface brightness within the half-light radius, see Section 3.4 of Baldry et al. 2010 and references therein). It follows that any spectroscopic survey that bases itself upon SDSS photometry, such as GAMA, will suffer from the same flaw. Cross & Driver (2002) have quantified the surface brightness dependency that the luminosity distribution inherently suffers from, and advise that a bivariate brightness distribution (BBD) is the best way to quantify and remove SB bias. Cross & Driver (2002) point out that a sample that is complete to $\mu_{\mathrm{lim}} \geq 24\,\mathrm{mag\,arcsec^{-2}}$ has very little uncertainty in its Schechter parameters due to SB selection effects, as the L^* population that defines the fitting is fully sampled (see also section 4.1.2 of Driver et al. 2005). In due course, VST KIDS imaging will provide GAMA with such a catalogue. For now, however, it must be accepted that the *SDSS* input catalogue will not contain all faint,
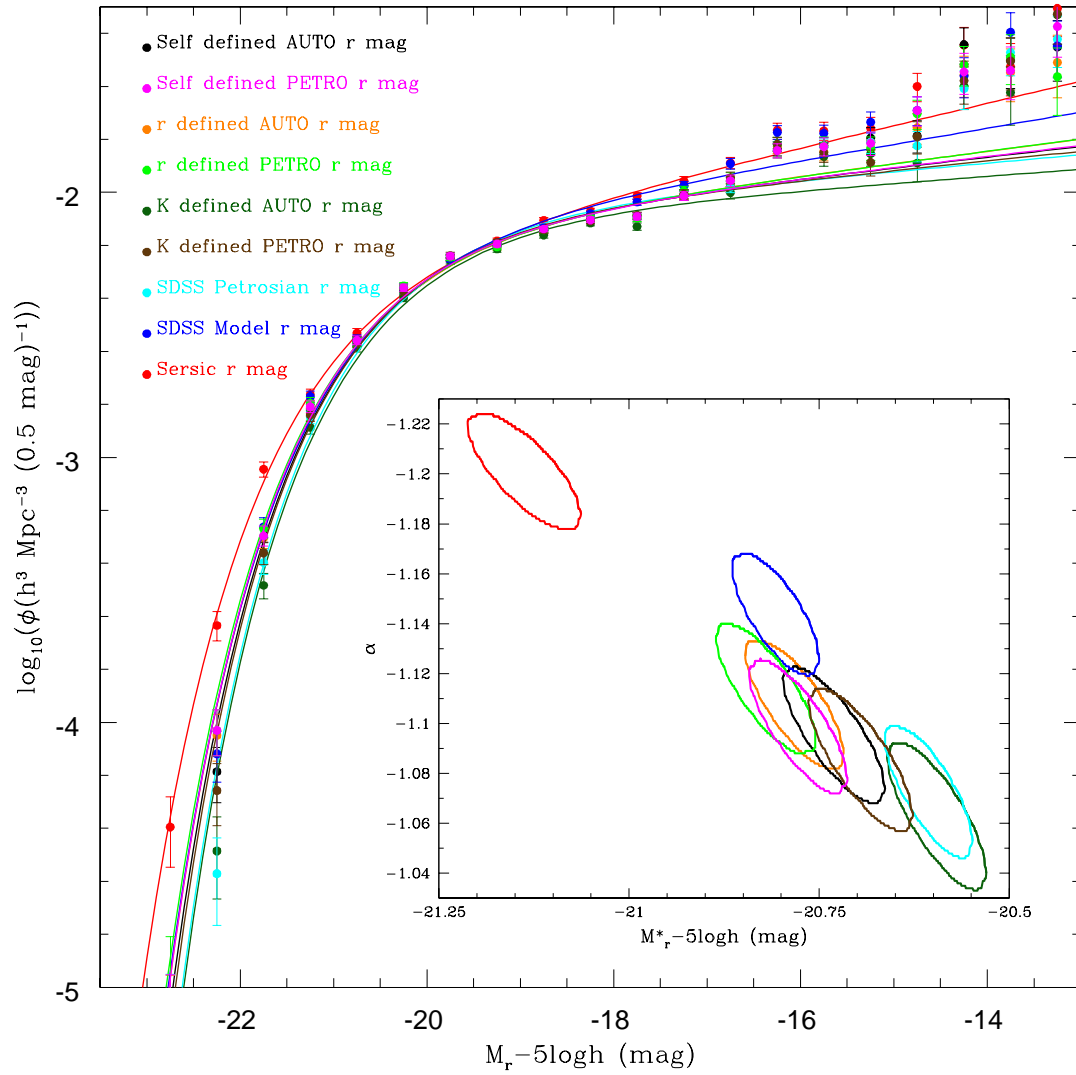
Figure 5.1: Luminosity distributions, and the best fitting Schechter functions, calculated using different aperture definitions. Inset: 1 sigma chi-squared best-fit contours in the M^*-α plane. Errors on luminosity distribution points are Poissonian errors.

low surface brightness galaxies. The luminosity functions presented in this section are for samples that are surface brightness complete to $\mu_{r,50} < 23\,\mathrm{mag\,arcsec^{-2}}$, and suffer from varying levels of completeness between $23 < \mu_{r,50} < 26\,\mathrm{mag\,arcsec^{-2}}$. As the luminosity functions presented in the Section 5.1.4 are for a specifically low redshift sample, however, the effects of the surface brightness selection bias should be minimised. In the next section, I shall attempt to quantify the effects of surface brightness bias on the GAMA sample, by constructing bivariate brightness distributions.

5.2 The effects of surface brightness bias on GAMA data

In order to examine the effects of surface brightness on GAMA data, I derive the joint luminosity - surface brightness (bivariate brightness) distributions, following the method outlined in Driver et al. (2005). Certain assumptions must be made in order to convert from observed to intrinsic parameters, and selection criteria must be imposed to guarantee a complete sample. These criteria are discussed in Sections 5.2.1 and 5.2.2.

5.2.1 Cosmology

An $h = 1$, $H_0 = 100h\,\mathrm{km\,s^{-1}\,Mpc^{-1}}$, $\Omega_M = 0.3$, $\Omega_\Lambda = 0.7$ cosmological model was adopted. Redshift limits are imposed upon the sample. Galaxies outside of the interval $0.0033 \leq z \leq 0.1$ are rejected. The lower limit was defined as the limit where the photometry of large, luminous objects becomes unreliable due to uncertainties in $v_{peculiar}$ (Driver et al., 2005). The upper limit was selected in order to limit the effects of evolution (Prescott et al., 2009; Baldry et al., 2005). K corrections were derived separately for each galaxy within the sample, using v4.2 of the KCORRECT package (Blanton & Roweis, 2007). K corrections were calculated from SDSS, UKIDSS and GALEX photometry. At least 5 datapoints ($ugriz$) were available for the SED calculation of every galaxy within the sample, with a maximum of 11 datapoints ($FUV, NUV, ugrizYJHK$) in areas that are covered by all three surveys. In order to remove any aperture inconsistency, $ugrizYJHK$ datapoints used the r-defined GAMA photometry, as described in Section 4.2.2.

The low-redshift nature of the galaxy sample makes the use of an evolution correction unnecessary (see section 3.2.2). As such, $E(z) = 0$ was used.

5.2.2   Data used to construct the BBDs

Calculation of surface brightness

As discussed in the previous chapter (particularly Section 4.5.1), low quality data makes the calculation of Sérsic apertures and magnitudes unrealistic in some filters (particularly the SDSS u filter). To construct the bivariate-brightness distributions, SExtractor Kron-like AUTO magnitude photometry was used, and is denoted X_{Kron}. Apertures were defined using the r band dataset (see Section 4.2.2). All magnitudes were extinction corrected, via Schlegel et al. (1998) dust maps.

The Sérsic effective radius (r_e) was used as the measure of the galactic radius. It is defined as the radius that contains half of the total flux, and accounts for the ellipticity of the aperture (unlike the SDSS Petrosian radius). The Sérsic effective radius is taken from the `SIGMA` pipeline, summarised in Section 4.2.4. As the galaxy profile was defined using r band data, the effective radius in the r band provides the half light radius in each band. The apparent mean surface brightness inside the effective radius ($\langle \mu_X \rangle$) was calculated using Equation 5.1:

$$\langle \mu_X \rangle = X_{\mathrm{Kron}} + 2.5 \log_{10}(2\pi \mathrm{r}_{\mathrm{e}}^2) \tag{5.1}$$

where X is the filter. The absolute mean surface brightness within the effective radius ($\langle \mu^X \rangle$) was calculated using Equation 5.2:

$$\langle \mu^X \rangle = \langle \mu_X \rangle - 10 \log_{10}(1 + \mathrm{z}) - \mathrm{K(z)} - \mathrm{E(z)} \tag{5.2}$$

Where X is the filter, and $K(z)$ is the K correction for the source. As no evolutionary correction was required, $E(z) = 0$.

Sample selection limits

Although the GAMA 12 region has a deeper photometry limit ($r_{\mathrm{petro,SDSS}} = 19.8\,\mathrm{mag}$, see Driver et al. 2010), here the dataset is limited to $r_{\mathrm{petro,SDSS}} = 19.4\,\mathrm{mag}$. This selection allows all three GAMA regions to be combined as one larger sample. Baldry et al. (2010) define the explicit apparent surface brightness limits of the GAMA sample to be $15.0 < \langle \mu_{r,50} \rangle < 26\,\mathrm{mag\,arcsec^{-2}}$, where $\langle \mu_{r,50} \rangle$ is the mean SB within the circular Petrosian half light radius in the r band. They note, however, that the sample is incompletely

Sample	$m_{X,Faint}$ (AB mag)	μ^X_{Bright} (mag arcsec^{-2})	μ^X_{Faint} (mag arcsec^{-2})	Area (deg^2)
u$_{Kron}$	20.0, 20.6	16.77	24.77	143.9
g$_{Kron}$	19.6, 19.6	16.57	23.57	143.9
r$_{SDSS}$	19.4, 19.4	16	23	143.9
r$_{Kron}$	18.9, 19.1	16	23	143.9
i$_{Kron}$	18.4, 18.6	15.62	22.62	143.9
z$_{Kron}$	18.1, 18.2	15.40	22.40	143.9
Y$_{Kron}$	17.9, 18.1	15.31	22.31	128.8
J$_{Kron}$	17.7, 17.7	15.14	22.14	132.4
H$_{Kron}$	17.1, 17.5	14.84	21.84	129.7
K$_{Kron}$	17.0, 17.2	14.97	21.97	132.7

Table 5.2: Survey limits of the sample used within this dataset. Two magnitude limits are shown. The first accounts defines a sample that is complete in apparent magnitude and has complete colour coverage. The latter defines a sample that is only apparent magnitude complete. For all samples except for r_{SDSS}, the sample faint limit is defined as the bin before the number counts turnover, when the $r_{SDSS} < 19.4$ mag sample is sorted into a histogram of 0.1 mag bins.

sampled between $23.0 < \langle \mu_{r,50} \rangle < 26$ mag arcsec^{-2}.

The minimum angular size of objects (rad$_{50,\text{min}}$) within the dataset is also defined by the SDSS survey. Size measurements at small scales are affected by the PSF, and an incorrect measurement in the SDSS dataset would remove an object from the GAMA source catalogue. Appendix A of Driver et al. (2005) illustrates that the minimum recoverable size is slightly smaller than the survey seeing (the minimum seeing-corrected half light radius is $\sqrt{0.37x^2 + 0.37x + 0.1}$, where x is the seeing FWHM). Using the median seeing of the SDSS (~ 1.6 arcsec: Shen et al. 2003), in order to limit the effects that seeing conditions could have upon the compact objects in the sample, a rad$_{50,\text{sdss Petro}} > 1$ arcsec limit is utilised. The size distribution of sources within the unfiltered catalogue are shown in Figure 5.2.

The GAMA sample has also undergone rigorous star-galaxy separation, visual classification and masking cuts. These are detailed in Baldry et al. (2010). All sources that fail these selections are removed.

The magnitude and surface brightness limits used here follow the prescription laid out in Driver (1999). The faint apparent magnitude limits of the sample (m_{Faint}) for the nine wavebands is shown in Table 5.2. A constant m_{Bright} limit of 9 mag is used. The r-defined aperture photometry used here has one major advantage over the standard SDSS photom-
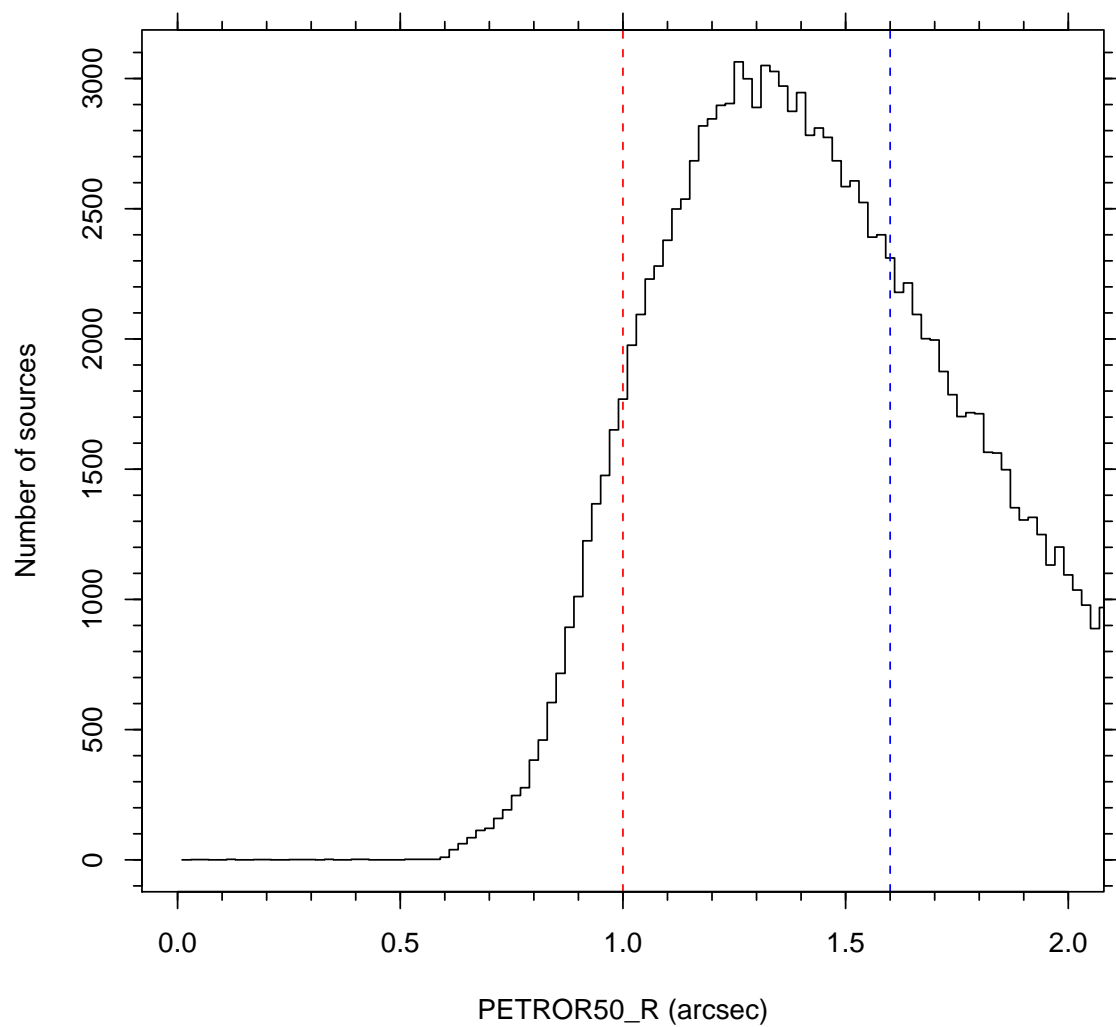
Figure 5.2: The distribution of SDSS PETROR50_R in the unfiltered catalogue. The red line designates the minimum size used within this sample. Shen et al. (2003) use a more conservative cut. This is illustrated by the blue line.

etry: elliptical apertures fit the shape of inclined galaxies more effectively than the circular SDSS Petrosian photometry. A more detailed discussion of the GAMA photometry can be found in Section 4.2.

The faint magnitude limit of each sample is found by looking at how the population is distributed in luminosity. In a complete sample (within this redshift range), the number of galaxies should continuously increase as the faint luminosity limit decreases. The colour distribution should also broaden. By plotting a histogram of the galaxies by magnitude (Figure 5.3), it is possible to estimate the faint limit from the magnitude where the distribution stops increasing. The samples in Figure 5.3 are split into magnitude bins of $0.1\,$mag. From the colour distribution (Figure 5.4), the magnitude at which colour incompleteness starts to occur can be estimated.

Two Kron magnitude samples are defined. The first Kron magnitude sample is cut at either the bin before the number counts turn over, or at the point where colour incompleteness begins, depending on which is the brighter. The second, deeper sample, is defined solely by the number count turnover. As the SDSS photometry is used to define the selection criteria, only one SDSS photometry sample is produced, with r_{SDSS} limited at $r = 19.4\,$mag.

The μ^X parameter used here (see section 5.2.2) is based upon an elliptical aperture and does not correspond exactly to the circular SDSS $\mu^{X,50}$ parameter. Determining the offset between these parameters is a two step process. Firstly, the conversion to an elliptical aperture can be determined using Equation 5.3 (Equation 9 of Driver et al. 2005):

$$\langle\mu_X\rangle_{Circular} = \langle\mu_X\rangle_{MajorAxis} + 2.5\log_{10}(\frac{b}{a}) \qquad (5.3)$$

Equation 5.3 shows that the surface brightness calculated using a circular aperture cannot be fainter than a surface brightness determined from an elliptical aperture. The second step is more complicated. The conversion between a circular $\langle\mu_X\rangle$ and $\langle\mu_{X,50}\rangle$ is dependent on the Sérsic profile of the galaxy in question. Graham & Driver (2005) calculate the theoretical discrepancy between $\langle\mu_X\rangle$ and $\langle\mu_{X,50}\rangle$ for different Sérsic profiles with $0.1 \leq \eta \leq 10$ (their Equation 8 and Table 1, η is the Sérsic index). $\langle\mu_X\rangle - \langle\mu_{X,50}\rangle$ ranges from 0 (for $\eta < 1$), to $2.45\,$mag$\,$arcsec^{-2} (when $\eta = 10$). The use of $\langle\mu_{X,50}\rangle$ will therefore give a brighter surface brightness for systems with $\eta > 1$. The surface brightness parameters therefore depend on the properties of the sample of galaxies. A sample of
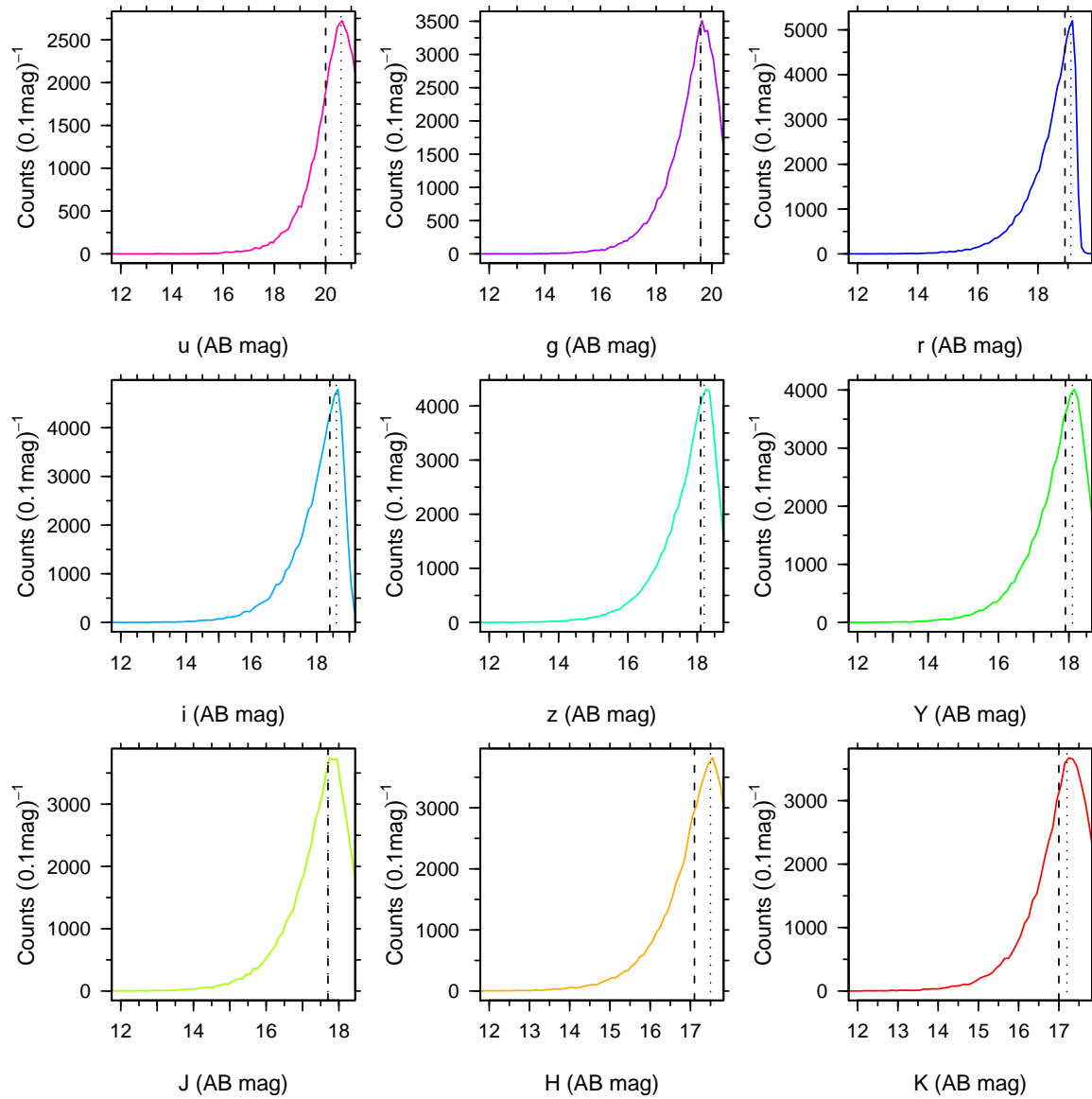
Figure 5.3: Number counts for all sources that pass the redshift quality, star-galaxy separation and SDSS magnitude, surface brightness and size criteria, split into bins 0.1mag. The vertical lines are the $m_{X,\text{Faint}}$ limits from Table 5.2

Colour	Median (mag)	3σ clipped Standard Deviation (mag)
$u - r$	1.77	0.56
$g - r$	0.57	0.22
$r - i$	0.38	0.09
$r - z$	0.60	0.18
$r - Y$	0.69	0.25
$r - J$	0.86	0.33
$r - H$	1.16	0.33
$r - K$	1.03	0.37

Table 5.3: Median $r - X$ colours and 3σ clipped standard deviations for all sources that pass the redshift quality, star-galaxy separation and SDSS magnitude, surface brightness and size criteria, and are brighter than the colour complete $m_{X,\text{Faint}}$ limit in Table 5.2

circular, low Sérsic index galaxies would have the same surface brightness when using $\langle \mu_r \rangle$ as those derived using $\langle \mu_{r,50} \rangle$. A sample of inclined, high Sérsic galaxies, however, will have much fainter derived surface brightnesses using $\langle \mu_r \rangle$; potentially $\sim 5 \, \text{mag arcsec}^{-2}$ fainter for an $\eta = 10, \frac{b}{a} = 0.1$ galaxy. To guarantee an unbiased sample, the sample is limited in effective surface brightness at $\langle \mu^r \rangle = 23.0 \, \text{mag arcsec}^{-2}$.

As the BBDs are constructed using the r band-defined AUTO photometry, the r band aperture is used to define the effective radius in every band. Effective surface brightness limits can therefore be calculated in other bands (Equation 5.4) from the r band surface brightness limit and the median source colour (Table 5.3):

$$\langle \mu_X \rangle_{limit} = \langle \mu_r \rangle_{limit} - (r - X) \tag{5.4}$$

To summarise - the samples are cut using the following selections:

- $r_{\text{SDSS,Petro}} \leq 19.4 \, \text{mag}$

- $15.0 \leq \langle \mu_{r,50} \rangle \leq 23 \, \text{mag arcsec}^{-2}$

- Passes the GAMA star-galaxy separation, visual classification and masking cuts.

- $\text{rad}_{50,\text{SDSS,Petro}} > 1 \, \text{arcsec}$

- $\mu^X_{\text{Bright}} \leq \langle \mu^X \rangle \leq \mu^X_{\text{Faint}} \, \text{mag arcsec}^{-2}$

- $9 \leq m_X \leq m_{X,\text{Faint}} \, \text{mag}$

- $0.0033 \leq z \leq 0.1$
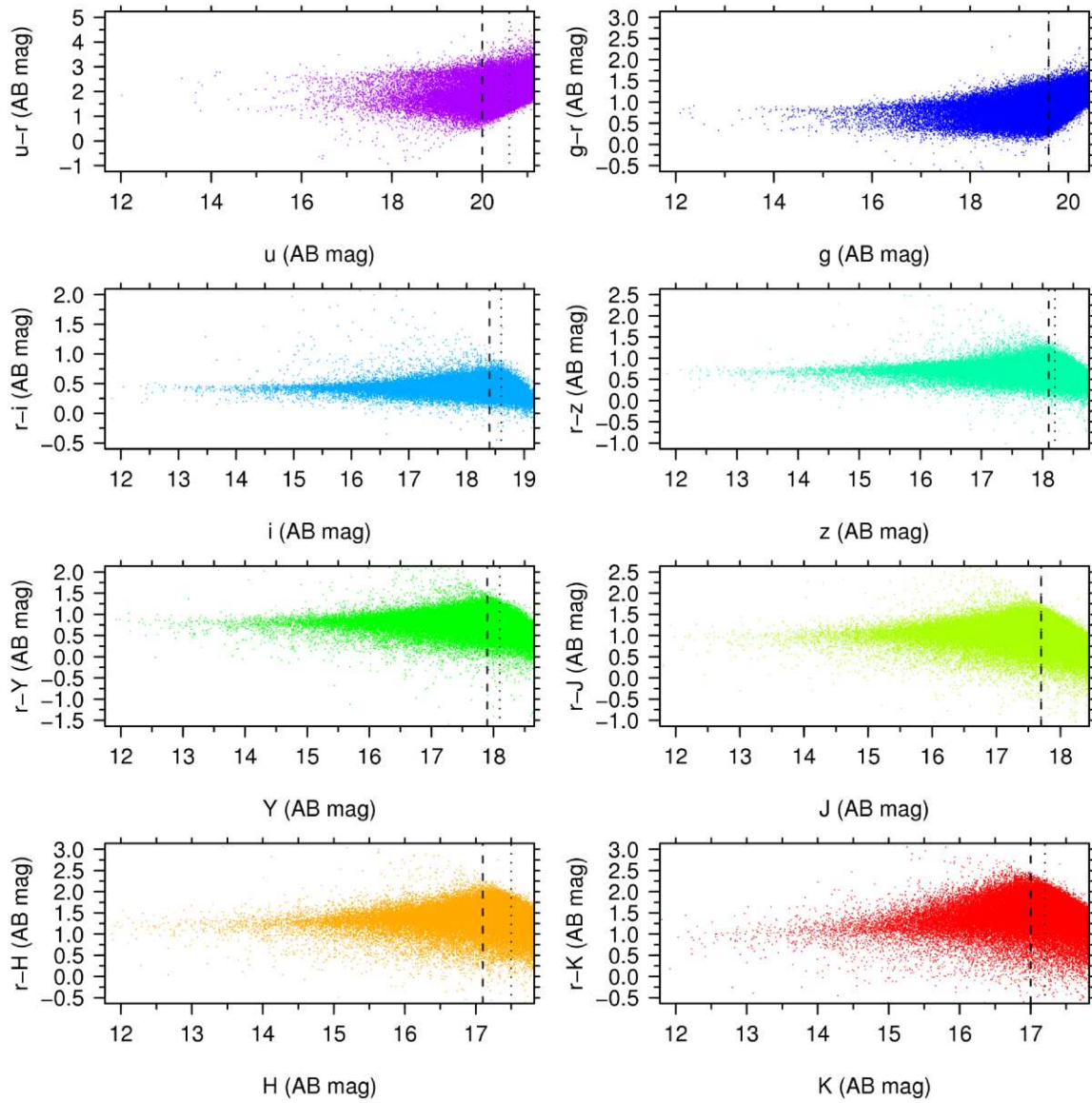
Figure 5.4: The $r - X$ colours for all sources that pass the redshift quality, star-galaxy separation and SDSS magnitude, surface brightness and size criteria. The vertical lines are the $m_{X,\text{Faint}}$ limits from Table 5.2

Spectroscopic completeness

Whilst GAMA is among the most complete galaxy surveys ever undertaken (Driver et al., 2010; Robotham et al., 2010), there are still sources within the sample that have not been targeted, or have produced an unreliable redshift. These sources are predominantly low surface brightness, low luminosity sources. In order to limit the bias that this effect causes to the distribution, it must be accounted for using a completeness correction.

The completeness correction must be calculated from the photometric system used to define the target selection. The target selection was defined using $r_{\mathrm{SDSS,Petro}}$ photometry, and was therefore used to calculate the luminosity and surface brightness of each source. The sample is sorted into $0.1\,\mathrm{mag} \times 0.1\,\mathrm{mag\,arcsec}^{-2}$ bins. Within each bin the total number of sources is calculated, as is the number of sources with reliable spectroscopy ($Z\_QUALITY > 2$). In order to correct for completeness, the reliable sources are weighted. The weighting was calculated using:

$$C = \frac{N_{\mathrm{Total}}}{N_{\mathrm{Reliable\ spectra}}} \tag{5.5}$$

The weight of each galaxy is independent of the photometric method used to calculate the BBD. Figure 5.5 shows how C varies as a function of apparent magnitude and surface brightness. This method assumes that the z distribution of the low quality/unobserved sources is the same as the reliable sources. It is likely that this assumption is faulty. However, as GAMA is more complete than any previous survey, the effects of this bias are the smallest. Without follow up observations, there is no way of calculating the true z distribution of the low quality sources. In the circumstances, this is the best approximation that can be made.

Visibility weighting

Visibility theory (Phillipps et al. 1990, and Appendix B of Cross et al. 2001), allows the calculation of the distance where a galaxy of known luminosity and surface brightness becomes too faint to observe. The existing theory has been modified to account for the specific apertures GAMA uses. Appendix C outlines the modifications that have been made. In Figure 5.6, the visibility of the object type most difficult to detect (a small, faint spiral galaxy) is calculated.
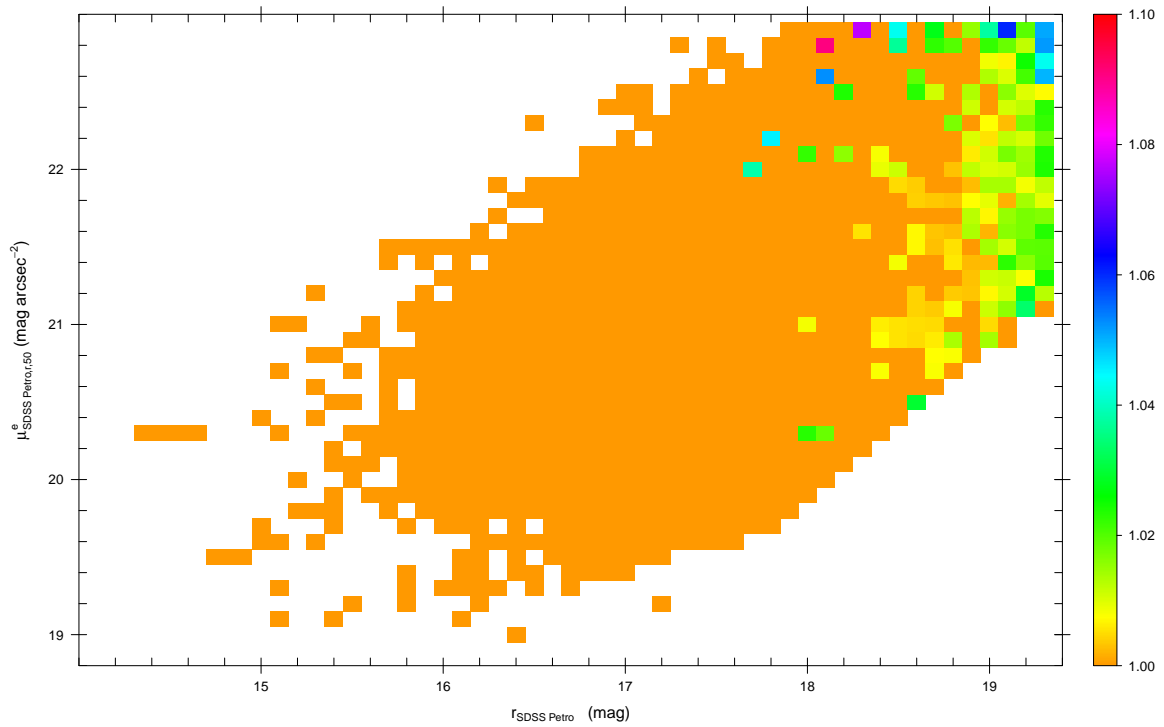
Figure 5.5: The weighting (C) as a a function of apparent magnitude and apparent surface brightness. Each galaxy is allocated into a $0.1\,\mathrm{mag} \times 0.1\,\mathrm{mag\,arcsec}^{-2}$ bin, and allocated a weighting based on the fraction of galaxies in that bin with reliable spectra. The GAMA sample is highly complete, with the majority of bins requiring no weighting at all. For clarity, only bins containing 3 or more galaxies that pass the sample criteria are shown.
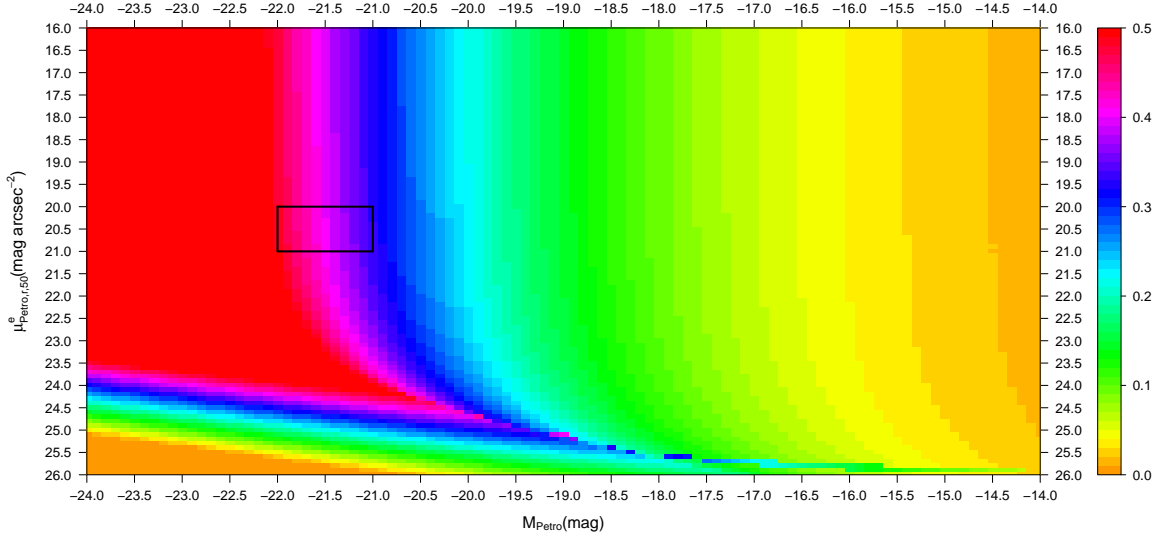
Figure 5.6: Overall redshift completeness limits in the $M,\mu^{r,50}$ plane (SDSS photometry). The redshift limit colours range from $z = 0.5$ (red), to $z = 0$ (orange). Limits were calculated using visibility theory (see Appendix C). The box denotes the normalisation region, which is complete within the redshift limits of the sample.

It is apparent that in some sections of the BBD, visibility incompleteness is a problem. Fainter than $\sim M_r = -18$ mag, the majority of sources will not be detected at the high z limit of the sample. In order to account for this when using the $\frac{1}{V_{max}}$ methodology, it would be necessary to calculate each bin's visible volume using visibility theory, from the GAMA coverage area, the sample's minimum limit and the maximum redshift visibility theory says a source within the bin could be observed to. The H function in the SWML method (Equation 1.11) fulfils the same role on a source by source basis. The H function works by taking the survey limits and the redshift of the source, and calculates which M,μ bins the source could lie within. As such, each source is only weighted by the bins it could lie within (implicitly accounting for the visibility of the source), so further correction is unnecessary.

Differences in photometric method

The photometry used here (X_{Kron}), differs from the photometry used to define the input catalogue ($r_{\mathrm{SDSS,Petro}}$). The change in photometric method is treated as a change in filter. In Section 3.2.1, when $ugrizYJHK$ luminosity distributions were derived from a B band limited sample, a variable magnitude limit was developed, that was based upon the B band magnitude limit of the survey and the $B - X$ colour of each source. The same principle is applied in this case. Variable magnitude and surface brightness limits are derived

for each source within the colour incomplete samples (Equation 5.6). The survey limits are taken from $r_{\text{SDSS,Petro}}$ photometry, and are discussed in Section 5.2.2.

$$m_{\text{Faint lim},i} = 19.4 - (r_{\text{SDSS,Petro,i}} - X_{Kron,i})$$
$$\mu^X_{\text{Faint lim},i} = 23 - (\langle \mu^{r,50}_i \rangle - \langle \mu^X_i \rangle)$$

(5.6)

For the colour complete samples, constant magnitude and surface brightness limits are used.

Derivation of the bivariate brightness distribution, and functional fitting

In order to calculate the bivariate brightness distribution, the bivariate SWML method described in Section 1.6.2 is implemented. Choloniewski and modified-model function parameters are derived using the prescription detailed in Sections 1.6.3 and 5.2.3.

Normalisation

The SWML method calculates the relative density between bins, but requires normalisation to calculate the true luminosity distribution of the Universe. This is undertaken by calculating the number density of galaxies within a $1\,\text{mag} \times 1\,\text{mag}\,\text{arcsec}^{-2}$ region centred at $M^*_{\text{SDSS Petro}}$, $\mu^{r,50,*}$. This region is herein referred to as the normalisation region.

The total volume enclosed by the GAMA area and the redshift selection boundaries ($143.9\,\text{deg}^2$, $0.0033 < z < 0.1$) is found to be $V_{\text{GAMA}} = 367,051h^{-3}\,\text{Mpc}^3$. Area incompleteness is accounted for in the sample by multiplying this volume by the fraction $f_{\text{inc}} = \frac{a}{143.9}$, where a is the sample's area coverage (Table 5.2). The ψ distribution is normalised by scaling the luminosity density within the normalisation region calculated using the SWML method to the equivalent luminosity density calculated using the $\frac{1}{V_{max}}$ method. The BBD correction for cosmic variance is calculated using statistics in Driver et al. (2010). Figure 20 of Driver et al. (2010) states that the GAMA regions are 85% as dense as the entire SDSS area. The universal ϕ^* parameter can therefore be calculated by scaling the GAMA ϕ^* parameter by $\frac{1}{0.85}$. The entire weighting process is shown Equation 5.7:

$$\phi^*_{\text{universal}} = \frac{\phi^*_{\text{SWML}}}{0.85} \times \frac{\frac{N_{\text{galaxies in norm region}}}{V_{\text{GAMA}} \times f_{\text{inc}}}}{\sum_{\text{M},\mu \text{ in norm region}} \psi_{\text{SWML}(M,\mu)}}$$

(5.7)

In order for the normalisation calculation to be reliable, all sources that pass the luminosity, surface brightness and redshift selection criteria within the normalisation region must be detectable. In the normalisation region selected, it would be possible to observe throughout the redshift limits of this sample (Figure 5.6), with visibility only becoming an issue above $z = 0.2$.

For samples defined using other filters, the same prescription is followed. A $1\,\mathrm{mag} \times 1\,\mathrm{mag\,arcsec}^{-2}$ normalisation region is defined around M_X^*, μ_X^*. The best-fitting ϕ^* parameters are scaled using Equation 5.7. The normalisation region is tested for visibility completeness. The filter's absolute magnitude visibility limit is derived from the r band absolute magnitude visibility limit (Figure 5.6) and the median colours from Table 5.3. In all filters, the normalisation region is not visibility limited for a median colour source, and a source with colour $+ 2.5\sigma$ should also be unaffected.

5.2.3 The GAMA-SDSS/UKIDSS Bivariate brightness distributions

Comparison between colour complete and deeper, colour-incompleteness corrected samples

BBDs have been calculated for both colour complete, and deeper colour-incompleteness corrected samples. The apparent magnitude limits of these samples are shown in Table 5.2.

Choloniewski functions are fit to both distributions, using χ^2 minimisation, where χ^2 is given by:

$$\chi^2 = \sum_{\text{All bins}} (\frac{\log_{10}(\psi_{\text{observed}}) - \log_{10}(\psi_{\text{function}})}{\psi_{\text{err}}})^2 \tag{5.8}$$

ψ_{err} is the Poissonian uncertainty of the bin (i.e., $\frac{\psi_{jk}}{\sqrt{N_{jk}}}$, where N_{jk} is the number of galaxies within the jk bin). The uncertainty for an empty bin is calculated from the ψ value the bin would have if it contained one galaxy.

As the functional form has six free parameters, it is not appropriate to use an exhaustive-search technique to find the minimum χ^2 value. Instead, a simulated-annealing algorithm is utilised to ascertain the optimal result. Simulated-annealing is a technique that works

by taking the current solution, and replacing it with a nearby solution, chosen with a probability that depends on the difference between the results (in this case, $\Delta\chi^2$), and a 'temperature' parameter that is slowly reduced as the algorithm iterates. Thus, at the start of the algorithm (when the 'temperature' is large) the solution is allowed to move randomly (even to results with a higher χ^2), but as the temperature decreases only steps that minimise χ^2 are taken. By allowing movement to larger χ^2 at the start of the algorithm, the possibility that the optimisation process will become stuck within local minima is diminished. Local minima are a distinct possibility in this case, given the quality of the data and the number of free parameters. The OPTIM algorithm that is distributed with the R programming language is executed, with the "SANN" method chosen. The algorithm is set to iterate 10 thousand times. It is also set to produce a Hessian matrix. The Hessian matrix is a matrix of second-order partial derivatives of a function, i.e., it describes the local variation (curvature) of the function as those parameters are changed. Intuitively, if the second-order derivative is large, the greater the variation in the function around the minima, and the greater the certainty that the parameters returned are correct. If the second-order derivative is small, the function's value varies only slightly even with large parameter changes, and our certainty that the returned parameters are accurate is diminished. By inverting the Hessian matrix, a matrix of covariant errors is produced, where large parameters signify significant uncertainty in the function's value, and small parameters show low uncertainty. The variant and covariant errors shown in this section (e.g. Table 5.4)are taken from this covariant matrix.

A modified BBD functional form

Unfortunately, the Choloniewski function has not been found to fit the BBD well. Cross et al. (2001) find that in their 2dFGRS sample, the luminosity distribution does not follow the monovariate Schechter parametrisation, and this causes their functional misfit. Ball et al. (2006) find that the functional fit they produce from a sample of galaxies taken from the VAGC cannot fit the broadening surface brightness distribution, an issue also highlighted by Driver et al. (2005). Ball et al. (2006) discuss whether the bimodality of the dwarf and giant galaxy populations means that the sample must be treated as two distinct populations, in order to account for the differing physical processes that are occurring. Using UKIDSS K band data, Smith et al. (2009) find that the Choloniewski

function cannot simultaneously model the broadening of the surface brightness distribution with luminosity or the variation in the luminosity-surface brightness relationship at faint luminosity.

The Choloniewski function tries to account for the evolution in the latter relationship, but does so incorrectly. The $\beta_\mu(M - M^*)$ term has the effect of simulating a μ^* that varies with all M, not just for M fainter than a certain magnitude (this magnitude is herein referred to as M_σ, and may differ from M^*). The Choloniewski function cannot model any variation in σ_μ.

Figure 5.7 shows the $ugrizYJHK$ BBDs produced using the GAMA dataset. These BBDs are split into intervals of constant luminosity, illustrating the variation in the surface brightness distribution with luminosity. At bright magnitudes (e.g., in the r band, $M_{r,\text{Kron}} - 5\log_{10}(\text{h}) < -19.25\,\text{mag}$), the surface brightness distribution is Gaussian, and not evolving. It peaks around $\mu^{*,r,\text{Kron}} = 20.75\,\text{mag}\,\text{arcsec}^{-2}$. Fainter than this, the surface brightness distribution broadens and dims.

It is apparent that the functional fit must be changed to account for the surface brightness evolution. The modified functional form described here is an attempt to make such a modification. β_μ and σ_μ are modelled as linearly increasing variables fainter than M_σ (Equation 5.9):

$$\sigma_\mu = \sigma_{var} + E \times R(M - M_\sigma)$$
$$\mu^* = \mu^*_{var} + \beta_\mu \times R(M - M_\sigma)$$

$$(5.9)$$

where R is the Ramp function ($R(x) = x$, when $x > 0$, otherwise $R(x) = 0$), M_σ is the magnitude at which the surface brightness distribution starts to evolve, and the E and β_μ parameters control the extent of the broadening and peak surface brightness evolution. The modified functional form is shown in Equation 5.10:

$$\psi(M,\mu) = \frac{\phi^* 0.4\ln(10)10^{-0.4(M - M^*_X)(\alpha+1)}e^{-10^{-0.4(M - M^*_X)} - \frac{1}{2}(\frac{\mu^X - \mu^{X,*}_{var} - \beta_\mu \times R(M - M_{\sigma,X})}{\sigma^X_{var} + E \times R(M - M_{\sigma,X})})^2}}{\sqrt{2\pi}(\sigma^X_{var} + E \times R(M - M_{\sigma,X}))}$$

$$(5.10)$$

The $\sigma^X_{var} + E \times R(M - M_{\sigma,X})$ parameter has been introduced to simulate a σ_μ that broadens with decreasing luminosity fainter than $M_{\sigma,X}$. The $\beta_\mu \times R(M - M_{\sigma,X})$ term models a μ^* that varies with luminosity. The modified function fit has 8 free parame-
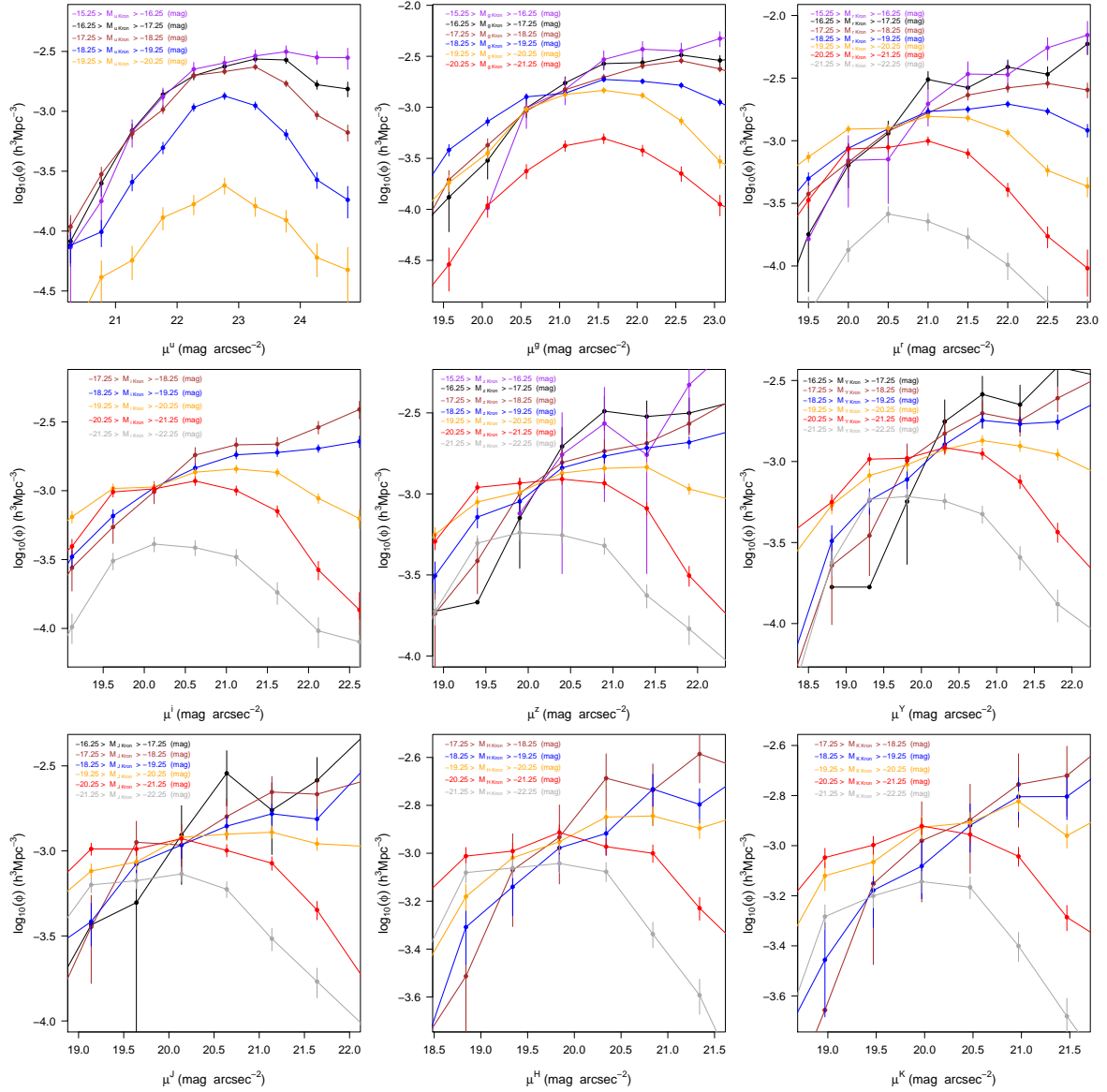
Figure 5.7: The surface brightness distribution of the X_{Kron} samples, split into luminosity intervals.

ters, 2 more than the standard Choloniewski function. Unfortunately, it is therefore more computationally expensive to generate the best solution. So that the simulated-annealing algorithm described in Section 5.2.3 is run to the same precision, over 200 thousand iterations are required. As the best-fitting solution to the modified function can never produce a worse fit than the Choloniewski function (the functions are equivalent when $M_\sigma = 0$ and $E = 0$, with the best-fitting Choloniewski $\mu^* = \mu^*_{var} - \beta M^*$), the relative quality of the fit must account for the number of degrees of freedom. In order to provide such an indicator, the reduced χ^2 statistic for the functional fit to both the modified and unmodified samples is estimated.

Calculation of total luminosity density from Choloniewski parameters

By summing the luminosity density across the entire range of surface brightness and luminosity, the total luminosity density, j, can be calculated from the BBD. It is apparent however, that such a summation is not possible - the BBD data is subject to both surface brightness and absolute magnitude limits, and an accurate derivation of the luminosity density beyond those boundaries is impossible. Instead, the total luminosity density is calculated analytically, using:

$$j = \int_{-\infty}^{\infty} \int_{0}^{\infty} \psi(L, \mu) dL d\mu \tag{5.11}$$

where $\psi(L, \mu)$ is calculated using a functional form, such as Equation 1.12 or 5.10 (if those functions are converted to take L,μ arguments, rather than their current M,μ definition). It can be shown (e.g. Section 4 of Cross & Driver 2002), that the total luminosity density can be calculated from the Choloniewski function using the expression:

$$j_\lambda = 0.4\ln(10)\phi^{*,\lambda} L^*_\lambda \Gamma(\alpha_\lambda + 2) \tag{5.12}$$

where j_λ is the total luminosity density for the filter. The alterations made in section 5.2.3 to the Choloniewski function to create the modified-model function modify the shape of the surface brightness distribution. However, the area underneath the distribution remains constant. Therefore, Equation 5.12 can also be used to calculate the total luminosity density from the modified-model functional form. Converting Equation 5.12 into the

absolute magnitude space, and using units of solar luminosity ($h\,L_{\odot,\lambda}\,\mathrm{Mpc}^{-3}$), Equation 5.12 becomes:

$$j_\lambda = \phi^*_\lambda 10^{-0.4(M^{*,\lambda}-M_{\odot,\lambda})}\Gamma(\alpha_\lambda + 2) \tag{5.13}$$

where ϕ^*_λ, $M^{*,\lambda}$, α_λ and $M_{\odot,\lambda}$ are all wavelength dependent parameters. However, as j_λ is dependent on the range of the filter it is measured in, comparing this statistic between filters is not particularly useful. Following Section 1.4.1, the energy density per unit interval ($\nu f(\nu)$) can be calculated, using Equation 1.9. This statistic has no dependency upon the passband, allowing the variation with wavelength to be quantified.

The best fitting parameters for the deeper sample are presented in Table 5.4, and for the shallower, colour-complete sample in Table 5.5. χ^2 parameters for these fits are shown in Tables 5.6 and 5.7. The model parameters are very interdependent. The covariance matrix generated from the fit to the deeper r_{Kron} photometry is shown in Table 5.8. The best-fitting Choloniewski parameters for $ugrizYJK$ filters agree within the 90% confidence interval boundaries. The H band parametrisations do not agree. However, as the Choloniewski parameters are degenerate, a small perturbation in the distribution can modify the best-fitting solution in such a way that the best-fitting parameters differ greatly whilst the shape only slightly varies. Generally, the M^* parameters in the NIR would seem to disagree with those expected from the best-fitting one dimensional Schechter function (e.g. Table 3.3). The residuals seem to confirm that at the turnover there are discrepancies between the best-fitting model and the data (see the lower illustration in Figures D.5, D.6, D.7, and D.8). Overall, however, the quality of the fit in those filters (see Table 5.6), is better than in the optical passbands. A second run of the optimisation algorithm, with different starting parameters, provided results similar to the first. The results presented here utilise the optimal (i.e., lowest χ^2) solution, regardless of the run it is taken from.

Variation in parameters with wavelength

The following relationships between the best fitting model parameters and the wavelength of the filter are found. The M^*_X and $\mu^{X,*}$ parameters brighten as the filter's wavelength increases. The slope of the luminosity distribution (the α parameter) increases with wavelength. The scale of the effect that magnitude variation ($M - M^*$) has on the surface

Photometry	Sources	$M^* - 5\log_{10}(h)$ (mag)	α	ϕ^* ($h^3\,Mpc^{-3}$)	σ_μ (mag arcsec^{-2})	$\mu^{X,*}$ (mag arcsec^{-2})	β_μ (arcsec^{-2})
$r_{\text{SDSS Petro}}$	11657	-21.08 ± 0.03	-1.24 ± 0.01	0.0095 ± 0.0004	0.793 ± 0.017	19.91 ± 0.03	0.517 ± 0.011
u_{Kron}	9457	-18.70 ± 0.05	-1.10 ± 0.02	0.0179 ± 0.0004	1.093 ± 0.031	22.78 ± 0.03	0.217 ± 0.023
g_{Kron}	10124	-20.23 ± 0.05	-1.16 ± 0.02	0.0136 ± 0.0003	1.148 ± 0.029	21.40 ± 0.05	0.325 ± 0.021
r_{Kron}	9871	-21.05 ± 0.05	-1.19 ± 0.02	0.0109 ± 0.0003	1.195 ± 0.036	20.62 ± 0.05	0.404 ± 0.019
i_{Kron}	8796	-21.41 ± 0.06	-1.20 ± 0.02	0.0100 ± 0.0003	1.247 ± 0.047	20.26 ± 0.05	0.451 ± 0.022
z_{Kron}	7884	-21.51 ± 0.05	-1.11 ± 0.02	0.0119 ± 0.0003	1.245 ± 0.045	20.13 ± 0.06	0.415 ± 0.026
Y_{Kron}	6528	-21.78 ± 0.07	-1.15 ± 0.02	0.0096 ± 0.0003	1.264 ± 0.064	19.84 ± 0.06	0.454 ± 0.027
J_{Kron}	5747	-21.86 ± 0.06	-1.10 ± 0.02	0.0100 ± 0.0003	1.262 ± 0.062	19.72 ± 0.06	0.443 ± 0.034
H_{Kron}	5864	-22.39 ± 0.08	-1.14 ± 0.02	0.0087 ± 0.0003	1.263 ± 0.063	19.30 ± 0.06	0.460 ± 0.030
K_{Kron}	4820	-21.55 ± 0.07	-0.94 ± 0.03	0.0139 ± 0.0004	1.242 ± 0.055	19.97 ± 0.09	0.341 ± 0.053

Table 5.4: Best fitting Choloniewski function parameters for the Bivariate brightness distributions. These datapoints are for samples that will suffer from colour incompleteness, but use varying magnitude limits for each object within the SWML algorithm to correct for this bias. Quoted errors show the 90% confidence interval limits for a system with 5 degrees of freedom, when all other parameters are fixed to the best-fitting solution. Minimum-χ^2 parameters for this dataset are shown in Table 5.6.

Photometry	Sources	$M^* - 5\log_{10}(h)$ (mag)	α	ϕ^* ($h^3\ Mpc^{-3}$)	σ_μ (mag arcsec^{-2})	$\mu^{X,*}$ (mag arcsec^{-2})	β_μ (arcsec^{-2})
u_{Kron}	7257	-18.68 ± 0.04	-1.15 ± 0.03	0.0159 ± 0.0005	1.087 ± 0.029	22.82 ± 0.04	0.196 ± 0.029
g_{Kron}	10124	-20.20 ± 0.05	-1.14 ± 0.02	0.0140 ± 0.0004	1.151 ± 0.032	21.40 ± 0.04	0.330 ± 0.021
r_{Kron}	9148	-21.04 ± 0.05	-1.18 ± 0.02	0.0112 ± 0.0003	1.197 ± 0.039	20.63 ± 0.05	0.396 ± 0.020
i_{Kron}	8135	-21.36 ± 0.05	-1.18 ± 0.02	0.0105 ± 0.0003	1.251 ± 0.051	20.30 ± 0.05	0.434 ± 0.025
z_{Kron}	7588	-21.50 ± 0.07	-1.11 ± 0.02	0.0120 ± 0.0004	1.248 ± 0.048	20.09 ± 0.04	0.432 ± 0.025
Y_{Kron}	6073	-21.77 ± 0.06	-1.15 ± 0.02	0.0096 ± 0.0003	1.265 ± 0.065	19.89 ± 0.06	0.428 ± 0.027
J_{Kron}	5747	-21.90 ± 0.06	-1.11 ± 0.02	0.0097 ± 0.0003	1.260 ± 0.060	19.68 ± 0.06	0.450 ± 0.032
H_{Kron}	5015	-21.84 ± 0.07	-0.94 ± 0.03	0.0141 ± 0.0004	1.234 ± 0.061	19.67 ± 0.08	0.342 ± 0.042
K_{Kron}	4403	-21.57 ± 0.09	-0.96 ± 0.04	0.0131 ± 0.0005	1.206 ± 0.055	19.91 ± 0.06	0.325 ± 0.047

Table 5.5: Best fitting Choloniewski function parameters for the Bivariate brightness distributions. These parameters are for samples that have been cut to a brighter apparent magnitude in order to guarantee that they are colour complete. Quoted errors show the 90% confidence interval limits for a system with 5 degrees of freedom, when all other parameters are fixed to the best-fitting solution. The $r_{\text{SDSS Petro}}$ sample is the same as the sample detailed in Table 5.4, and so is not shown. Minimum-χ^2 parameters for this dataset are shown in Table 5.7.

Photometry	Choloniewski χ^2	χ^2_{red}	Modified function χ^2	χ^2_{red}
$r_{\text{SDSS Petro}}$	765.77	6.381	690.11	5.848
u_{Kron}	343.69	2.135	269.08	1.692
g_{Kron}	425.37	2.934	319.50	2.234
r_{Kron}	527.81	3.383	399.15	2.592
i_{Kron}	531.77	3.569	381.40	2.595
z_{Kron}	488.35	3.300	322.78	2.211
Y_{Kron}	419.17	2.851	311.80	2.150
J_{Kron}	396.89	2.775	291.80	2.069
H_{Kron}	367.51	2.644	264.11	1.928
K_{Kron}	305.69	2.351	209.93	1.640

Table 5.6: Best-fitting model χ^2 parameters for the Bivariate brightness distributions.

Photometry	Choloniewski χ^2	χ^2_{red}	Modified function χ^2	χ^2_{red}
u_{Kron}	316.93	2.099	239.85	1.610
g_{Kron}	415.15	2.863	307.43	2.150
r_{Kron}	488.19	3.191	353.75	2.343
i_{Kron}	503.45	3.402	359.74	2.464
z_{Kron}	494.55	3.411	323.82	2.265
Y_{Kron}	410.78	2.873	302.70	2.147
J_{Kron}	397.49	2.780	292.55	2.075
H_{Kron}	326.26	2.435	217.65	1.649
K_{Kron}	293.18	2.327	202.28	1.631

Table 5.7: Best-fitting model χ^2 parameters for the Bivariate brightness distributions. These parameters are for samples that are colour complete.

Parameter	$\delta M_r^* - 5\log_{10}h$ (mag)	$\delta\alpha$	$\delta\phi^*$ ($h^3\ Mpc^{-3}$)	$\delta\sigma_\mu$ (mag arcsec^{-2})	$\delta\mu^{X,*}$ (mag arcsec^{-2})	$\delta\beta_\mu$ (arcsec^{-2})
$\delta M_r^* - 5\log_{10}h$ (mag)	1.85×10^{-3}	4.25×10^{-4}	1.46×10^{-5}	-4.61×10^{-5}	1.09×10^{-3}	-1.59×10^{-4}
$\delta\alpha$	4.25×10^{-4}	1.42×10^{-4}	4.02×10^{-6}	-2.06×10^{-5}	2.61×10^{-4}	-5.10×10^{-5}
$\delta\phi^*$ ($h^3\ Mpc^{-3}$)	1.46×10^{-5}	4.02×10^{-6}	1.31×10^{-7}	-1.52×10^{-7}	8.80×10^{-6}	-1.31×10^{-6}
$\delta\sigma_\mu$ (mag arcsec^{-2})	-4.61×10^{-5}	-2.06×10^{-5}	-1.52×10^{-7}	1.11×10^{-4}	-8.63×10^{-6}	3.01×10^{-5}
$\delta\mu^{X,*}$ (mag arcsec^{-2})	1.09×10^{-3}	2.61×10^{-4}	8.80×10^{-6}	-8.63×10^{-6}	1.03×10^{-3}	-2.24×10^{-4}
$\delta\beta_\mu$ (arcsec^{-2})	-1.59×10^{-4}	-5.10×10^{-5}	-1.31×10^{-6}	3.01×10^{-5}	-2.24×10^{-4}	8.80×10^{-5}

Table 5.8: The covariance matrix for the deeper r_{Kron} sample.

brightness (i.e., the β_μ parameter) increases from the UV onwards, peaks around the Y band, and then tails off in the NIR. A similar effect occurs in the width (σ_μ) of the surface brightness distribution, though the peak occurs later, between J and H. No systematic variation in ϕ^* is seen.

Fit to r band SDSS Petrosian photometry

The lower illustration in Figure 5.8 compares the $r_{\mathrm{SDSS,Petro}}$ BBD and the best fit using the Choloniewski model.

The model is generally a good fit to the data, though there are abnormalities in some areas. The model is underpredicting the density of compact, bright sources centred around $M_r = -22\,\mathrm{mag}$, $\mu^{r,50} = 18.5\,\mathrm{mag\,arcsec^{-2}}$. It overpredicts the luminosity density in the faintest surface brightnesses bins, and slightly overpredicts in the centre of the distribution (around $M_r = -18\,\mathrm{mag}$, $\mu^{r,50} = 20\,\mathrm{mag\,arcsec^{-2}}$). The model is underpredicting the number of faint, compact sources, particularly fainter than $M_r = -17\,\mathrm{mag}$.

Figure 5.9 shows how the limiting volume of the sample varies, with the $r_{\mathrm{SDSS,Petro}}$ BBD overlain (shown using a logarithmic luminosity density scaling). Three selection boundaries are shown; defining the region that contains coverage of 3×10^3, 10^4 and $10^5\,h^{-3}\,\mathrm{Mpc^3}$. The bins the majority of the sample reside within are not constrained by the visibility limitations that are inherent in GAMA. In the surface brightness plane, the peak of the distribution is unaffected by the survey constraints; the minimum size limit occurs ~ 3 bins from the peak of the distribution. Bins within the r_{SDSS} sample have a median complement of 43.0 galaxies. The normalisation region contains 2589 sources, and is shown in green. It is far from the survey constraints.

Fit to r band GAMA Kron photometry

The upper illustration in Figure 5.10 compares the r_{Kron} BBD and the best fit using the Choloniewski model.

The Choloniewski function is a good fit to the r_{Kron} data. The overdensity of compact, bright sources that is present in the best-fitting SDSS r_{Petro} model also occurs in the r_{Kron} dataset. As with the aforementioned SDSS model, the luminosity density at the edges of the surface brightness distribution is also underestimated, and the model overestimates
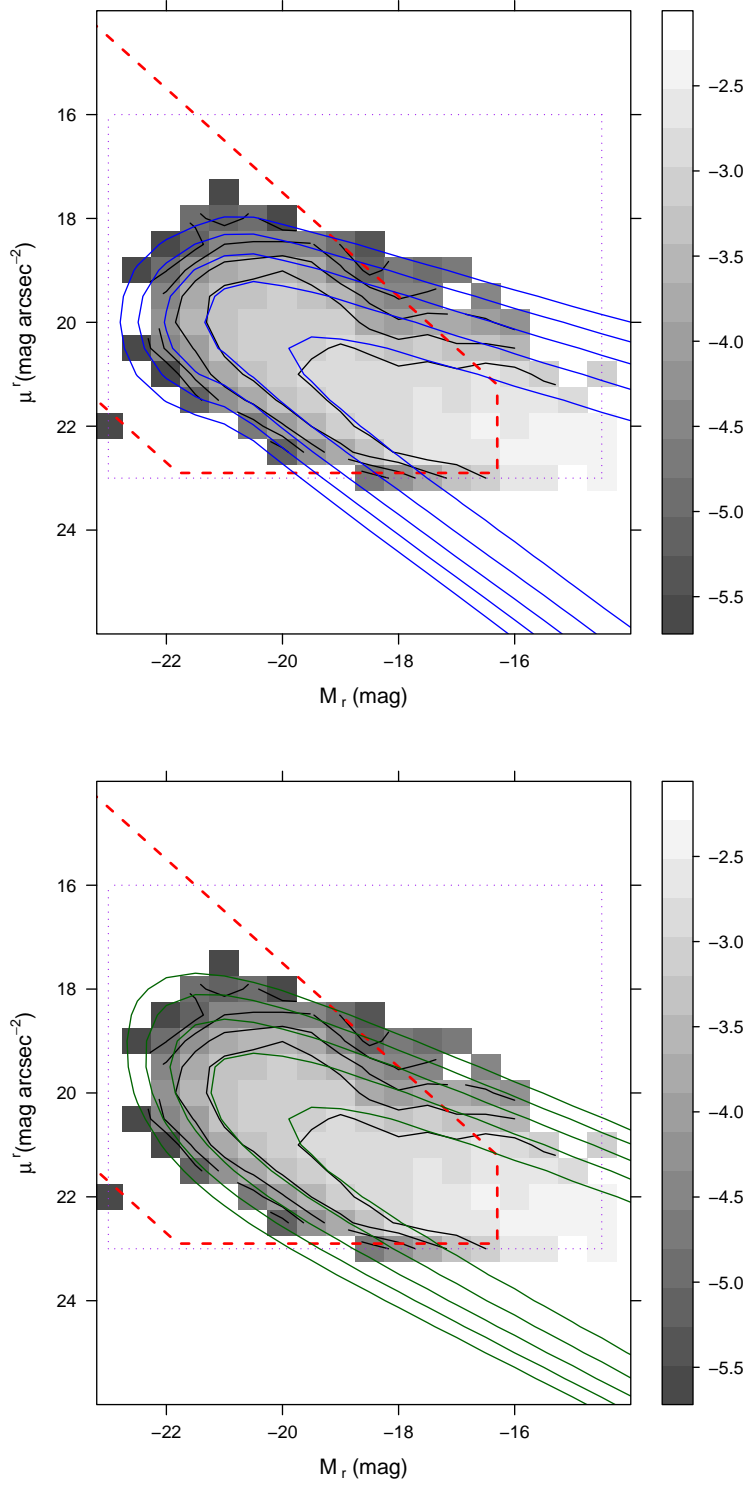
Figure 5.8: $r_{\mathrm{SDSS,Petromag}}$ BBDs for the deeper, colour-incompleteness corrected sample. The lower figure illustrates the best-fitting Choloniewski function, the upper figure illustrates the best-fitting modified-model function. The red dashed line bounds the region where the sampled volume is greater than $3\times10^4\,h^{-3}\,\mathrm{Mpc}^3$. The purple dotted line denotes the M-SB space that the BBD SWML algorithm was limited to. The colour scale illustrates the variation in luminosity density between bins. Contours are shown at $10^{-5}\,h^3\,\mathrm{Mpc}^{-3}$, $10^{-4.5}\,h^3\,\mathrm{Mpc}^{-3}$, $10^{-4}\,h^3\,\mathrm{Mpc}^{-3}$, $10^{-3.5}\,h^3\,\mathrm{Mpc}^{-3}$, and $10^{-3}\,h^3\,\mathrm{Mpc}^{-3}$.
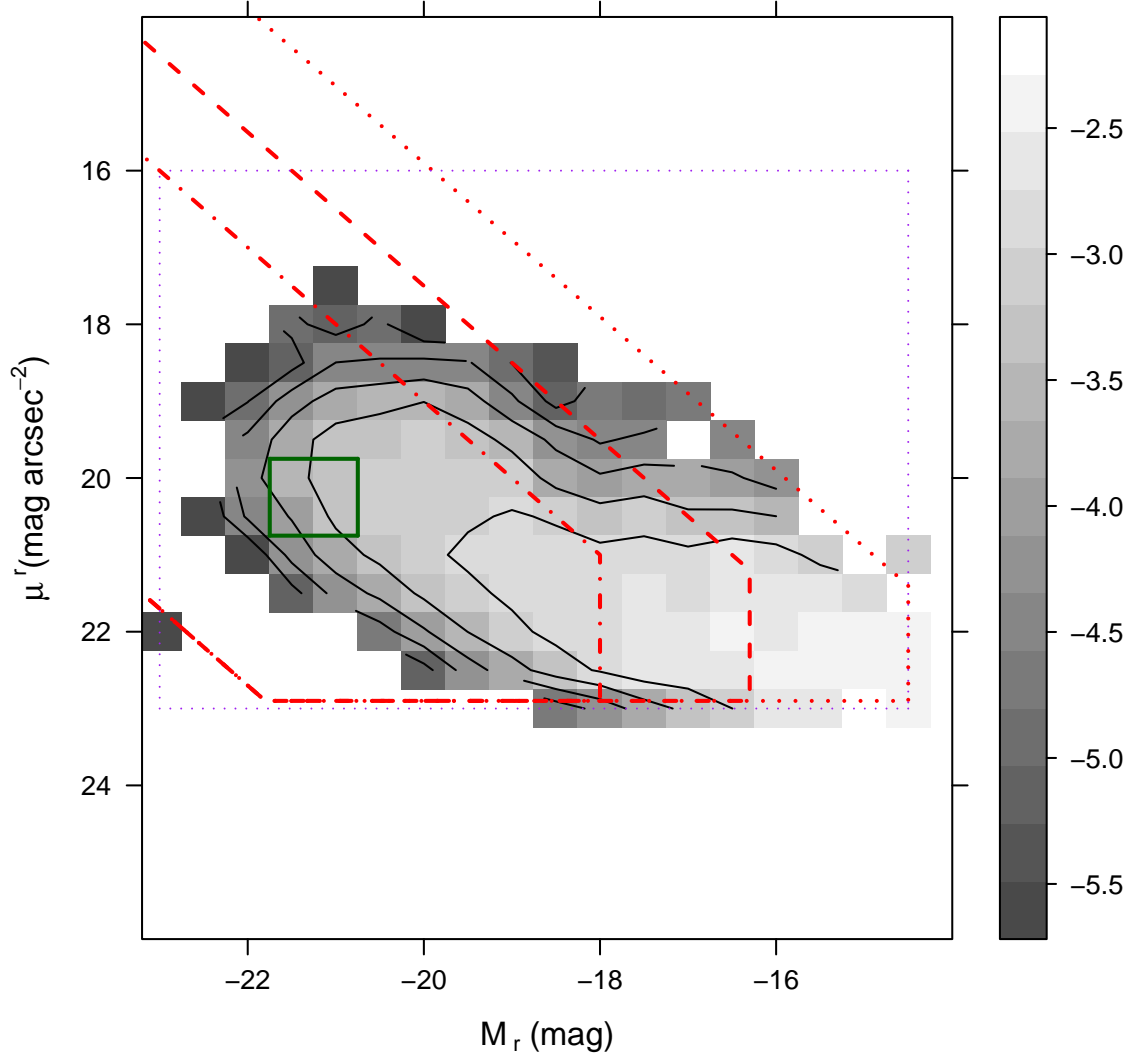
Figure 5.9: The variation in sampled volume for the r band SDSS Petrosian sample, with the BBD shown. The boundaries shown contain sampled volumes of $3 \times 10^5 \, h^{-3} \, \mathrm{Mpc}^3$ (dot-dash line), $3 \times 10^4 \, h^{-3} \, \mathrm{Mpc}^3$ (dashed line), and $3 \times 10^3 \, h^{-3} \, \mathrm{Mpc}^3$ (dotted line). The region used to normalise the BBD is bordered by a green boundary.

the density around $M_r = -18\,\mathrm{mag}$, $\mu^r = 20\,\mathrm{mag\,arcsec^{-2}}$. The best-fitting M^* and α parameters are similar.

There are differences between the r band models. The r_{SDSS} BBD has a far smaller variation in surface brightness than the r_{Kron} BBD (σ_μ for the Kron photometry is $0.402\,\mathrm{mag\,arcsec^{-2}}$ larger). The best-fitting parameters that describe the surface brightness distribution vary greatly between models. This may be a product of the different method used to calculate the surface brightness. The SDSS BBD uses the Petrosian half-light radius to calculate the size of the source, whilst the Kron BBD uses the r band effective radius (determined by the SIGMA wrapper). There is a discrepancy between surface brightness estimates using these methods, with the size of the offset dependent on the Sérsic index of the source's profile. Graham & Driver (2005) calculate an offset of $\langle\mu\rangle_e - \langle\mu\rangle_{50} = 0.01\,\mathrm{mag\,arcsec^{-2}}$ for an $n = 1$ profile, rising to $\langle\mu\rangle_e - \langle\mu\rangle_{50} = 0.52\,\mathrm{mag\,arcsec^{-2}}$ for an $n = 4$ profile. The best-fitting Petrosian model predicts a slightly larger luminosity density of bright, compact sources, and faint extended sources, whilst the best-fitting Kron model predicts a much larger luminosity density of bright, extended sources and faint, compact sources. This is shown in Figure 5.11

Fit to GAMA Kron photometry

Appendix D contains the BBDs produced from GAMA Kron photometry, the best fitting models and the scale of the discrepancy between the models and the data itself. The photometry in u to K is generally well fit by the model, but there are inconsistencies in certain areas. The best-fitting models generally underestimate the speed of the downturn, and thus overpredict the luminosity density of compact, high luminosity sources. They overpredict the luminosity density from faint, compact sources. The luminosity density from bright, extended sources is also often greater in the data than the model.

5.3 Comparisons with previous surveys

Within other filters, there have been few attempts at generating a BBD and fitting the distribution with a Choloniewski function. The results published in the literature are reproduced in Table 5.9. Where published results are comparable to GAMA results, a
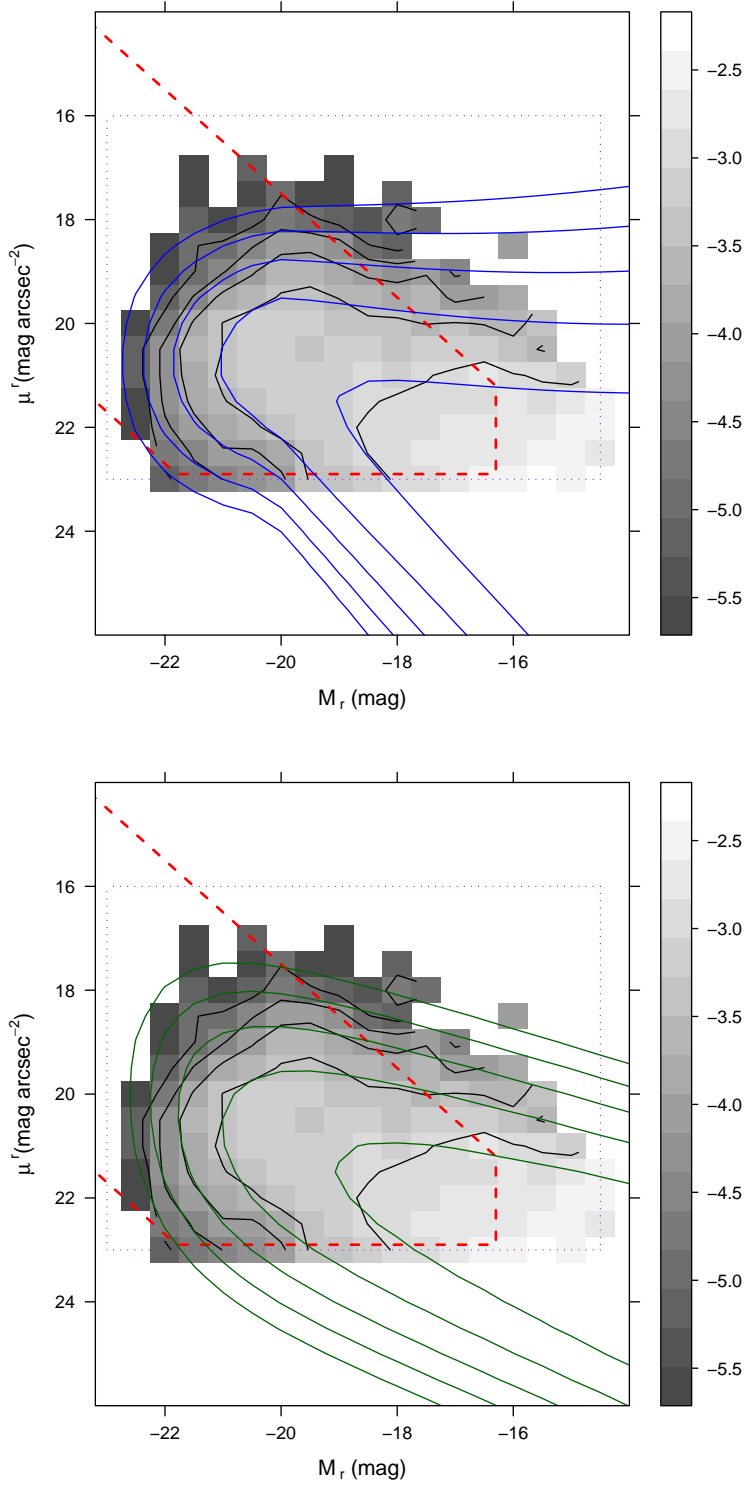
Figure 5.10: r_{Kron} BBDs for the deeper, colour-incompleteness corrected sample. The lower figure illustrates the best-fitting Choloniewski function, the upper figure illustrates the best-fitting modified-model function. The red dashed line bounds the region where the sampled volume is greater than $3 \times 10^4 \, h^{-3} \, \mathrm{Mpc}^3$. The purple dotted line denotes the M-SB space that the BBD SWML algorithm was limited to. Contours are shown at $10^{-5} \, h^3 \, \mathrm{Mpc}^{-3}$, $10^{-4.5} \, h^3 \, \mathrm{Mpc}^{-3}$, $10^{-4} \, h^3 \, \mathrm{Mpc}^{-3}$, $10^{-3.5} \, h^3 \, \mathrm{Mpc}^{-3}$, and $10^{-3} \, h^3 \, \mathrm{Mpc}^{-3}$.
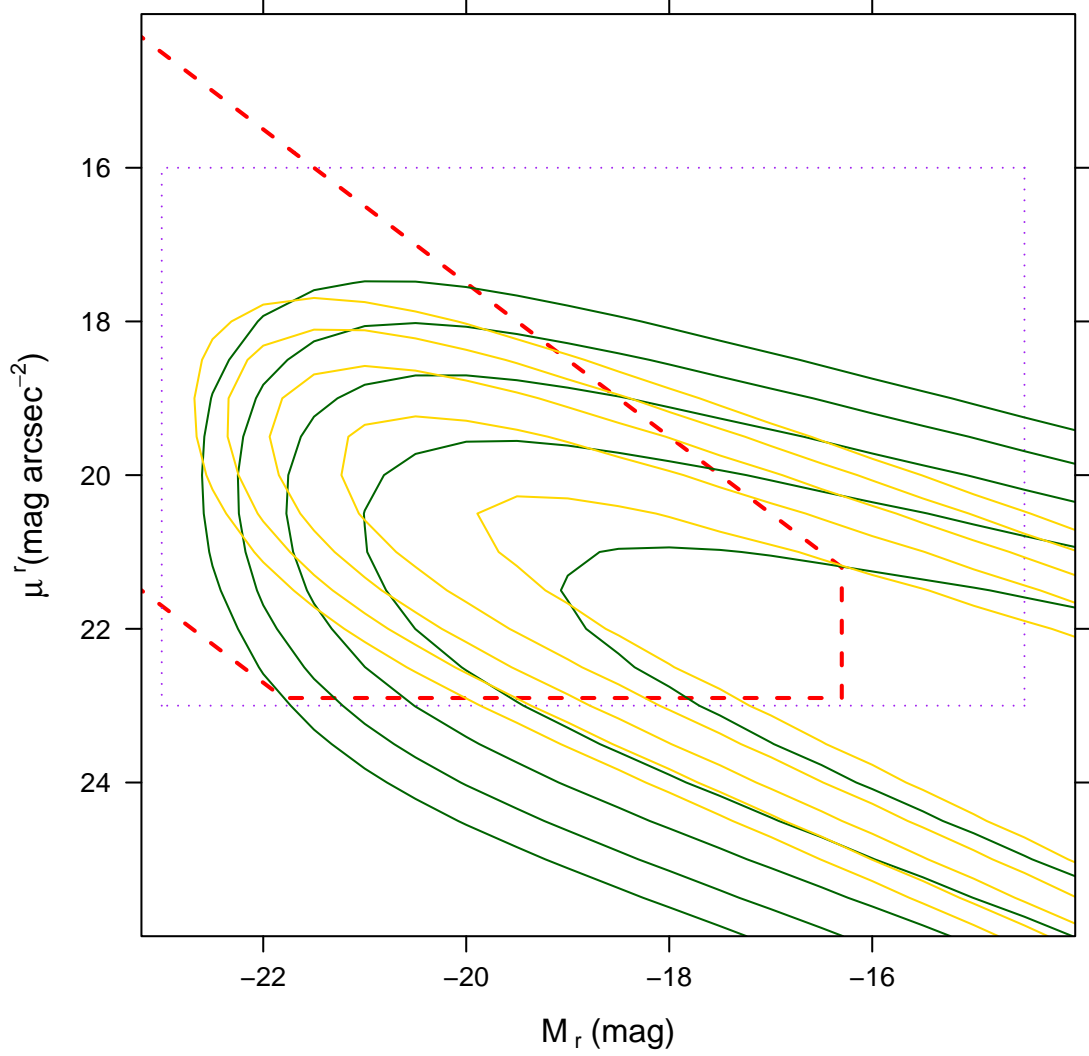
Figure 5.11: A comparison between the GAMA r_{Kron} and $r_{SDSSPetro}$ best-fitting Choloniewski functions. The $r_{SDSSPetro}$ function is shown in yellow, the r_{Kron} function is shown in green. The purple dashed line denotes the region of M-μ space that the r band BBD SWML algorithm was limited to. The red line bounds the region where the sampled volume is greater than $3 \times 10^4 \, h^{-3} \, \mathrm{Mpc}^3$. Contours are shown at $10^{-5} \, h^3 \, \mathrm{Mpc}^{-3}$, $10^{-4.5} \, h^3 \, \mathrm{Mpc}^{-3}$, $10^{-4} \, h^3 \, \mathrm{Mpc}^{-3}$, $10^{-3.5} \, h^3 \, \mathrm{Mpc}^{-3}$, and $10^{-3} \, h^3 \, \mathrm{Mpc}^{-3}$.

Author	Filter	$M^*-5\log_{10}(h)$ (mag)	α	ϕ^* (h^3 Mpc^{-3})	σ_μ (mag arcsec^{-2})	$\mu^{X,*}$ (mag arcsec^{-2}) / $r_{e,*}$ (kpc)	β_μ (arcsec^{-2})
Ball et al. (2006)	SDSS r	-21	-1.3	0.0017	0.79	$\mu^{r,*} = 21$	0.094
Cross & Driver (2002)	2dF b_j	-19.72	-1.05	0.0206	0.52	$\mu^{b_j,*} = 22.45$	0.28
Driver et al. (2005)	B_{MGC}	-19.37	-0.99	0.0213	0.86	$\mu^{B,*} = 22.0$	0.33
de Jong & Lacey (1999)	I	-22.17	-0.93	0.0014	0.28	$r_{e,*} = 6.09$	-0.25
Smith et al. (2009)	K_{Vega}	-22.96	-0.38	0.0201	0.67	$\mu^{K,*} = 17.36$	0.19

Table 5.9: Best-fitting Choloniewski function parameters from other surveys. In the case of de Jong & Lacey, where the BBD is generated in M-r_e, the $r_{e,*}$ parameter is quoted. Parameters from v1 of Ball et al. are shown, as the parameters they have published may result from a local minima (Ball & Loveday, priv. comm). Parameters have not been converted onto the AB magnitude system.

comparison between models is made in Section 5.3.

r band BBD compared to the VAGC model

Ball et al. (2006), use the VAGC (Blanton et al. 2005) to generate a BBD using the $r_{\text{SDSS,Petro}}$ photometric system. The VAGC dataset is based upon SDSS DR4 photometry. Their published Choloniewski function parameters have an extreme $\mu^{r,*}$ parameter, which infers that the fitting has found a local minima. Following communication with the authors, the GAMA model has been compared to the function parameters they published in an earlier draft (v1 on arXiv). Very different M^*, μ^* and ϕ^* best-fitting model parameters are found (see Table 5.9). A comparison between the models is shown in Figure 5.12. The GAMA model predicts a higher density of bright, compact sources and faint, extended sources. As the GAMA model underestimates the number of bright, compact sources compared to the $r_{\text{SDSS,Petro}}$ distribution, the Ball et al. model greatly differs from the GAMA distribution.

The discrepancy between their result and this result may be due to limitations present within their dataset. They remove galaxies with large axis ratios (greater than that of an E7 elliptical), biasing their sample against elongated sources. The GAMA survey utilise a comprehensive star-galaxy separation (see Baldry et al. 2010), that finds extra compact sources that would otherwise be discounted in the SDSS main spectroscopic survey. These selection effects will have two results. Firstly, they would produce less faint, extended sources within their model fit: they state the effects of the axial-ratio cut will be to reduce the population of exponential type sources. Secondly, the GAMA distribution will contain a higher density of compact, bright sources than their model. Both of these trends can be
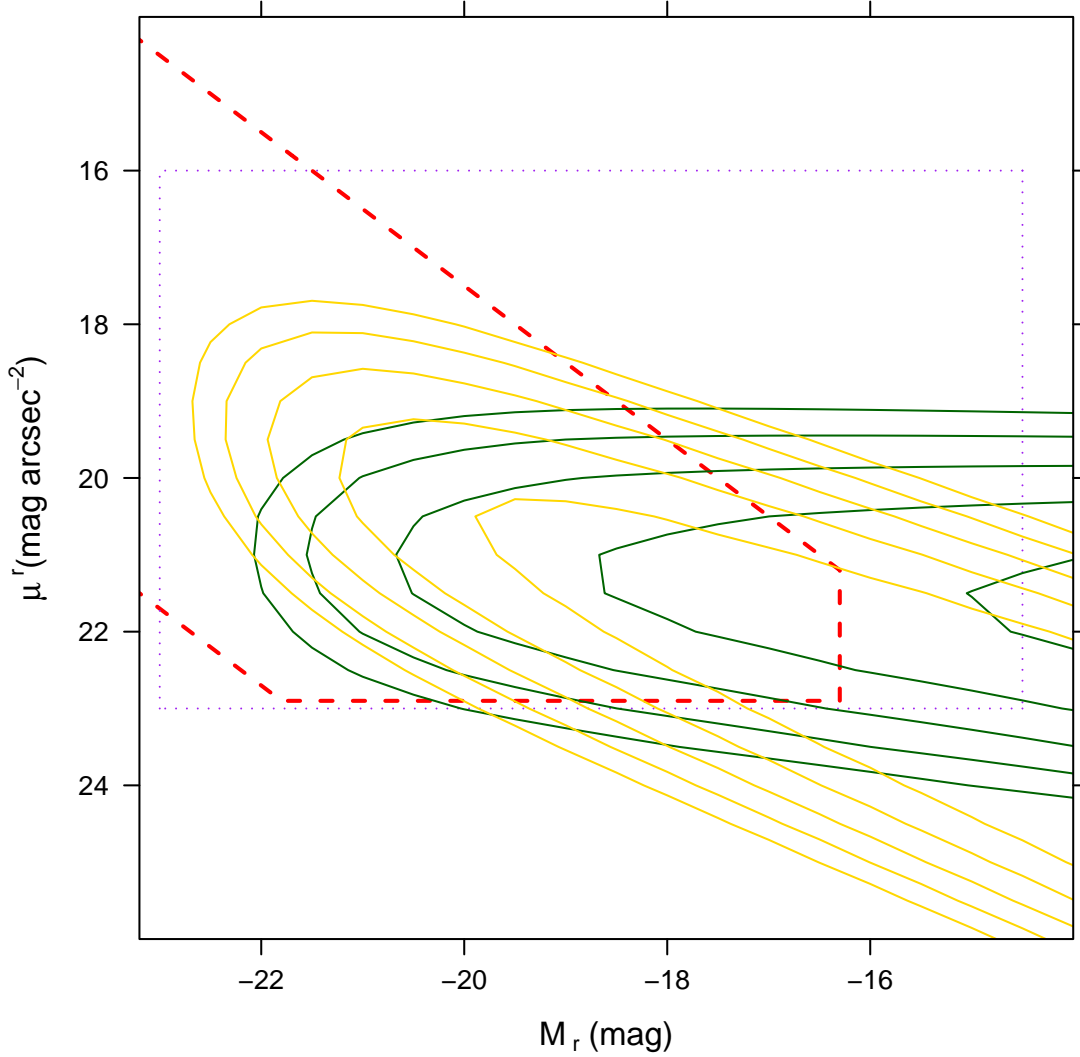
Figure 5.12: A comparison between the best-fitting $r_{SDSSPetro}$ Choloniewski function from VAGC data (Ball et al., 2006), and the best-fitting $r_{SDSSPetro}$ Choloniewski functions from GAMA data. The GAMA function is shown in yellow; the Ball et al. (2006) function is shown in green. The purple dotted line denotes the region of M-μ space that the r band BBD SWML algorithm was limited to. The red dashed line bounds the region where the sampled volume is greater than $3 \times 10^4 \, h^{-3} \, \text{Mpc}^3$. Contours are shown at $10^{-5} \, h^3 \, \text{Mpc}^{-3}$, $10^{-4.5} \, h^3 \, \text{Mpc}^{-3}$, $10^{-4} \, h^3 \, \text{Mpc}^{-3}$, $10^{-3.5} \, h^3 \, \text{Mpc}^{-3}$, and $10^{-3} \, h^3 \, \text{Mpc}^{-3}$.

seen within Figure 5.12.

g band BBD compared to the MGC/2dF models

The 2dF (Cross et al., 2001) and MGC (Driver et al., 2005) BBDs are from observations taken using filters very similar to the g band SDSS passband. The best-fitting GAMA model has a much brighter M^* parameter (accounting for the filter offset), and a fainter

μ^* than those previous surveys. The discrepancy between the best fitting models can be seen in Figures 5.13 and 5.14.

Despite the disparity in parameters, the MGC and GAMA BBD models are similar (Figure 5.13). The GAMA model has a higher density of faint, compact sources, but is slightly underdense elsewhere. The latter effect may be an issue of cosmic variance within the MGC region. The MGC is overdense by $\sim 20\%$ compared to the SDSS survey as a whole (Section 3.2.3), and its BBD has not been normalised to account for this. The former effect may be due to variations in the star-galaxy separation used between the MGC and GAMA samples. Liske et al. (2006) predict that between $M_B = -17$ and $M_B = -14\,\text{mag}$, the MGC will lose $\sim 6\%$ of the luminosity density because of high surface brightness incompleteness. This selection effect may lower the luminosity density in a number of BBD bins, which would have a cumulative impact on the functional fitting, potentially causing some of the discrepancy shown in Figure 5.13.

The GAMA and 2dF models are very dissimilar (Figure 5.14). As with the MGC-GAMA comparison, the difference in photometric method may be partly to blame. The 2dF BBD is derived using isophotal magnitudes. Due to technical constraints present at the time of analysis, the effective surface brightness for the 2dF distribution is calculated from the central surface brightness, under the assumption that every source can be modelled as a perfect exponential disc (section 4.1 of Cross et al. 2001). While this method works admirably for exponential-profile sources, it is in error for the compact de-Vaucouleurs profile sources. It biases the BBD against the high-surface brightness bins. Unsurprisingly, the GAMA sample's model predicts a much higher density of faint, compact sources.

K band BBD compared to the UKIDSS model

The UKIDSS (Smith et al., 2009) BBD is taken from observations using the same filter and instrument as the GAMA K band BBD. The difference between the best-fitting BBD models is shown in Figure 5.15. The UKIDSS BBD has a higher luminosity density of compact sources, particularly brighter objects. It has a much lower density of extended objects. This can be explained by two factors. Firstly, Smith et al. note that they anticipate visibility incompleteness at $M_K - 5\log_{10}(\text{h}) > -19\,\text{mag}$. This effect would decrease the number of faint, extended objects considerably, undoubtedly producing the unusually large best-fitting α parameter ($\alpha = -0.38$). Secondly, when r band Kron and
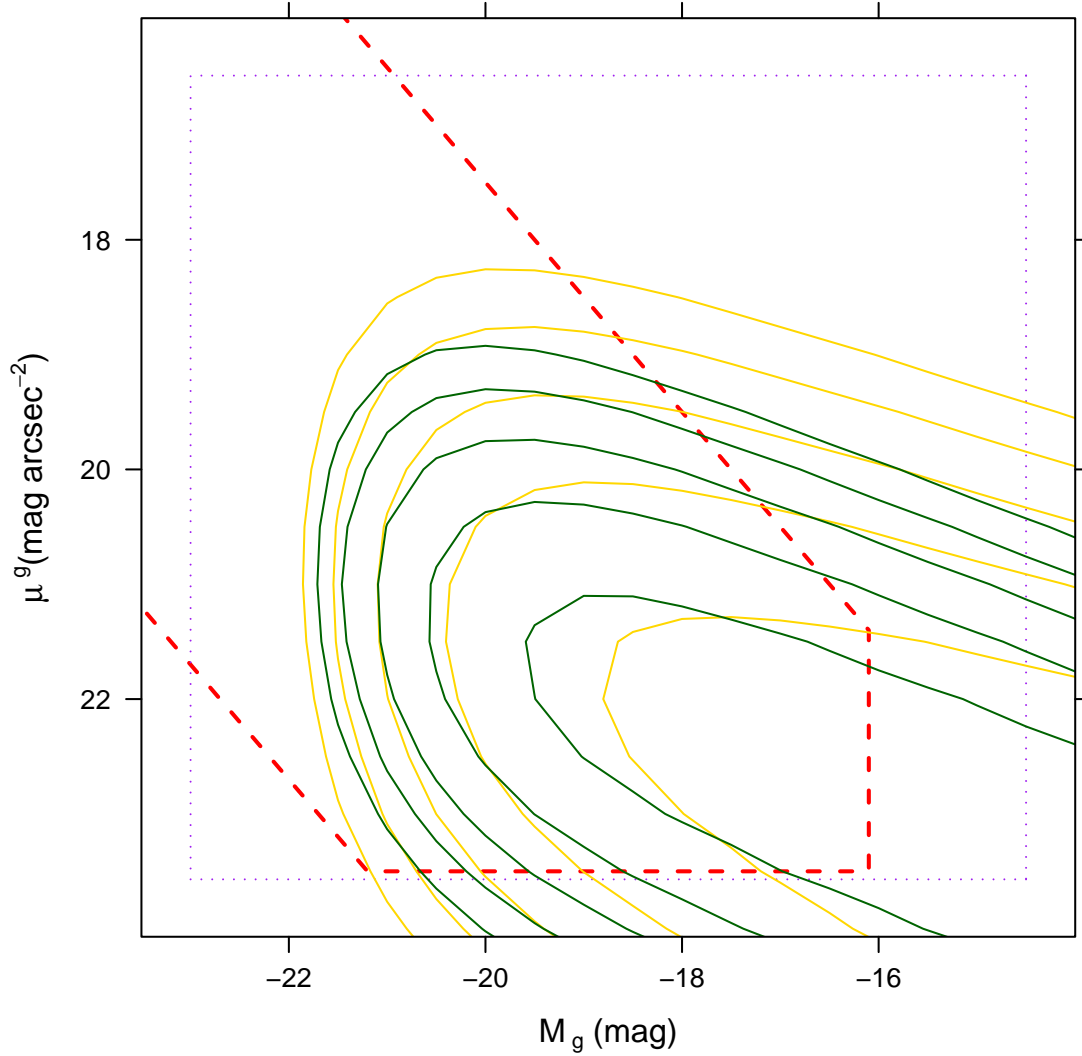
Figure 5.13: A comparison between the best-fitting B_{Kron} Choloniewski function from MGC data (Driver et al., 2005), and the best-fitting g_{Kron} Choloniewski functions from GAMA data. In this figure, the MGC M^* and $\mu^{B,*}$ model parameters have been shifted to the g band in order to account for the filter offset. The GAMA function is shown in yellow; the Driver et al. (2005) function is shown in green. The purple dotted line denotes the region of M-μ space that the g band BBD SWML algorithm was limited to. The red dashed line bounds the region where the sampled volume is greater than $3 \times 10^4 \, h^{-3} \, \mathrm{Mpc}^3$. Contours are shown at $10^{-5} \, h^3 \, \mathrm{Mpc}^{-3}$, $10^{-4.5} \, h^3 \, \mathrm{Mpc}^{-3}$, $10^{-4} \, h^3 \, \mathrm{Mpc}^{-3}$, $10^{-3.5} \, h^3 \, \mathrm{Mpc}^{-3}$, and $10^{-3} \, h^3 \, \mathrm{Mpc}^{-3}$.
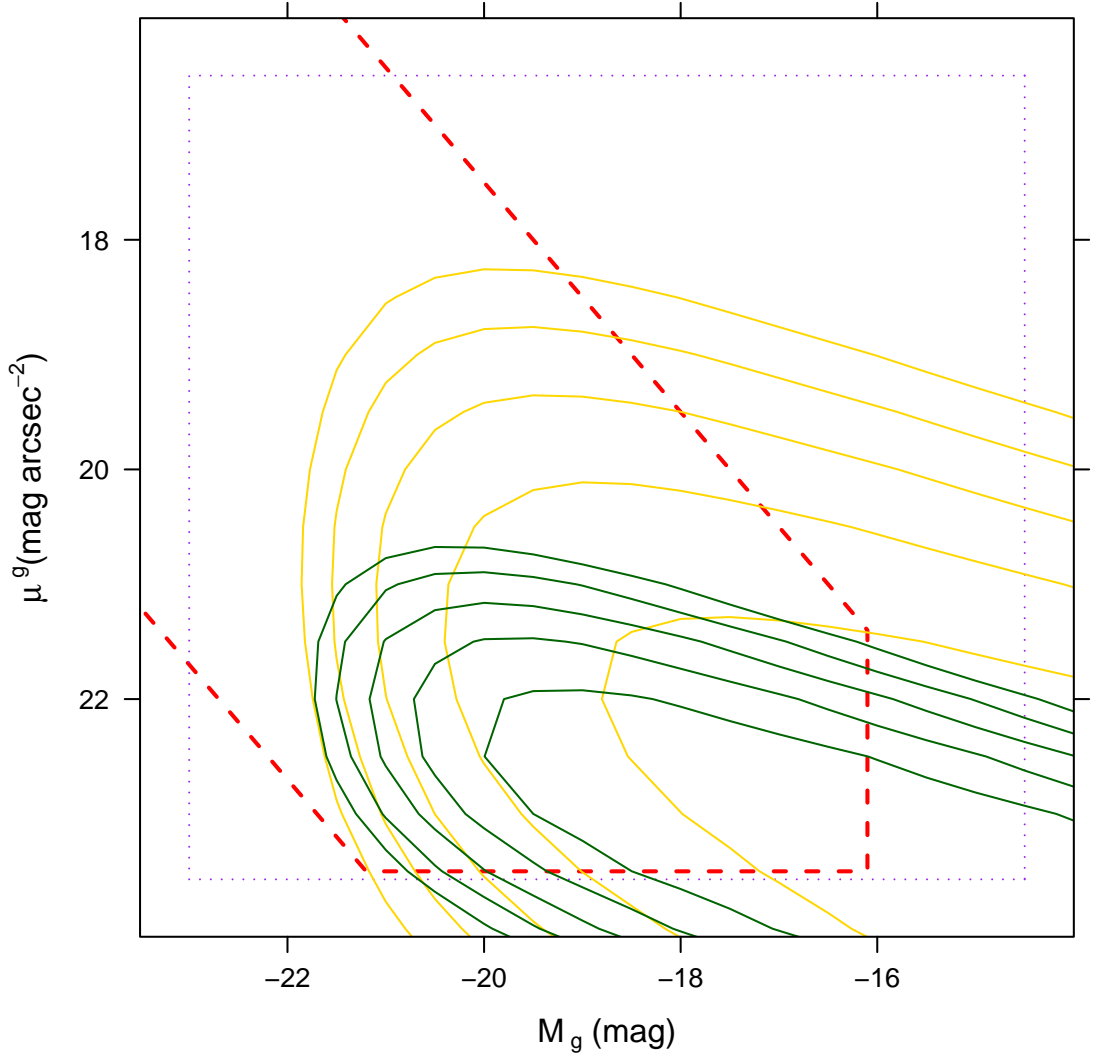
Figure 5.14: A comparison between the best-fitting b_j Choloniewski function from 2dF data (Cross et al., 2001), and the best-fitting g_{Kron} Choloniewski functions from GAMA data. In this figure, the 2dF M^* and $\mu^{b_j,*}$ model parameters have been shifted to the g band in order to account for the filter offset. The GAMA function is shown in yellow; the Cross et al. (2001) function is shown in green. The purple dotted line denotes the region of M-μ space that the g band BBD SWML algorithm was limited to. The red dashed line bounds the region where the sampled volume is greater than $3 \times 10^4\, h^{-3}\, \mathrm{Mpc}^3$. Contours are shown at $10^{-5}\, h^3\, \mathrm{Mpc}^{-3}$, $10^{-4.5}\, h^3\, \mathrm{Mpc}^{-3}$, $10^{-4}\, h^3\, \mathrm{Mpc}^{-3}$, $10^{-3.5}\, h^3\, \mathrm{Mpc}^{-3}$, and $10^{-3}\, h^3\, \mathrm{Mpc}^{-3}$.
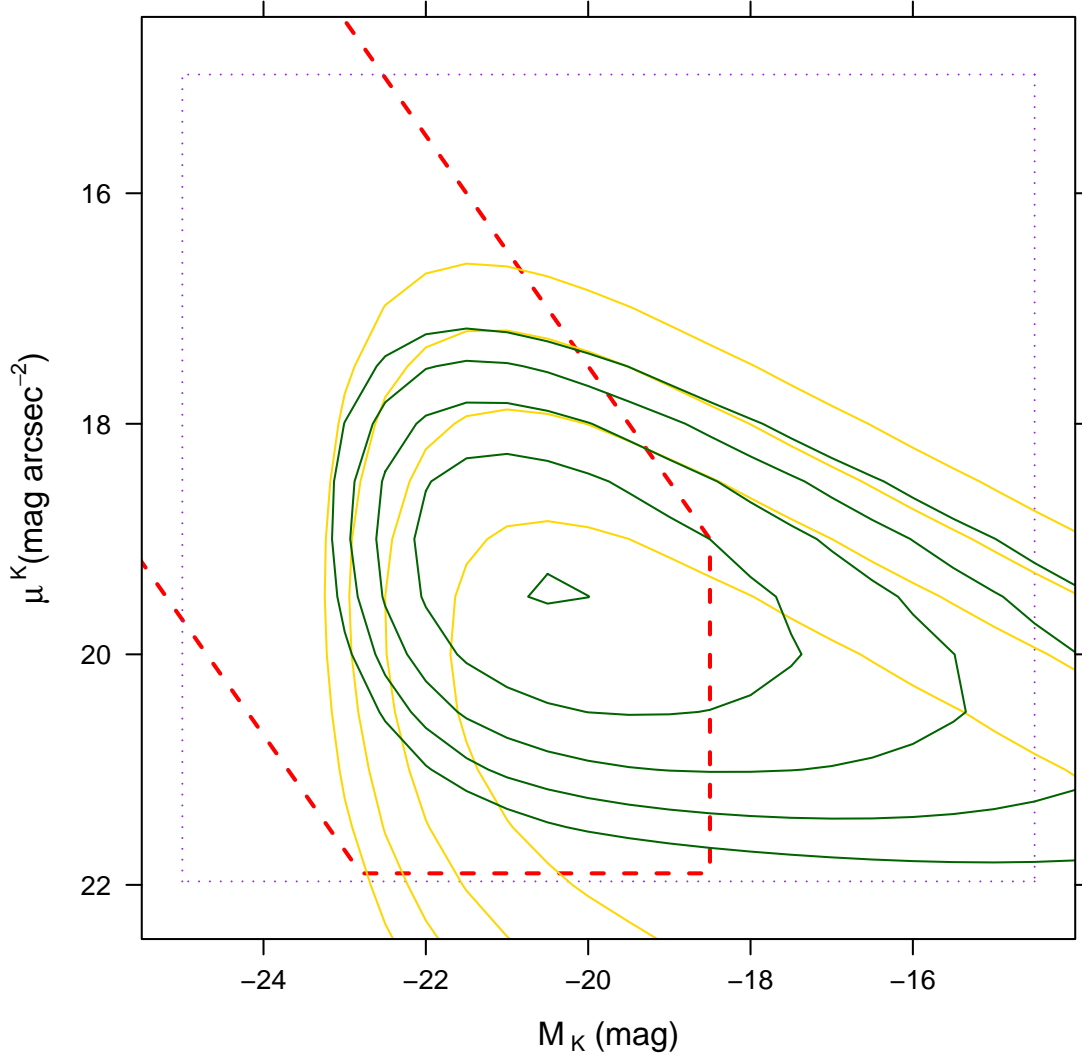
Figure 5.15: A comparison between the best-fitting K_{Petro} Choloniewski function from UKIDSS-LAS data (Smith et al., 2009), and the best-fitting K_{Kron} Choloniewski functions from GAMA data. In this figure, the UKIDSS M^* and $\mu^{K,*}$ model parameters have been shifted onto the *AB* magnitude system band. The GAMA function is shown in yellow; the Smith et al. (2009) function is shown in green. The purple dotted line denotes the region of M-μ space that the *K* band BBD SWML algorithm was limited to. The red dashed line bounds the region where the sampled volume is greater than $3\times10^4\,h^{-3}\,\mathrm{Mpc}^3$. Contours are shown at $10^{-5}\,h^3\,\mathrm{Mpc}^{-3}$, $10^{-4.5}\,h^3\,\mathrm{Mpc}^{-3}$, $10^{-4}\,h^3\,\mathrm{Mpc}^{-3}$, $10^{-3.5}\,h^3\,\mathrm{Mpc}^{-3}$, and $10^{-3}\,h^3\,\mathrm{Mpc}^{-3}$.

Petrosian BBDs are compared (Figure 5.11), the Kron magnitude BBD model was found to predict higher densities of bright, extended sources.

Quality of modified-model fits

The best-fitting modified-model parameters to the GAMA samples are shown in Table 5.10 (and for the colour-complete sample in Table 5.11), and the best fitting models to the r_{Kron} and r_{SDSS} datasets are shown in the upper illustration of Figures 5.10 and 5.8. Comparing the discrepancy between the modified models, and the standard Choloniewski best fits (i.e. Figures 5.10 and 5.8), the modified model is a better fit to the general shape of the contour (particularly the density of bright, extended source). Both models overpredict the luminosity density from bright, compact sources. However, the overprediction provided by the modified function is not so great.

The modified function has two more degrees of freedom than the Choloniewski function. In order to test whether it is a more realistic fit to the data, the reduced χ^2 of the data must be examined. The reduced χ^2 values for the best-fitting models (modified and unmodified) are shown in Tables 5.6 and 5.7. Two things are apparent:

1. While the models are not necessarily a good fit ($\chi^2_{red} > 1$), the quality of the fit improves towards the NIR. Different processes may cause this improvement. It may be that the data quality is improved. The decrease in dust attenuation in the NIR makes the calculation of true surface brightness profiles and luminosity easier, producing higher-quality distributions that are easier to fit models to. Alternatively, it may be a statistical effect. The sample sizes decrease as wavelength increases. For the larger samples, the Poissonian errors may cease to be the major cause of uncertainty. If this is the case, the bin weighting will be underestimated for those samples, and this will increase the χ^2 parameter.

2. As the χ^2_{red} statistic for the modified model is much smaller in all filters, the modified functional form is a better description of the data. This would indicate that there is a form of surface brightness evolution occurring with luminosity, and that any modelling must account for this or the recovered parameters will be systematically biased.

Variation of luminosity distribution with surface brightness

Figure 5.16 illustrates the variation in luminosity distribution between surface brightness intervals. In every filter, there is a general pattern. The faintest surface brightness bins

Photometry	$M^* - 5\log_{10}(h)$ (mag)	α	ϕ^* ($h^3\ Mpc^{-3}$)	σ_μ (mag arcsec^{-2})	$\mu_{var}^{X,*}$ (mag arcsec^{-2})	β_μ (arcsec^{-2})	E (arcsec^{-2})	$M_\sigma - 5\log_{10}(h)$ (mag)
$r_{\text{SDSS Petro}}$	-21.24 ± 0.06	-1.31 ± 0.01	0.0077 ± 0.0002	0.704 ± 0.026	19.96 ± 0.03	0.579 ± 0.015	0.057 ± 0.014	-20.77 ± 0.06
u_{Kron}	-18.65 ± 0.05	-1.12 ± 0.02	0.0184 ± 0.0006	0.992 ± 0.031	22.77 ± 0.04	0.304 ± 0.040	0.117 ± 0.034	-18.40 ± 0.18
g_{Kron}	-20.36 ± 0.06	-1.28 ± 0.02	0.0108 ± 0.0003	1.010 ± 0.034	21.47 ± 0.05	0.501 ± 0.038	0.151 ± 0.031	-19.52 ± 0.12
r_{Kron}	-21.32 ± 0.06	-1.36 ± 0.02	0.0072 ± 0.0002	1.023 ± 0.039	20.75 ± 0.05	0.650 ± 0.039	0.184 ± 0.036	-20.16 ± 0.10
i_{Kron}	-21.77 ± 0.06	-1.42 ± 0.02	0.0058 ± 0.0002	1.054 ± 0.042	20.45 ± 0.05	0.800 ± 0.048	0.247 ± 0.038	-20.40 ± 0.10
z_{Kron}	-21.90 ± 0.06	-1.37 ± 0.02	0.0067 ± 0.0002	1.036 ± 0.045	20.18 ± 0.06	0.809 ± 0.059	0.285 ± 0.055	-20.69 ± 0.10
Y_{Kron}	-22.01 ± 0.07	-1.33 ± 0.02	0.0065 ± 0.0002	1.059 ± 0.050	20.05 ± 0.06	0.770 ± 0.064	0.266 ± 0.055	-20.80 ± 0.12
J_{Kron}	-22.10 ± 0.07	-1.30 ± 0.02	0.0067 ± 0.0002	1.062 ± 0.054	19.91 ± 0.06	0.780 ± 0.082	0.297 ± 0.071	-20.90 ± 0.14
H_{Kron}	-22.36 ± 0.08	-1.25 ± 0.02	0.0074 ± 0.0003	1.066 ± 0.054	19.65 ± 0.07	0.777 ± 0.083	0.286 ± 0.072	-21.14 ± 0.13
K_{Kron}	-21.82 ± 0.08	-1.19 ± 0.04	0.0094 ± 0.0004	1.045 ± 0.058	19.95 ± 0.07	0.742 ± 0.120	0.348 ± 0.091	-20.89 ± 0.17

Table 5.10: The best fitting modified-model function parameters for the Bivariate brightness distributions. These datapoints are for samples that will suffer from colour incompleteness, but use varying magnitude limits for each object within the SWML algorithm to correct for this bias. The dataset fit to the model is the same dataset fit to the unmodified function, so sample sizes are shown in Table 5.4. χ^2 parameters for this dataset are shown in Table 5.6. Uncertainties are calculated from the 90% confidence intervals for a system with 7 degrees of freedom, when all other parameters are fixed to the best-fitting solution.

(i.e., the red or grey data sets) have a limited impact on the luminosity distribution at the bright end (e.g. $M_i < -20\,\text{mag}$), but gradually increase until they dominate the luminosity distribution at the faint end (e.g. $M_r > -17\,\text{mag}$). Unlike the medium surface brightness populations (for instance, the blue data), there is no sign of a turnover. As the faintest surface brightness bins are removed when a sample suffers from surface brightness incompleteness, this would support the assertion of Driver et al. (2005), that the detection of a faint-end upturn is primarily an issue of surface brightness completeness: the deeper the sample, the stronger the upturn.

Conversely, the highest surface brightness bins (i.e., the black dataset) provide a large fraction of the luminosity density in the brightest bins, but after a point (e.g. $M_Y = -20.5\,\text{mag}$), their luminosity distribution turns over and provides progressively less. An interesting effect then occurs. The luminosity density starts to rise again, and in the NIR filters a second turnover may be visible. For instance, in the H band the black data seems to peak at both $M_H = -21\,\text{mag}$ and $M_H = -18\,\text{mag}$. The black dataset may be showing the luminosity density from both the compact dwarf and giant populations. However, without an analysis of the sources by their morphological type, this cannot be proved, and it may just be caused by low-number statistics.

5.4 Calculation of total luminosity density and comparison to models

In this section, I calculate the total luminosity density, j (Section 5.2.3). By examining this statistic, and how it varies between filters (e.g., Wright 2001, Section 3.4), constraints can be put upon the cosmic star formation history (CSFH, Hopkins & Beacom 2006; Wilkins et al. 2008b), the initial mass function (IMF, Wilkins et al. 2008a), and population synthesis models (Fioc & Rocca-Volmerange, 1997). In order to remove the dependency on the filter passband that is inherent in j, I also derive the energy density per unit interval, $\nu f(\nu)$, using Equation 1.9. The $\nu f(\nu)$ statistic allows comparison between energy density per unit interval calculated via the BBD methods, and those calculated previously using both luminosity function and BBD methods, and to theory. In order to calculate j, the luminosity of the sun within the passband ($M_\odot$) must be known. The $M_\odot$ parameters from Table 2.1 are used within this section. First, however, the functional forms should
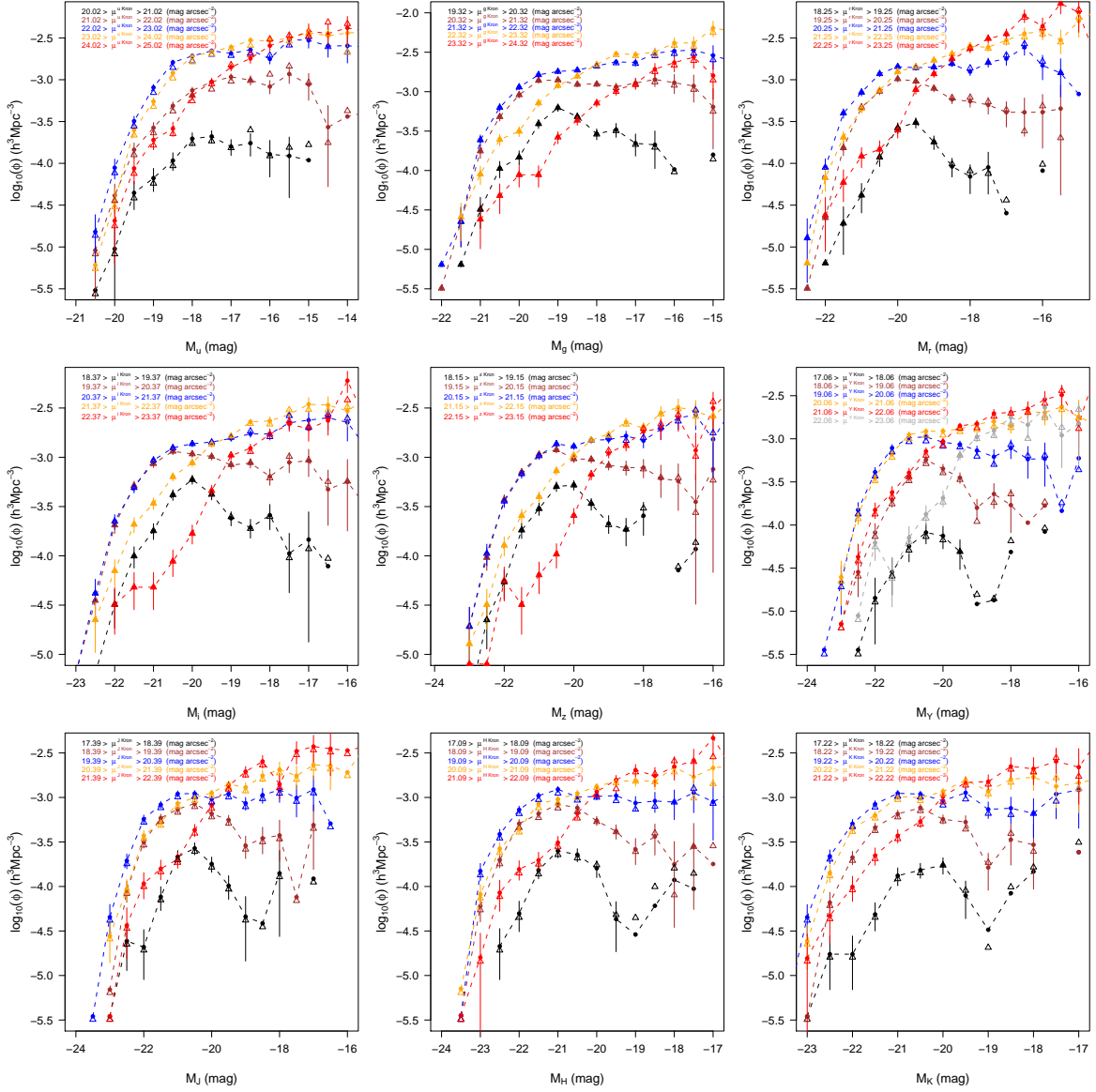
Figure 5.16: The luminosity distribution of the X_{Kron} samples, split into surface brightness intervals. Filled circles show the deeper, colour-incompleteness corrected sample. Triangles show the colour complete sample. For reasons of clarity, only uncertainties from the deeper sample are shown.

Photometry	$M^* - 5\log_{10}(h)$ (mag)	α	ϕ^* ($h^3\,Mpc^{-3}$)	σ_μ (mag arcsec^{-2})	$\mu_{var}^{X,*}$ (mag arcsec^{-2})	β_μ (arcsec^{-2})	E (arcsec^{-2})	$M_\sigma - 5\log_{10}(h)$ (mag)
u_{Kron}	-18.72 ± 0.05	-1.23 ± 0.03	0.0146 ± 0.0005	0.990 ± 0.036	22.78 ± 0.05	0.350 ± 0.062	0.167 ± 0.054	-18.33 ± 0.19
g_{Kron}	-20.30 ± 0.06	-1.25 ± 0.02	0.0114 ± 0.0003	1.011 ± 0.035	21.46 ± 0.05	0.515 ± 0.040	0.155 ± 0.031	-19.49 ± 0.12
r_{Kron}	-21.29 ± 0.06	-1.36 ± 0.02	0.0075 ± 0.0002	1.019 ± 0.041	20.75 ± 0.05	0.655 ± 0.046	0.205 ± 0.035	-20.16 ± 0.10
i_{Kron}	-21.74 ± 0.06	-1.42 ± 0.02	0.0060 ± 0.0002	1.044 ± 0.044	20.46 ± 0.06	0.815 ± 0.057	0.284 ± 0.057	-20.37 ± 0.10
z_{Kron}	-21.88 ± 0.06	-1.37 ± 0.02	0.0068 ± 0.0002	1.031 ± 0.044	20.18 ± 0.06	0.813 ± 0.064	0.302 ± 0.062	-20.70 ± 0.11
Y_{Kron}	-22.03 ± 0.07	-1.36 ± 0.02	0.0063 ± 0.0002	1.053 ± 0.052	20.04 ± 0.06	0.801 ± 0.076	0.303 ± 0.077	-20.80 ± 0.13
J_{Kron}	-22.11 ± 0.08	-1.30 ± 0.02	0.0067 ± 0.0002	1.060 ± 0.054	19.91 ± 0.06	0.795 ± 0.085	0.307 ± 0.073	-20.89 ± 0.14
H_{Kron}	-22.27 ± 0.07	-1.22 ± 0.03	0.0082 ± 0.0003	1.061 ± 0.055	19.64 ± 0.07	0.716 ± 0.098	0.283 ± 0.080	-21.16 ± 0.16
K_{Kron}	-21.82 ± 0.07	-1.19 ± 0.04	0.0094 ± 0.0004	1.028 ± 0.063	19.94 ± 0.07	0.670 ± 0.126	0.373 ± 0.126	-21.00 ± 0.18

Table 5.11: The best fitting modified-model function parameters for the Bivariate brightness distributions. These parameters are for samples that have been cut to a brighter apparent magnitude in order to guarantee that they are colour complete. The dataset fit to the model is the same dataset fit to the unmodified function, so sample sizes are shown in Table 5.5. The $r_{\text{SDSS Petro}}$ sample is the same as the sample detailed in Table 5.10, and so is not shown. χ^2 parameters for this dataset are shown in Table 5.6. Uncertainties are calculated from the 90% confidence intervals for a system with 7 degrees of freedom, when all other parameters are fixed to the best-fitting solution.

be tested to ascertain whether they can be integrated beyond our current limits. In the next section I examine the distribution of local galaxies to see if the galaxy distribution changes radically beyond our surface brightness and magnitude limits.

5.4.1 Beyond the GAMA BBD limits

In order to calculate the total luminosity density from a surface brightness/magnitude limited sample of galaxies, the bivariate brightness distribution must be modelled using a functional form (section 1.6). However, if the distribution radically alters beyond our magnitude and surface brightness limits, the total luminosity density derived via this function may greatly differ from the true value.

Karachentsev et al. (2004) have produced an all-sky catalogue of 451 galaxies within 10 Mpc, complete with B band absolute magnitude and surface brightness parameters. Within 8 Mpc, Karachentsev et al. state that the catalogue is ~ 70-80% complete. Although it covers a tiny volume, and will therefore suffer strongly from the effects of cosmic variance, this sample is a good representation of the population of galaxies within the Universe. In Figure 5.17, I plot the distribution of these sources in M-μ space, and how it compares with the g band BBD. The absolute magnitude and surface brightness of the Karachentsev et al. sources have been offset onto the g band magnitude system.

What is immediately apparent is that the vast majority of nearby galaxies lie where both the Choloniewski and modified-model functional forms would suggest. This indicates that the total luminosity density calculated by integrating these functions will be a good approximation to the true result. However, very few sources have $\mu < 21\,\mathrm{mag\,arcsec^{-2}}$, and no sources have $\mu < 21\,\mathrm{mag\,arcsec^{-2}}$ and $M_g > -15\,\mathrm{mag}$. The modified-model fit in the g band anticipates a greater density of sources in this area than the Choloniewski fit. This may be an indication that the modified-model is only a better guide to the bright end of the luminosity distribution. In the next section I will calculate the total luminosity density from both Choloniewski and modified-model functions.
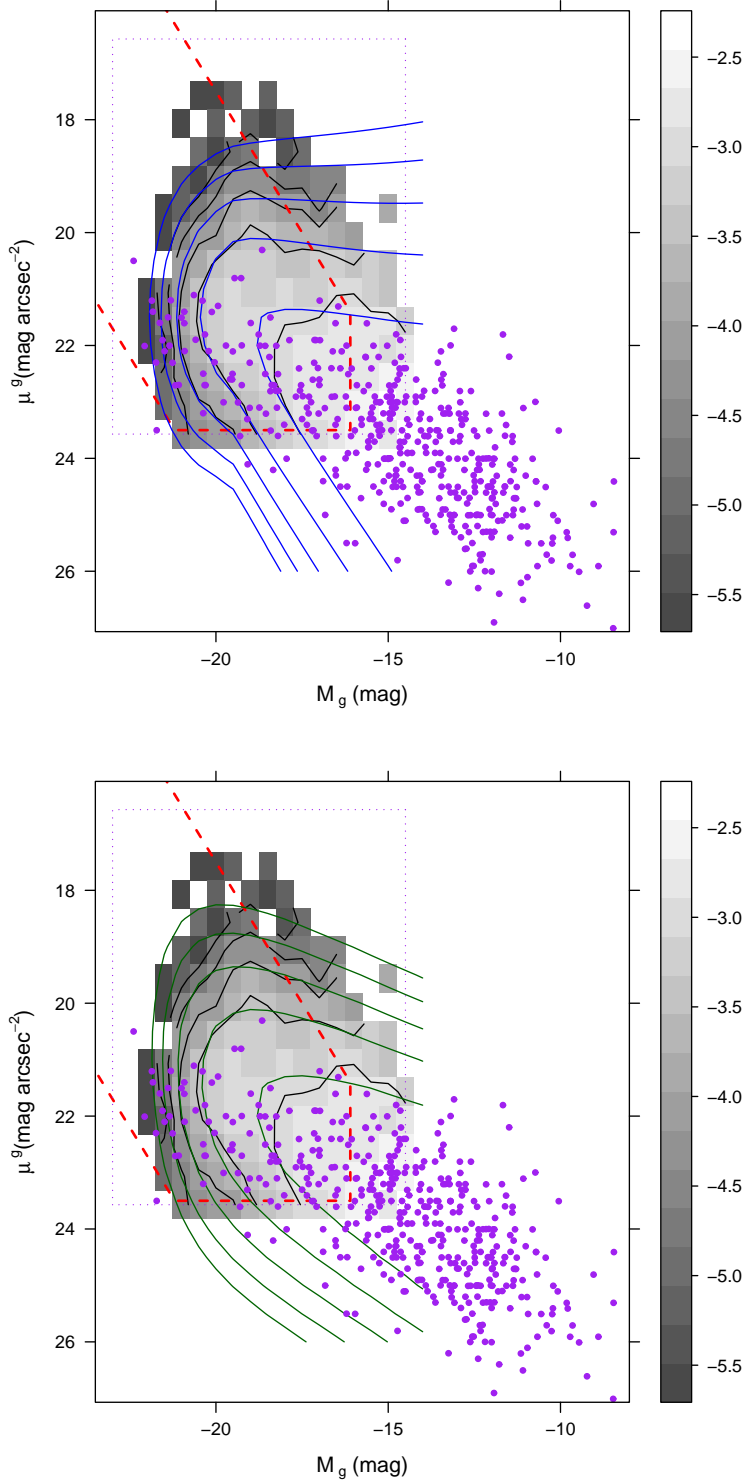
Figure 5.17: The distribution of local galaxies from Karachentsev et al. (2004), relative to the *g* band BBDs for the deeper sample. The local galaxies are shown as purple dots. The top figure shows the fit to the modified-model function, the bottom figure the fit to the Choloniewski function. The purple dots denotes the region the SWML algorithm was limited to. The red line denotes the region that has complete coverage within a $30000\,\mathrm{Mpc}^3$ volume.

Band	Choloniewski j ($\times10^8\,h\,L_{\odot,\lambda}\,\mathrm{Mpc}^{-3}$)	Choloniewski $\nu f(\nu)$ ($\times10^{34}\,h\,W\,\mathrm{Mpc}^{-3}$)	Modified model j ($\times10^8\,h\,L_{\odot,\lambda}\,\mathrm{Mpc}^{-3}$)	Modified model $\nu f(\nu)$ ($\times10^{34}\,h\,W\,\mathrm{Mpc}^{-3}$)
r_{SDSS}	2.38±0.20	6.62±0.55	2.43±0.24	6.74±0.66
u_{Kron}	2.06±0.18	2.13±0.19	2.05±0.22	2.13±0.22
g_{Kron}	2.17±0.19	5.29±0.47	2.19±0.25	5.35±0.60
r_{Kron}	2.53±0.25	7.03±0.68	2.61±0.31	7.25±0.86
i_{Kron}	2.84±0.31	7.48±0.82	3.03±0.40	7.98±1.04
z_{Kron}	3.37±0.31	7.56±0.69	3.59±0.43	8.06±0.97
Y_{Kron}	3.54±0.45	7.00±0.90	3.58±0.50	7.08±0.97
J_{Kron}	3.82±0.41	5.95±0.65	4.06±0.54	6.34±0.84
H_{Kron}	6.67±0.95	6.99±0.98	6.09±0.95	6.39±1.00
K_{Kron}	6.68±0.80	3.34±0.40	6.90±1.21	3.45±0.61

Table 5.12: j and $\nu f(\nu)$ statistics from the deepest cut sample Bivariate brightness distributions, derived from the best-fitting Choloniewski and modified model parameters.

5.4.2   Calculation of j and $\nu f(\nu)$ parameters

By integrating the best-fitting Choloniewski and modified-model functions over the entire L-μ plane, j and $\nu f(\nu)$ statistics can be calculated for the BBD (see section 5.2.3). Table 5.12 shows the j and $\nu f(\nu)$ statistics calculated from the best-fitting parametrisations to the deepest sample BBD. Table 5.13 contains the same statistics, this time calculated from the GAMA CSED sample (Driver et al, in prep), and from a combined MGC-UKIDSS-SDSS sample generated in Chapter 3. The GAMA CSED and MGC-UKIDSS-SDSS work assume their samples do not suffer from surface brightness incompleteness. They calculate the monovariate luminosity distribution, fit the Schechter function to the result and derive total luminosity density parameters by integrating the best-fitting Schechter parametrisation over all L (using the method described in section 1.4.1).

5.4.3   Comparison between methods

Figure 5.18 illustrates the variation in $\nu f(\nu)$ as a function of wavelength, and how it varies between datasets. Five datasets are shown: the $\nu f(\nu)$ parameters derived by integrating the Choloniewski and modified models (from Table 5.12) are shown as the red and blue datasets, the parameters derived from the MGC-SDSS-UKIDSS sample (Chapter 3, shown in Table 5.13) are shown as the black data, and the dark green datapoints are taken from the GAMA CSED paper (Driver, in prep, also shown in Table 5.13). In addition to the data in Tables 5.12 and 5.13, $\nu f(\nu)$ parameters were also calculated via the luminosity density bins within the deepest cut sample BBD. These parameters are shown as the orange dataset in Figure 5.18. As this data only accounts for the luminosity density within the region sampled by the BBD, it produces a lower estimate of the total luminosity den-

Band	MGC-SDSS-UKIDSS LF j ($\times 10^8 h$ $L_{\odot,\lambda}$ Mpc^{-3})	$\nu f(\nu)$ ($\times 10^{34} h$ W Mpc^{-3})	GAMA LF j ($\times 10^8 h$ $L_{\odot,\lambda}$ Mpc^{-3})	$\nu f(\nu)$ ($\times 10^{34} h$ W Mpc^{-3})
u	1.91	1.98	2.05	2.13
g	2.17	5.31	2.03	4.97
r	2.29	6.35	2.33	6.48
i	2.66	6.99	2.58	6.78
z	3.07	6.89	3.12	6.99
Y	3.24	6.41	3.08	6.09
J	3.17	4.95	3.57	5.56
H	5.38	5.65	5.24	5.49
K	6.98	3.48	6.08	3.04

Table 5.13: j and $\nu f(\nu)$ statistics from the GAMA CSED paper (Driver et al, in prep), and a combined MGC-SDSS-UKIDSS sample detailed in Chapter 3.

sity in all bands than any other GAMA dataset.

It is apparent in Figure 5.18 that, within the uncertainty, the $\nu f(\nu)$ parameters derived from the GAMA dataset agree. On a global basis, therefore, surface brightness incompleteness (which should affect the green data and not the blue or red data) does not have a strong effect on the GAMA sample closer than $z = 0.1$. The NIR/optical discrepancy that was reduced by the MGC-SDSS-UKIDSS sample is again not obviously apparent in GAMA data. However, the uncertainty on the parameters is still great; within 1σ Poisson uncertainties both a shallow fall and a sharp rise in total luminosity density from z to Y are allowed. It should also be noted that the i and z parameters are significantly higher using the modified-model BBD data, rather than the standard Choloniewski BBD. The Choloniewski BBD reduces the deficit between z and Y datapoints, but shows the unusual J band dip that was present in the MGC-SDSS-UKDISS sample. This dip is not present in the modified-model sample, but there is a dip between z and Y.

In section 5.3 it was shown that the modified model is a better fit to the data than the Choloniewski function, and unlike the GAMA CSED data, it accounts for any surface brightness bias (however small) present in the data. Herein, when comparing to other results and theory, the $\nu f(\nu)$ parameters derived by integrating the best-fitting modified model are used as the GAMA CSED dataset.

5.4.4 Comparison with previous surveys

Figure 5.19 illustrates the variation in $\nu f(\nu)$ as a function of wavelength, comparing it with $\nu f(\nu)$ parameters from the literature. An Sa-type galaxy SED model from Poggianti
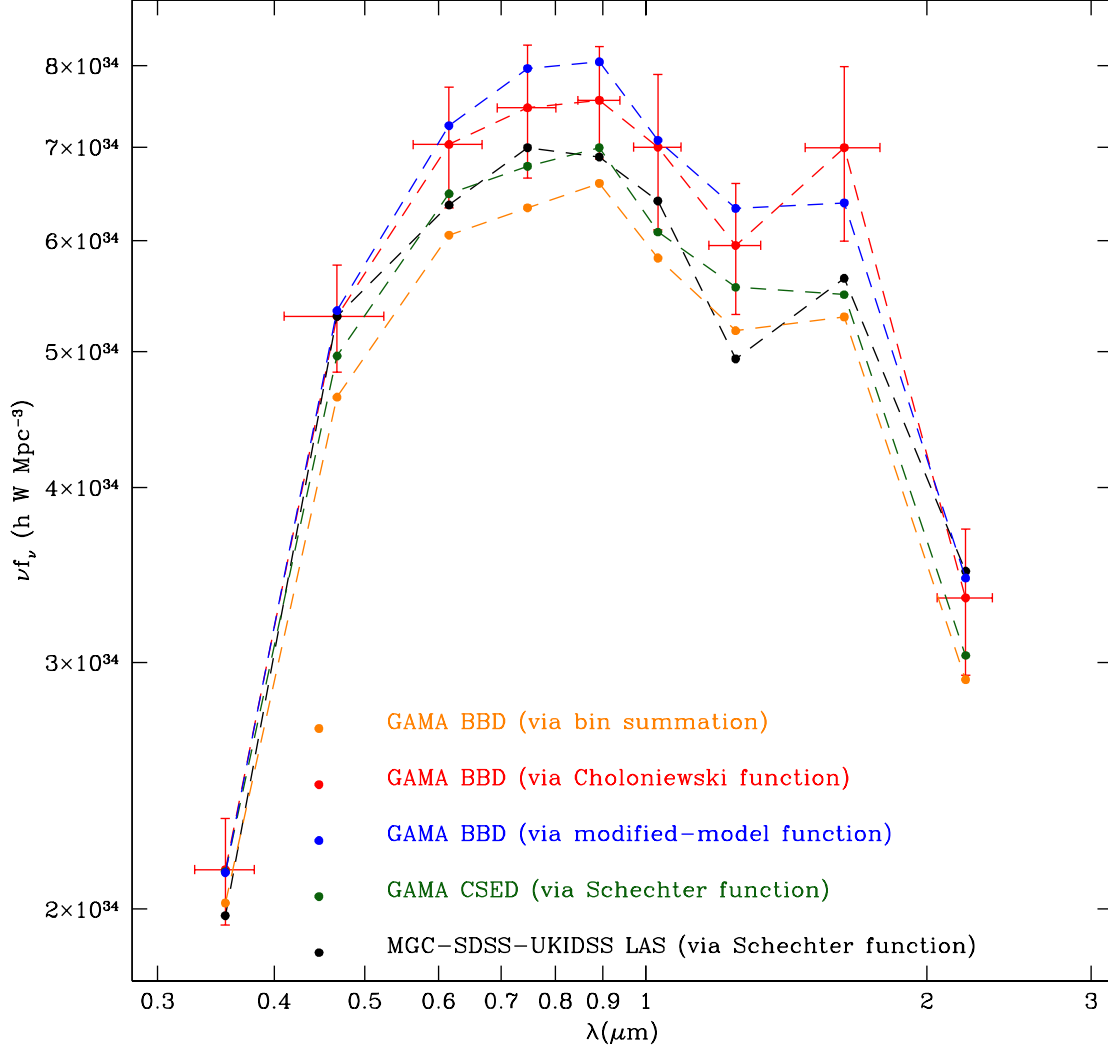
Figure 5.18: The variation in $\nu f(\nu)$ with wavelength. Five datasets are shown. The orange datapoints are derived by summing the luminosity density within the bins the BBD sampled (this method therefore ignores all luminosity density outside the sampled region). Red datapoints are taken from the integration of the best fitting Choloniewski parameters (Table 5.12), blue datapoints from the integration of the best fitting modified-model parameters (also Table 5.12), green datapoints from the GAMA CSED paper (Driver, in prep), and black datapoints from the MGC-SDSS-UKIDSS sample of Chapter 3 (also shown in Table 5.13). Errors for the red dataset are shown, in order to provide a guide to the uncertainty on each datapoint.

(1997) is shown to guide the eye. The GAMA data shown are the parameters derived by integrating the best-fitting modified-model function (shown in Table 5.12, and the blue data in Figure 5.18). The MGC-SDSS-UKIDSS data is taken from Chapter 3, and also shown in Table 5.13. The $\nu f(\nu)$ parameters follow the basic trends shown by those within the literature; an increase from u to r, flatten between r and z, and then a downturn from z to K. GAMA $\nu f(\nu)$ parameters are greater in the optical filters (particularly riz) than either the MGC-SDSS-UKIDSS or SDSS survey data, whilst being similar to prior results in the NIR (particularly K). The overdensity in the optical may be due to the overestimation of the bright end of the BBD, and the difficulty in fitting the distribution in these filters. It is apparent in Figure 5.18 that the dispersion in $\nu f(\nu)$ parameters between GAMA datasets is largest in the riz passbands. The parameters derived from the modified model in these passbands, whilst agreeing within the uncertainty, are larger than those produced using either the Choloniewski or the Schechter function integration techniques.

5.4.5 Comparison with models

Figure 5.20 illustrates the variation in $\nu f(\nu)$, and how it compares with previously calculated $\nu f(\nu)$ statistics. The CSFH+IMF combinations used to generate the $\nu f(\nu)$ predictions are the same as those used in Figure 3.13, and were derived by Steven Wilkins from models in Wilkins et al. (2008a), Wilkins et al. (2008b), and Hopkins & Beacom (2006). The blue model uses the canonical IMF shown in Equation 1.10 and a CSFH taken from FIR indicators in Hopkins & Beacom (2006). The brown model uses the canonical IMF shown in Equation 1.10, but with a flatter than Salpeter high mass slope ($\alpha = -2.15$), and a CSFH taken from FIR indicators in Hopkins & Beacom (2006). The purple curve using the canonical IMF shown in Equation 1.10, with a CSFH taken from the stellar mass indicators in Wilkins et al. (2008b).

The energy density is calculated without dust attenuation. A multiplying factor approach is used to find the pre-attenuated energy density, with that factor derived using the method set out in Driver et al. (2008). The multiplying factors for the $ugrizYJHK$ passbands are, in that order, $\times 2.27$, $\times 1.69$, $\times 1.56$, $\times 1.47$, $\times 1.41$, $\times 1.35$, $\times 1.32$, $\times 1.22$, and $\times 1.15$ (again, the same as the multipliers used in Chapter 3). The dust corrected data are shown as the hollow points in Figure 5.20.
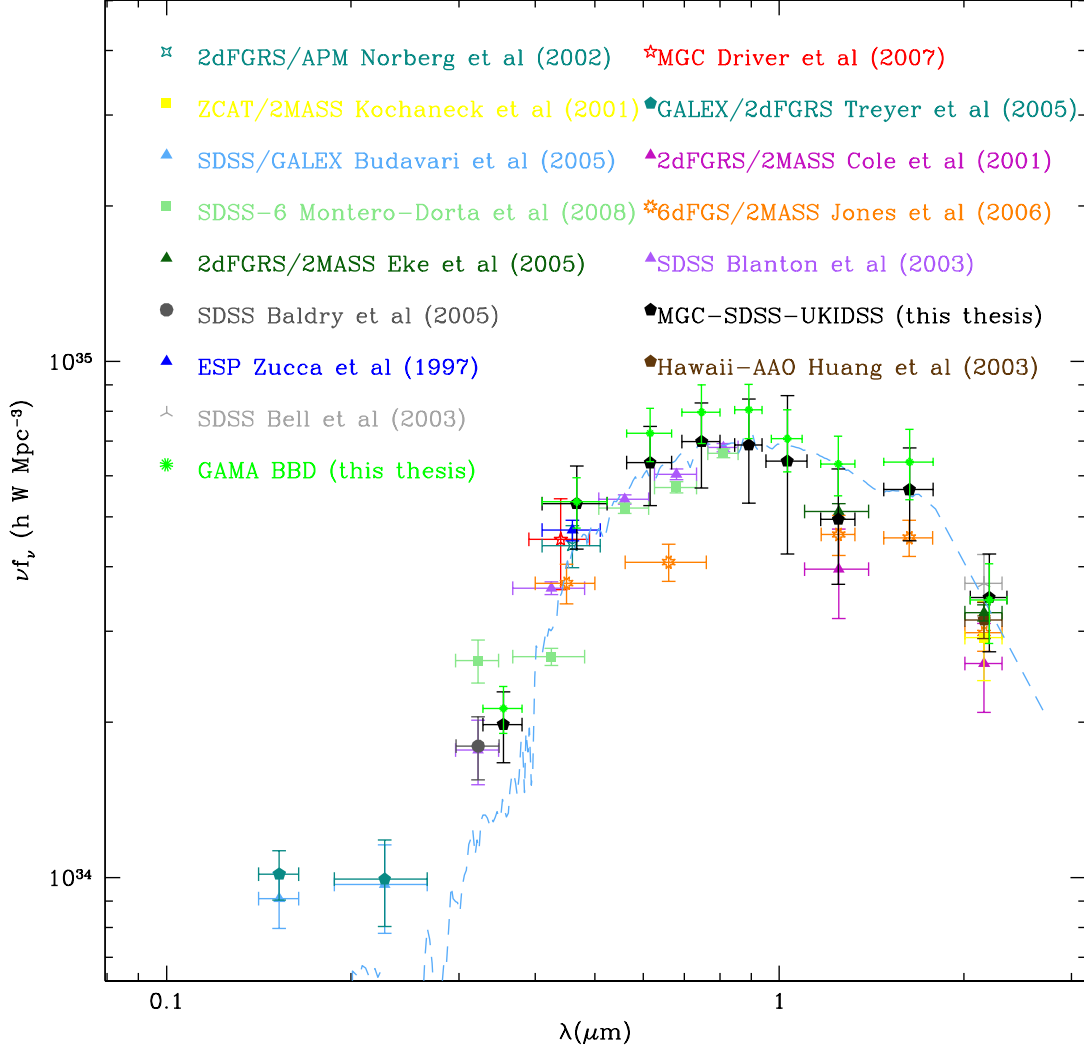
Figure 5.19: Cosmic energy output from 0.1 to 3 μm. The model line shows the SED of a 13.2Gyr Sa-type galaxy from the spectral template library of Poggianti (1997). Data shown is taken from Baldry et al. (2005), Bell et al. (2003), Blanton et al. (2003), Budavári et al. (2005), Cole et al. (2001), Driver et al. (2007), Eke et al. (2005), Jones et al. (2006), Huang et al. (2003), Kochanek et al. (2001), Montero-Dorta et al. (2008), Norberg et al. (2002), Treyer et al. (2005) and Zucca et al. (1997). The GAMA BBD dataset (green) uses the $\nu f(\nu)$ results provided by the integration of the modified model function, shown in Table 5.12. The MGC-SDSS-UKIDSS data (black) is taken from Chapter 3.
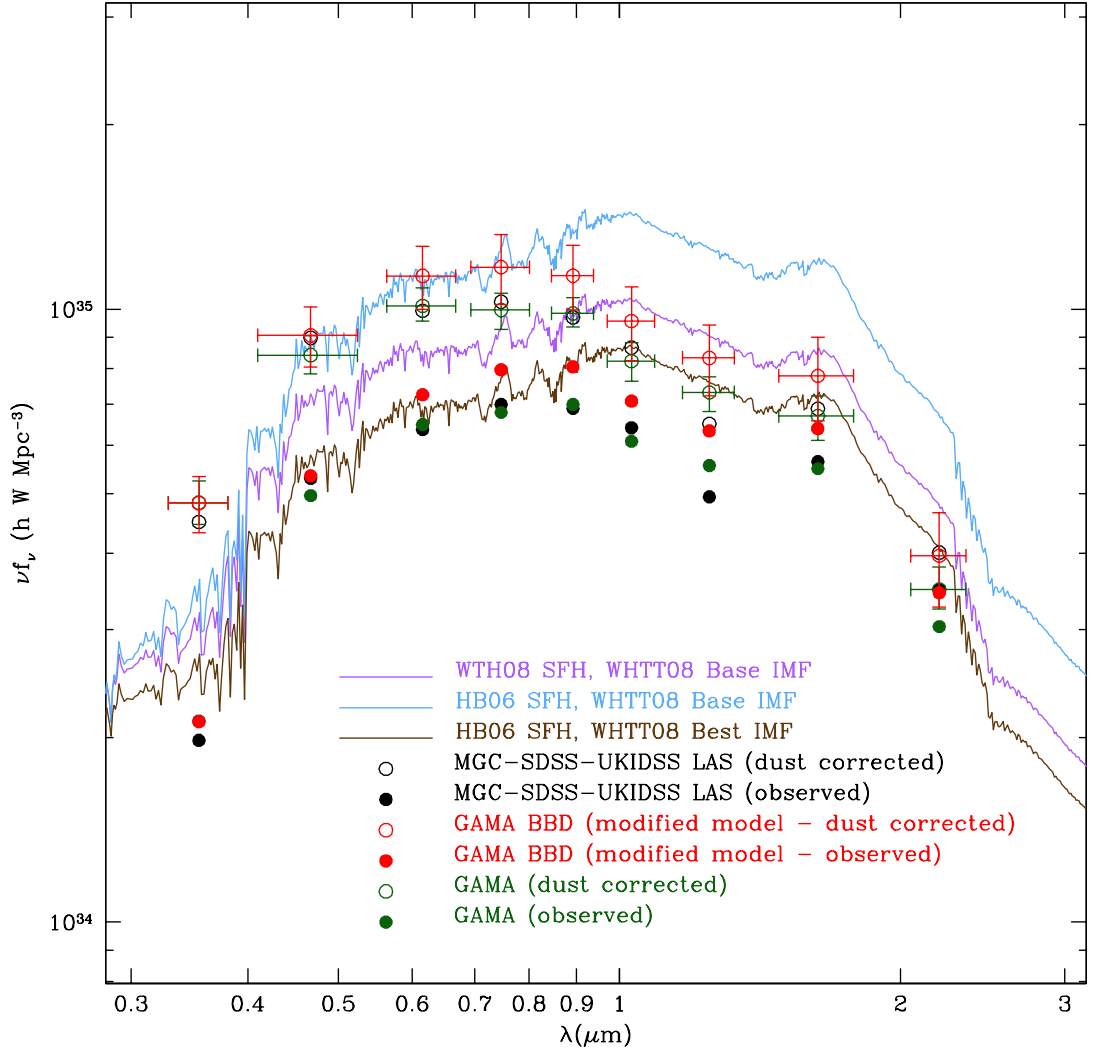
Figure 5.20: The variation in $\nu f(\nu)$ with wavelength, compared with predictions from different CSFH+IMF combinations (Wilkins, priv. comm.), and datapoints from other measurements. Hollow points show the position of the data when it is corrected for the effects of dust attenuation, using multiplying factors taken from Driver et al. (2008). Uncertainties are calculated from the 90% confidence intervals on the best-fitting parameters. CSFH models are taken from Wilkins et al. (2008a). IMF models come from Wilkins et al. (2008b) (WTH08), or Hopkins & Beacom (2006) (HB06). Red datapoints are taken from this paper (the modified-model parameters in Table 5.12), green datapoints from the GAMA CSED paper (Driver, in prep), and black datapoints from the MGC-SDSS-UKIDSS sample of Chapter 3.

The parameters derived from GAMA output an energy density that agrees with those produced from the MGC-SDSS-UKIDSS sample. Unfortunately, neither set of data agree with predictions made using combined IMF+CSFH models. In both cases, the energy density per unit interval observed in the NIR is significantly lower than the predictions

would infer, and is too high in the u band. The IMF+CSFH data are based on a number of assumptions. Different population synthesis models (Chen et al. 2010 compares 6 different codes), IMF functional forms (see section 1 of Kroupa & Weidner 2005 for a discussion of the literature), evolutionary variations in chemical enrichment (Calura et al., 2010) or the form of the IMF (Larson, 1998; Davé, 2008) could all modify these predictions. These issues will be discussed further in later work (Robotham & Weidner, in prep, and Wilkins et al, in prep). As the GAMA and MGC datapoints are produced via Kron photometry, they will underestimate the true luminosity density parameters (see section 5.1). Reproducing this work with Sérsic photometry should remove this effect, as Sérsic photometry accounts for the extra luminosity that lies outside the Kron aperture, pushing a greater number of sources into the brighter magnitude bins, thus changing the shape of the luminosity distribution.

Further constraints are provided by combining the GAMA dataset with observations in other parts of the EM spectra. In particular, combining GAMA data with Herschel-ATLAS imaging (Eales et al., 2009; Smith et al., 2010) will allow quantification of the optical-NIR luminosity that has been attenuated by dust, and then re-emitted in the FIR, testing the dust attenuation approach of Driver et al. (2008) that is used here. HI observations of the GAMA regions are also planned using ASKAP (Johnston et al., 2008), as part of the DINGO survey (Meyer, 2009). This will provide an accurate measurement of the hydrogen gas mass, and will calibrate the SFR used in these models (e.g. via Kennicutt 1998b). However, as ASKAP is not yet functional, and Herschel-ATLAS has not finished observing, these measurements have to wait.

For now, it is noted that the CSED measurements made in the optical and the NIR agree with those previously derived from other datasets, and that these measurements do not agree with predictions from current CSFH+IMF models. Work is underway to resolve this issue.

6

Summary

In this chapter I outline the main results of this thesis, and how this work could be improved.

6.1 Results

In the previous chapters, I have presented luminosity distributions produced from a B band selected sample of MGC-SDSS-UKIDSS galaxies, and bivariate brightness distributions from an r band selected sample of GAMA galaxies. I have fitted functional forms to these distributions, and derived total luminosity density and energy density per unit interval statistics from these populations. I summarise my results below.

6.1.1   Schechter function fitting

Quality of fit

In Chapter 3, Schechter functions are fit to the luminosity distributions produced from a sample of MGC-SDSS-UKIDSS galaxies. Generally, the reduced χ^2 parameters indicate that the Schechter function was a good fit to the data, with upturns in the luminosity distribution at the faint end only seen in i and z (see Figure 3.10, $M_i \sim -16.5$ mag and $M_z \sim -17$ mag). However, the MGC-SDSS-UKIDSS sample in Chapter 3 was not only defined using a brighter limiting magnitude than its equivalent GAMA sample in Chapter 5 ($r < 18.76$ mag in the MGC sample, $r < 19.1$ mag in the GAMA sample), but covered a smaller area (30.88 sq deg, compared to GAMA's 144 sq deg).

In Chapter 5, the GAMA luminosity distribution is shown as a function of surface brightness (Figure 5.16). It is apparent that not only is there an upturn (which can also be seen in the BBDs presented in Figures 5.8 and 5.10, and Appendix D), but that the upturn is caused by the faintest surface brightness objects (the red dataset). With next generation imaging (e.g., VST KIDS, VISTA VIKING), as the samples probe ever deeper, it is likely that the inability of the Schechter function to model the faint end will become ever more apparent.

Effects of aperture definition

Figure 5.1 shows the best-fitting Schechter functions for the same sample of galaxies, when different photometric systems are used to derive their luminosity. A number of effects are illustrated:

1. Regardless of the passband used to define the aperture, there is approximately the same variation in M^* and α between samples that use Petrosian or Kron photometry.

2. Modifying the `SExtractor` detection threshold has a limited effect on the global properties of the best-fitting luminosity function ($M^* - 5\log_{10}$h $\pm$ 0.055 mag, $\alpha \pm$ 0.014, $\phi^* \pm 0.0005$ h^{3}Mpc^{-3}). The luminosity function parameters are predominantly constrained by the bright galaxies.

3. Changing the passband used to define the aperture will modify the best-fitting luminosity function parameters ($M^* - 5\log_{10} h \pm \sim 0.2$ mag, $\alpha \pm \sim 0.05$, $\phi^* \pm \sim$

$0.001 \, \text{h}^3\text{Mpc}^{-3}$). However, these parameters are degenerate, and the total luminosity density (j) agrees with uncertainties.

4. Changing from a circular to an elliptical aperture system produces a large offset ($\sim 0.2 \, \text{mag}$) in M^*. Whilst the other Schechter parameters compensate slightly, the total luminosity density produced from an elliptical aperture system is nonetheless greater.

5. Total magnitude system luminosity distributions (e.g. SDSS MODELMAG, or Sérsic magnitudes) produce smaller α parameters than the equivalent Kron/Petrosian distributions; -1.203 using Sérsic photometry, -1.111 using r-defined AUTO photometry.

6. Using a Sérsic magnitude system produces a greater density of bright objects, causing a noticeably brighter M^* parameter. Following examination of some of the brighter sources (see Section 5.1.4 for details), this effect is judged to be real, and not a flaw in the Sérsic pipeline.

This last point is of particular interest. Calculations of the total luminosity density made by non-Sérsic methods may underestimate the true total luminosity density by $\sim 15\%$. This result has two caveats. Firstly, every galaxy must be capable of being modelled with a Sérsic profile (particularly, a single component Sérsic profile). Secondly, it requires every galaxy profile to be non-truncated. The total luminosity density, in reality, may lie somewhere between the Sérsic and non-Sérsic results.

6.1.2 BBD function fitting

Quality of fit

In Chapter 5, modifications to the standard BBD functional form, the Choloniewski model, are discussed and implemented, in the form of a modified functional form (Equation 5.10). In Chapter 5, both models are fit to $ugrizYJHK$ GAMA samples, and the quality of the fit is compared. In every passband, the modified model provides a smaller reduced-χ^2 (Tables 5.7 and 5.6); an indicator that it is a better fit to the data than the traditional Choloniewski function. Two BBD samples are generated in each passband, using different limiting apparent magnitudes. With the exception of the H filter, in every case the

197

resulting best-fitting parameters agree within 90% confidence intervals. The discrepancy in H is presumed to be caused by degeneracy between the model parameters.

Comparison with other models

Section 5.3 compares the r, g and K best-fitting Choloniewski models to their equivalents in the literature, from the VAGC, 2dF, MGC and UKIDSS catalogues. Good agreement is found with the MGC model, in particular, with discrepancies with the other models appearing to stem from selection biases or sample incompleteness. Section 5.2.3 examines the discrepancy between BBDs produced using SDSS (Figure 5.8) and GAMA (Figure 5.10) photometry. The change in size measurement, from SDSS' Petrosian radius to GAMA's effective radius, greatly revises the surface brightness distribution, making it much broader (σ_μ for the Kron photometry is $0.402\,\mathrm{mag\,arcsec^{-2}}$ larger).

6.1.3 Total luminosity density

Agreement between methods

In Chapter 3, total luminosity density and energy density statistics were calculated from the best-fitting Schechter luminosity function parameters to a B-band selected MGC-SDSS-UKIDSS population of galaxies. This dataset was compared to results from earlier surveys in Figure 3.12, and seems to remove (or, at least, reduce) the apparent NIR-optical discrepancy. In Chapter 5, the same statistics were derived from the best-fitting Choloniewski parameters to an r band selected GAMA-SDSS-UKIDSS population of galaxies. Figure 5.20 illustrates how the latter parameter, pre and post-dust attenuation, varies with wavelength. It is apparent that the parameters from both measurements agree within uncertainties, and also agree with a further measurement made by Driver et al (in prep). The datapoints are therefore shown to be robust.

Disagreement with theory

Also shown on Figures 3.13 and 5.20 are predictions made using IMF and cosmic star formation history (CSFH) models. Whilst the observed results agree, the theoretical predictions are a poor fit to the data. There are a number of possible reasons for this disagreement. The IMF functional form may be wrong, and no chemical-enrichment evolution or IMF evolution is accounted for. Population synthesis models may not be precise

enough, particularly when modelling evolution off the main sequence. In order to solve these problems, further work is necessary, and the $\nu f(\nu)$ results produced within this thesis should help to constrain the theory.

6.2 Further work

In this section, I outline improvements that could be made to increase the accuracy and utility of the results presented in this thesis.

6.2.1 Improvements to the method

In this section, I discuss some possible changes that would enhance this work.

GAMA sample selection

The GAMA sample, as discussed in Section 2.4, is an apparent magnitude limited population based upon Petrosian photometry from the SDSS survey dataset. The photometry outlined in Chapter 4 is shown to be a major improvement to the SDSS photometric method; the move from circular to elliptical apertures greatly improves measurement of extended sources, and the extension to $YJHK$ allows the derivation of consistent NIR and optical colours. However, in order to guarantee a sample that is unbiased against extended sources, follow up observation of sources that are fainter than the r_{sdss} limit, but are actually brighter when measured using GAMA photometry, should be made.

Evolution correction

The results that are described within this thesis assume that no evolution is occurring (i.e. $E(z) = 0$). Whilst this may be true (for instance, Prescott et al. 2009 show no u band evolution in their lowest z points for a range of galaxy types in SDSS data), greater effort should be made to ascertain what effect it is having. Loveday et al (in prep), use GAMA spectroscopy with SDSS photometry, in an attempt to quantify evolution within the GAMA sample. Future work should repeat his test using the more accurate GAMA extended-source photometry.

Peculiar velocities

Within the luminosity distribution and BBD samples (Chapters 3 and 5), all sources with redshift below $z < 0.0033$ are removed, in order to limit the effects of the local velocity field. 1829 sources in the GAMA sample have good quality spectra ($nQ > 3$), but $z < 0.0033$. If these sources were corrected for these effects, rather than removed, the size of each sample would increase by a small fraction ($\sim 1\%$).

Redshift completeness

The bivariate brightness distribution accounts for redshift incompleteness using a simplistic weighting (Section 5.2.2). This weighting assumes that the redshift distribution of the sources that are included in the sample is the same as those that were missed. In reality, this is unlikely to be the case. Further attempts to derive spectra of these missing sources would diminish the effects of this bias, increasing the accuracy of the resulting BBD.

Increased redshift limits

Given the uncertainty on the evolutionary correction, the distributions produced within this thesis were limited at $z = 0.1$. The GAMA sample extends far beyond this (see Driver et al. 2010). When K+E corrections are accounted for, the sample could be extended to $z = 0.2$ or further, increasing both the number of sources and the volume examined, and diminishing the effect of Poissonian uncertainties.

6.2.2 Improvements to data

In this section, I discuss what data would augment the GAMA survey, as it currently stands.

Increase in Area

Whilst the GAMA survey covers over 4 times more area than the preceding MGC (144 sq deg, compared to 30.88 sq deg), it only covers a small fraction of the total SDSS area, and will still suffer from the effects of cosmic variance (Driver & Robotham, 2010). An expansion of the GAMA area to encompass two additional regions is planned. Additionally, this will increase the size of the sample, further reducing the effects of Poissonian uncertainty.

Deeper data

Unfortunately, SDSS and UKIDSS data is too shallow to undertake high-quality galaxy profiling, particularly multi-component fitting (as Section 4.4.2 shows, the SDSS u band has difficulty providing accurate single-component fits). However, both surveys will soon be superseded. VST KIDS and VISTA VIKING (Arnaboldi et al., 2007) will observe > 2 mag deeper than SDSS and UKIDSS. Both surveys will cover the GAMA regions, and should provide the resolution and depth necessary to accurately model galaxies. This should remove the necessity of using aperture photometry to define a dataset - eliminating a potential bias in sample selection.

Other wavelengths

As well as NIR and optical surveys, the GAMA regions will be observed in passbands ranging from the radio to the UV. CSED datapoints in the FIR (via Herschel-Atlas matching, Eales et al. 2009) will indicate the level of dust re-emission, testing the dust attenuation theories used to calculate the pre-attenuated points in Figures 3.13 and 5.20. GALEX (Wyder et al., 2005) matching in the UV can constrain the age and metallicity of the galaxy, via galaxy SED modelling (see Figure 4.23). Radio data can be used to calculate the mass of hydrogen gas in the nearby Universe, helping to calibrate star formation rates (SFR). The DINGO (Meyer, 2009) survey intends to survey the GAMA regions using ASKAP (Johnston et al., 2008). This additional data, along with more accurate NIR and optical data, will extend constraints on galaxy formation and evolution theories, providing the observational support required to test IMF and stellar population models, define accurate multi-wavelength SEDs of galaxies, as well as constrain cosmological simulations.

A

Gaussian convolution proof

In this appendix I derive Equation 4.4.

A Gaussian:

$$f(x) = \sqrt{\frac{a}{2\pi}} e^{\frac{-ax^2}{2}} \tag{A.1}$$

has the Fourier transform:

$$F(k) = \frac{1}{\sqrt{2\pi}} e^{-\frac{k^2}{2a}} \text{ where: } \frac{1}{\sigma} = \sqrt{a} \tag{A.2}$$

So, for two Gaussian with $a = n, a = m$:

$$
\begin{aligned}
F_n(k) &= \frac{1}{\sqrt{2\pi}} e^{-\frac{k^2}{2n}} \\
G_m(k) &= \frac{1}{\sqrt{2\pi}} e^{-\frac{k^2}{2m}}
\end{aligned}
\tag{A.3}
$$

The product of the F and G Fourier transforms is the equivalent of the convolution of their functions:

$$C(k) = \sqrt{2\pi}F_n(k)G_m(k) \text{ (where } \sqrt{2\pi} \text{ is a scaling factor)} \tag{A.4}$$

$$C(k) = \frac{1}{\sqrt{2\pi}}e^{-\frac{k^2}{2}(\frac{1}{a}+\frac{1}{b})}$$
$$C(k) = \frac{1}{\sqrt{2\pi}}e^{-\frac{k^2}{2q}} \tag{A.5}$$
$$\text{where: } \frac{1}{q} = \frac{1}{a} + \frac{1}{b}$$

This is the Fourier Transform of:

$$c(x) = \sqrt{\frac{q}{2\pi}}e^{-\frac{qx^2}{2}} \tag{A.6}$$

It follows therefore, that to generate an image with $\sigma = \sigma_d$ from an image with $\sigma = \sigma_{image}$ we require an Gaussian with:

$$\sigma_{req} = \sqrt{(\sigma_d)^2 - (\sigma_{image})^2} \tag{A.7}$$

Or in terms of the FWHM:

$$\frac{\text{FWHM}_{\text{req}}}{2\sqrt{2ln2}} = \sqrt{(\frac{\text{FWHM}_{\text{d}}}{2\sqrt{2ln2}})^2 - (\frac{\text{FWHM}_{\text{image}}}{2\sqrt{2ln2}})^2} \tag{A.8}$$

Rearranged, this gives Equation 4.4 above:

$$\sigma_{req} = \sqrt{(\frac{\text{FWHM}_{\text{d}}}{2\sqrt{2ln2}})^2 - (\frac{\text{FWHM}_{\text{image}}}{2\sqrt{2ln2}})^2} \tag{A.9}$$

B

Variation between passbands

In this appendix I discuss the variability with wavelength of a source within the GAMA master catalogue, and how the convolution process affects the quality of its imaging in the GAMA mosaics.

Figure B.1 shows the 18 200x200 pixel images of the piece of sky containing SDSS object 588848900968480848; 9 cutouts from the standard image mosaics, and 9 from the convolved image mosaics. What is easily noticeable is that not only does the ability to see features of the object change dramatically between the u (top left) and K (bottom right) wavebands (spiral arms are visible in the optical, but in the K band there only seems to be a bar and a bulge component), but that objects around it appear and disappear (a small blip to the SE in the r band that may or may not be part of the object itself, at least 5 faint objects in the E of the frame in the NIR). The size of the object seems to halve from the g band to the J band, though this may be an effect of the image quality (the SDSS g band should have a much smoother background than the UKIDSS J). The apparent magnitude of the object itself changes by 2.8 magnitudes from u to its peak

in H (`SExtractor` calculates AB magnitudes using an r band-defined AUTO aperture of 16.67, 15.44, 14.85, 14.49, 14.32, 14.23, 14.04, 13.83, 14.11 mag in $ugrizYJHK$). This is probably due to the decrease in dust opacity from the UV to the NIR.

The convolved images also show greater variation between the object and the background (these images all use a linear scale between the 99.5% quantile pixel and 0, the background). For instance, the extended spiral arm to the left of the bulge in the u band becomes slightly more apparent in the convolved u band image. The size of the object in the convolved images generally looks greater than the standard images, though this again is probably due to the smoothing of the background making flux overdensities more apparent in the convolved images.
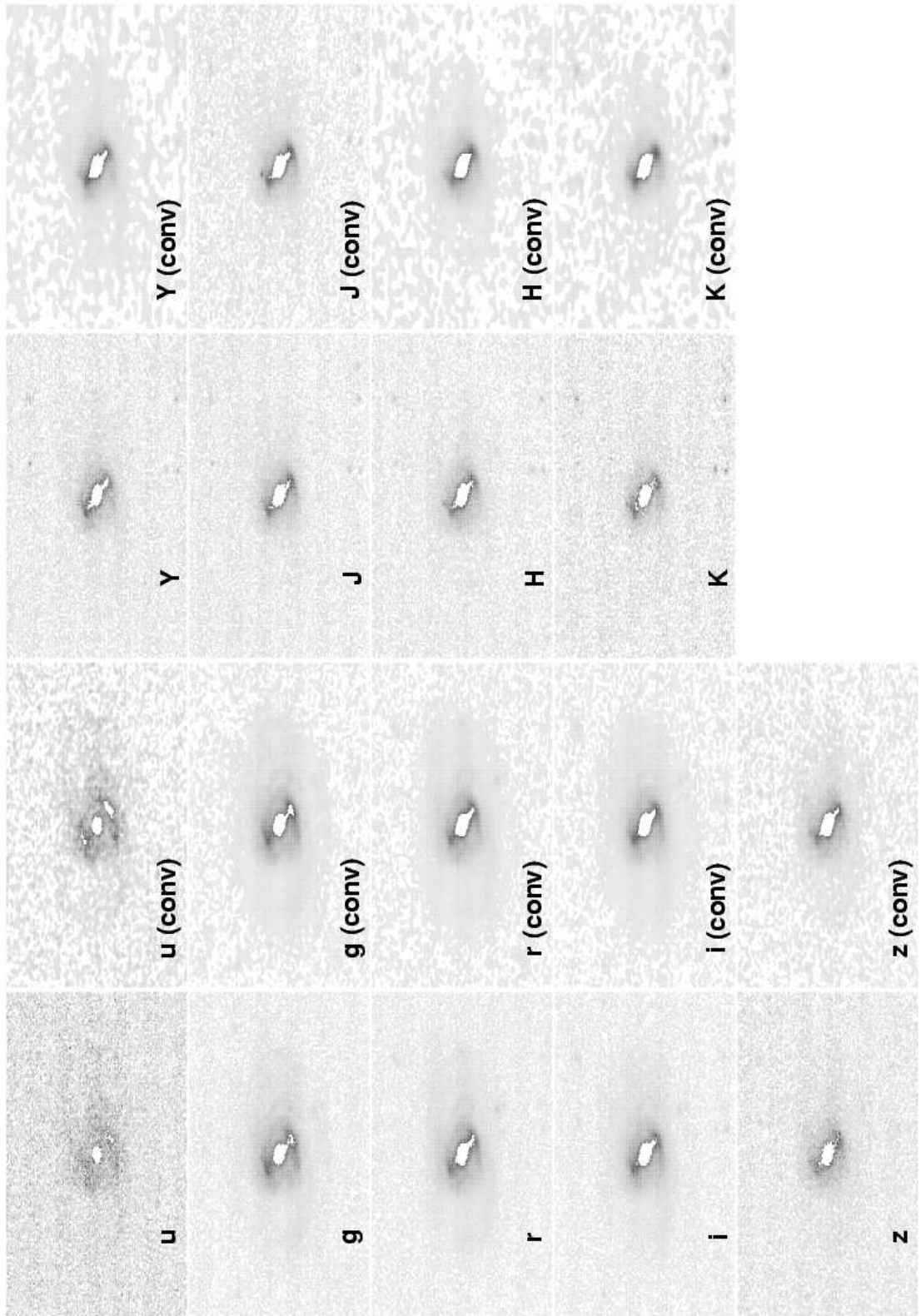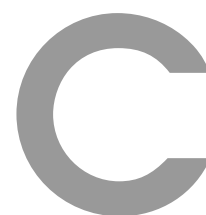
Figure B.1: The effects of convolution and the change in passband of observations of SDSS object 588848900968480848.

C

Visibility theory

In this appendix I describe the original isophotal visibility theory, and then outline the modifications I have made to use it with GAMA photometry.

To ascertain the completeness of a sample over a specified volume of sky, it is necessary to test that a galaxy of known absolute magnitude, M, and absolute surface brightness, μ^X, could be detected at the maximum distance limit. Phillipps et al. (1990) produced a method to calculate the redshift limit from a dataset's isophotal magnitude and central surface brightness limits (m_{lim}, μ_{lim}). Their method is still applicable to the imaging that the GAMA sample is taken from, and was imposed on the BBD calculated from 2dF data (Cross et al., 2001). However, the selection limits of the GAMA sample are defined using different criteria (Baldry et al., 2010). GAMA's photometric selection is based upon photometric systems that are not isophotally based (SDSS Petrosian and Fiber magnitudes), and the GAMA surface brightness limit is based upon the mean surface brightness of each galaxy, rather than its central surface brightness. As these constraints are tighter than the isophotal selection, the visibility theory is modified to use them instead.

C.1 Standard visibility theory

The first constraint from Phillipps et al. sets is a limit on the luminosity distance to the galaxy:

$$d_1 = (f(\mu_{lim} - \mu_0))^{\frac{1}{2}} 10^{0.2(m_{lim} - M - 25 - K(z))} \text{ Mpc} \tag{C.1}$$

where f is a function that calculates the fraction of light that is above the limiting surface brightness threshold. This is dependent on the profile of the galaxy - their equation B2 gives the parametrisation for an exponential profile spiral galaxy. $K(z)$ calculates the magnitude of the K correction for an object at z. μ_0 is the central surface brightness of the source. As d_1 is a luminosity distance, the redshift limit (z_1) can be found from the relation:

$$d_1 = 2cH_0^{-1}((1 + z) - (1 + z)^{\frac{1}{2}}) \tag{C.2}$$

which can be solved numerically.

The second constraint is a limit on the angular size of the galaxy:

$$d_2 = \frac{C}{\theta_{lim}}(g(\mu_{lim} - \mu_0))10^{0.2(\mu_0 - M)} \text{ Mpc} \tag{C.3}$$

where C is a constant that is dependent on the galaxy profile:

$$C = \frac{2 \times 10^{-5}}{\sqrt{2\pi}} \tag{C.4}$$

for an exponential profile source). g is a function that calculates the size (in scalelengths) from the centre of the galaxy to the limiting surface brightness isophote, θ_{lim} is the minimum size limit. As d_2 is an angular diameter distance, the redshift limit from this constraint (z_2) can be found from the relation:

$$d_2 = 2cH_0^{-1}((1 + z)^{-1} - (1 + z)^{\frac{-3}{2}}) \tag{C.5}$$

The redshift limit for a M, μ^X source will be $min(z_1, z_2)$.

C.2 Modifications for GAMA

Unfortunately, the GAMA selection criteria are not based upon isophotal apertures. As such, it is necessary for us to make some adjustments to the standard theory in order to use it. In this section, I detail these changes. As SDSS photometry was used to limit our sample, all photometry within this section utilises that system.

C.2.1 Conditions

In order to calculate the distance limits in this section, it is necessary for us to make a series of assumptions. Firstly, it is assumed that the type of galaxy that is most affected by the visibility incompleteness is a faint, exponential type. Where necessary, sources are therefore assumed to follow an exponential ($n = 1$) profile:

$$I(R) = I_0 e^{-\frac{R}{a}} \tag{C.6}$$

where a is the scalelength of the galaxy.

It is also assumed that the isophotal surface brightness limit of the survey, μ_{lim}, can be approximated from the surface brightness of an object that has flux equal to the background rms noise, and covers 1 pixel. From the GAMA mosaics (Chapter 4), it is found that:

$$\mu_{lim} \sim 26.39 \text{mag arcsec}^{-2} \tag{C.7}$$

The observed central surface brightness of the galaxy (μ_0) is related to the observed mean surface brightness within the Petrosian half light radius ($< \mu_{r,50} >$). For a $n = 1$ profile galaxy, the relation takes the form:

$$< \mu_{r,50} >= \mu_0 + 1.822 - 0.699 - 0.01 \tag{C.8}$$

The offset parameters are taken from Equations 7,9 and Table 1 of Graham et al. (2005), respectively.

For an average galaxy, the K correction is assumed to be solely as a function of redshift. The functional form used here is:

$$K(z) = 0.95z \tag{C.9}$$

C.2.2   SDSS Petrosian magnitude constraint

The first GAMA constraint is due to the SDSS Petrosian magnitude limit. The Petrosian aperture is defined so that it is redshift independent: the fraction of the source's light detected with the Petrosian radius should stay constant, regardless of its distance from us. In this case, the limiting factor will come when the profile's light emission drops below the threshold at which it can be measured. The distance limit is calculated using:

$$d_1 = 10^{0.2(m_{lim} - (M - 2.5log_{10}[f(\mu_0^X)]) - 25 - K(z))} \text{ Mpc} \tag{C.10}$$

where f is a function that calculates the fraction of the light emission above the isophotal surface brightness limit of the survey. An exponential galaxy profile, and a limiting isophotal surface brightness threshold (Equation C.7) are assumed. f is calculated using the equation:

$$f(\mu_0^e) = \frac{\int_0^{r=R_1} 2\pi w I(w) dw}{\int_0^{r=\infty} 2\pi w I(w) dw} = 1 - (1 + x)e^{-x} \tag{C.11}$$

where $x = \frac{R_1}{a} = \frac{\mu_{lim}^X - \mu_0^X}{1.086}$. μ_0^X is calculated from the absolute $< \mu^{r,50} >$ parameter using Equation C.8. μ_{lim}^X is calculated from μ_{lim} using:

$$\mu_{lim}^X = \mu_{lim} - 10log(1 + z) - K(z) \tag{C.12}$$

$f = 0$ when $\mu_{lim}^X < \mu_0^X$. The completeness limits due to the SDSS Petrosian magnitude selection are shown in Figure C.1

C.2.3   Intrinsic surface brightness constraint

A further constraint will be the intrinsic surface brightness limit chosen for the sample. In each M, μ_{lim}^X bin, the redshift completeness limit can be derived by solving Equation C.12, where μ_{lim}^X is the value of the bin and μ_{lim} is the intrinsic surface brightness limit of the sample (e.g. $\mu_{r,lim} = 23 \, \text{mag arcsec}^{-2}$). This presupposes that the surface brightness constraint chosen is far above the detection threshold for the data, and that there is no difficulty in observing a source even at the sample's maximum distance.
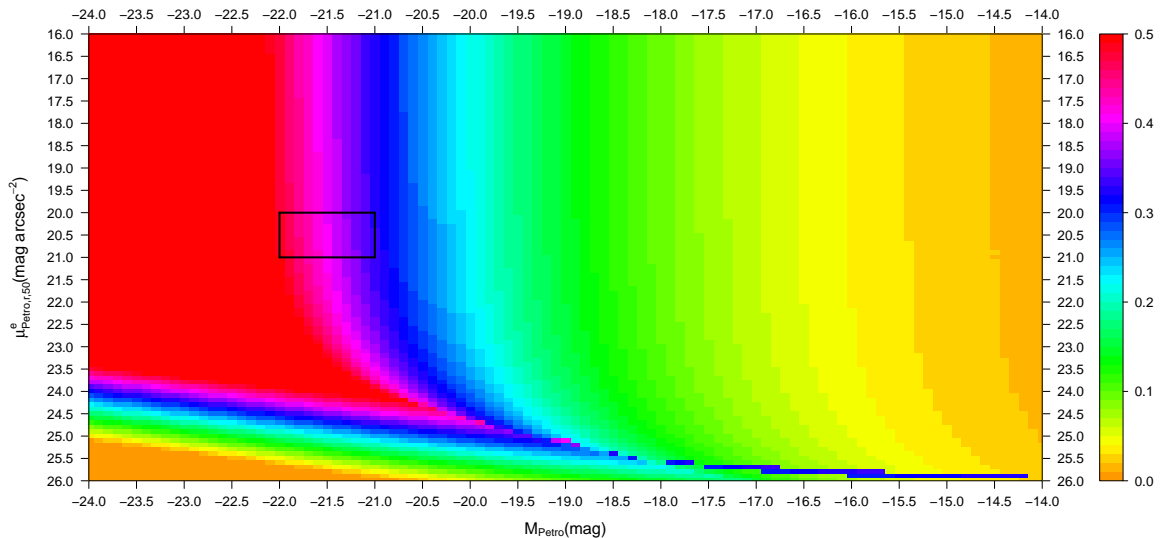
Figure C.1: Redshift completeness limits due to the GAMA Petrosian magnitude selection in the M, μ^X plane. The redshift limit colours range from $z = 0.5$ (red), to $z = 0$ (orange).

C.2.4 SDSS surface brightness detection constraint

The third constraint resolves the loophole in section C.2.3. Here the maximum distance that an object of known M, μ^X_{lim} will be observed is calculated. Sources that are fainter than a certain surface brightness will not be detectable because their central surface brightness will fall below the isophotal surface brightness detection limit of the SDSS survey (μ_{lim}). This effect will predominantly affect extended source detection. A minimum size limit of $\text{petrorad}_{r,50} = 1$ arcsec is imposed.

The prescription laid out by Phillipps et al. is followed. The angular diameter distance constraint is calculated using Equation C.3. $n = 1$ is assumed, the observed central brightness of the galaxy (μ^X_0) is calculated using Equation C.8 and μ_{lim} is taken from Equation C.7. The constant C is the same as in Equation C.4. g is calculated using the equation:

$$g(\mu_0) = 0.4 ln(10)(\mu_{X,lim} - \mu^X_0 - 10 log(1 + z) - K(z)) \tag{C.13}$$

also taken from Phillipps et al. The completeness limits due to the SDSS Petrosian surface brightness selection are shown in Figure C.2. This method assumes that the mean surface brightness calculation is a bias-free process, and can be accurately estimated regardless of the redshift or surface brightness of the source.
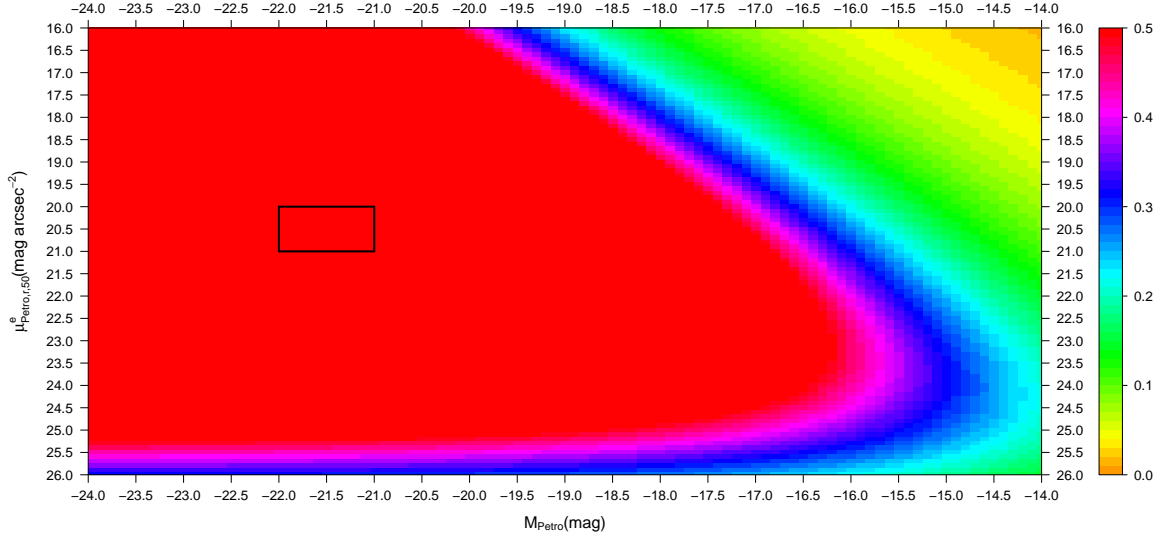
Figure C.2: Redshift completeness limits due to the GAMA Petrosian surface brightness selection in the M,μ^e plane. The redshift limit colours range from $z = 0.5$ (red), to $z = 0$ (orange). This figure was generated using a minimum size limit of petrorad$_{r,50} = 1.6$ arcsec (as used by Shen et al. 2003), rather than the 1 arcsec used within this paper, and using the SDSS hard-surface brightness limit of $26\,\mathrm{mag\,arcsec^{-2}}$.

C.2.5   SDSS Fiber magnitude constraint

The third GAMA constraint is due to the SDSS Fibermag limit imposed on our sample ($r_{fibermag,SDSS} < 22.5\,\mathrm{mag}$). As the fiber magnitude is a fixed size magnitude (3 arcsec in diameter), in order to calculate the fraction of light within the aperture it is necessary to assume a galaxy profile. The fiber magnitude is most likely to remove highly extended objects. In order to ascertain completeness, an exponential profile (Equation C.6) and a highly extended source are tested. petrorad$_{r,50} = 20$ arcsec is used ($\sim$ the 99.9% quantile from sources within the GAMA master catalogue). petrorad$_{r,50}$ is the radius containing 50% of the flux within the Petrosian aperture. Following Equation 6 of Graham et al. (2005), this is equivalent to an effective radius (radius$_{r,50}$) of 20.18 arcsec for a $n = 1$ Sérsic profile. The third constraint becomes:

$$d_3 = 10^{0.2(m_{lim}-(M-2.5log_{10}[h(r)])-25-K(z))}\;\mathrm{Mpc} \qquad (C.14)$$

where h is a function of the effective radius of the galaxy, used to calculate the fraction of light from the galaxy's profile that will be emitted within the 3 arcsec diameter of the

fibermag aperture:

$$h(r) = \frac{\int_0^{r=1.5} 2\pi w I(w) dw}{\int_0^{r=\infty} 2\pi w I(w) dw} \tag{C.15}$$

Realistically, light below the isophotal surface brightness limit of the data will not be included. If R_1 is the radius at which this occurs:

$$h(r) = \frac{\int_0^{1.5} 2\pi w I(w) dw}{\int_0^{R_1} 2\pi w I(w) dw} \tag{C.16}$$

If R_1 is smaller than the aperture's radius, $h(r) = 1$. The truncation radius, R_1, for an exponential profile can be calculated as

$$R_1 = \frac{(\mu_{lim}^X - \mu_0^X)a}{1.086} \tag{C.17}$$

where μ_{lim}^X is the isophotal limit (Equation C.12), μ_0^X is the central surface brightness of the galaxy (from Equation C.8) and a is the scalelength of the galaxy. Equation C.16 function simplifies to:

$$h(r) = \frac{2\pi a^2 I_0 (1 - (1+x)e^{-x})}{2\pi a^2 I_0 (1 - (1+y)e^{-y})} = \frac{(1 - (1+x)e^{-x})}{(1 - (1+y)e^{-y})} \tag{C.18}$$

where $x = \frac{r}{a}$ and $y = \frac{R_1}{a}$.

The half light radius ($\text{radius}_{r,50}$) $= 1.69a$ (when $r = \text{radius}_{r,50}$, by definition $(1+x)e^{-x} = 0.5$). Also, $R_1 = \frac{(\mu_{lim}^X - \mu_0^X)a}{1.086}$, so $y = \frac{(\mu_{lim}^X - \mu_0^X)}{1.086}$. Equation C.18 becomes:

$$h(r) = \frac{(1 - (1 + \frac{r}{\text{radius}_{r,50}/1.69})e^{-\frac{r}{\text{radius}_{r,50}}/1.69})}{(1 - (1 + \frac{(\mu_{lim}^X - \mu_0^X)}{1.086})e^{-\frac{(\mu_{lim}^X - \mu_0^X)}{1.086}})} \tag{C.19}$$

The completeness limits due to the SDSS fiber magnitude selection are shown in Figure C.3.

C.2.6   Redshift limits

d_1 and d_3 (from Sections C.2.2 and C.2.5) are luminosity distances. d_2 (Section C.2.4) is an angular diameter distance. The maximum redshift solutions for these constraints can be found using Equations C.2 and C.5. Our GAMA sample surface brightness maximum redshift solutions can be found by solving Equation C.12.
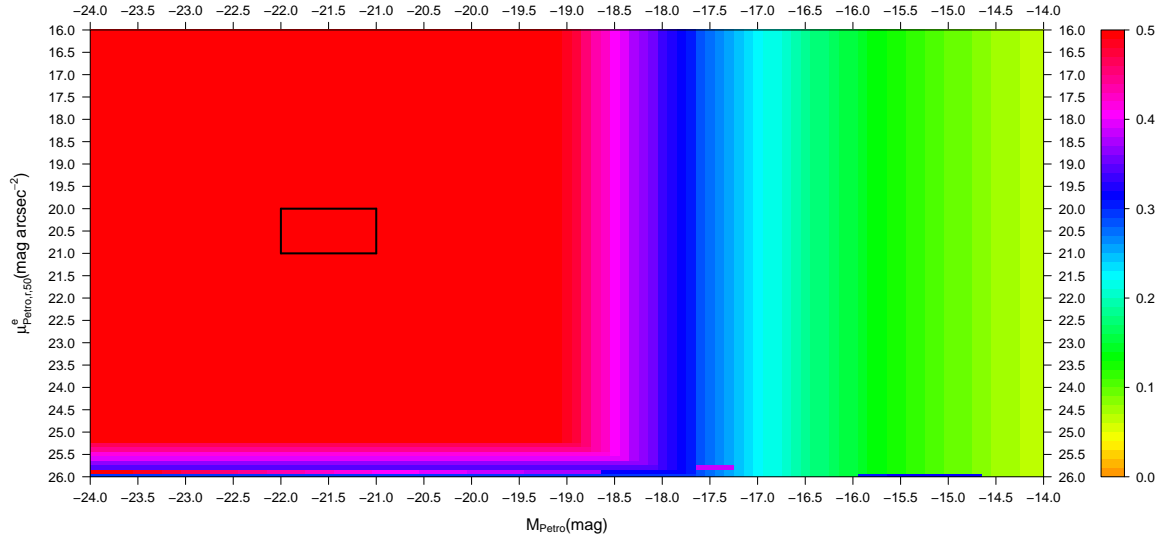
Figure C.3: Redshift completeness limits due to the GAMA Fiber magnitude selection in the M,μ^X plane. The redshift limit colours range from $z = 0.5$ (red), to $z = 0$ (orange).

The redshift limit for a source of known $M,\mu^{r,50}$ is $min(z_1, z_2, z_3, z_4)$.

D

BBDs from the data and the best fitting models to the data

In this chapter I reproduce images of the BBDs derived using $ugizYJHK$ Total photometry (r band data is shown in Figure 5.10, within the text), and the best-fitting functions (Choloniewski and modified-model) to the data.

Figure D.1: u_{Kron} BBDs for the deeper sample. The top figure shows the fit to the modified-model function, the bottom figure the fit to the Choloniewski function. The purple area denotes the region the SWML algorithm was limited to. The red line denotes the region that has complete coverage within a $30000\,\text{Mpc}^3$ volume.

Figure D.2: g_{Kron} BBDs for the deeper sample. The top figure shows the fit to the modified-model function, the bottom figure the fit to the Choloniewski function. The purple area denotes the region the SWML algorithm was limited to. The red line denotes the region that has complete coverage within a $30000\,\mathrm{Mpc}^3$ volume.
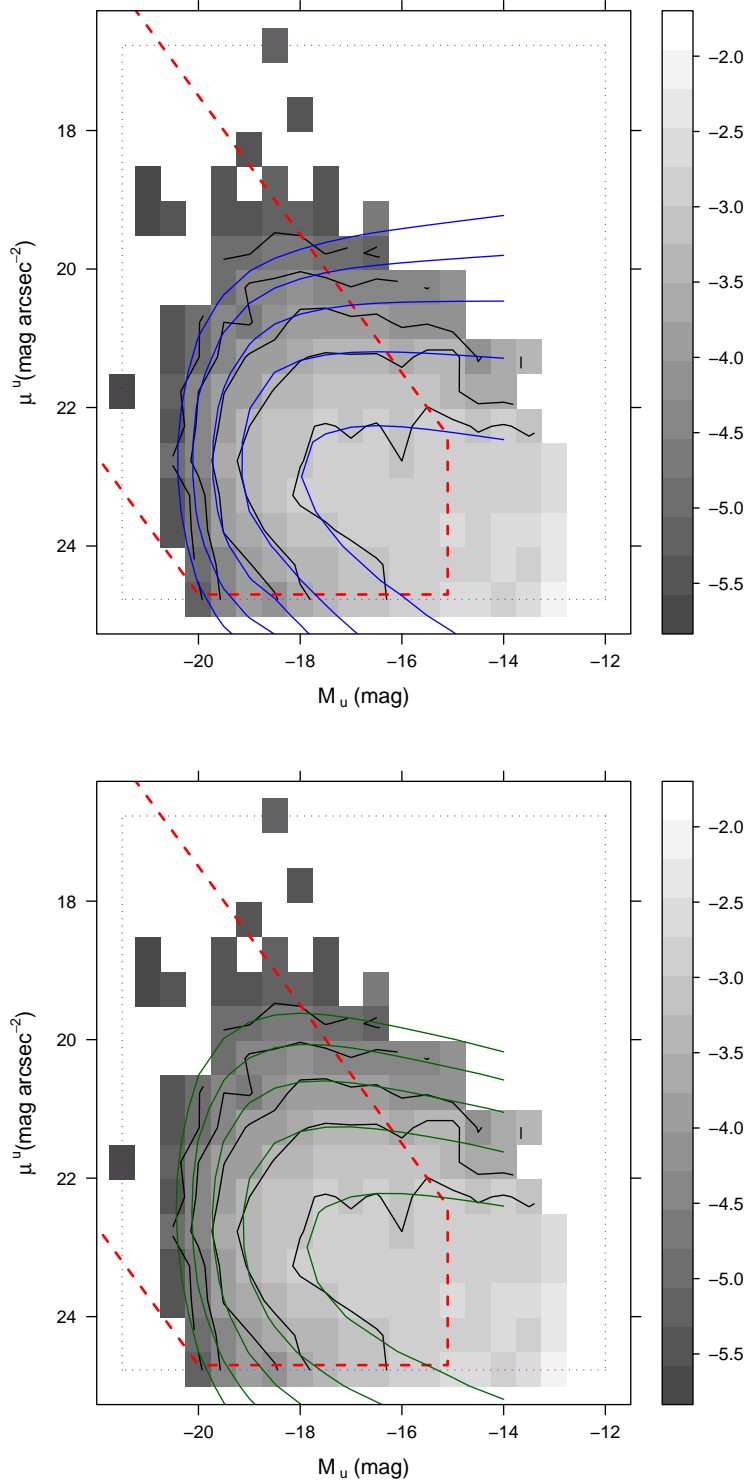
Figure D.3: i_{Kron} BBDs for the deeper sample. The top figure shows the fit to the modified-model function, the bottom figure the fit to the Choloniewski function. The purple area denotes the region the SWML algorithm was limited to. The red line denotes the region that has complete coverage within a $30000\,\mathrm{Mpc}^3$ volume.
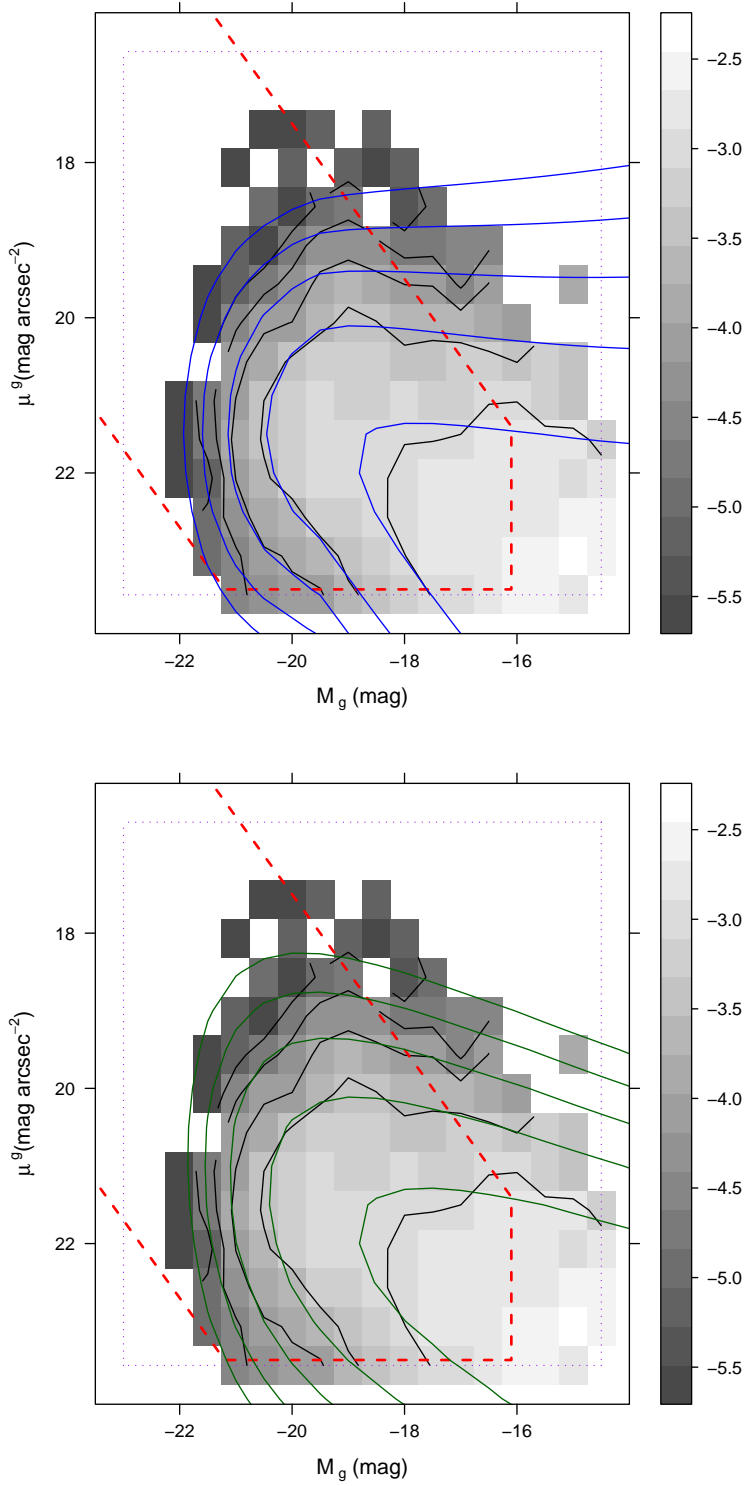
Figure D.4: z_{Kron} BBDs for the deeper sample. The top figure shows the fit to the modified-model function, the bottom figure the fit to the Choloniewski function. The purple area denotes the region the SWML algorithm was limited to. The red line denotes the region that has complete coverage within a $30000 \, \mathrm{Mpc}^3$ volume.

Figure D.5: Y_{Kron} BBDs for the deeper sample. The top figure shows the fit to the modified-model function, the bottom figure the fit to the Choloniewski function. The purple area denotes the region the SWML algorithm was limited to. The red line denotes the region that has complete coverage within a $30000\,\mathrm{Mpc}^3$ volume (accounting for the smaller area of coverage within this filter).
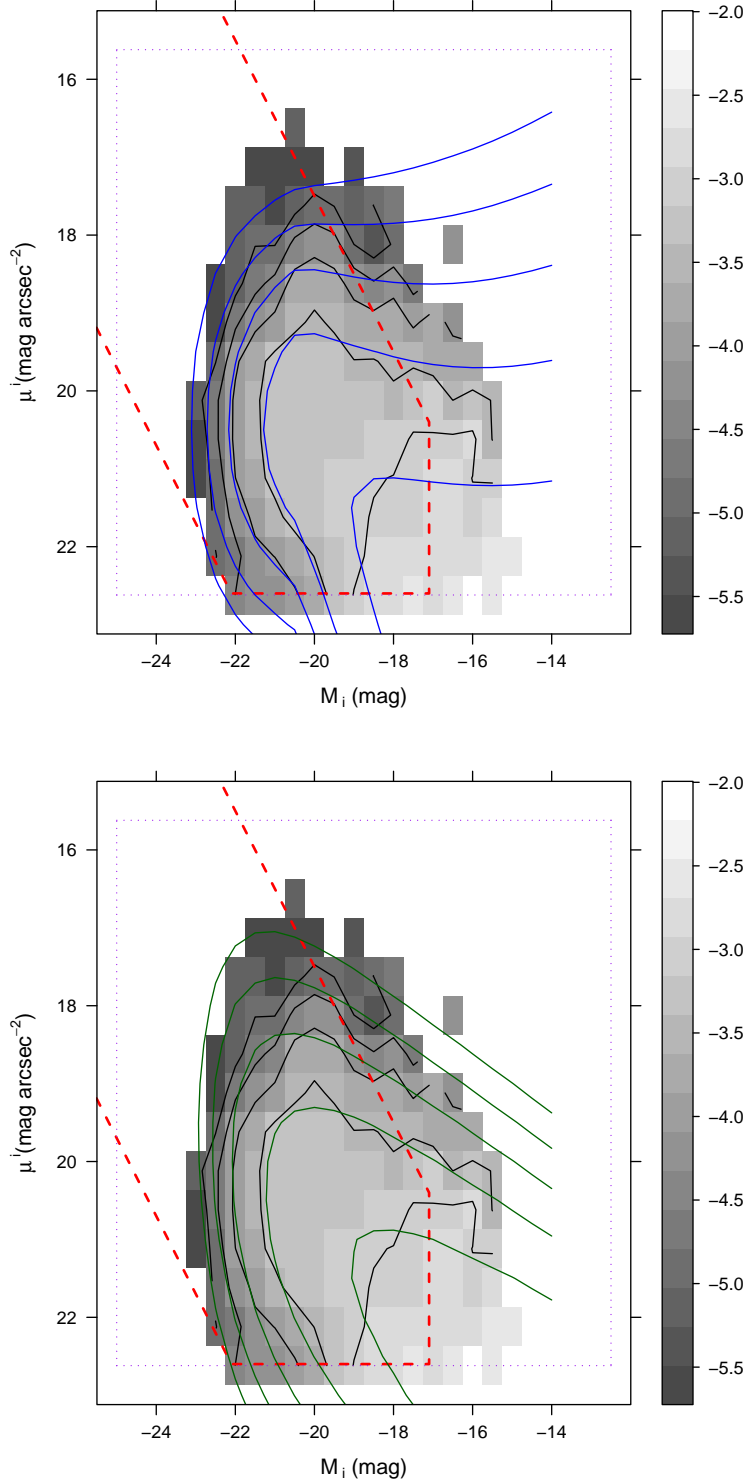
Figure D.6: J_{Kron} BBDs for the deeper sample. The top figure shows the fit to the modified-model function, the bottom figure the fit to the Choloniewski function. The purple area denotes the region the SWML algorithm was limited to. The red line denotes the region that has complete coverage within a $30000\,\mathrm{Mpc}^3$ volume (accounting for the smaller area of coverage within this filter).
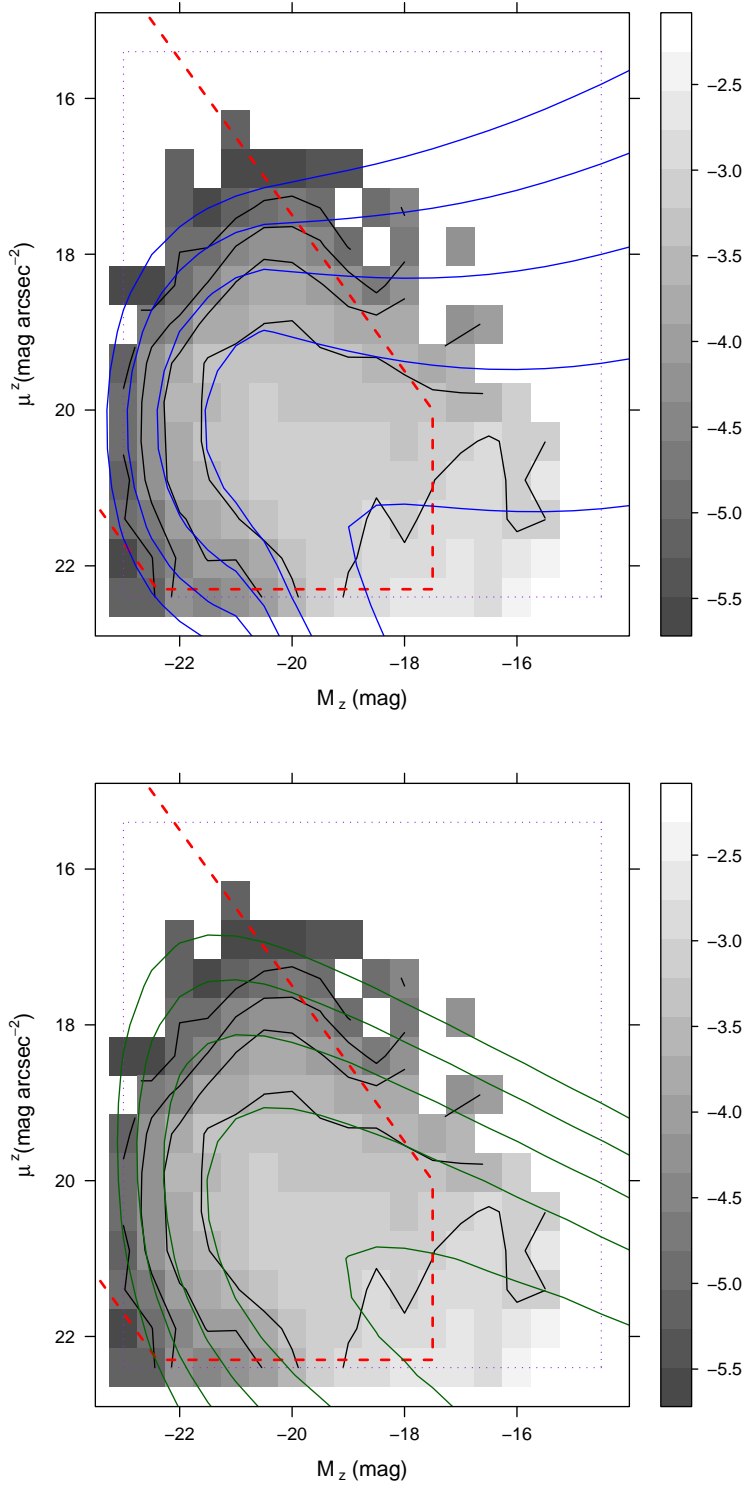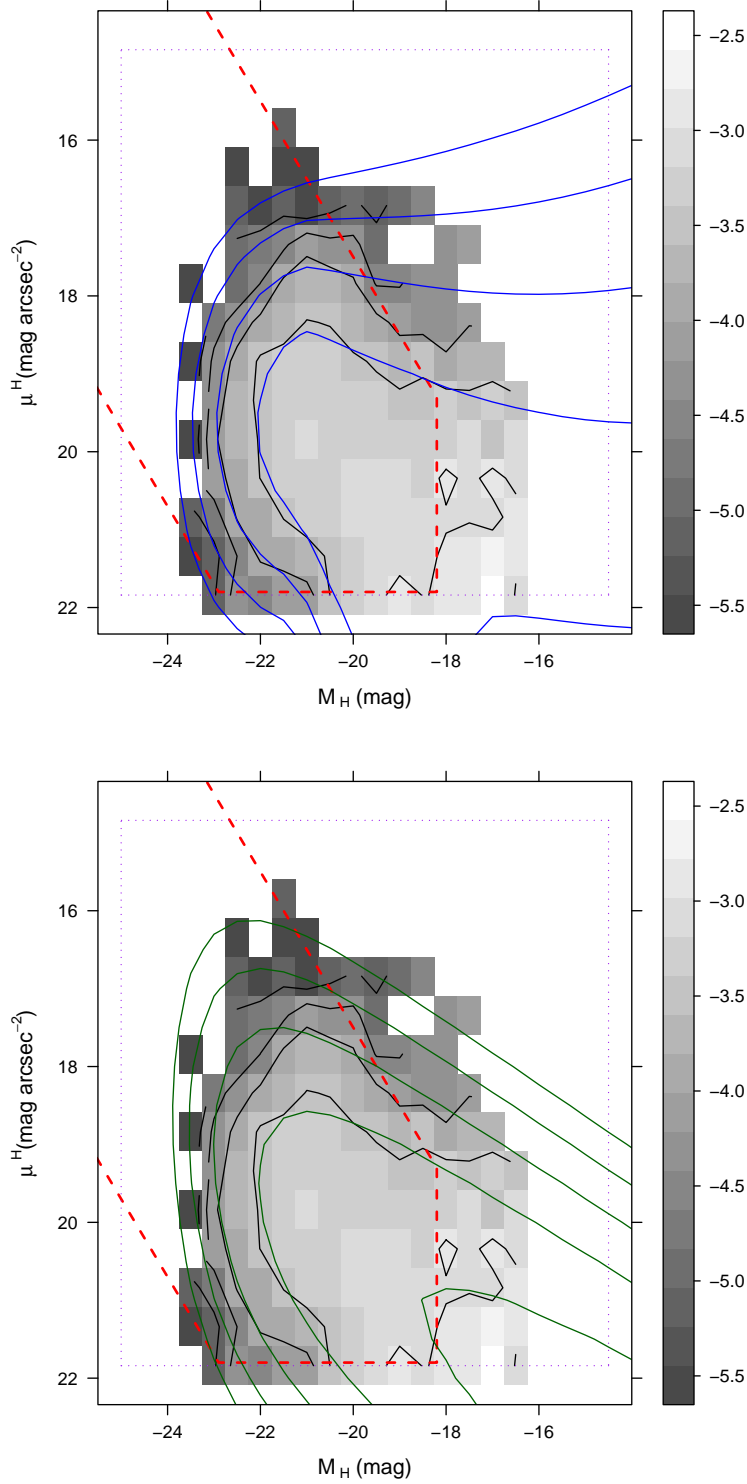
Figure D.7: H_{Kron} BBDs for the deeper sample. The top figure shows the fit to the modified-model function, the bottom figure the fit to the Choloniewski function. The purple area denotes the region the SWML algorithm was limited to. The red line denotes the region that has complete coverage within a $30000\,\mathrm{Mpc}^3$ volume (accounting for the smaller area of coverage within this filter).
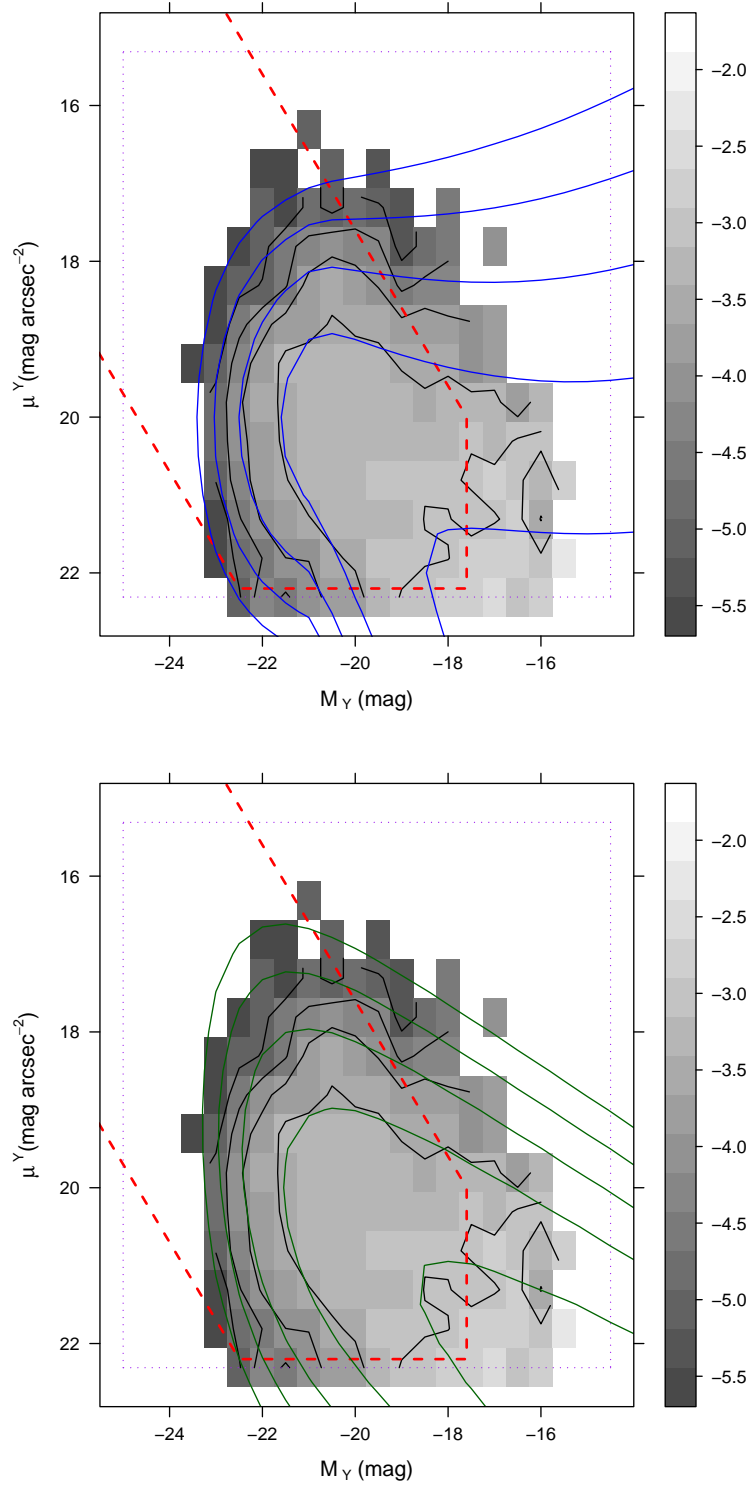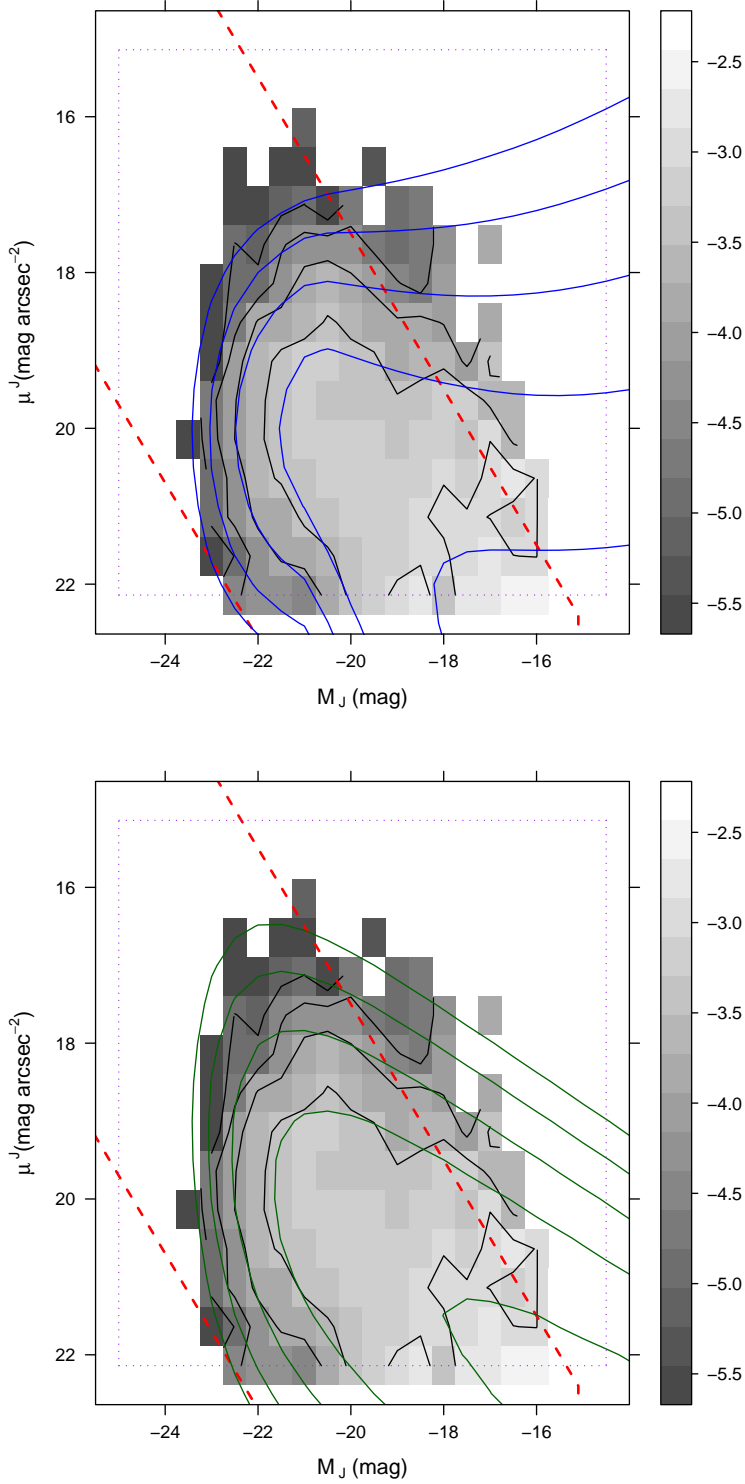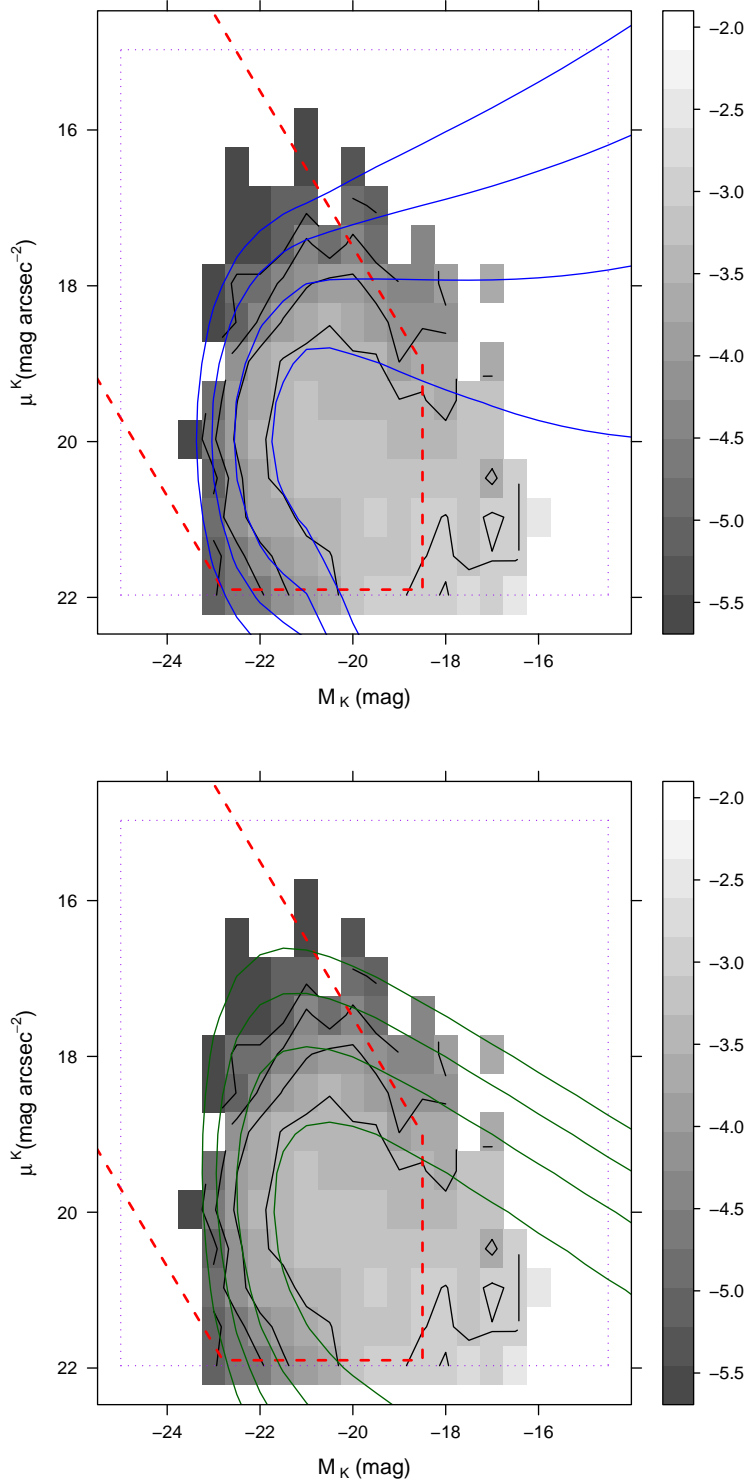
Figure D.8: K_{Kron} BBDs for the deeper sample. The top figure shows the fit to the modified-model function, the bottom figure the fit to the Choloniewski function. The purple area denotes the region the SWML algorithm was limited to. The red line denotes the region that has complete coverage within a $30000\,\mathrm{Mpc}^3$ volume (accounting for the smaller area of coverage within this filter).

Online resources

[1] - http://www.eso.org/~jliske/mgc/

[2] - http://www.ucolick.org/~cnaw/sun.html

[3] - http://www.sdss.org

[4] - http://surveys.roe.ac.uk/wsa

[5] - http://das.sdss.org

[6] - http://www.gama-survey.org

[7] - http://heasarc.gsfc.nasa.gov/docs/software/fitsio/fitsio.html

Bibliography

Abazajian, K., et al. 2004, AJ, 128, 502, arXiv:astro-ph/0403325

Abell, G. O. 1958, ApJS, 3, 211

Adelman-McCarthy, J. K., et al. 2007, ApJS, 172, 634, 0707.3380

——. 2008, ApJS, 175, 297, 0707.3413

Al Sufi, A. 964, Book of Fixed Stars, 1

Alexander, S. 1852, AJ, 2, 97

Alongi, M., Bertelli, G., Bressan, A., Chiosi, C., Fagotto, F., Greggio, L., & Nasi, E. 1993, A&AS, 97, 851

Andreon, S. 2002, A&A, 382, 495, arXiv:astro-ph/0111207

Arnaboldi, M., Neeser, M. J., Parker, L. C., Rosati, P., Lombardi, M., Dietrich, J. P., & Hummel, W. 2007, The Messenger, 127, 28

Baes, M., Fritz, J., Gadotti, D. A., Smith, D. J. B., Dunne, L., da Cunha, E., et al. 2010, A&A, 518, L39+, 1005.1773

Bahcall, J. N. 1975, ApJ, 200, L1

Baldry, I. K., & Glazebrook, K. 2003, ApJ, 593, 258, arXiv:astro-ph/0304423

Baldry, I. K., Glazebrook, K., & Driver, S. P. 2008, MNRAS, 388, 945, 0804.2892

Baldry, I. K., Glazebrook, K., et al. 2005, MNRAS, 358, 441, arXiv:astro-ph/0501110

Baldry, I. K., Robotham, A. S. G., Hill, D. T., et al. 2010, MNRAS, 404, 86, 0910.5120

Ball, N. M., Loveday, J., Brunner, R. J., Baldry, I. K., & Brinkmann, J. 2006, MNRAS, 373, 845, arXiv:astro-ph/0507547

Bastian, N., Covey, K. R., & Meyer, M. R. 2010, ARA&A, 48, 339, 1001.2965

Bastian, N., & Goodwin, S. P. 2006, MNRAS, 369, L9, arXiv:astro-ph/0602465

Bell, E. F., McIntosh, D. H., Katz, N., & Weinberg, M. D. 2003, ApJS, 149, 289, arXiv:astro-ph/0302543

Benson, A. J., Bower, R. G., Frenk, C. S., Lacey, C. G., Baugh, C. M., & Cole, S. 2003, ApJ, 599, 38, arXiv:astro-ph/0302450

Bertin, E., & Arnouts, S. 1996, A&AS, 117, 393

Bertin, E., Mellier, Y., Radovich, M., Missonnier, G., Didelon, P., & Morin, B. 2002, in Astronomical Society of the Pacific Conference Series, Vol. 281, Astronomical Data Analysis Software and Systems XI, ed. D. A. Bohlender, D. Durand, & T. H. Handley, 228–+

Bland-Hawthorn, J., Vlajić, M., Freeman, K. C., & Draine, B. T. 2005, ApJ, 629, 239, arXiv:astro-ph/0503488

Blanton, M. R., Dalcanton, J., Eisenstein, D., Loveday, J., Strauss, M. A., SubbaRao, M., Weinberg, D. H., et al. 2001, AJ, 121, 2358

Blanton, M. R., Hogg, D. W., Bahcall, N. A., Brinkmann, J., Britton, M., et al. 2003, APJ, 592, 819, arXiv:astro-ph/0210215

Blanton, M. R., & Roweis, S. 2007, AJ, 133, 734, arXiv:astro-ph/0606170

Blanton, M. R., Schlegel, D. J., Strauss, M. A., et al. 2005, AJ, 129, 2562, arXiv:astro-ph/0410166

Bower, R. G., McCarthy, I. G., & Benson, A. J. 2008, MNRAS, 390, 1399, 0808.2994

Brown, G. S., & Tinsley, B. M. 1974, ApJ, 194, 555

Brown, R. J. N. et al. 2003, MNRAS, 341, 747

Bruzual, G., & Charlot, S. 2003, MNRAS, 344, 1000, arXiv:astro-ph/0309134

Budavári, T., Szalay, A. S., Charlot, S., Seibert, M., Wyder, T. K., et al. 2005, ApJ, 619, L31, arXiv:astro-ph/0411305

Burbidge, E. M., & Burbidge, G. R. 1965, ApJ, 142, 634

Calura, F., Recchi, S., Matteucci, F., & Kroupa, P. 2010, MNRAS, 406, 1985, 1004.0832

Calzetti, D., Armus, L., Bohlin, R. C., Kinney, A. L., Koornneef, J., & Storchi-Bergmann, T. 2000, ApJ, 533, 682, arXiv:astro-ph/9911459

Calzetti, D., Kinney, A. L., & Storchi-Bergmann, T. 1994, ApJ, 429, 582

Casali, M., et al. 2007, A&A, 467, 777

Chabrier, G. 2001, ApJ, 554, 1274, arXiv:astro-ph/0107018

——. 2003, PASP, 115, 763, arXiv:astro-ph/0304382

Chen, X. Y., Liang, Y. C., Hammer, F., Prugniel, P., Zhong, G. H., Rodrigues, M., Zhao, Y. H., & Flores, H. 2010, A&A, 515, A101+, 1002.2013

Choi, J., & Nagamine, K. 2010, MNRAS, 407, 1464, 0909.5425

Choloniewski, J. 1985, MNRAS, 214, 197

Cohen, M., Wheaton, W. A., & Megeath, S. T. 2003, AJ, 126, 1090, arXiv:astro-ph/0304350

Cole, S., Aragon-Salamanca, A., Frenk, C. S., Navarro, J. F., & Zepf, S. E. 1994, MNRAS, 271, 781, arXiv:astro-ph/9402001

Cole, S., Lacey, C. G., Baugh, C. M., & Frenk, C. S. 2000, MNRAS, 319, 168, arXiv:astro-ph/0007281

Cole, S., Norberg, P., Baugh, C. M., Frenk, C. S., et al. 2001, MNRAS, 326, 255, arXiv:astro-ph/0012429

Colgate, S. A. 1979, ApJ, 232, 404

Colless, M., Dalton, G., Maddox, S., Sutherland, W., Norberg, P., Cole, S., et al. 2001, MNRAS, 328, 1039, arXiv:astro-ph/0106498

Condon, J. J. 1992, ARA&A, 30, 575

Cross, N., & Driver, S. P. 2002, MNRAS, 329, 579, arXiv:astro-ph/0110402

Cross, N., Driver, S. P., Couch, W., Baugh, C. M., Bland-Hawthorn, J., et al. 2001, MNRAS, 324, 825, arXiv:astro-ph/0012165

Cross, N. J. G., Driver, S. P., Liske, J., Lemon, D. J., Peacock, J. A., Cole, S., Norberg, P., & Sutherland, W. J. 2004, MNRAS, 349, 576, arXiv:astro-ph/0312317

Curtis, H. D. 1920, JRASC, 14, 317

da Costa, L. N., Geller, M. J., Pellegrini, P. S., Latham, D. W., Fairall, A. P., et al. 1994, ApJ, 424, L1

da Costa, L. N. et al. 1988, ApJ, 327, 544

da Costa, L. N., Pellegrini, P. S., Willmer, C., de Carvalho, R., Maia, M., Latham, D. W., & Geary, J. C. 1989, AJ, 97, 315

Davé, R. 2008, MNRAS, 385, 147, 0710.0381

Davis, M., Efstathiou, G., Frenk, C. S., & White, S. D. M. 1985, ApJ, 292, 371

Davis, M., & Huchra, J. 1982, ApJ, 254, 437

Davis, M., & Peebles, P. J. E. 1983, ApJ, 267, 465

de Grandi, S., Guzzo, L., Böhringer, H., Molendi, S., et al. 1999, ApJ, 513, L17, arXiv:astro-ph/9812423

de Jong, R. S., & Lacey, C. 1999, Ap&SS, 269, 569, arXiv:astro-ph/9910066

Diehl, R. et al. 2006, Nature, 439, 45, arXiv:astro-ph/0601015

Dreyer, J. L. E. 1888, MmRAS, 49, 1

Driver, S. P. 1999, ApJ, 526, L69, arXiv:astro-ph/9909469

Driver, S. P., Allen, P. D., et al. 2006, MNRAS, 368, 414, arXiv:astro-ph/0602240

Driver, S. P., Hill, D. T., Kelvin, L. S., Robotham, A. S. G., et al. 2010, ArXiv e-prints, 1009.0614

Driver, S. P., Liske, J., Cross, N. J. G., De Propris, R., & Allen, P. D. 2005, MNRAS, 360, 81, arXiv:astro-ph/0503228

Driver, S. P. et al. 2009, Astronomy and Geophysics, 50, 050000, 0910.5123

Driver, S. P., Popescu, C. C., Tuffs, R. J., Graham, A. W., Liske, J., & Baldry, I. 2008, ApJ, 678, L101, 0803.4164

Driver, S. P., Popescu, C. C., Tuffs, R. J., Liske, J., Graham, A. W., Allen, P. D., & de Propris, R. 2007, MNRAS, 379, 1022, 0704.2140

Driver, S. P., & Robotham, A. S. G. 2010, MNRAS, 407, 2131, 1005.2538

Eales, S., Dunne, L., et al. 2009, ArXiv e-prints, 0910.4279

Efstathiou, G., Ellis, R. S., & Peterson, B. A. 1988, MNRAS, 232, 431

Einstein, A. 1948, Reviews of Modern Physics, 20, 35

Eke, V. R., Baugh, C. M., Cole, S., Frenk, C. S., King, H. M., & Peacock, J. A. 2005, MNRAS, 362, 1233, arXiv:astro-ph/0412049

Elmegreen, B. G. 2006, ApJ, 648, 572, arXiv:astro-ph/0605520

Felten, J. E. 1976, ApJ, 207, 700

Fioc, M., & Rocca-Volmerange, B. 1997, A&A, 326, 950, arXiv:astro-ph/9707017

——. 1999, ArXiv Astrophysics e-prints, arXiv:astro-ph/9912179

Fisher, K. B., Huchra, J. P., Strauss, M. A., Davis, M., Yahil, A., & Schlegel, D. 1995, ApJS, 100, 69, arXiv:astro-ph/9502101

Freeman, K. C. 1970, ApJ, 160, 811

Friedmann, A. 1924, Zeitschrift fur Physik, 21, 326

Gallego, J., García-Dabó, C. E., Zamorano, J., Aragón-Salamanca, A., & Rego, M. 2002, ApJ, 570, L1, arXiv:astro-ph/0210062

Gallego, J., Zamorano, J., Aragon-Salamanca, A., & Rego, M. 1995, ApJ, 455, L1+

Geller, M. J., & Huchra, J. P. 1989, Science, 246, 897

Geller, M. J., Huchra, J. P., & de Lapparent, V. 1987, in IAU Symposium, Vol. 124, Observational Cosmology, ed. A. Hewitt, G. Burbidge, & L. Z. Fang, 301–312

Georgakakis, A., Hopkins, A. M., Sullivan, M., Afonso, J., Georgantopoulos, I., Mobasher, B., & Cram, L. E. 2003, MNRAS, 345, 939, arXiv:astro-ph/0307377

Gill, D. 1887, The Observatory, 10, 267

Graham, A. W. 2001, AJ, 121, 820, arXiv:astro-ph/0011256

Graham, A. W., & Driver, S. P. 2005, Publications of the Astronomical Society of Australia, 22, 118, arXiv:astro-ph/0503176

Graham, A. W., Driver, S. P., Petrosian, V., Conselice, C. J., Bershady, M. A., Crawford, S. M., & Goto, T. 2005, AJ, 130, 1535, arXiv:astro-ph/0504287

Gunn, J. E., & Knapp, G. R. 1993, in Astronomical Society of the Pacific Conference Series, Vol. 43, Sky Surveys. Protostars to Protogalaxies, ed. B. T. Soifer, 267–+

Halley, E. 1716, Royal Society of London Philosophical Transactions Series I, 29, 390

Hambly, N. C., et al. 2008, MNRAS, 384, 637, 0711.3593

Herschel, J. F. W. 1864, Royal Society of London Philosophical Transactions Series I, 154, 1

Herschel, W. 1784, Royal Society of London Philosophical Transactions Series I, 74, 437

——. 1786, Royal Society of London Philosophical Transactions Series I, 76, 457

——. 1789, Royal Society of London Philosophical Transactions Series I, 79, 212

Hewett, P. C., Warren, S. J., Leggett, S. K., & Hodgkin, S. T. 2006, MNRAS, 367, 454, arXiv:astro-ph/0601592

Hill, D. T., Driver, S. P., Cameron, E., Cross, N., Liske, J., & Robotham, A. 2010a, MNRAS, 295, 1002.3788

Hill, D. T., Kelvin, L. S., Driver, S. P., Robotham, A. S. G., et al. 2010b, MNRAS, 666

Høg, E., Fabricius, C., Makarov, V. V., et al. 2000, A&A, 355, L27

Hopkins, A. M. 2004, ApJ, 615, 209, arXiv:astro-ph/0407170

Hopkins, A. M. 2007, in Astronomical Society of the Pacific Conference Series, Vol. 380, Deepest Astronomical Surveys, ed. J. Afonso, H. C. Ferguson, B. Mobasher, & R. Norris, 423–+

Hopkins, A. M., & Beacom, J. F. 2006, ApJ, 651, 142, arXiv:astro-ph/0601463

Hoskin, M. 1999, The Cambridge Concise History of Astronomy (Cambridge University Press), 286–287

Hoskin, M. A. 1976, Journal for the History of Astronomy, 7, 169

Hoversten, E. A., & Glazebrook, K. 2008, ApJ, 675, 163, 0711.1309

Hu, F. X., Hamabe, M., Okamura, S., & Su, H. J. 1989, Ap&SS, 158, 43

Huang, J.-S., Glazebrook, K., Cowie, L. L., & Tinney, C. 2003, APJ, 584, 203, arXiv:astro-ph/0209440

Hubble, E. 1929, Proceedings of the National Academy of Science, 15, 168

——. 1936a, ApJ, 84, 270

Hubble, E. P. 1925, Popular Astronomy, 33, 252

——. 1936b, Realm of the Nebulae (Realm of the Nebulae, by E.P. Hubble. New Haven: Yale University Press, 1936), 59

Huchra, J., Davis, M., Latham, D., & Tonry, J. 1983, ApJS, 52, 89

Huchra, J. P., Geller, M. J., de Lapparent, V., & Corwin, Jr., H. G. 1990, ApJS, 72, 433

Huggins, W., & Miller, W. A. 1864, Royal Society of London Philosophical Transactions Series I, 154, 437

Humason, M. L., Mayall, N. U., & Sandage, A. R. 1956, AJ, 61, 97

Ivezić, Ž., Lupton, R. H., Schlegel, D., et al. 2004, Astronomische Nachrichten, 325, 583, arXiv:astro-ph/0410195

Johnston, S., Taylor, R., et al. 2008, Experimental Astronomy, 22, 151, 0810.5187

Jones, D. H., Peterson, B. A., Colless, M., & Saunders, W. 2006, MNRAS, 369, 25, arXiv:astro-ph/0603609

Karachentsev, I. D., Karachentseva, V. E., Huchtmeier, W. K., & Makarov, D. I. 2004, AJ, 127, 2031

Kelvin, L. S., Driver, S. P., & Robotham, A. S. G. 2010, MNRAS, 666

Kennicutt, R. C. et al. 2009, ApJ, 703, 1672, 0908.0203

Kennicutt, Jr., R. C. 1992, ApJ, 388, 310

——. 1998a, ARA&A, 36, 189, arXiv:astro-ph/9807187

——. 1998b, ApJ, 498, 541, arXiv:astro-ph/9712213

Kiang, T. 1961, MNRAS, 122, 263

Kintner, E. C. 1971, AJ, 76, 409

Kirby, E. M., Jerjen, H., Ryder, S. D., & Driver, S. P. 2008, AJ, 136, 1866, 0808.2529

Kirchhoff, G. 1863, Annalen der Physik, 194, 94

Kirkpatrick, J. D. et al. 1999, ApJ, 519, 802

Kirshner, R. P., Oemler, Jr., A., & Schechter, P. L. 1978, AJ, 83, 1549

Kleinmann, S. G. 1992, in Astronomical Society of the Pacific Conference Series, Vol. 34, Robotic Telescopes in the 1990s, ed. A. V. Filippenko, 203–212

Kochanek, C. S. et al. 2001, ApJ, 560, 566, arXiv:astro-ph/0011456

Köppen, J., Weidner, C., & Kroupa, P. 2007, MNRAS, 375, 673, arXiv:astro-ph/0611723

Kron, R. G. 1980, ApJS, 43, 305

Kroupa, P. 2006, ArXiv Astrophysics e-prints, arXiv:astro-ph/0605072

Kroupa, P. 2007, in IAU Symposium, Vol. 241, IAU Symposium, ed. A. Vazdekis & R. F. Peletier, 109–119

Kroupa, P., & Weidner, C. 2003, ApJ, 598, 1076, arXiv:astro-ph/0308356

Kroupa, P., & Weidner, C. 2005, in Astrophysics and Space Science Library, Vol. 327, The Initial Mass Function 50 Years Later, ed. E. Corbelli, F. Palla, & H. Zinnecker, 175–+, arXiv:astro-ph/0410461

Lada, C. J., & Lada, E. A. 2003, ARA&A, 41, 57, arXiv:astro-ph/0301540

Larson, R. B. 1998, MNRAS, 301, 569, arXiv:astro-ph/9808145

Lawrence, A., Warren, S. J., et al. 2007, MNRAS, 379, 1599, arXiv:astro-ph/0604426

Leavitt, H. S., & Pickering, E. C. 1912, Harvard College Observatory Circular, 173, 1

Liske, J., Driver, S. P., Allen, P. D., Cross, N. J. G., & De Propris, R. 2006, MNRAS, 369, 1547, arXiv:astro-ph/0604211

Liske, J., Lemon, D. J., Driver, S. P., Cross, N. J. G., & Couch, W. J. 2003, MNRAS, 344, 307, arXiv:astro-ph/0207555

Longhetti, M., & Saracco, P. 2009, MNRAS, 394, 774, 0811.4041

Madau, P. 1997, in American Institute of Physics Conference Series, Vol. 393, American Institute of Physics Conference Series, ed. S. S. Holt & L. G. Mundy, 481–490, arXiv:astro-ph/9612157

Maddox, S. J., Efstathiou, G., Sutherland, W. J., & Loveday, J. 1990, MNRAS, 243, 692

Maraston, C., Daddi, E., Renzini, A., Cimatti, A., Dickinson, M., Papovich, C., Pasquali, A., & Pirzkal, N. 2006, ApJ, 652, 85, arXiv:astro-ph/0604530

Marigo, P. et al. 2010, in IAU Symposium, Vol. 262, IAU Symposium, ed. G. Bruzual & S. Charlot, 36–43

Martin, N. F., Ibata, R. A., Bellazzini, M., Irwin, M. J., Lewis, G. F., & Dehnen, W. 2004, MNRAS, 348, 12, arXiv:astro-ph/0311010

Massey, P. 2003, ARA&A, 41, 15

Mauch, T., & Sadler, E. M. 2007, MNRAS, 375, 931, arXiv:astro-ph/0612018

Mayall, N. U. 1960, Annales d'Astrophysique, 23, 344

Mayall, N. U., & de Vaucouleurs, A. 1962, AJ, 67, 363

Meyer, M. 2009, in Panoramic Radio Astronomy: Wide-field 1-2 GHz Research on Galaxy Evolution, 0912.2167

Miller, G. E., & Scalo, J. M. 1979, ApJS, 41, 513

Misiriotis, A., Popescu, C. C., Tuffs, R., & Kylafis, N. D. 2001, A&A, 372, 775, arXiv:astro-ph/0104346

Montero-Dorta, A. D., , & Prada, F. 2008, ArXiv e-prints, 0806.4930

Morrison, J. E. 1995, in Astronomical Society of the Pacific Conference Series, Vol. 77, Astronomical Data Analysis Software and Systems IV, ed. R. A. Shaw, H. E. Payne, & J. J. E. Hayes, 179–+

Nasim, O. W. 2010, The British Journal for the History of Science, 43, 353

Neugebauer, G., & Leighton, R. B. 1969, Two-micron sky survey. A preliminary catalogue

Norberg, P., Cole, S., Baugh, C. M., Frenk, C. S., et al. 2002, MNRAS, 336, 907, arXiv:astro-ph/0111011

Oemler, Jr., A., Tucker, D. L., Kirshner, R. P., Lin, H., Shectman, S. A., & Schechter, P. L. 1993, in Astronomical Society of the Pacific Conference Series, Vol. 51, Observational Cosmology, ed. G. L. Chincarini, A. Iovino, T. Maccacaro, & D. Maccagni, 81–+

Oke, J. B., & Gunn, J. E. 1983, ApJ, 266, 713

Parry, O. H., Eke, V. R., & Frenk, C. S. 2009, MNRAS, 396, 1972, 0806.4189

Peebles, P. J. E., & Hauser, M. G. 1974, ApJS, 28, 19

Peng, C. Y., Ho, L. C., Impey, C. D., & Rix, H. W. 2007, in Bulletin of the American Astronomical Society, Vol. 38, Bulletin of the American Astronomical Society, 804–+

Petrosian, V. 1976, ApJ, 209, L1

Pflamm-Altenburg, J., & Kroupa, P. 2009, ApJ, 706, 516, 0910.1089

Phillipps, S., Davies, J. I., & Disney, M. J. 1990, MNRAS, 242, 235

Phillipps, S., & Driver, S. 1995, MNRAS, 274, 832, arXiv:astro-ph/9511133

Pier, J. R., Munn, J. A., et al. 2003, AJ, 125, 1559, arXiv:astro-ph/0211375

Poggianti, B. M. 1997, A&AS, 122, 399, arXiv:astro-ph/9608029

Pohlen, M., Beckman, J. E., Hüttemeister, S., Knapen, J. H., Erwin, P., & Dettmar, R. 2004, in Astrophysics and Space Science Library, Vol. 319, Penetrating Bars Through Masks of Cosmic Dust, ed. D. L. Block, I. Puerari, K. C. Freeman, R. Groess, & E. K. Block , 713–+, arXiv:astro-ph/0405541

Prescott, M., Baldry, I. K., & James, P. A. 2009, MNRAS, 397, 90, 0904.0349

Price, S. D. 2009, Space Sci. Rev., 142, 233

Reid, I. N., Gizis, J. E., & Hawley, S. L. 2002, AJ, 124, 2721

Reid, I. N. et al. 1999, ApJ, 521, 613, arXiv:astro-ph/9905170

Robertson, H. P. 1935, ApJ, 82, 284

Robotham, A., Driver, S. P., Norberg, P., et al. 2010, Publications of the Astronomical Society of Australia, 27, 76, 0910.5121

Rood, H. J., Page, T. L., Kintner, E. C., & King, I. R. 1972, ApJ, 175, 627

Salpeter, E. E. 1955, ApJ, 121, 161

Sandage, A. 1978, AJ, 83, 904

Sandage, A., & Tammann, G. A. 1975, ApJ, 196, 313

——. 1981, A revised Shapley-Ames Catalog of bright galaxies

Saunders, W., Rowan-Robinson, M., Lawrence, A., Efstathiou, G., Kaiser, N., Ellis, R. S., & Frenk, C. S. 1990, MNRAS, 242, 318

Scalo, J. M. 1986, Fund. Cosmic Phys., 11, 1

Schaye, J. et al. 2010, MNRAS, 402, 1536, 0909.5196

Schechter, P. 1976, ApJ, 203, 297

Schlegel, D. J., Finkbeiner, D. P., & Davis, M. 1998, ApJ, 500, 525, arXiv:astro-ph/9710327

Schmidt, M. 1965, ApJ, 141, 1

——. 1968, ApJ, 151, 393

Secchi, A. 1869, Astronomische Nachrichten, 73, 129

Sérsic, J. L. 1963, Boletin de la Asociacion Argentina de Astronomia La Plata Argentina, 6, 41

Shapley, H. 1918, PASP, 30, 42

——. 1919, PASP, 31, 261

Shapley, H., & Ames, A. 1932, Annals of Harvard College Observatory, 88, 41

Shen, S., Mo, H. J., White, S. D. M., Blanton, M. R., Kauffmann, G., Voges, W., Brinkmann, J., & Csabai, I. 2003, MNRAS, 343, 978, arXiv:astro-ph/0301527

Slipher, V. M. 1913, Lowell Observatory Bulletin, 2, 56

Smith, A. J., Loveday, J., & Cross, N. J. G. 2009, MNRAS, 397, 868, 0806.0343

Smith, D. J. B., Dunne, L., Maddox, S. J., Eales, S., et al. 2010, ArXiv e-prints, 1007.5260

Sodre, Jr., L., & Lahav, O. 1993, MNRAS, 260, 285

Somerville, R. S., Lee, K., Ferguson, H. C., Gardner, J. P., Moustakas, L. A., & Giavalisco, M. 2004, ApJ, 600, L171, arXiv:astro-ph/0309071

Strauss, M. A., Weinberg, D. H., Lupton, R. H., Narayanan, V. K., et al. 2002, AJ, 124, 1810, arXiv:astro-ph/0206225

Taylor, M. B. 2006, in Astronomical Society of the Pacific Conference Series, Vol. 351, Astronomical Data Analysis Software and Systems XV, ed. C. Gabriel, C. Arviset, D. Ponz, & S. Enrique, 666–+

Tifft, W. G., & Gregory, S. A. 1976, ApJ, 205, 696

Tinsley, B. M. 1972, A&A, 20, 383

Tonry, J., & Davis, M. 1979, AJ, 84, 1511

Treyer, M., Wyder, T. K., Schiminovich, D., et al. 2005, ApJ, 619, L19, arXiv:astro-ph/0411308

van der Kruit, P. C. 2001, in Astronomical Society of the Pacific Conference Series, Vol. 230, Galaxy Disks and Disk Galaxies, ed. J. G. Funes & E. M. Corsini, 119–126, arXiv:astro-ph/0010354

van Maanen, A. 1921, PASP, 33, 200

VERITAS Collaboration. 2009, Nature, 462, 770, 0911.0873

Vorontsov-Vel'Yaminov, B. A., & Arkhipova, V. P. 1968, in Morphological catalogue of galaxies., 4 (1968), 0–+

Walcher, J., Groves, B., Budavári, T., & Dale, D. 2010, Ap&SS, 257

Walker, A. G. 1937, Proceedings of the London Mathematical Society, s2-42, 90, http://plms.oxfordjournals.org/content/s2-42/1/90.full.pdf+html

Warren, S. J., Hambly, N. C., Dye, S., et al. 2007, MNRAS, 375, 213, arXiv:astro-ph/0610191

Weidner, C., & Kroupa, P. 2004, MNRAS, 348, 187, arXiv:astro-ph/0310860

——. 2005, ApJ, 625, 754, arXiv:astro-ph/0502525

Weidner, C., Kroupa, P., & Larsen, S. S. 2004, MNRAS, 350, 1503, arXiv:astro-ph/0402631

White, S. D. M., Frenk, C. S., Davis, M., & Efstathiou, G. 1987, ApJ, 313, 505

Wilkins, S. M., Hopkins, A. M., Trentham, N., & Tojeiro, R. 2008a, MNRAS, 391, 363, 0809.2518

Wilkins, S. M., Trentham, N., & Hopkins, A. M. 2008b, MNRAS, 385, 687, 0801.1594

Willmer, C. N. A. 1997, AJ, 114, 898, arXiv:astro-ph/9707246

Wright, E. L. 2001, ApJ, 556, L17, arXiv:astro-ph/0102053

Wunderlich, E., & Klein, U. 1988, A&A, 206, 47

Wyder, T. K., Treyer, M. A., Milliard, B., Schiminovich, D., Arnouts, S., et al. 2005, APJL, 619, L15, arXiv:astro-ph/0411364

York, D. G., et al. 2000, AJ, 120, 1579, arXiv:astro-ph/0006396

Yun, M. S., Reddy, N. A., & Condon, J. J. 2001, ApJ, 554, 803, arXiv:astro-ph/0102154

Zacharias, N., Urban, S. E., Zacharias, M. I., et al. 2000, AJ, 120, 2131

Zucca, E., Zamorani, G., Vettolani, G., et al. 1997, A&A, 326, 477, arXiv:astro-ph/9705096

Zwicky, F. 1957, Morphological astronomy (Berlin: Springer, 1957)